AN ABSTRACT OF THE THESIS OF

Kathy Q. Hu for the degree of Master of Science in Mechanical Engineering presented on 20 January 2023.

Title: An Investigation of the Feasibility of a Process-Intensified Differential Temperature Water-Gas Shift Reactor with Integrated Pt/Al_2O_3 Catalyst

Abstract approved: _____

Brian M. Fronk

There has been serious interest in hydrogen as a source of energy in the United States due to its capability of delivering a sustainable, carbon-free energy future. Currently, most hydrogen in the United States is produced via the steam methane reforming of natural gas, which converts methane to hydrogen through a series of energy-intensive and carbon-producing reactions, one being the water-gas shift (WGS) reaction. Previous research suggests that the implementation of a differential temperature WGS reactor operating under optimal temperature conditions reduces the required reactor volume to achieve a specific CO conversion level and the hydrogen production cost associated with the overall steam reforming process. This thesis investigates the feasibility of utilizing a plate architecture WGS microreactor with integrated platinum-ceria catalyst to intensify the WGS reaction with the goal of increasing overall hydrogen yield of the steam-methane reforming process and bridging the gap towards a sustainable hydrogen future.

First, modeling from previous research was used to inform the design and manufacture of a sub-scale WGS microreactor prototype. Next, a catalyst recipe for a platinum catalyst with ceria precursor supported on washcoated alumina was developed and coated onto the walls of the reaction channels in the prototype. Finally, an experimental test set-up with a reacting gas loop and integrated cooling loop was designed, constructed, and configured to

enable chemical testing of the WGS reactor prototype. The WGS reactor prototype with integrated catalyst was assembled and integrated onto the test loop. The thermal behavior of the prototype was validated using inert gases, but sealing challenges arose due to the high number of mechanically sealed surfaces.

The results of catalyst adhesion characterization studies suggest that enhancing the surface roughness of the substrate's surface greatly improves the adhesion of the platinum catalyst. The results of the test loop experiments suggest that difficulties in sealing plate architecture-style reactors make this type of design mechanically feasible but impractical for realizing the potential of the intensified water-gas shift reaction.

An Investigation of the Feasibility of a Process-Intensified Differential Temperature Water-Gas Shift Reactor with Integrated Pt/Al_2O_3 Catalyst

by

Kathy Q. Hu

A THESIS

submitted to

Oregon State University

in partial fulfillment of
the requirements for the
degree of

Master of Science

Presented 20 January 2023
Commencement June 2023

Master of Science thesis of Kathy Q. Hu presented on 20 January 2023.

APPROVED:

Major Professor, representing Mechanical Engineering

Head of the School of Mechanical, Industrial, and Manufacturing Engineering

---

Dean of the Graduate School

I understand that my thesis will become part of the permanent collection of Oregon State University libraries. My signature below authorizes release of my thesis to any reader upon request.

Kathy Q. Hu, Author

ACKNOWLEDGEMENTS

Thank you to my advisor, Dr. Brian Fronk, for taking a chance on a seventeen year-old. You have been a consistently positive role model in my life for a very long time now. Your mentorship helped guide me through my journey into engineering and you have shaped me into a better engineer.

It was a joy to be able to work with my friends Thomas and Bryan. Thank you both for your help and companionship throughout the research process.

This work was partially funded through the RAPID Institute under the U.S. Department of Energy contract (DE-EE0007888-10-4) and through the High Impact Opportunity Project program under the Oregon Innovation Council. I would like to acknowledge Dr. Goran Jovanovic and Lucas Freiberg for their technical expertise and collaboration on this project.

TABLE OF CONTENTS

TABLE OF CONTENTS (Continued)

Page

TABLE OF CONTENTS (Continued)

TABLE OF CONTENTS (Continued)

LIST OF FIGURES

LIST OF FIGURES (Continued)

Figure Page

LIST OF FIGURES (Continued)

Figure Page

LIST OF FIGURES (Continued)

Figure Page

LIST OF FIGURES (Continued)

Figure Page

LIST OF FIGURES (Continued)

Figure Page

LIST OF FIGURES (Continued)

LIST OF TABLES

LIST OF TABLES (Continued)

LIST OF TABLES (Continued)

Table | Page

LIST OF APPENDIX FIGURES

For Mae.

Chapter 1: Introduction

1.1 Background

The vast majority of energy consumed in the United States is sourced from coal, petroleum, and natural gas. In 2021, the U.S. Energy Information Administration (EIA) estimated that fossil fuels provided 79% of the energy consumed in the United States to power the end use sectors of transportation, residential power, commercial power, and industrial processes [1]. A breakdown of energy sources and consumption in the United States for 2021 is shown below in Figure 1.1.

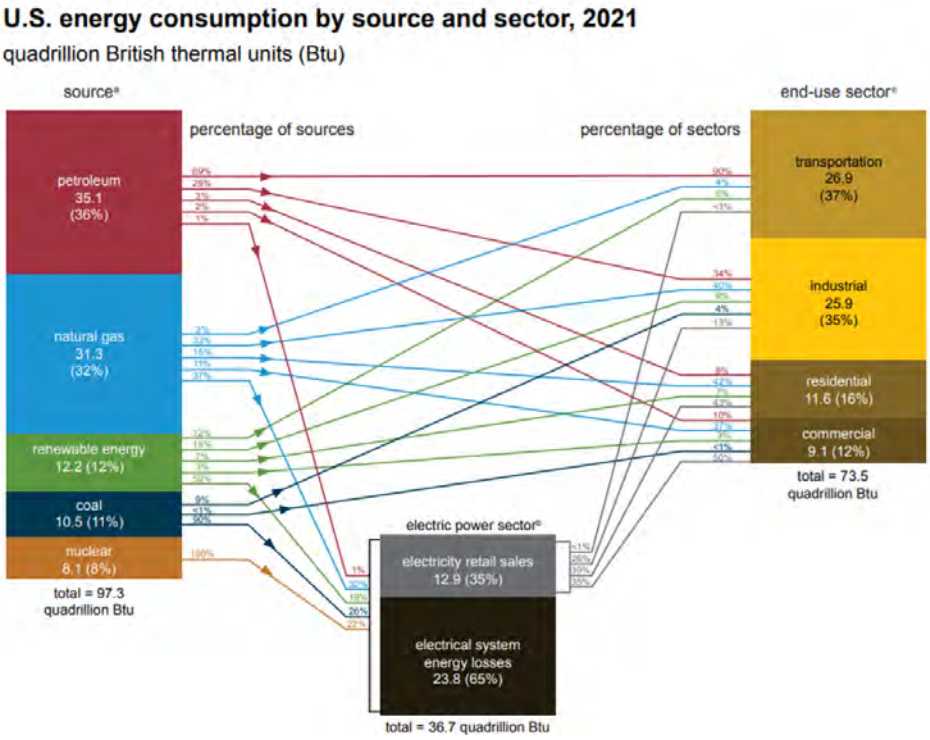

Figure 1.1: U.S. energy consumption by source and sector for 2021 [1].

The finite supply of these nonrenewable resources motivates the development of more sustainable energy sources and systems. One promising energy carrier is hydrogen, which can store and deliver usable energy to each of the aforementioned end-use sectors. The

desirability for hydrogen as an energy carrier builds on its most important attributes: it is storable, light, reactive, energy-dense per unit mass, and can be readily produced at an industrial scale. There is renewed interest in the use of hydrogen for clean energy systems because it can be utilized without direct emissions of greenhouse gases and it can be produced from a diverse range of low-carbon energy sources. These attributes make hydrogen a critical piece in building a resilient and sustainable energy future.

1.2 The hydrogen economy

In the past, there have been several pushes for hydrogen as an alternative energy carrier. However, little of this interest translated into a sustainable investment into hydrogen because most efforts were focused on the single end-use sector of transportation and not on other sectors such as heating, power generation, and electricity storage. This time around, there are several complementary reasons as to why it may be different. Hydrogen can:

1. Deliver dramatic greenhouse gas emission reductions, which aligns well with policies regarding target emission reductions,
2. Provide energy security, stimulate economic development, decrease local air pollution, and increase access to energy,
3. Ensure the growth of renewable electricity, and
4. Benefit from previous positive experiences in the clean energy sphere.

On a global scale, 76% of dedicated hydrogen is produced from natural gas and 23% is produced from coal [2]. **In the United States, 95% of hydrogen is produced from the steam-methane reforming (SMR) of natural gas** [3]. The International Energy Association (IEA) provides an estimate of the cost of producing hydrogen from natural gas in 2018 with and without carbon capture, utilization, and storage (CCUS) for various world regions, shown below in Figure 1.2. The cost of hydrogen derived from the SMR process without CCUS in the United States is approximately $1 per kilogram of hydrogen, with

natural gas costs, capital expenses (CAPEX), and operational expenses (OPEX) accounting for \$0.49, \$0.34, and \$0.17 of this cost, respectively.

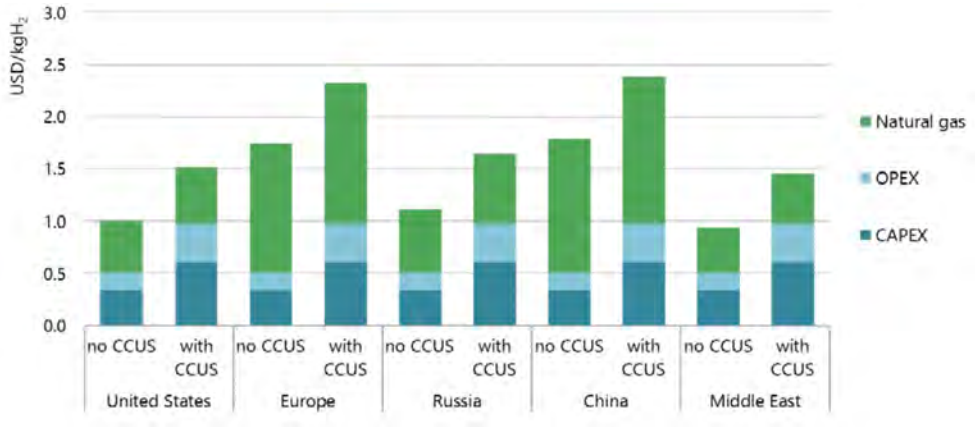

Figure 1.2: Hydrogen production costs using natural gas with and without CCUS in various world regions in 2018 [2].

The availability of low-cost gas is a crucial cost determinant for hydrogen derived from natural gas, yet the EIA estimates that there only exists enough natural gas in the United States to last 84 more years [4]. As natural gas reserves deplete and costs rise, so too will the cost of producing hydrogen via steam-methane reforming, which motivates more efficient use of remaining natural gas reserves. In the long term, it is desirable to completely transition away from utilizing natural gas and other fossil fuels for the production of hydrogen, but to make this happen, we must initially develop large-scale, low-cost, and high-efficiency hydrogen production processes that reduce the cost and carbon emissions of hydrogen, and stimulate wider use of hydrogen throughout the energy ecosystem. More efficient reforming of natural gas can be a bridging technology between the hydrogen economy of today and that of a future driven by 100% low-carbon energy.

1.3 Hydrogen production

The U.S. Department of Energy's Office of Energy Efficiency & Renewable Energy (EERE) highlights three broad categories of technologies for the production of hydrogen [5]:

1. Thermochemical processes
    - Various thermochemical processes transform feedstocks such as natural gas, coal, and biomass into hydrogen.
    - Prominent examples of industrially mature hydrogen production pathways include the steam-methane reforming of natural gas, coal and biomass gasification, and partial oxidation.
2. Electrolysis
    - Electrolyzers utilize electricity to split water into its constituents, hydrogen (H_2) and oxygen (O_2).
    - While a well-developed and commercially available technology, as of 2020, hydrogen produced from electrolysis costs \$6/kg [6], which is six times the cost of deriving hydrogen from natural gas. The costs associated with electrolysis are higher than thermochemical processes because of greater energy demand [7].
3. Photolysis
    - Photolytic processes utilize light energy to split water into hydrogen and oxygen.
    - While these technologies are currently not viable for large scale production due to insufficient advances in research and development, they offer the potential for low-carbon and sustainable hydrogen production in the long-term.

Despite these various technologies, steam-methane reforming of natural gas dominates the commercial hydrogen production market in the United States.

1.4 Targets and legislation

In light of the ever-growing impacts of climate change, enacting legislation and setting targets for the commercialization of renewable energy is a crucial step in the transition to a clean, carbon-neutral energy future. In the U.S. hydrogen sector, there are several key laws and initiatives that have been enacted to incentivize and pave the path for clean hydrogen production.

1. **Energy Policy Act of 2005:** The Energy Policy Act of 2005 was enacted to improve U.S. energy policies by providing incentives for the development for various energy technologies. Title VIII established a research and development program for the development, demonstration, and commercialization of hydrogen energy. This legislation was the first major push since the Energy Policy Act of 1992 to develop the hydrogen economy, but the goals of this title of the legislation fell short due to heavy concurrent promotion of fossil fuel use and technologies [8].

2. **Hydrogen Shot:** The U.S. Department of Energy launched its Hydrogen Shot initiative in June 2021 to accelerate the affordability and abundance of clean hydrogen. The Hydrogen Shot initiative seeks to reduce the cost of producing hydrogen from clean, carbon-neutral production pathways from $5 per kilogram to $1 per kilogram in one decade. If the goals of the Hydrogen Shot initiative are achieved, projections show the potential for a 16% reduction in carbon dioxide emissions by 2050 along with the creation of 700,000 jobs and $140 billion in revenues by 2030 [9].

Figure 1.3: The U.S. Department of Energy's Hydrogen Shot "1 1 1" initiative aims to reduce the cost of clean hydrogen by 80% to $1 per 1 kilogram in 1 decade [9].

3. **Infrastructure Investment and Jobs Act:** The Infrastructure Investment and Jobs Act (IIJA), also known as the Bipartisan Infrastructure Bill, is a sweeping infrastructure bill that was enacted in November 2021. This bill appropriates $9.5 billion to the research, development, and demonstration of clean hydrogen programs. The majority of the funding ($8 billion) is allotted to the newly created Office of Clean Energy Demonstration for the development of four regional clean hydrogen hubs across the United States [10].

   This landmark bill explicitly defines "clean hydrogen" in U.S. law. As of the publication of this thesis, clean hydrogen is defined as hydrogen “produced with a carbon intensity equal to or less than 2 kilograms of carbon-dioxide equivalent produced at the site of production per kilogram of hydrogen produced.” This definition is subject to change after consultation with the Environmental Protection Agency.

   In December of 2022, the Department of Energy announced their intent to issue another $750 million in funding to reduce the cost of clean-hydrogen technologies. This investment is to speed up the technical advances and scale-up that is required to realize the Hydrogen Shot goal of producing clean hydrogen for $1 per kilogram by 2031 [11].

These described policies are critical for the long-term development and preservation of a clean hydrogen economy. In the near-term, efforts must be made to improve current hydrogen production pathways and decrease the carbon intensity associated with these production methods.

1.5 Steam-methane reforming of natural gas

Presently, 95% of hydrogen in the U.S. is produced from the steam-methane reforming (SMR) of natural gas, making it the most common method of hydrogen production in the U.S. The SMR reaction is represented by the following equation:

$$CH_4 + H_2O \rightleftharpoons CO + 3H_2 \tag{1.1}$$

$$\Delta H_{rxn} = 206 \text{ kJ/mol}$$

As Equation 1.1 illustrates, steam and methane react in the presence of a catalyst to form syngas (carbon monoxide and hydrogen). SMR catalysts are typically Ni-based because of their low cost; however, Ni is typically less active and prone to deactivation by oxidation and carbon formation [12]. As a result, noble metals such as Ru, Rh, Pd, Ir, and Pt are also used as the active catalyst metal.

At standard conditions, this reaction is strongly endothermic, so heat must be supplied to the reaction for it to proceed. This is typically from the combustion of natural gas, but could also be supplied via concentrated solar-thermal power [13] or low-cost electricity.

Steam-methane reforming typically occurs at high temperatures of 800°C to 1000°C and high pressures of 30 to 40 bar [12]. Modern steam-methane reforming plants consist of the four major processes as illustrated in Figure 1.4 below.

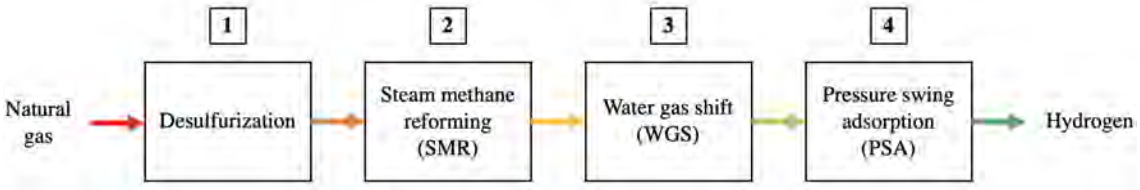

Figure 1.4: Modern steam-methane reforming process

1. Desulfurization
    - The desulfurizer removes hydrogen sulfide (H_2S) from natural gas feedstock through liquid adsorption [14].
2. Steam-methane reforming
    - Methane and steam react to form hydrogen, carbon monoxide, and trace amounts of carbon dioxide.
    - Conventional SMR reactors consist of fixed-bed reactor tubes filled with nickel-based catalyst pellets.
3. Water-gas shift

- The product stream from the steam-methane reformer is cooled to 350°C and enters a conventional two-stage water-gas shift reactor.
- Carbon monoxide and steam react in the presence of a catalyst to form hydrogen and carbon dioxide.

4. Pressure swing adsorption
    - Pressure swing adsorption utilizes specific absorptive materials to trap contaminants at high pressures.
    - Carbon dioxide, carbon monoxide, methane, and water are removed from the gas stream and high purity (>99%) hydrogen exits.

1.6 Water-gas shift reaction

Syngas derived from the SMR reaction contains carbon monoxide that can be further converted into hydrogen through the water-gas shift reaction (WGSR). The WGSR, shown in Equation 1.2 below, is an intermediate reaction in overall reforming processes and it is considered one of the most important reactions for hydrogen production because it increases hydrogen yield from natural gas feedstock.

$$CO + H_2O \rightleftharpoons CO_2 + H_2 \tag{1.2}$$

$$\Delta H_{rxn} = -41.1 \text{ kJ/mol}$$

The WGSR is a mildly exothermic reversible reaction where carbon monoxide and steam react in the presence of a catalyst to form carbon dioxide and hydrogen. The WGSR is thermodynamically favored at low temperatures (i.e. the reaction will favor the products at lower temperatures) yet kinetically favored at high temperatures (i.e. the reaction will proceed faster at higher temperatures). Consequently, conventional WGS reactors operate adiabatically in two stages: a high temperature shift (HTS) and a low temperature shift (LTS). The HTS typically occurs between 350-450°C while the LTS typically occurs between 190-250°C. Because the WGSR is kinetically favored at higher temperatures, the bulk of

the CO conversion occurs in the HTS reactor in order to take advantage of the higher reaction rates. The LTS reactor is then used to convert remaining CO to hydrogen.

1.7 The potential for process intensification

Recent work by Tolley and Fronk [15] suggests that the WGSR can be intensified through the use of a diabatic microreactor to dramatically reduce component size and production cost. However, Tolley and Fronk's work was limited to a simulated demonstration of the diabatic reactor concept. Applying the principles of process intensification to the diabatic reactor concept results in a differential temperature, plate architecture WGS microreactor design. This improved design increases modularity, decreases costs, and improves the yield of hydrogen from natural gas feedstock when compared to conventional WGS reactor technologies.

The purpose of this thesis is to investigate the experimental feasibility of intensifying the WGSR for a representative steam-methane reforming process using a plate architecture microreactor prototype with integrated cooling channels to achieve the optimal temperature profile for maximum CO conversion.

1.8 Thesis scope

The organization of this thesis is as follows:

- Chapter 2 provides an overview of prior investigations of the water-gas shift reaction and reactor design, and establishes the need for further research and development.
- Chapter 3 presents the design and manufacture of the process-intensified water-gas shift reactor.
- Chapter 4 details the selection and synthesis procedure of a water-gas shift catalyst for the microreactor.
- Chapter 5 outlines the design and construction of the high-temperature test loop

used to experimentally evaluate the process-intensified water-gas shift reactor under reacting flow conditions.

- Chapter 6 presents and evaluates the results and characterizations of the catalyst, reactor, and experimental studies.
- Chapter 7 summarizes final thoughts and recommends avenues for future work.

The ultimate goal is to bridge current hydrogen production technologies to clean hydrogen technologies in order to advance a secure, affordable, and net-zero carbon energy future.

Chapter 2: Literature review

2.1 Water-gas shift thermodynamics

The thermodynamics of the water-gas shift reaction describe whether or not the reaction will occur. Thermodynamic equilibrium of the water-gas shift reaction is described by the Gibbs free energy change and the equilibrium constant of the reaction as function of temperature [16]:

$$\Delta G(kJ/mol) = -32.197 + 0.03104T - \frac{1774.7}{T} \tag{2.1}$$

$$log(K_{eq}) = -2.4198 + 0.0003855T + \frac{2180.6}{T} \tag{2.2}$$

The correlations for the Gibbs free energy change in Equation 2.1 and the WGS equilibrium constant in Equation 2.2 are functions only of T, the reaction temperature. Thermodynamically, pressure has no effect on the equilibrium of the reaction is because the reaction is equimolar. However, pressure has an effect on the equilibrium constant kinetically, which is later described in Section 2.2.

Figure 2.1 graphically represents the thermodynamic equilibrium of the WGSR as described by the Gibbs free energy change and the equilibrium constant of the reaction as function of temperature. The Gibbs free energy of the reaction increases relatively linearly while the equilibrium constant decays exponentially as a function of temperature. As the reaction temperature increases, the product yield of the WGSR will decrease as a result of a lower equilibrium constant, thus describing why the WGSR is thermodynamically favored at lower temperatures.

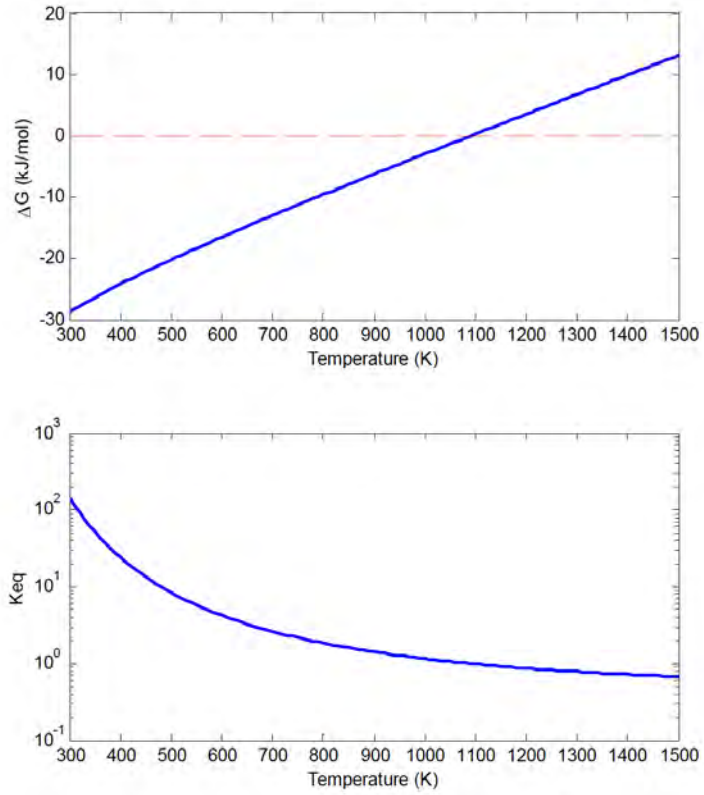

Figure 2.1: Thermodynamic equilibrium of the WGS reaction described by the Gibbs free energy change (Eq. 2.1) and equilibrium constant (Eq. 2.2) as a function of temperature [16].

2.2 Water-gas shift kinetics

The kinetics of the water-gas shift reaction, i.e. the rate and pathway at which water-gas shift reactants are transformed into products, is a well-studied area of research. Many kinetic models have been developed to predict the behavior of this reaction, enabling designers and researchers to optimize reactor designs.

Broadly, researchers apply two methods to model the kinetic expressions of the WGSR: the microkinetic method and the empirical method. Smith R J *et al.* describe these models as follows [17]:

1. Microkinetic models

- The mechanisms for the WGSR over a metal oxide catalyst are known as the redox and associative mechanisms.
- In the redox mechanism, the oxidation reduction cycle is responsible for the reaction. This mechanism proposes that steam oxidizes the surface of the catalyst, producing hydrogen as a byproduct. The catalst surface is then reduced to convert CO to CO_2.
- In the associative mechanism, an adsorbed species interacts to form an adsorbed intermediate that then decomposes into the WGSR products of hydrogen and carbon dioxide.

2. Empirical models

- Experimental data is used to model the WGSR over high temperature, low temperature, and noble metal catalysts.
- Generally, the associative mechanism is modeled by the Langmuir Hinshelwood and Eley-Rideal type models.

Although the equilibrium of the WGSR is not significantly affected by pressure, operating at higher pressures improves the kinetics of the reaction by reducing the catalyst requirements per unit mass of gas reacted due to increased contact time. Atwood *et al.* experimentally concluded that the rate of the WGSR over an iron oxide-chromium oxide catalyst approximately doubled as the pressure increased from atmospheric pressure to 10.13 bar [18].

2.3 Water gas shift catalysis

Catalysts are substances that supplement reactions to increase the reaction rate without being consumed in the process. Catalysts typically speed up a reaction by reducing the activation energy or changing the reaction mechanism without affecting the equilibrium of the reaction.

The WGS reaction occurs too slowly for practical applications without the use of a catalyst, so a catalyst must be introduced to speed up the rate of the WGS reaction. Catalysis for the WGSR is a mature and populated area of ongoing research since there exist many different catalyst materials and forms. The water-gas shift reaction is catalyzed heterogeneously where the catalyst is typically a solid metal nanoparticle adsorbed onto a metal oxide support while the reactants are dry gases and steam.

2.3.1 High temperature shift catalysts

As mentioned in Section 1.6, the high temperature shift typically occurs in the range of 350-450°C. Most HTS catalysts are Cr_2O_3 (8-10 wt%) supported on Fe_2O_3 (80-90%) with promoters/stabilizers such as CuO_2 or Al_2O_3. $Fe_2O_3 - Cr_2O_3$ based catalysts have seen widespread commercial success for more than 60 years. These HTS catalysts are advantageous because they:

1. are low cost,
2. have a long lifespan (3-5 years), and
3. resist poisoning from the process gases.

Despite these qualities, Fe_2O_3-based HTS catalysts are majorly limited because they:

1. exhibit low volumetric activity,
2. are pyrophoric (i.e. ignite spontaneously when exposed to air),
3. require an activation procedure, and

4. are highly sensitive to the steam/gas ratio.

Due to their low volumetric activity below 350°C, Fe-based catalysts pose too significant volume and weight constraints for feasible use in a low-volume WGS reactor. As a result of these limitations, different catalysts discussed later in Section 2.3.3 have also been researched and developed for the WGSR.

2.3.2 Low temperature shift catalysts

Conversely, the low temperature shift occurs between 190-250°C. LTS catalysts are typically Cu-based with $Cu/ZnO/Al_2O_3$ being the most popular commercial LTS catalyst. Cu is the active phase while ZnO and Al_2O_3 are used as promoters/stabilizers to increase Cu dispersion and enhance stability. Cu-based LTS catalysts also see widespread commercial use because they are:

1. low cost,
2. stable, and
3. the most active among all catalysts below 240°C.

However, just like the Fe-based HTS catalysts, the Cu-based LTS catalysts are limited because they:

1. exhibit low volumetric activity,
2. are pyrophoric (i.e. ignite spontaneously when exposed to air),
3. require an activation procedure,
4. are highly sensitive to temperatures above 280°C, and
5. deactivate when exposed to liquid water.

While more active at lower temperatures than Fe-based HTS catalysts, Cu-based LTS catalysts do not exhibit the activity required for smaller volume WGS reactors, which often

makes the WGS reactor the largest reactor in steam-methane reforming process [19]. The costs associated with large reactors are high, and thus, the limitations of these catalyst motivate the use of different catalyst materials that enable smaller WGS reactor volumes.

2.3.3 Precious metal catalysts

Precious metal catalysts deposited on a metal support material enable coatings with a highly dispersed form of the precious metal, which ensures high catalytic efficiency due to its well-stabilized form on the support surface [20]. These catalysts have considerable importance for industry because they allow more effective and economic usage of the costly metals.

Ratnasamy and Wagner identified precious metal catalysts supported on partially reducible oxide supports as front-runners for catalyzing the WGSR for several reasons [21]. These catalysts:

1. exhibit excellent stability and catalytic activity for temperatures between 250-400°C,
2. are non-pyrophoric [22],
3. resist deactivation due to coking and thermal sintering, and
4. do not require pretreatment.

Promoters such as ceria have been shown to increase the activity and low-temperature performance of precious metals for the WGSR [23]. Ceria- and titania-supported platinum catalysts have been especially promising as water-gas shift catalysts because they are active over a wide range of temperatures and exhibit superior catalytically activity compared to standard Fe-based HTS and Cu-based LTS catalysts. For example, Cu-based catalysts require 2.5 times more catalyst weight to achieve 90% conversion when compared to Pt-based catalysts to achieve 98% conversion [24].

Pt-based catalysts supported on ceria or titania are bifunctional, i.e. both the metal and the support are involved with the reaction pathway [25]. The precious metal (e.g. Pt)

offers CO adsorption sites while the partially reducible metal oxide support (e.g. Ce or Ti) offers oxygen storage capabilities, which facilitates oxidation of the CO [21]. Non-reducible supports such as alumina are also common for catalyzing the WGS reaction. Just like the standard Fe- and Cu-based catalysts, Pt-based catalysts experience limitations in the form of deactivation due to sintering and over-reduction. Catalyst deactivation is further discussed in Section 2.3.6.

In 2001, Ferrandon compared the catalytic activity of metal oxide catalysts such as MnO_x and CuO to noble metals such as Pt and Pd supported on am alumina washcoat. They concluded that Pt and Pd supported on alumina exhibited superior catalytic activity than that of MnO_x and CuO for the oxidation of CO to CO_2; additionally, it was found that the alumina washcoat was well anchored to the metallic support.

Studies performed by Wheeler *et al.* compared the activities of alumina-supported noble metals (Ni, Pd, Pt, Rh, and Ru) when ceria is added as a promoter [23]. Figure 2.2 from their results reports that the addition of ceria to the platinum catalyst resulted in the most pronounced improvement in conversion from a maximum CO conversion of 45% to 75%.

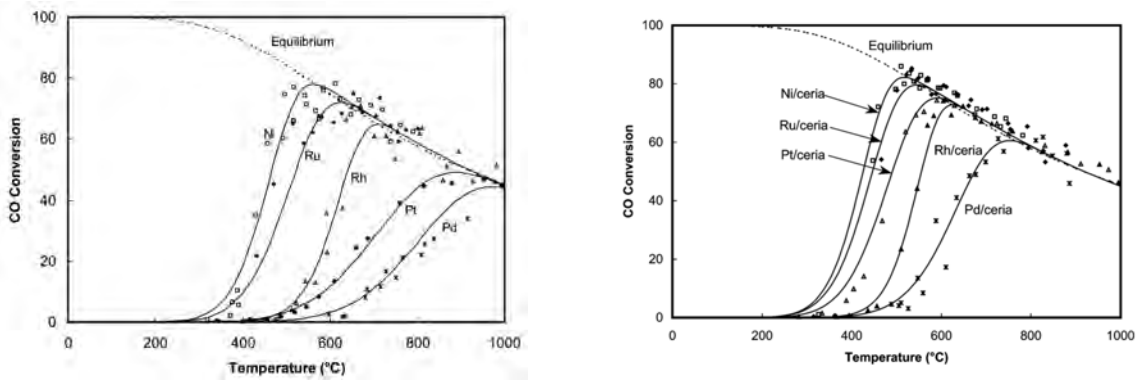

Figure 2.2: CO conversions in water–gas-shift reaction on noble metals supported on alumina foam monolith (left) compared to noble metals promoted by ceria (right) investigated by Wheeler *et al.* [23].

The effects of platinum and ceria loading on conversion were investigated, with Figure 2.3 below showcasing that a 5% loading of both Pt and Ce resulted in the best conversion.

Despite the fact that Figure 2.2 reports Ni as the best active metal for highest CO conversion, it resulted in the undesirable promotion of carbon formation on the catalyst.

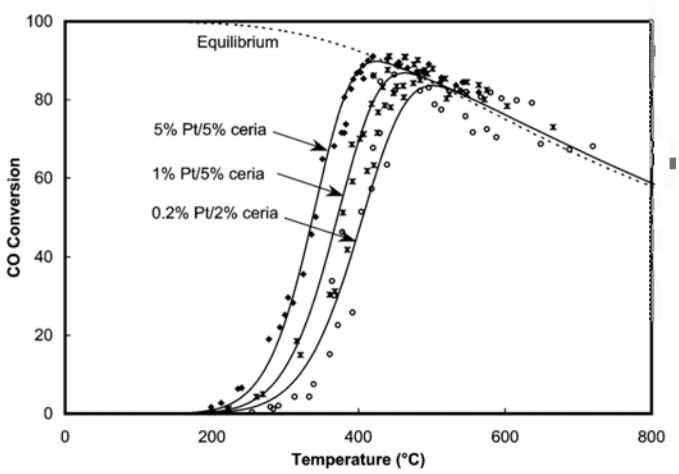

Figure 2.3: The effect of different Pt and Ce loadings investigated by Wheeler *et al.* [23].

Methanation is also an undesirable process that can deactivate the catalyst, but it was shown that the Pt/CeO_2 catalysts did not experience methanation when the CO conversion was at its maximum. As a result of their studies, they concluded that 5 wt% Pt and 5 wt% Ce supported on Al_2O_3 catalysts were the most stable and resistant to deactivation out of the metals that were tested (Ni, Pd, Pt, Rh, and Ru).

Thinon et. al compared the effectiveness of Rh, Ru, and Pt based catalysts for the WGSR within a commercial parallel plate reactor. Comparison of the data obtained for the Pt catalysts from the parallel plate reactor with those obtained from a single fixed bed reactor showed deviations of 20–30% in the kinetic parameters. They found that Rh and Ru based catalysts produced significant amounts of methane. $Pt/CeO_2/Al_2O_3$ and Pt/TiO_2 were found to be the most active catalysts for the high temperature water-gas shift while gold and copper catalysts showed promising results for low temperature applications, but they require testing at lower CO partial pressures [26].

2.3.4 Catalyst development for microstructured reactors

Germani & Schuurman produced a $Pt/CeO_2/Al_2O_3$ catalyst for their studies on the WGSR through microstructured platelets [27]. First, an aqueous suspension of alumina powder

(Alfa Aesar, 3 mum powder) with a commercial type of methylhydroxyethyl-cellulose binder (Clariant) was prepared. This suspension was used to slurry-coat the channels of the microstructured platelets and any suspension deposited outside the channels was carefully removed. A scanning electron micrograph (SEM) image of a cross section of the alumina washcoat layer inside one of the microchannels can be seen in Figure 2.4 below.

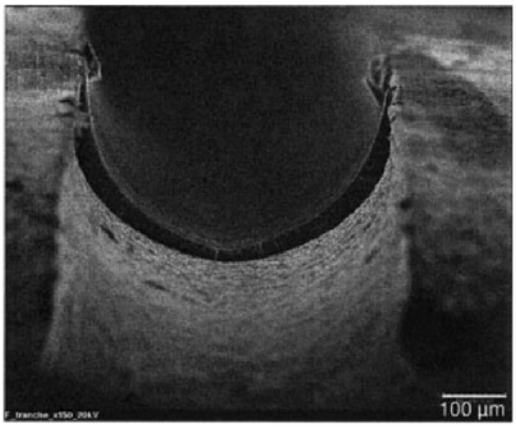

Figure 2.4: Alumina slurry washcoat in steel microchannel by Germani & Schuurman [27].

Minimal cracking was observed in the SEM of the washcoat layer. The washcoat thickness is estimated to be between 29 μm and 39 μm with an average washcoat weight of 106 mg per reaction platelet. The thickness of the alumina washcoat and the weight of the washcoat can be used to calculate an alumina washcoat density of 1450 kg/m^3, which is typical for other alumina washcoats [28]. This corroborates uniform deposition of the washcoat throughout the microchannels of the platelets.

After coating, the platelets were calcined at 600°C. The washcoat was then impregnated to incipient wetness with a cerium precursor solution (4.78 wt% Ce^{3+} from $Ce(NO_3)_3 * 6H_2O$, Alfa Aesar: Reaction 99.5%) using a paintbrush. It was followed by drying and calcination at 400°C for 2 h. The washcoat was then impregnated six times to incipient wetness with a platinum precursor solution (1.17 wt% Pt^{2+} from $Pt(NH_3)_4OH_2$, Alfa Aesar: solution, Pt 8-11% w/w) using a paintbrush. The final catalyst coating was calcined for 10 h at 550°C.

The metal weight percentages were measured using atomic emission spectroscopy, where

the following composition of the catalyst was found:

0.79 wt% Pt, 3.40 wt% Ce, 46.44 wt% Al

The BET surface area of the pure $\gamma - Al_2O_3$ was equal to 82 m^2/g, which decreased to 72 m^2/g after impregnation with ceria and the platinum solution. The procedure proposed by Perrichon *et al.* was used to measure a Pt dispersion of 67% [29]. To characterize the adhesion of the catalyst, the following two tests were performed:

1. Fall test
    - Platelets were dropped three times on a hard surface from a 50 cm height with the channels facing down, and the weight loss was monitored.
2. Ultrasonic test
    - Using a method informed by research by Valentini *et al.* [30], platelets were immersed in petroleum ether inside of a sealed beaker then treated in a sonicator for 30 minutes.

For the fall test, no weight loss was recorded for any of the platelets. The largest recorded weight loss for the ultrasonic test was 1.7% of the initial washcoat weight. The data from Germani & Schurrman's experiments suggests a dual-site associative mechanism, where ceria provides an adsorption site for water while platinum provides an adsorption site for carbon monoxide. The rate-determining step of the reaction involves the formation of a complex between a carboxyl species and a hydroxyl group that decomposes over a free platinum site into the WGSR products.

A comprehensive study performed by He *et al.* in 2020 investigated the effect of slurry properties and reactor characteristics on the preparation of a washcoated $Pt/\gamma - Al_2O_3$ catalyst on the walls of a FeCrAlloy and 316L stainless steel microreactor [31]. Good adhesion was shown to the substrates using polyvinyl alcohol as the binder, 20 wt% $\gamma - Al_2O_3$, and pH = 3.5. The washcoat was was shown to exhibit excellent coating adhesion on FeCrAlloy in rectangular and round channels due to the formation of an alumina film over

the surface during thermal pretreatment. The researchers also investigated the adhesion of the catalyst on three channel shapes for 316L stainless steel: circular, square, and rectangular. These washcoated layers are showcased in Figure 2.5 below.

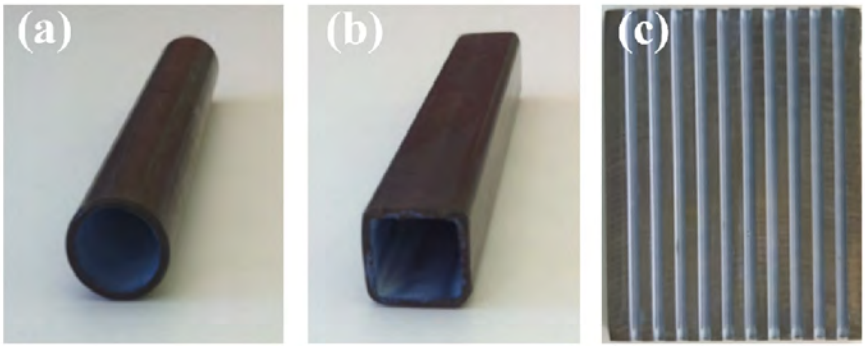

Figure 2.5: Washcoated layer on 316 L stainless steel with different channel shapes: (a) circular (diameter = 8 mm), (b) square (width × height × length = 8 × 8 × 100 mm), (c) parallel rectangular microchannels (width × height × length = 1.5 × 1 × 50 mm) [31].

Each sample's coating mass was measured before the sample was immersed in a glass beaker containing acetone and sonicated for 3 hours at 40 kHz. Afterwards, the mass was remeasured to quantify the weight loss of the coating. For the geometries shown in Figure 2.5, the researchers observed a weight loss of 0.66 wt%, 8.24 wt% and 11.49 wt% for the circular, square, and rectangular washcoat geometries, respectively. Compared to the FeCrAlloy, which experienced no weight loss, the coating exhibited poorer adhesion. This observation can be attributed to the rougher surface and higher number of anchoring sites of the FeCrAlloy than that of stainless steel, which resulted in a stronger interlocking of the washcoated particles onto the surface irregularities over the substrate. More importantly, the thin layer of alumina that was formed on the FeCrAlloy surface after calcination greatly improved the adhesion strength. In the case of the 316 L stainless steel, an iron oxide was formed on the surface after calcination. It was thus assumed that the alumina washcoat has a stronger adhesion affinity with the alumina on FeCrAlloy than with iron oxide on stainless steel, but still exhibits good adhesion with both.

2.3.5 Calcination

Calcination is the process of heat treating a solid material at high temperatures to oxidize the material and remove impurities from its surface. It is an important pretreatment technique for this research because the oxidation of the stainless steel reactor substrate increases surface roughness, thus promoting better adhesion of the catalyst to the walls of the reaction channel [31].

Calcination of the catalyst itself is another important application of this process in the preparation of a suitable catalyst for the water-gas shift reaction. Typically, two calcination processes are applied for precious metal catalysts on partially reducible metal supports: one thermal cycle is used to calcine the support and the other cycle is used to reduce the precious metal. The calcination of the support material is important in ensuring a homogeneous support surface density, finalizing the surface area of the support structure, and locking in the support's pore structure [32]. The reduction of the active metal component is important in enhancing catalyst activity, removing moisture from the catalyst, and promoting strong metal-support interactions [32].

2.3.6 Catalyst deactivation

Over time, WGS catalysts may undergo deactivation after prolonged use through two main mechanisms: coking and sintering [33].

1. **Coking** is the blocking of the metal surface due to accumulation of carbon on the metal.

2. **Sintering** is the formation of larger metal particles on the surface, which lowers overall surface area and activity.

Thermal sintering of the metal support crystallites is the primary deactivation method of HTS catalysts [21]. Thermal sintering occurs more rapidly at higher temperatures, so reaction temperatures should be limited to less than 500°C. At start-up and during normal

operation of the reactor, some sintering is unavoidable. It is an irreversible process that is a function of time: data suggests the catalyst's deactivation rate is fastest during the first few months of operation before stabilizing with very gradual aging after the first year. LTS catalysts can show distinct zones of deactivation but HTS catalysts exhibit more gradual deactivation that is spread throughout the catalyst bed. For HTS catalysts, this translates to a decrease in the CO conversion and the spreading-out of the reactor's temperature profile.

Research performed by Wang *et al.* investigated the mechanism responsible for the deactivation of ceria-supported precious metals for catalysis of the WGSR [34]. They concluded that deactivation of a Pd/Ce catalyst occurs more rapidly at 400°C than at 250°C when operating at otherwise similar conditions. By heating a fresh catalyst in H_2, H_2O, CO, or CO_2, it was shown that the catalyst deactivates due to the presence of CO. These findings show that ceria–supported precious metals could be active and stable for the WGSR if steps are taken to prevent metal particle size growth at higher temperatures around 400°C.

Similarly, Goguet *et al.* investigated effect of carbon deposition on the deactivation of a Pt/CeO_2 catalyst during the reverse WGSR [35]. This team of researchers also concluded that the Pt catalyst deactivated due to the presence of CO at 400°C. No evidence of deactivation due to metal sintering was found, indicating that deactivation of a Pt/CeO_2 catalyst is due only to coking.

The deactivation of precious metal catalysts can be costly because they must be regenerated or reapplied, causing delays and a decrease in overall hydrogen yield throughout the steam reforming process. These concerns have led researchers to carry out the studies that have been discussed to develop stable, inexpensive catalysts that do not exhibit degradation due to coking or sintering.

2.3.7 Metal foam supports

The use of monolithic porous metal foams as catalyst supports is well-established for various applications, such as fuel cell applications [36] and automotive waste-gas purification [37]. Metal foams can be particularly useful as catalyst supports because they have a high surface area to volume ratio and exhibit low heat capacity characteristics, which promotes rapid response to changes in operating conditions. Most notably, enhanced gas permeability through the porous foam increases the likelihood of reactant gas adsorption onto the active sites of the catalyst, which promotes the effectiveness of the catalyst [38]. The web-like structure of the foam support can be seen below in Figure 2.6 below.

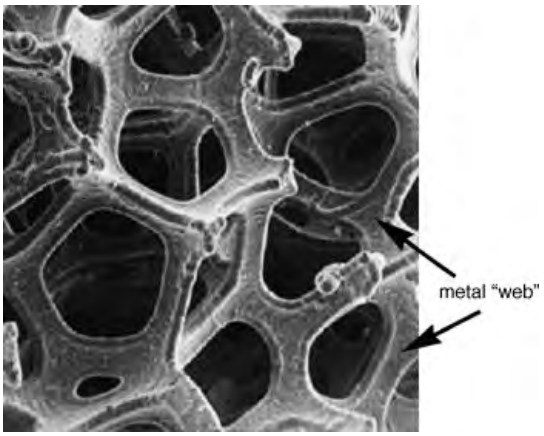

Figure 2.6: The porous structure of metal foam supports promotes high catalyst loading [38].

The uniform and high porosity of the metal structures helps to promote excellent flow characteristics, alleviating potential concerns related to maldistribution of the reactant fluids as they enter the support. Foams are highly configurable and easily constructed, which allows them to conform to space and size limitations of specialized reactor geometries. High thermal conductivity of the metal allows for rapid heat transfer through the foam, which is desirable for minimizing the localization of heat in a reactor [39]. These aforementioned characteristics make metal foam supports an attractive and advantageous option for use for hydrogen production applications as a WGS catalyst support. Despite these advantages,

barriers to practical implementation of the foam supports include high costs relative to traditional catalyst supports and limited availability.

Fecralloy® (AEA Technology), commonly styled as FeCrAlloy, is a proprietary alloy of approximately 73% Fe/20% Cr/5% Al/2% Y and is a popular metal foam support material. Due to its high aluminium and chromium content, it is suitable for use up to temperatures of 1425°C. The addition of yttrium to the alloy improves the adherence of the protecting oxide, which increases the service life of the material, especially under alternating temperature conditions [40]. An image of a FeCrAlloy sheet is shown in Figure 2.7 below.

Figure 2.7: Fecralloy®, a popular metal foam support material, shown in sheet form [40].

In 2006, Chin *et al.* investigated the catalytic activity and surface kinetic parameters of a series of washcoated $Pt/Fe/\gamma - Al_2O_3$ catalysts supported on FeCrAlloy for the selective oxidation of CO in H_2. The researchers compared the catalytic properties of the foam-supported catalyst to a powdered $\gamma - Al_2O_3$-supported Pt catalyst of the same compositions and found that both catalysts exhibited similar reaction properties, though the presence of Fe impurities in the washcoat, likely from the metal foam structure, was found to have a significant impact on the properties of the foam-based catalysts. This research concluded that washcoated $Pt/Fe/\gamma - Al_2O_3$ catalysts on a metal foam support is a viable catalyst synthesis technique.

More recent research performed by Roy *et al.* in 2014 studied the use of a Pd-Rh/metal foam catalyst in a tubular heat exchanger platform reactor for the production of hydrogen through the SMR process [38]. The Pd-Rh/metal foam catalyst exhibited steady catalytic activity while maintaining thermal stability during a 200 hour stability test and yielded a 96.7% conversion rate of CH_4 to H_2. Compared with commercially available alumina-supported Ni and Ru catalysts, the Pd-Rh/metal foam catalyst showed better CH_4 conversion and thermal stability at 710°C, confirming the viable use of metal foam supports for high temperature SMR applications.

2.4 Conventional WGS reactor studies

As aforementioned, conventional WGS reactors operate in two stages: a high-temperature shift (HTS) which is typically at 350°C to 450°C and 10–60 bar, and a low-temperature shift (LTS) which operates around 200°C and 10–40 bar. Typically, these reactors are packed bed reactors (PBR) that consist of a tubular housing filled with porous metal catalyst particles through which the reactants pass through [21].

PBRs are common in various chemical processing industries because they offer a number of advantages over other types of reactors. Gas flow that pass through a PBR can be modeled as plug flow, which dramatically simplifies fluid flow analyses compared to reactors such as fluidized bed reactors. PBRs provides high contact time between the reactants and the catalyst and often times boast a higher conversion rate per unit of catalyst weight when compared to other standard reactor types [41].

While advantageous in numerous ways, there are a number of disadvantages associated with utilizing PBRs. It is difficult to temperature control the packed bed reactors becuase they have low effective thermal conductivities. As a result, it can be difficult to heat the reactor uniformly, thus leading to hot spots that can deactivate the catalyst due to sintering [41].] Additionally, packed bed reactors can be prone to plugging as trace compounds present in reaction streams can deposit and collect in the void spaces between the catalyst pellets. This can result in significant pressure drops across the reactor bed, driving up operating

costs significantly [41]. In the case of the WGS reaction, these compounds tend to be steam-volatile components that collect in the HTS reactor bed.

2.4.1 Process conditions

Two key process variables affect the performance of the WGS reactor: temperature and the ratio of inlet steam to dry gas [21].

1. Temperature
    - When the reaction is in equilibrium, reducing the gas effluent temperature leads to higher CO conversion.
    - When the reaction is not in equilibrium (i.e. kinetically limited), higher gas or bed temperatures can promote higher CO conversion.
    - Temperature rises of 30-75°C are common across commercial reactors.
2. Inlet steam/carbon ratio

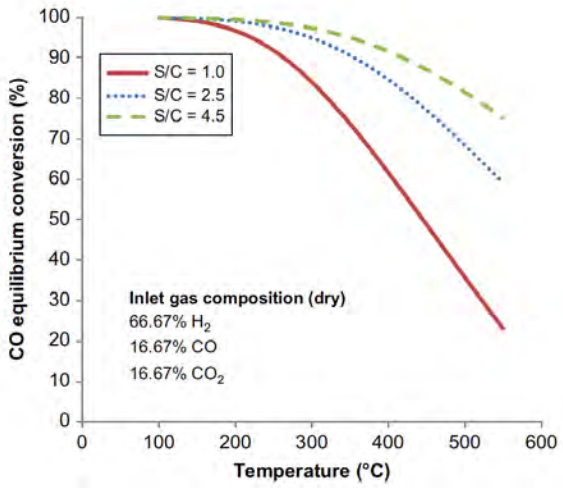

Figure 2.8: Effect of steam/carbon (S/C) ratio on the equilibrium conversion of CO at atmospheric pressure [24].

- The steam/dry gas ratio affects both the thermodynamic and kinetic properties of the WGSR.

- As shown in Figure 2.8, higher steam/dry gas ratios increase the reaction rate of the WGSR.
- A minimum steam to gas ratio of 0.4 is recommended to minimize the undesirable production of methane by the Fischer Tropsch reaction.

Two minor process variables also impact the performance of the WGSR: pressure and catalyst activity.

1. Pressure
    - Pressure affects the reaction kinetically due to pore diffusion limitations and partial pressure effects of the reactants.
    - Higher pressures improve overall CO conversion by improving the reaction rate when the reaction is kinetically limited, allowing smaller reactors to be used.
    - Operating pressure may be as high as 30 bar.
    - The typical catalyst contact time is approximately 3-9 seconds under normal pressures, but may be around 1 second for higher operation pressures.
2. Catalyst activity
    - As aforementioned in Section 2.3.3, catalyst choice is important in maximizing CO conversion.
    - Pt-based catalysts exhibit superior activity over a wider range of temperatures when compared to Fe- and Cu-based catalysts.

2.5 Microchannel WGS reactor studies

Microchannel reactors, common referred to as microreactors, are advantageous for the WGSR in particular because they can address issues related to temperature control, heat and mass transfer limitations, and catalyst use.

1. **Temperature control:** The WGSR is thermodynamically favored at lower temperatures but the exothermic nature of the reaction necessitates integrated cooling in the reactor to maintain isothermal operation and high conversion. Microreactors exhibit excellent temperature control due to their small dimensions and good thermal conductivity, which leads to improved isothermal conditions.

2. **Heat and mass transfer limitations:** The kinetics of the WGSR are observed to have multiple-second contact times for fixed-bed reactors, but the intrinsic kinetics of the reaction are measured to have contact times of milliseconds. Microchannel reactors can be used to take advantage of the intrinsic WGSR kinetics and to avoid the heat and mass transfer limitations associated with fixed-bed reactors.

3. **Catalyst use:** The use of thin washcoat layers of catalyst in these reactors eliminates the intraparticle diffusion limitations that can occur for fast reactions and reduces the amount of catalyst that is required for optimal conversion.

4. **Volume:** As the name implies, the required microreactor volume to achieve the desired yield of hydrogen can be significantly less than conventional LTS/HTS WGS reactors.

As a result, numerous researchers have investigated the potential of microchannel reactors for improving the performance of the WGSR when compared to standard HTS/LTS packed bed reactors.

2.5.1 1999: Tonkovich *et al.*

The first reported work of millisecond WGS reaction kinetics was performed in 1999 by Tonkovich *et al.*, who investigated the miniaturized deployment of the water-gas shift reaction through a microchannel reactor [42]. Prior to integration into parallel channels of a planar sheet architecture microreactor, a 5 wt% Ru/ZrO_2 catalyst was synthesized and tested first in powder form in a catalytic plug flow reactor (PFR) to characterize CO conversion.

A 3:1 ratio of steam to carbon monoxide was fed through the catalytic PFR at 300°C and the product slipstream was analyzed using a gas chromatograph. The performance of the powder catalyst used in the PFR can be seen in Figure 2.9 below. 99.8% CO conversion can be achieved with a selectivity of 100% to the desired products of H_2 and CO_2 at 50 ms contact times, but tests run with contact times above 100 ms show the formation of methane.

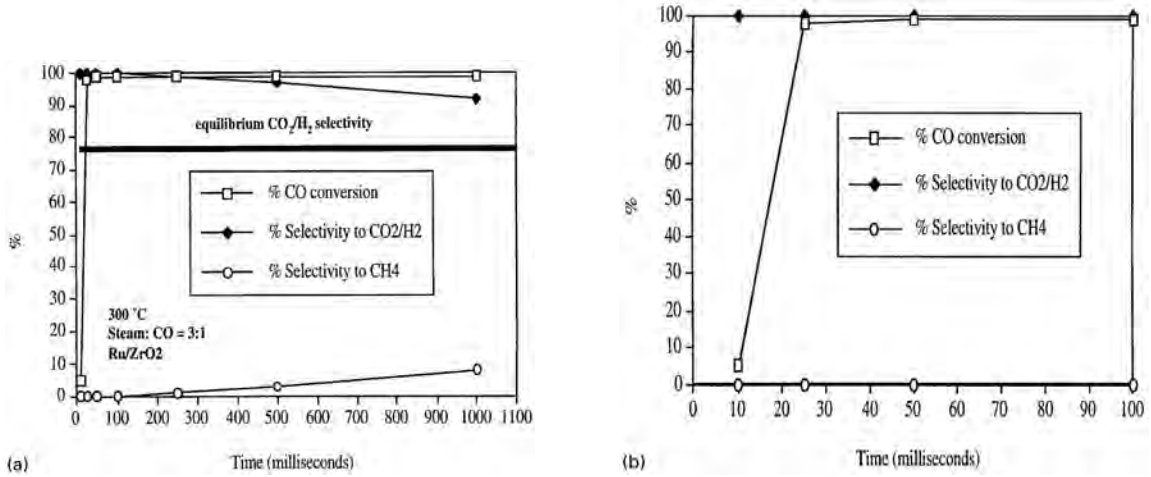

Figure 2.9: (a) Powder catalyst results for the WGSR at long contact times and (b) powder catalyst results for the WGSR at short contact times [42].

Once characterized, the catalyst was saturated into a porous nickel foam support in what is referred to as an *engineered-monolithic catalyst*. The engineered-monolithic catalyst was developed to retain the high activity of powder catalysts while maintaining a low pressure drop across the length of the structure; additionally, it facilitates rapid heat and mass transfer while providing a sufficient number of active catalyst sites. The results of the conversion studies with the engineered-monolithic catalyst are shown in Figure 2.10. Interestingly enough, at 300°C, the CO conversion is less than 10%; however, at temperatures of 500°C, the CO conversion reached 94.53%.

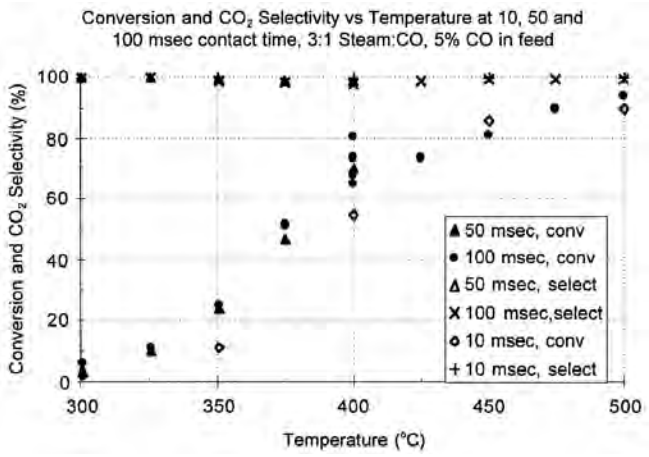

Figure 2.10: Engineered-monolithic catalyst results for the WGSR [42].

2.5.2 2006: Germani & Schuurman

In 2006, Germani & Scuurman performed experimental studies to model the kinetics of the WGSR over a $Pt/CeO_2/Al_2O_3$ catalyst in a microreactor [27].

Germani & Schuurman assessed the kinetics of the WGSR over a Pt/Ce/Al catalyst through stainless steel microchannels. Unlike Tonkovich *et al.*, Germani & Schuurman utilized a washcoated catalyst instead of an engineered-monolithic catalyst support structure. The platelets and reactor configuration can be seen in Figure 2.11 below.

Each plate is constructed of ASTM 316Ti stainless steel. Each 50 x 50 x 1 mm plate was engraved with with 49 channels that are 400 μm deep and 600 μm wide, as shown on the left of Figure 2.11. The reaction channel platelets are sandwiched between blank filler platelets and inserted into the stainless steel housing shown on the right of Figure 2.11. The filler platelets are required to ensure the gas flows through each channel. Two, four, and six reaction platelets were used while characterizing the activity of the catalysts. The details of the plate and microchannel geometries utilized in these studies are shown in Table 2.1 and Table 2.2 below, respectively.

The test article housing is designed such that the it can be disassembled and platelets can be removed for analysis after experimentation. The housing is used to compress the platelets and ensure that all gas flows through the channels and rectangular graphite gaskets

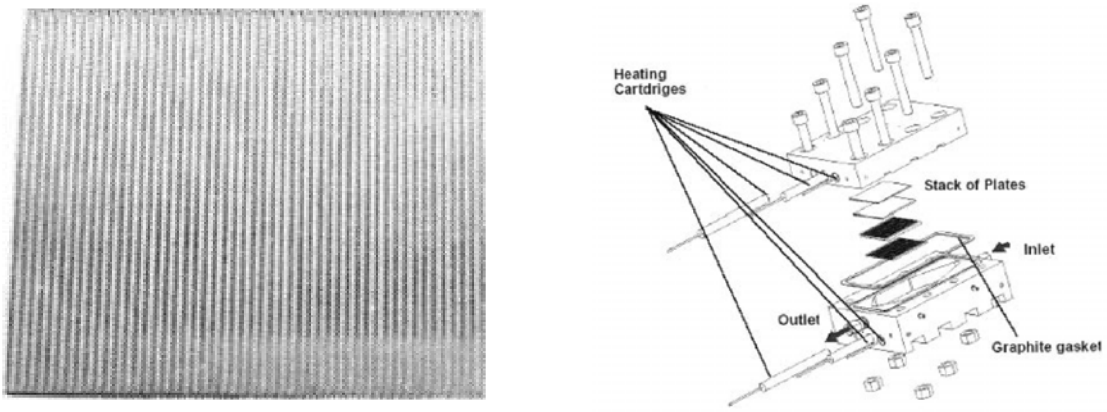

Figure 2.11: Microstructured platelet containing 49 channels used for the water-gas shift reaction (left) and exploded view of reactor housing with micro-structured platelets (right) by Germani & Schuurman [27].

Table 2.1: Experimental platelet geometries used by Germani & Schuurman [27]

Plate parameters	Value
Width	50 mm
Length	50 mm
Height	1 mm
No. reaction plates	2, 4, or 6

are used to seal the housing. The inlet section is of a triangular shape that allows a proper gas distribution through the microstructured platelets. Heating is provided by means of six 500 W heating cartridges inserted into the housing body and the reactor temperature was measured with a thermocouple located in the reactor housing close to the exit.

Mass-flow controllers regulate the dry gas streams during experimentation while a syringe pump meters water that is vaporized and mixed into the gaseous reactants stream. The mixture composition of the inlet reactant stream is detailed in Table 2.3 below. Once the reaction has occurred through the microchannel reactor, the effluent stream was analyzed at the reactor exit with an Inficon Transpector CIS2 mass spectrometer.

Before characterizing the activity of the catalyst, each batch of coated platelets was reduced in a flow of 10% H_2 in argon at a total flow rate of 200 Nml/min. The temperature was raised from 25 to 450°C at a rate of 4°C/min then kept at 450°C for 30 min. Next,

Table 2.2: Experimental microchannel geometries used by Germani & Schuurman [27]

Microchannel parameters	Value
No. channels per plate	49
Channel length	50 mm
Channel height	0.4 mm
Channel width	0.6 mm
Catalyst layer height	0.05 mm

Table 2.3: Experimental reactant stream composition used by Germani & Schuurman [27]

Gas	Mole fraction
H_2O	0.20
CO	0.10
CO_2	0.10
H_2	0.30
Ar	0.30

the reactor temperature was lowered to 200°C in a flow of 10% H2 in argon. Once at equilibrium, the flow was switched to pure argon and subsequently to the reactive flow.

The reaction stream was fed into the WGS reactor assembly at a range of various operating conditions. Table 2.4 summarizes the investigated range of process conditions that were used for the kinetic studies. Close to one hundred experiments were carried out, 70 of which were used to characterize the rate equation and parameter estimation for the activity of the WGS over the Pt/Ce catalyst.

Table 2.4: Range of experimental process conditions used by Germani & Schuurman [27]

Process variable	Range
Temperature	200-400°C
Flow rate	40-200 mL/min
Total pressure	1.0 bar
Steam/carbon ratio	0.1-2.5

The results of the reacting flow studies performed by Germani & Schuurman enabled them to characterize the kinetic performance of the $Pt/CeO_2/Al_2O_3$ catalyst as discussed previously in Section 2.3.

2.5.3 2020: Tolley

In 2020, Tolley investigated the potential of process intensifying the WGSR to improve the efficiency of hydrogen production from natural gas. In his work, he first modeled the performance of standard HTS/LTS packed bed reactors that are commercially employed for the WGSR using MATLAB. The process conditions that were used for the two-stage isothermal reactor can be seen below in Table 2.5.

Table 2.5: HTS/LTS process conditions used in Tolley's modeling [43].

Parameter	**Value**
Mass flow rate, $\dot{m}$	2.525 g/s
HTS inlet temperature, T_1	350°C
HTS inlet pressure, P_1	5.0 bar
HTS inlet mole fraction CO, $y_{CO,1}$	0.113
HTS inlet mole fraction H_2O, $y_{H2O,1}$	0.244
HTS inlet mole fraction CO_2, $y_{CO2,1}$	0.052
HTS inlet mole fraction H_2, $y_{H2,1}$	0.546
HTS inlet mole fraction CH_4, $y_{CH4,1}$	0.045
HTS outlet pressure. P_2	5.0 bar
LTS inlet temperature, T_3	200°C
LTS inlet pressure, P_3	5.0 bar
LTS outlet pressure, P_4	5.0 bar

He then modeled the performance of a single-stage differential temperature WGS microreactor with integrated cooling as a two-dimensional COMSOL Multiphysics model with the configuration and geometries shown in Figure 2.12 and Table 2.6, respectively.

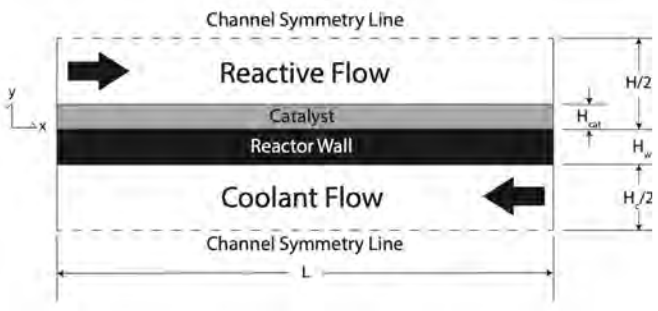

Figure 2.12: Differential temperature reactor model geometry with integrated cooling channel developed by Tolley [43].

Table 2.6: 2D model baseline parameters utilized by Tolley [43].

Parameter	Value
Reaction channel length, L	200 mm
Reaction channel height, H	1 mm
Reaction channel width, W	80 mm
Catalyst layer height, H_{cat}	0.05 mm
Coolant channel height, H_c	0.5 mm
Reactor wall thickness, H_w	0.5 mm
Number of reaction channels, N_r	200
Number of coolant channels, N_c	200

The baseline HTS/LTS model was used to showcase the improved performance of the differential temperature reactor. The modeled HTS packed bed reactor exhibits faster reaction kinetics than the differential temperature reactor, but it requires 4.83 more catalyst than the microreactor configuration to achieve 80% CO conversion for the same reactor volume. Figure 2.13 demonstrates that a differential temperature microreactor is capable of achieving higher CO conversions than the conventional HTS/LTS reactor in the volume range of 5.09×10^{-4} m^3 to 3.20×10^{-3} m^3.

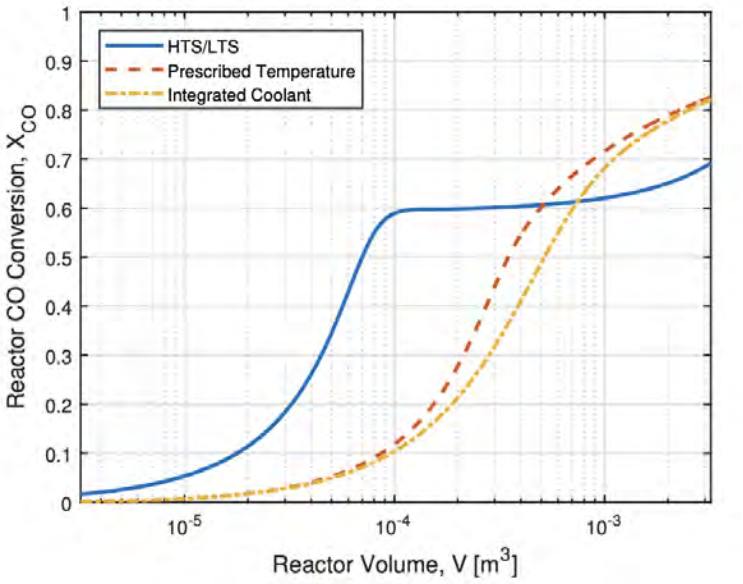

Figure 2.13: CO conversion vs. reactor volume of HTS/LTS model and integrated coolant model developed by Tolley [43].

The integrated coolant microreactor model requires 13.9% less reactor volume compared to the baseline HTS/LTS model to achieve 80% conversion. Most notably, this translates into an 82.2% reduction in required catalyst volume. The conversion profile as a function of temperature for the baseline HTS/LTS model and the baseline integrated cooling model in Figure 2.14 shows that the integrated coolant model better follows the optimal conversion profile of the reaction. However, this highly conservative model represents the minimum catalyst and reactor volume reductions that are possible.

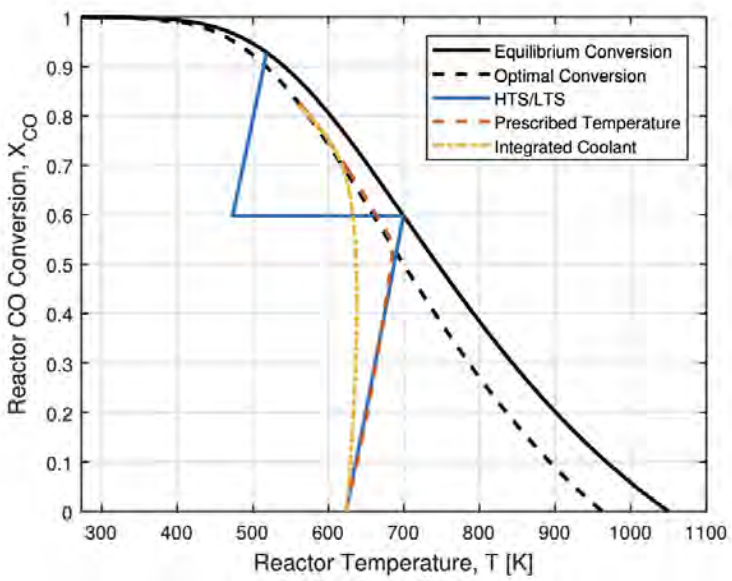

Figure 2.14: CO conversion vs. reactor temperature of HTS/LTS model and integrated coolant model developed by Tolley [43].

The results for the baseline integrated microreactor model suggest that even higher conversions can be achieved than the initial chosen geometries. To determine the process conditions and geometries for the most optimal conversion, Tolley performed parametric studies in which he varied the:

1. Reactor inlet temperature,
2. Catalyst layer thickness, and
3. Applied cooling length.

The results of the parametric studies suggest that even higher reductions in catalyst and reactor volume can be achieved if:

1. The reactor is operated at higher temperatures,
2. Catalyst packing is increased, and
3. Longer cooling lengths are applied.

The optimal temperature progression and conversion profile from the parametric studies is shown in Figure 2.15.

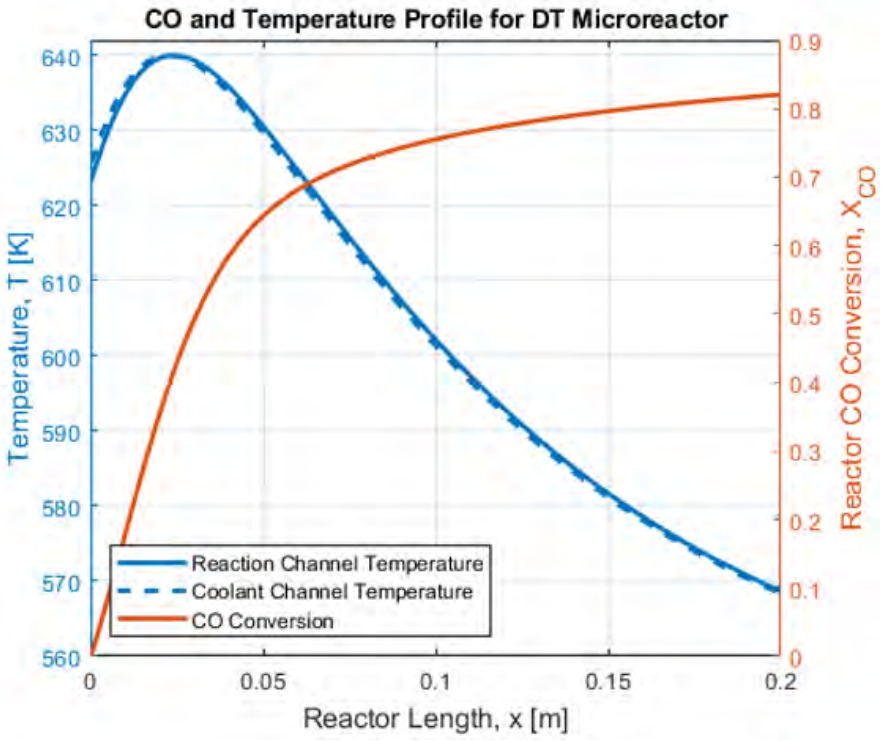

Figure 2.15: The optimal temperature and conversion profile obtained from the parametric studies of a differential temperature diabatic WGS reactor developed by Tolley [43].

For a conversion of 82%, the differential temperature diabatic WGS reactor requires 3.20 L of reactor volume when compared to the 11.18 L required by the packed bed HTS/LTS reactor, which equates to a reactor volume reduction of 71.4%. The microreactor only

requires 0.64 L of catalyst volume when compared to the 4.47 L required by the packed bed reactor model, which equates to a total reaction volume reduction of 85.7% [15]. The modeled improvement compared to the baseline is summarized in Table 2.7.

Table 2.7: Modeled improvement over baseline

	Two-stage plug flow reactor	**Single-stage microchannel reactor**	**Reduction compared to baseline**
Conversion	82%	82%	-
Internal reactor volume	11.18 L	3.20 L	71.4%
Catalyst volume	4.47 L	0.64 L	85.7%

The general influence of these process and design parameters on reactor performance informed the design of an initial monolithic WGS microreactor prototype. Tolley developed the physical prototype of the modeled reactor shown in Figures 2.16 through 2.19 to realize the potential of the process intensified WGS reactor. The prototype is reminiscent of a brazed plate heat exchanger in which the coolant stream flows in counterflow from the reactant stream.

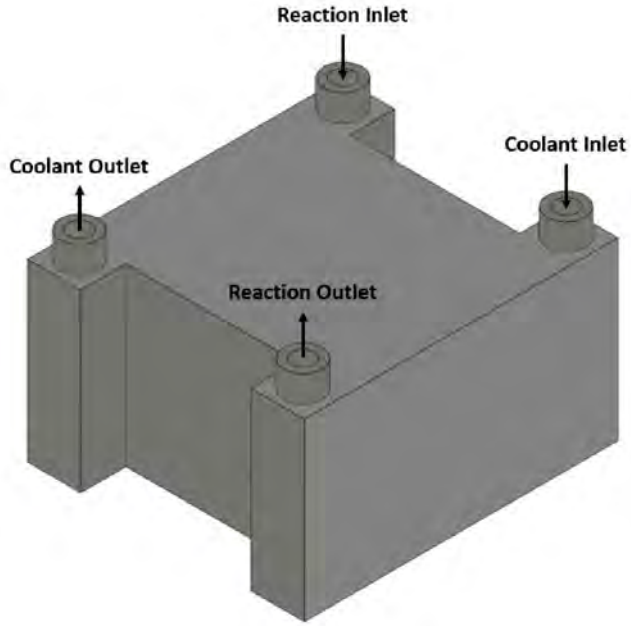

Figure 2.16: Monolithic reactor model developed by Tolley [43].

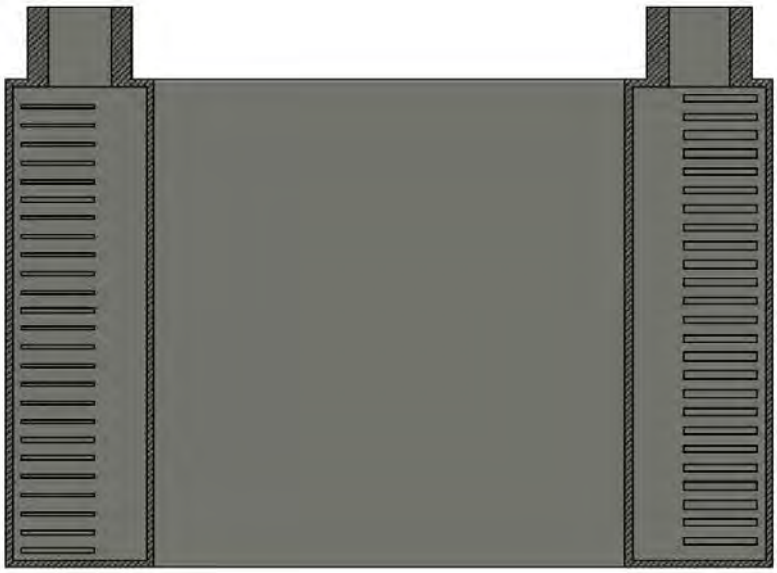

Figure 2.17: Section view of header chambers for the monolithic reactor model developed by Tolley [43].

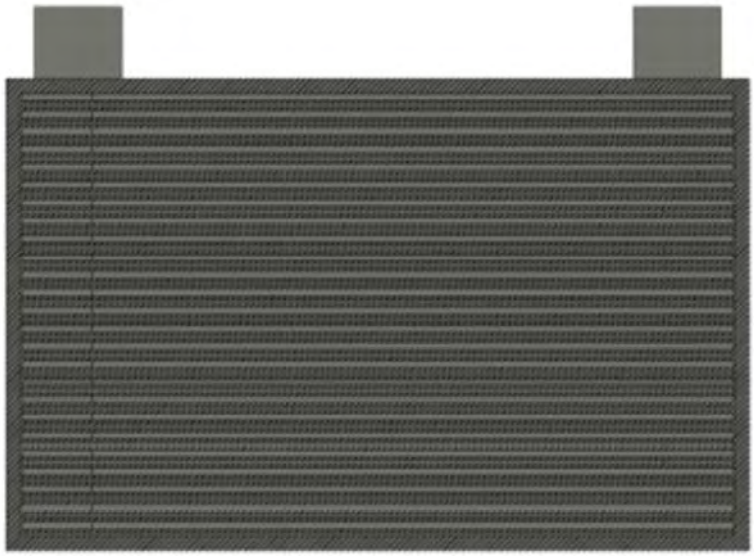

Figure 2.18: Section view of interior channels for the monolithic reactor model developed by Tolley [43].

Tolley's monolithic WGS prototype was additively manufactured with the geometries

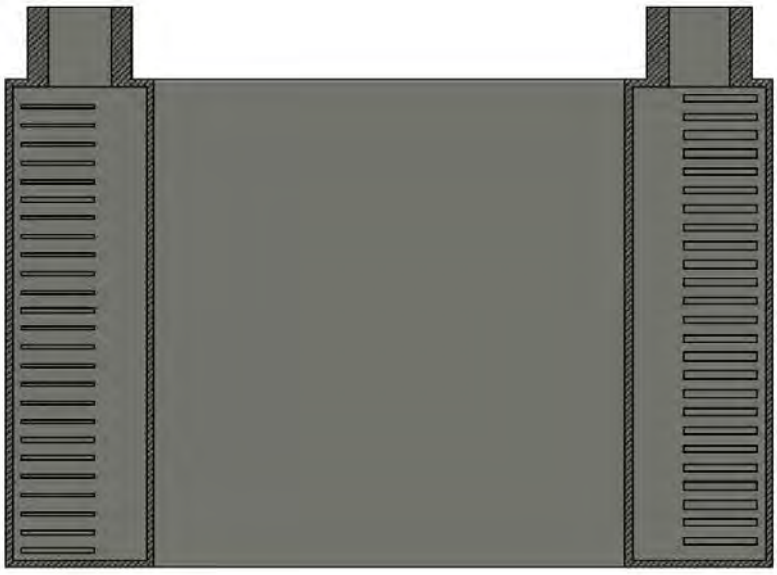

Figure 2.19: Flow path of reactant and coolant fluids for the monolithic reactor model developed by Tolley [43].

presented in Table 2.8. A picture of the microreactor prototype can be seen in Figure 2.20 with a pen for scale.

Table 2.8: Monolithic, additively manufactured WGS reactor prototype parameters [43].

Parameter	**Value**
Reaction channel quantity	25
Reaction channel length	100 mm
Reaction channel height	1 mm
Reaction channel width	80 mm
Coolant channel quantity	25
Coolant channel length	100 mm
Coolant channel height	0.5 mm
Coolant channel width	80 mm
Reactor wall thickness	0.5 mm

The prototype was manufactured from Inconel 718 using a laser powder bed fusion process, which is an additive manufacturing technique that utilizes high-powered lasers to selectively melt a metal powder. Once melted, the layers of metal fuse together on a molecular basis to form a homogeneous model. Additive manufacturing techniques such

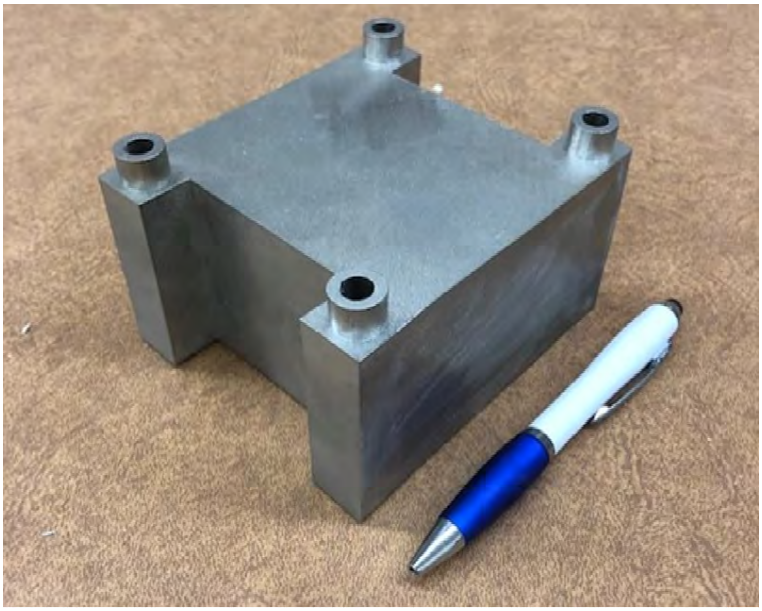

Figure 2.20: Additively manufactured monolithic reactor (pen for scale) developed by Tolley [43].

as laser powder bed fusion are powerful processes that can be leveraged in the production of WGS microreactors, but a number of obstacles related to cost and speed still need to be addressed to make additive manufacturing a competitively viable fabrication technique. Other manufacturing techniques, such as sinker electrical discharge machining described in Subsection 2.6, can be better suited for microreactor applications.

Limitations of the monolithic design made it difficult to uniformly coat a catalyst inside the walls, and as a result, reacting flow studies were not performed. Had a thin coat of platinum catalyst been applied to the walls of the channels of the monolithic prototype, modeling results suggest that the reactor would have been capable of producing approximately 4 kg of hydrogen per day, scaling up to 24 kg of hydrogen per day for actual production conditions.

Experimental studies quantified the heat exchanger effectiveness and pressure drop through the reactor. The collected test data concluded that the modeling results from Tolley's work is able to predict the actual thermal-hydraulic performance of the diabatic reactor with a reasonable level of accuracy. In conjunction with good agreement from

Germani & Schuurman's work, the experimental results confirm that the 2D COMSOL model can be used to predict the behavior of the reactor under reacting flow conditions.

2.6 Sinker electrical discharge machining

Sinker EDM is a technique that utilizes an electrode of the opposite impression to machine the desired impression into the work piece. An electrically non-conductive liquid, commonly known as a dielectric liquid, flows between the electrode and the work piece as a high voltage differential is applied between the two pieces of metal. The high voltage causes the electrical breakdown of the liquid, which produces an electrical arc that removes material from the metal work piece. A visualization of this process is shown in Figure 2.21.

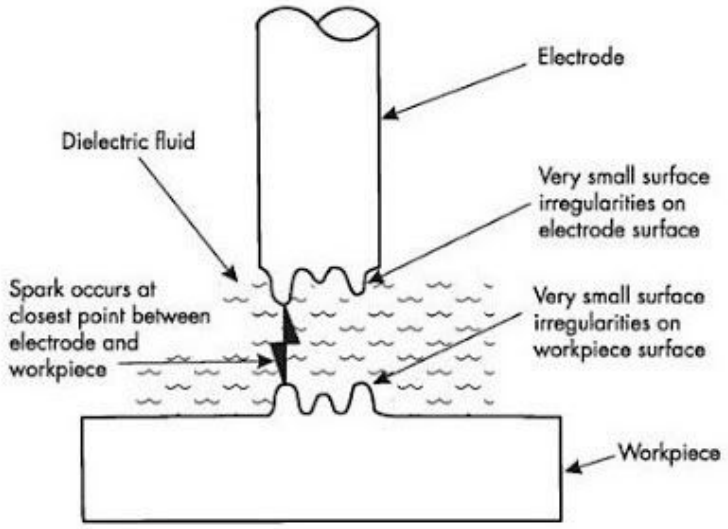

Figure 2.21: Visualization of the sinker EDM process [44].

Sinker EDM is advantageous when conventional milling is unable to be used in manufacturing thin geometries, such as a channel on a plate for a microreactor. Another added benefit of using sinker EDM is the addition of small surface irregularities on the work piece, which improves adhesion of catalyst to a reactor's reaction surfaces. One disadvantage of this manufacturing technique is that it is costly since it involves the creation of a negative as the die, which is typically created using CNC technology. Thus, sinker EDM may not

be suitable for mass production of components, but it is feasible for the prototypes. These factors make sinker EDM a good fit in manufacturing components for a plate architecture water-gas shift microreactor.

2.7 Summary

Increasing the yield of hydrogen from the water-gas shift reaction is an important step in optimizing the overall process of hydrogen production from natural gas. The work presented in this literature review outlines the pertinent findings of previous researchers in the catalysis and process improvement of the reaction. Alumina-supported platinum catalysts promoted by ceria have ubiquitously been shown to be the best catalyst in catalyzing the WGSR because they are stable, catalytically active, non-pyrophoric, do not require pretreatment, and are resistant to deactivation by means of thermal sintering or coking. Additionally, microchannel reactors have been shown to improve the performance of the water-gas shift reaction because they address issues related to temperature control, heat and mass transfer limitations, volume, and catalyst use while still achieving the same level of conversion when compared to industrially mature packed bed reactor technology.

The research performed by Tolley in 2020 suggests the implementation of a diabatic differential temperature WGS reactor operating under optimal conditions significantly reduces the reactor volume, catalyst volume, and cost of hydrogen production required to achieve the same CO conversion as conventional two-stage WGS reactors. Nonreactive testing of the monolithic prototype design suggests good thermal agreement with simulations, but further work must be done to integrate catalyst and experimentally validate a plate architecture reactor design.

2.8 Research emphasis

Tolley's computational flow studies discussed in Section 2.5.3 demonstrated the modeled cost reduction and conversion improvement of a differential temperature microreactor compared

to the baseline high-/low-temperature shift water-gas shift reactor. A monolithic prototype WGS reactor was additively manufacturing and tested without integrated catalyst, but there is still work that needs to be done to fully validate this model.

The objective of this research is to determine if a plate architecture water-gas shift reactor can be realized using advanced manufacturing methods, with integrated catalyst deposited using previously reviewed techniques, for use in the Solar Thermal Advanced Reactor System (STARS) module under development at PNNL. This research focuses on catalyst development and integration, reactor design and manufacture, and experimental system design and manufacture.

Chapter 3: Reactor

3.1 Purpose

The purpose of this chapter is to discuss the design philosophy, material selection, design, manufacture, and assembly of the sub-scale water gas shift reactor prototype.

3.2 Reactor design philosophy

There are many considerations that go into designing a reactor, and many of these considerations are closely intertwined with each other. The design of the plate architecture water-gas shift reactor was informed by—but not limited to—the requirements imposed by the following parameters:

1. **Process conditions:** The reaction's process conditions are the primary drivers of the reactor design. The conditions were informed by Tolley's simulation and then realistically tuned for experimental studies, as discussed later in Chapter 5.

2. **Material properties and limitations:** The design of the reactor must account for each material's physical response to the high temperature, medium pressure process conditions. The compatibility between the different solid materials and the fluids must also be assessed.

3. **Catalyst integration and volume:** It is a requirement to integrate catalyst for this reaction to achieve higher conversions. The catalyst must be easily integrated onto the walls of the reactor.

4. **Measurement instrument integration:** The design of the reactor must accommodate a fiber optic temperature sensor to measure the temperature profile.

5. **Manufacturability:** Due to the various challenges experienced in the fabrication of the monolithic test article using laser powder bed fusion (LPBF) additive manufac-

turing technology, the manufacturing strategy for the plate architecture design seeks to leverage advanced manufacturing processes.

6. **Safety:** Special care must be taken in the design of this reactor because of the high potential for hydrogen leaks to occur. Hydrogen, even in very low concentrations, is dangerous because it is highly flammable.

7. **Cost:** The overall design aims to reduce material, manufacturing, labor, and maintenance costs. As a cost-saving effort, the proof-of-concept prototype will be a sub-scale design of the reactor.

8. **Durability:** The reactor must be able to withstand thermal cycling and aging, especially during the testing process.

Balancing each of these considerations is no trivial task, and it is difficult to rank the importance of each set of requirements against each other. There are trade-offs regardless of the design requirements that are prioritized, and it is especially difficult to judge what is most important during the design process of novel technologies. Later on, Section 6.3 discusses the lessons-learned about the aforementioned design requirements.

3.3 Reactor prototype design

The WGS reactor employs a microscale parallel plate architecture design. A plate architecture design was selected for the process-intensified WGS because of the following favorable properties:

1. Enhanced heat and mass transfer phenomena at the microscale

2. Ease of integrating catalyst to the channels walls

3. Reduction in required catalyst volume

4. Increased modularity

5. Feasibility of sub-scale testing

The procurement of a full-scale model was infeasible due to cost and testing limitations, so a one-tenth sub-scale reactor was design and procured. The test article is both a reactor and a heat exchanger in which an integrated coolant fluid flows in counter-flow with the reaction gases. Figure 3.1 below depicts the general structure of a parallel plate reactor with counterflow heat exchange.

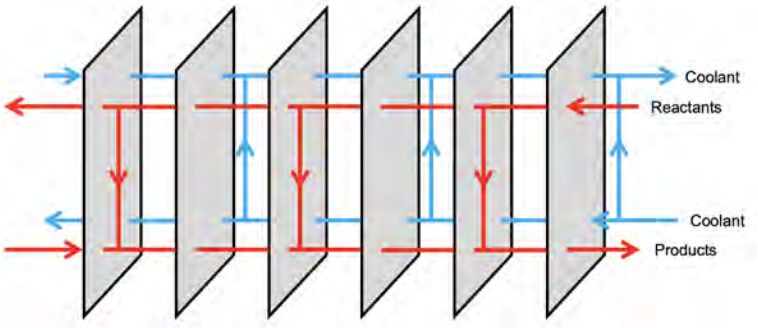

Figure 3.1: General depiction of a parallel plate architecture chemical reactor featuring counterflow heat exchange.

The reactor underwent several design iterations before the design was finalized for manufacture. The following sections describe each iteration leading up to the final design.

3.3.1 First design iteration

Because the bulk of the reactor is comprised of reactant and coolant plates, the initial iteration of the plate-architecture reactor focused on the design of the unit cell, as seen in Figure 3.2 below.

This first design featured a parallel plate, counterflow heat exchange setup with large 22.6 mm holes for the inlet and outlet fluids as well as a thin, complex gasket design. The plate dimensions were 100 mm x 200 mm x 1 mm.

There were several features in the first design that needed to be iterated upon. Firstly, the preliminary design focused only on the unit cell of the reactor and did not take the whole reactor design into account. There were no provisions for fastening or aligning the plates to

Figure 3.2: The first design iteration focused only on the design of the unit cell, which consists of a reactant plate, gasket, and coolant plate.

each other, nor were there provisions to support integration into the test loop. Additionally, the dimensions of the plate were not modeled after the simulation that this research is based off of. Finally, the design lacked integration of temperature instrumentation to validate the temperature profile of the reactor.

As a result of the numerous gaps and flaws with the initial design, another design iteration was needed to address the aforementioned issues.

3.3.2 Second design iteration

The second design iteration focused on developing the broader reactor, simplifying the plate and gasket design, and bringing the design closer to the modeled dimensions. Figure 3.3 below shows the updated unit cell design.

The unit cell for the second design iteration improves upon the original design in a few ways. The gasket design was simplified, the individual plate thickness was increased, and alignment provisions were included in the unit cell design. Sixteen units cells were combined to form the subscale reactor prototype showcased in Figure 3.4 below.

Figure 3.3: The unit cell design was simplified for the second design iteration.

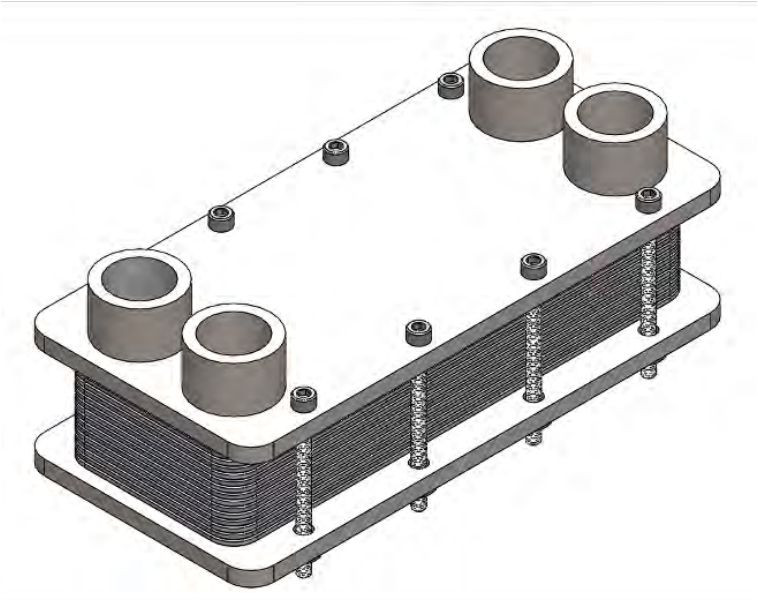

Figure 3.4: An isometric view of the second reactor design iteration.

Each plate has dimensions of 200 mm x 75 mm x 3 mm, with the top and bottom plates being 210 mm x 100 mm x 10 mm. When assembled, the reactor has dimensions of 210 mm x 100 mm x 73 mm (including the height of the connection ports). The ports are designed

to be tapped as 3/4" NPT female connections and the fasteners used to clamp the reactor together are 10-32 socket cap screws.

Despite the improvements to the reactor design, there were still a multitude of flaws with this design iteration. These flaws are as follows:

1. Instead of having the inlet and outlet ports of each plate on diagonal corners of the plate to promote flow across the, the ports were lined up on the same side of the plate, which renders a good majority of the flow channel useless. Positioning the inlet and outlet ports in the fashion represented by Figure 3.4 would negate the counterflow heat exchange interaction, which is a major design flaw.

2. The flow channel geometry is inconsistent with the geometries modeled by Tolley. The plate width is 75 mm and the actual channel width is 61 mm, but in Tolley's modeling, the reaction channel width is 80 mm, which is significantly greater than the width of the plate for this design. The behavior of the reaction is highly dependent on the volume of the reactant channel, which is less for this design than reported in Tolley's studies.

3. Though the plates of the reactor have alignment holes at the ends of each plate, the top and bottom pressure plates do not. This means that, while the plates can be aligned to each other, there is nothing that aligns the reactor body to the pressure plates. This is a major design flaw because the inlet and outlet connections to the process fluids can become misaligned, which could cause major leaks out of the reactor.

4. When compared to the size of the reactor, it is clear that the 10-32 socket cap screws do not possess the strength or robustness to clamp the reactor together. The shape of the socket head does not promote distribution of the force across a large surface area, which would place the fasteners at risk of breaking if tightened too hard. Different fasteners needed to be selected for the clamping application.

5. Like the last design, this iteration still lacked the proper accommodations for temperature instrumentation, which is necessary to measure the temperature profile.

3.3.3 Final design iteration

The final reactor design required a more holistic approach to balance the requirements listed in 3.2. Using the lessons learned from the previous design iterations, the design of the reactor was completely overhauled and each requirement was carefully considered and addressed to ensure that all requirements are met.

The final geometries of the reactant plate are shown in Figure 3.5. The coolant plates are the same geometry and design as the reactant plates, but mirrored across the vertical axis as shown in Figure 3.6. The basic details of the plates are described in Table 3.1.

Table 3.1: Geometry of final plate design

Parameter	**Value**
Length	200 mm
Width	100 mm
Height	2 mm
Material	316 stainless steel

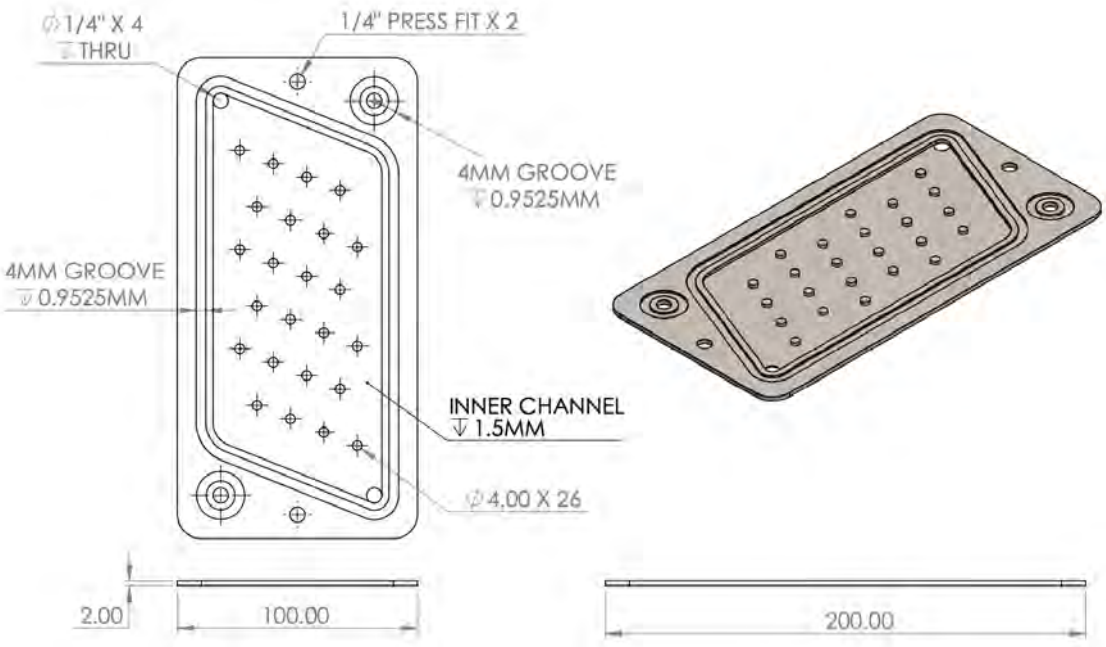

Figure 3.5: The final reactant plate design and geometries.

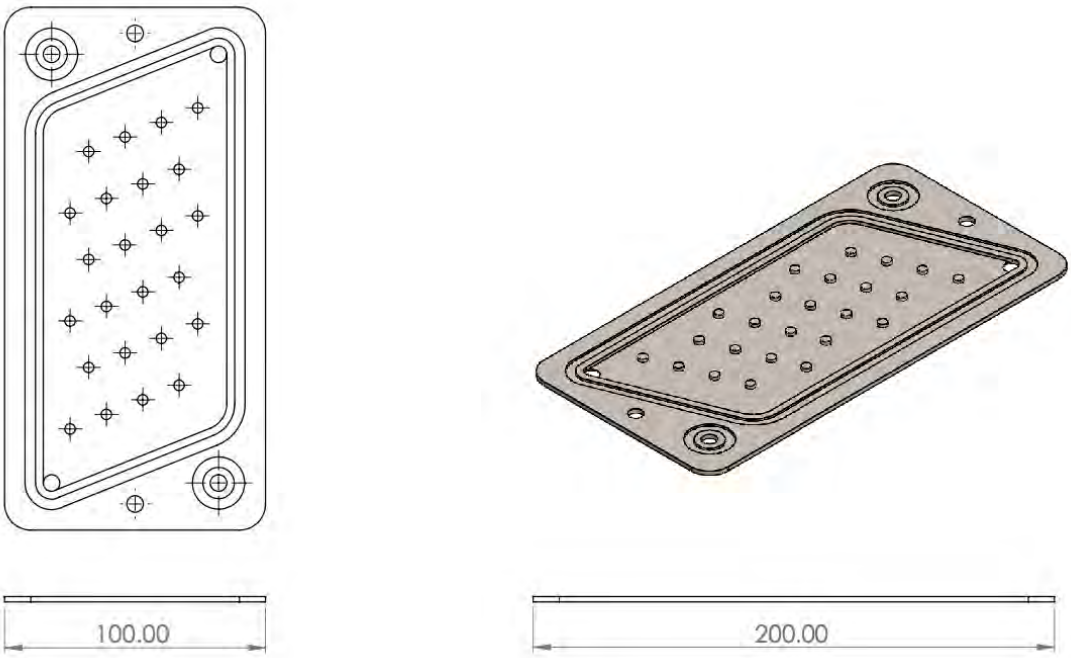

Figure 3.6: The final coolant plate design and geometries.

The gasket design was overhauled for the final design. Initially, the gaskets were needlessly complex and too thin for effective sealing. The new gasket and gasket groove, highlighted in Figure 3.7, is a much simpler design. This change was made to simplify manufacturing of the plate and gaskets, which cuts down on manufacturing costs and time.

The plate design also features 24 evenly-spaced posts in the flow channel. The posts provide structural support for the bottom face of the plate above, and in reactant channels, there is a minimal increase in the coated catalyst area due to the exposed post surface. The addition of these posts is in scope and made easy because of sinker EDM technology, which is discussed later in Section 3.5.

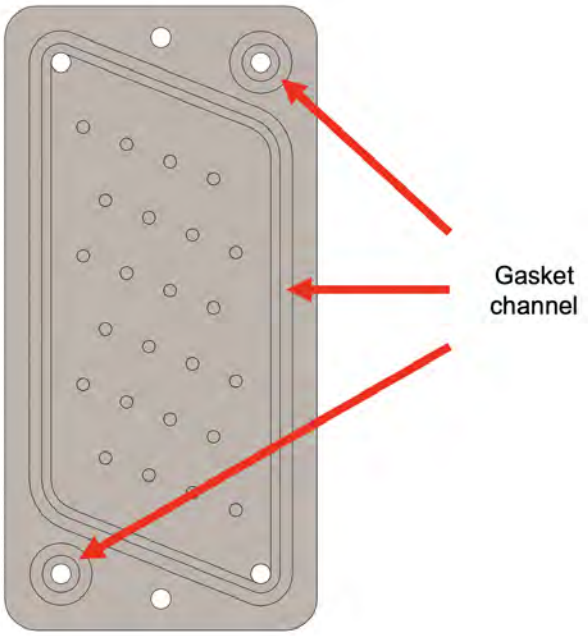

Figure 3.7: The final plate design features simplified gaskets.

A unit cell with a coolant plate, reactant plate, and accompanying gaskets can be seen in Figure 3.8.

Figure 3.8: Unit cell of final WGS reactor design.

The plates are sandwiched between two thick steel plates with bolt holes cut through them. These thick plates are CNC machined and their purpose is to evenly distribute the force from the bolts across the reactor. The dimensions of these two plates are shown in Figures 3.9 and 3.10 below.

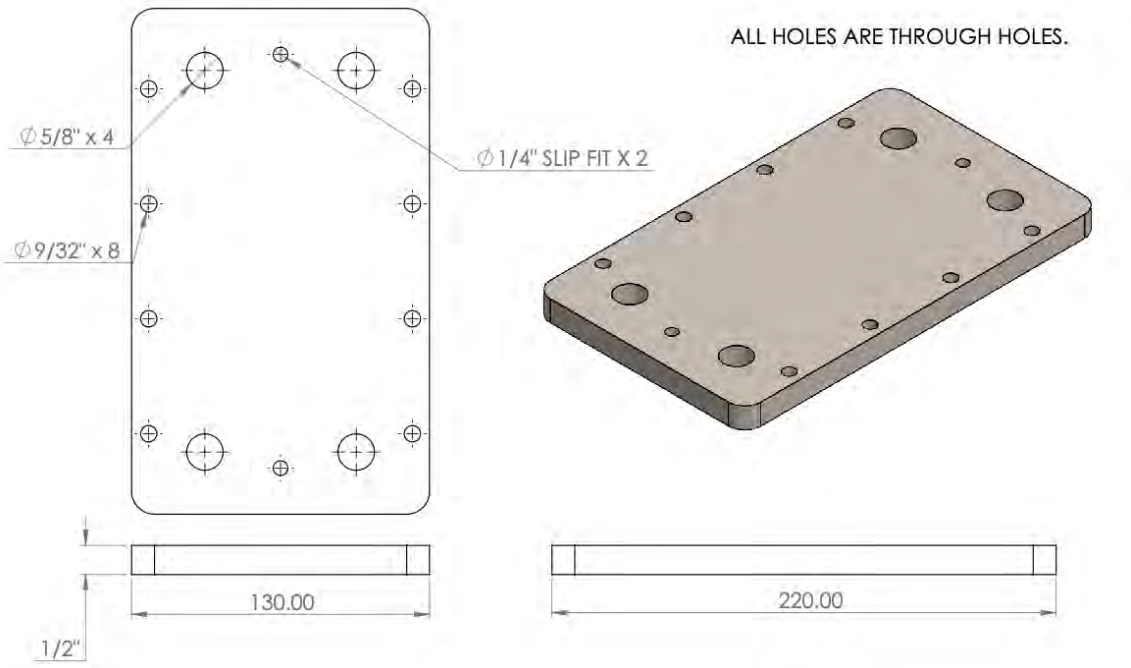

Figure 3.9: Top plate geometries and dimensions.

The top plate has dimensions of 220 mm x 130 mm x 12.7 mm. It features eight 9/32" bolt holes through which the bolts slip through to fasten and clamp the plates together. Two 1/4" slip fit holes are used to align the top plate with the rest of the reactor. Four 5/8" holes allows the top plate to slip over the 1/4" piping of the manifold plate without clearance issues. The bottom plate features similar dimensions, but different design features are incorporated.

The bottom plate of the reactor also has dimensions of 220 mm x 130 mm x 12.7 mm and it showcases the same eight 9/32" bolt holes for the clamping the reactor together. It features a recessed gasket groove for a plate-shaped gasket to prevent metal-on-metal sealing of the bottom plate surface against the bottom plate of the reactor.

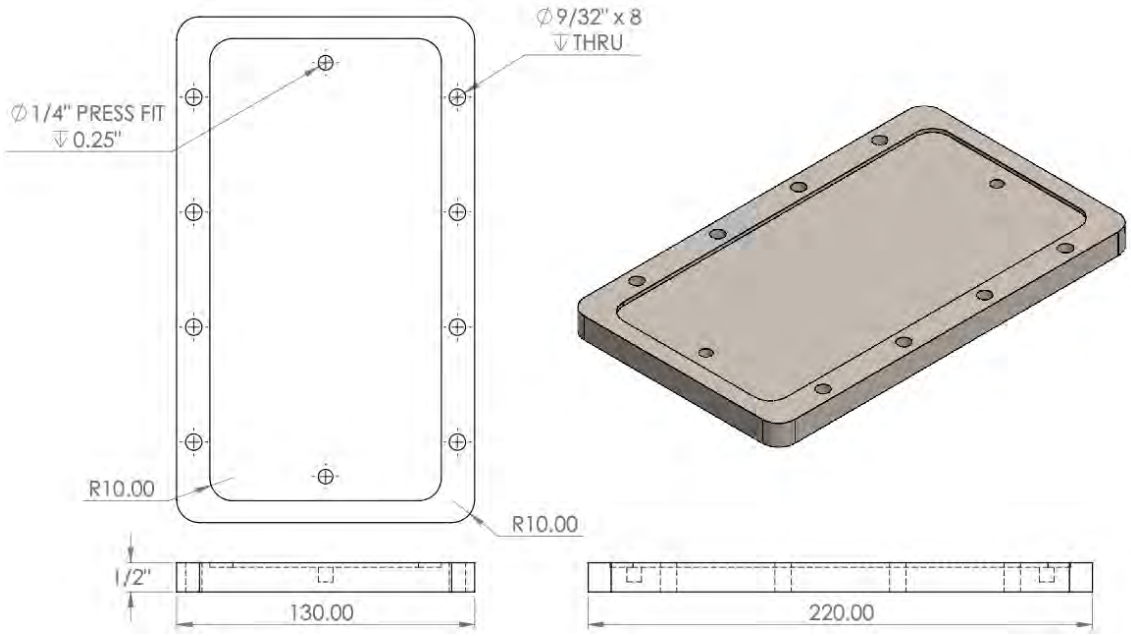

Figure 3.10: Bottom plate geometries and dimensions.

A manifold sits between the thick top plate and the first process plate. This manifold is needed to couple the reactor to the test loop, so it sits below the thick top plate to ensure proper sealing against the process plates. The manifold is a thin plate of steel with dimensions of 200 mm x 100 mm x 2 mm. 1/4" stainless steel tubing is welded to the inlet and outlet channels of the reactor to enable the use of Swagelok fittings to couple the reactor to the test loop. The design of the manifold is shown in Figure 3.11 below.

Two 1/4" x 4" hollow steel dowels are used to help keep the reactor components aligned. The dowels are press fit into the thick bottom plate and the plates slip fit around the dowels.

An instrumentation plate was specified to incorporate fiber optic continuous temperature measurement instrumentation into the reactor. The purpose of measuring the differential temperature profile across the reaction channel length is to corroborate the modeled temperature profile. The plate design and dimensions can be seen in Figure 3.12 below.

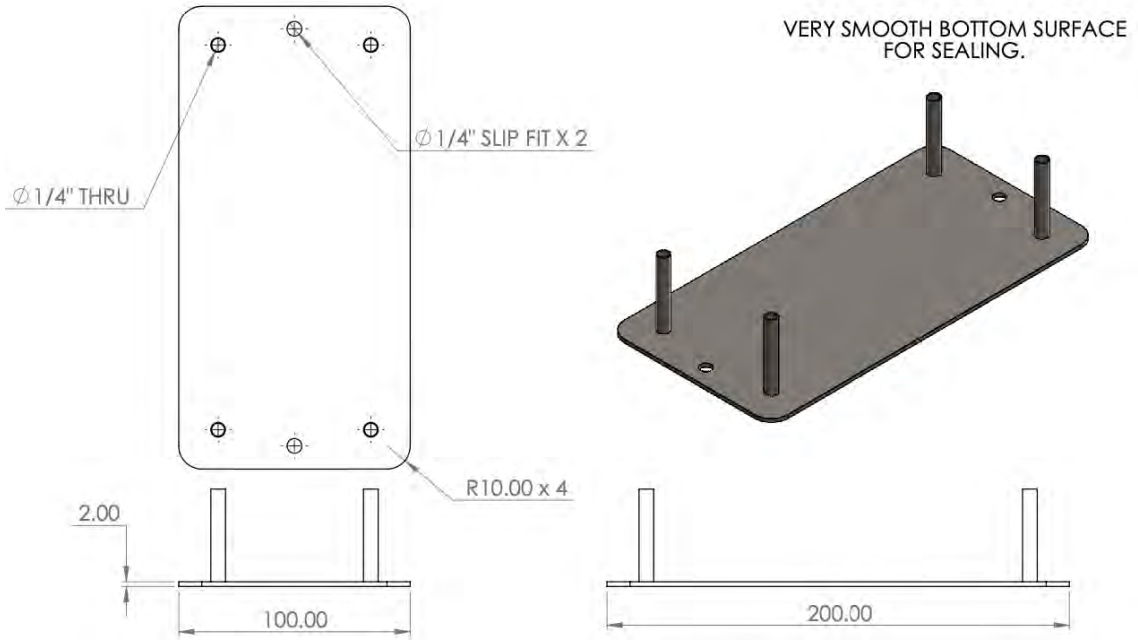

Figure 3.11: Manifold plate geometries and dimensions.

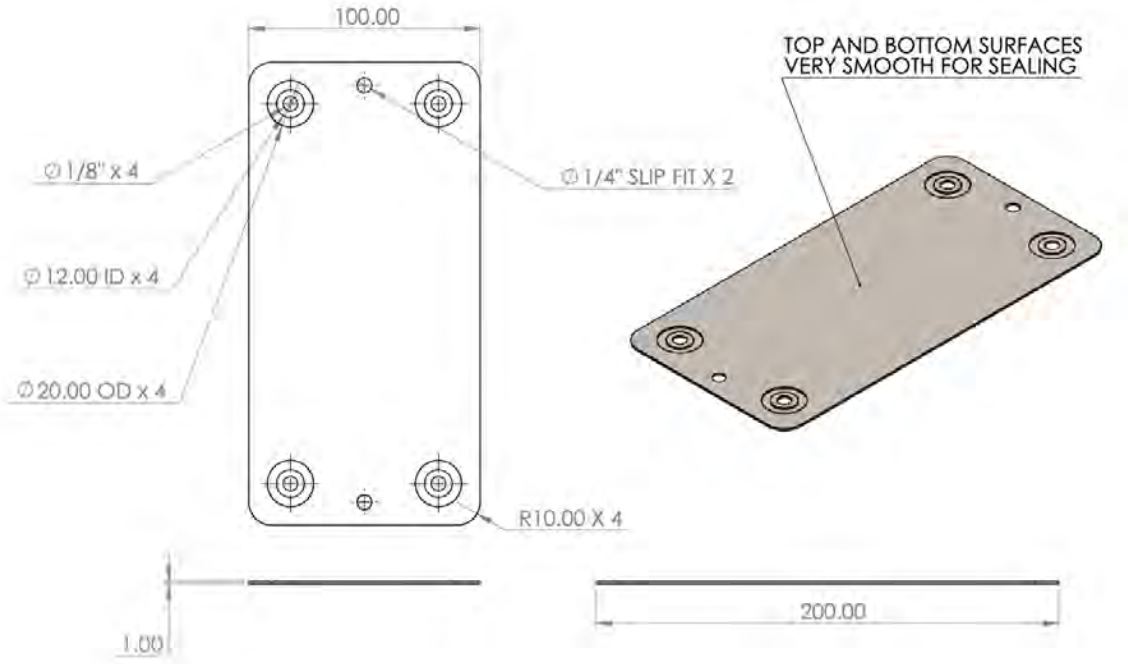

Figure 3.12: Instrumentation plate geometries and dimensions.

The instrumentation plate features very smooth surfaces to promote better sealing against the other plates in the reactor. The design incorporates the use of gaskets around the process fluid channels to prevent fluids from leaking out of the plate. The instrumentation plate is thinner than the other plates because its only purpose is to incorporate the fiber optic temperature sensor, which is 0.25 mm in diameter. It is also advantageous to keep the plate thin in order to minimize the heat transfer effects that the added material will have on the reaction physics.

Various views of the final reactor assembly are depicted in Figure 3.13.

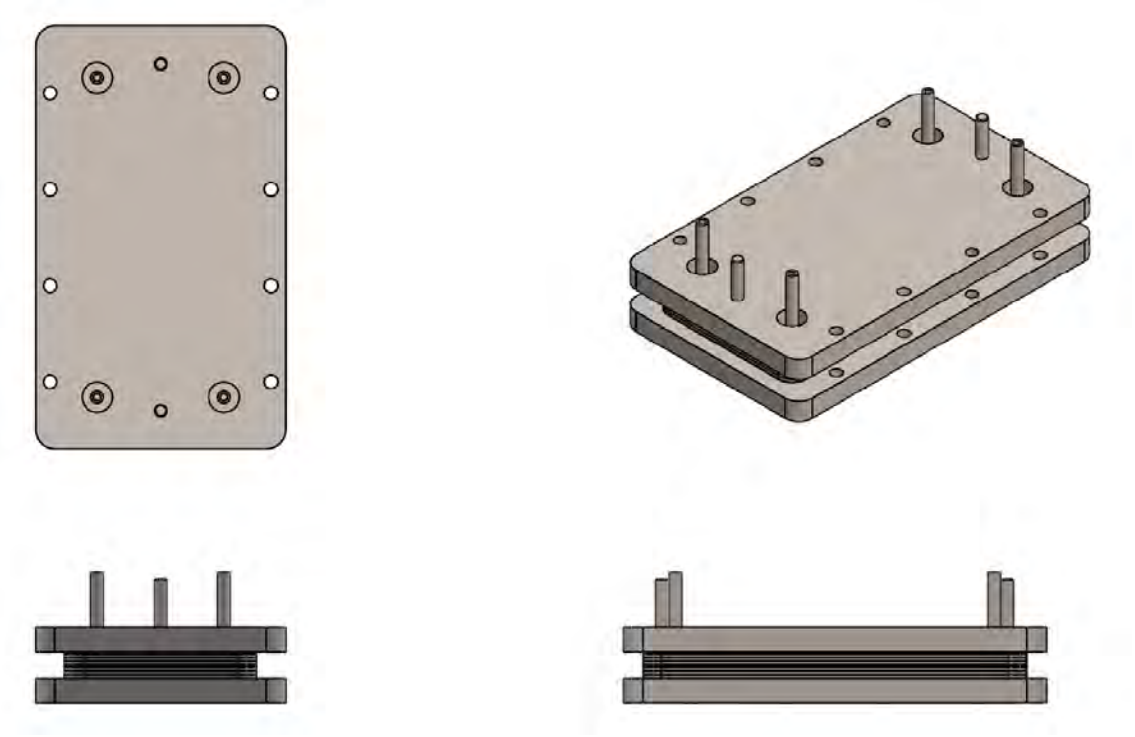

Figure 3.13: Final assembly of sub-scale WGS reactor prototype.

A complete set of drawings and solid models of each component can be found in Appendix A.1.

3.4 Reactor materials

A variety of materials were procured in the construction of the sub-scale microreactor prototype. The purpose of this section is to describe the materials that were selected and the rationale behind the material selection.

Plates: Grade 316 stainless steel (316SS) was chosen as the material for all plates. 316 stainless steel is an incredibly versatile material for chemical processes due to its resistance to corrosion and excellent stability and heat transfer characteristics at high temperatures. 316 stainless steel is resistant to hydrogen embrittlement [45] and it is also compatible with sinker EDM technology because it is a conductive material.

Gaskets: Crane-foil® graphite gasket sheet (Style 245 by John Crane) was selected as the gasket material due to its capabilities of sealing at high temperature capabilities, as conventional gaskets and O-rings cannot withstand the temperatures required for the process-intensified WGSR. This graphite gasket material can withstand temperatures between -240°C to 455°C and pressures up to 136 bar. It is chemically resistant to the reacting gases and coolant fluid and is easily sourced in 1/16" sheets. The material properties of the gasket material can be seen in Table 3.2 below.

Table 3.2: Material properties of Crane-foil graphite gasket material [46].

Parameter	**Value**
Temperature limits	-240°C to 455°C
Pressure limits	Up to 136 bar (g)
pH range	0-14
Composition	95% graphite
Density	1120 kg/m^3
Compressibility (ASTM F-36)	40%
Recovery (ASTM F-36)	20%
Sealability (ASTM F-37)	0.5 mL/hr

Fasteners: Eight 1/4-20 x 2" SAE Grade 8 bolts were used to bolt the reactor plates together to ensure a tight seal. Each bolt was tightened with a 1/4" stainless steel flat washer and a 1/4-20 stainless steel nut.

3.4.1 Bill of materials

A bill of materials for the sub-scale reactor prototype is presented in Table 3.3 below.

Table 3.3: Bill of materials for WGS reactor prototype

Component	**Quantity**
Reactant plate	6
Coolant plate	7
Bottom plate	1
Top plate	1
Sealing plate	1
Instrumentation plate	1
Gaskets	15

3.5 Reactor manufacture and assembly

The manufacture of the complete reactor assembly leveraged many both in-house and external resources. While the metal reactor structure itself was outsourced for manufacturing, the gaskets were made in-house. Post-manufacturing processing of the plates was also applied in-house to support catalyst coating and temperature instrumentation integration.

The purpose of this section is to describe the processes used to physically fabricate and realize the reactor design previously discussed in Section 3.3.3.

3.5.1 Plates

The manufacturing of the reactor plates and supporting structure was outsourced to Ram-Z Fab, a machine shop located in Corvallis, OR. Ram-Z Fab was selected as the manufacturer of choice due to its close proximity and good relationship with Oregon State University.

The original manufacturing strategy for fabricating the plates leveraged the use of conventional computer numerical control (CNC) machining processes in manufacturing all features and components. The decision to pursue conventional manufacturing processes was made after reviewing lessons-learned from the additively manufactured prototype, which

was plagued by high costs and long manufacturing delays. As such, the plates were designed and quoted with this in mind.

During the manufacturing process for the plates, Ram-Z Fab experienced difficulty using CNC techniques, specifically due the recessed geometries of the gasket channels and main channel. During machining of the wide main channel, the thin 0.5 mm floor of the plate did not have enough structural integrity to withstand machining, causing the tooling to break through the floor of the work piece. After multiple attempts to remedy this on the CNC, Ram-Z concluded that CNC machining was an infeasible option for fabricating the plates and turned to sinker electrical discharge machining (EDM) as the manufacturing solution for the reactor plates.

As aforementioned in Subsection 2.6, a benefit of sinker EDM is the addition of small surface irregularities on the work piece, represented in Figure 2.21 above. The presence of these irregularities would be disadvantageous for a sealing surface, but the sinker EDM die is not being used to machine any sealing surfaces. Rather, the die is used to machine the gasket channels and the main fluid channel into the plate, and a rough fluid channel is advantageous for catalyst adhesion. It was requested of Ram-Z Fab to maintain a rough surface finish of the fluid channel while keeping the sealing surfaces between plates smooth.

For the reactant plates, the surface irregularities from the sinker EDM die on the surface of the main channel are advantageous because, at a microscale, the increased surface area promotes better adhesion of the catalyst to the stainless steel substrate. In the coolant plates, the surface finish does not affect the flow of the liquid coolant that flows through the main channel. The surface finish of the gasket channels is also inconsequential because the graphite gasket material conforms to the shape of the channel regardless of the presence of microscale irregularities.

3.5.2 Gaskets

The graphite gaskets were manufactured in-house at ATAMI using the LPKF 2820P laser cutter. The LPKF 2820P laser engraver is a powerful tool that features a porous vacuum

bed, 355 nm, 20 um diameter focused beam at the substrate, 350 mm x 350 mm x 11 mm (XYZ) working area, and ±25 µm positioning accuracy. The LPKF has many applications that include cutting materials (metal shims, glasses, organic materials), cutting and drilling in flex circuits, and other PCB and device laser processing. Figure 3.14 below shows a staged photo of the researcher utilizing the LPKF for gasket manufacturing.

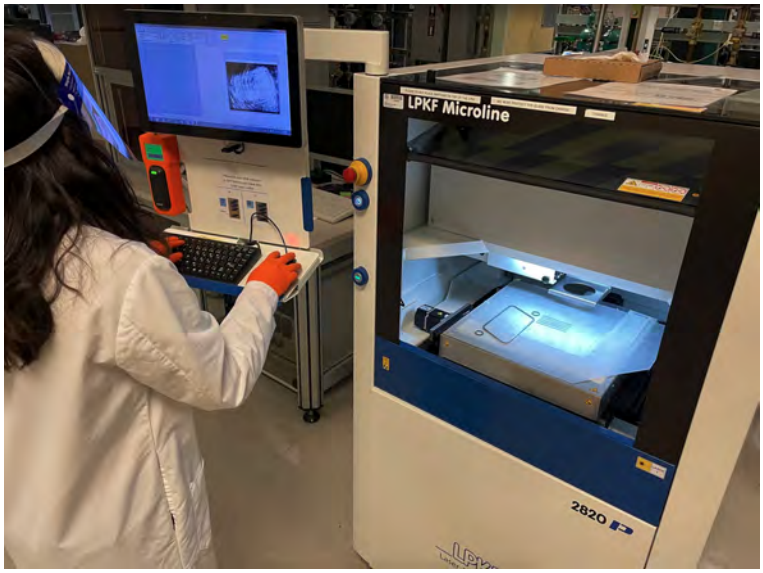

Figure 3.14: The researcher using the LPKF.

The gasket model must first be prepared and converted into the proper file format. The gasket was converted from a .SLDPRT to a .DXF file in SolidWorks, then input into the CircuitCAM software on the Design Studio Workstation at ATAMI to convert into a .LMD file format, which can be read by the LPKF laser cutter. Once converted, the file was loaded onto a flash drive and inserted into the laser cutter. This concluded the preparation of the file used to supply the cutting pattern to the laser cutter.

Two 610 mm x 610 mm x 1.59 mm (24" x 24" x 1/16") sheets of Cranefoil graphite gasket material were procured from McMaster Carr. Once received, the sheets were cut into sixteen 200mm x 100mm blanks using a box cutter. Each rectangular sheet was used to manufactured a single set of gaskets for a plate. Figure 3.15 below depicts one of the blanks loaded onto the bed of the laser cutter.

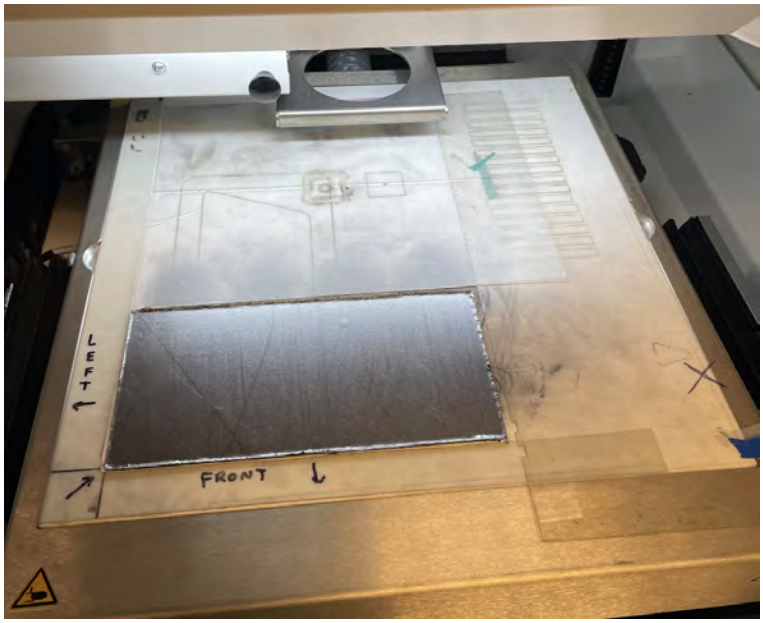

Figure 3.15: A blank gasket sheet loaded into the LPKF laser engraver. It is surrounded by static plastic sheets.

When loading the laser cutter with a gasket sheet, the rest of the porous vacuum bed should be covered with supplementary sheets to promote good suction of the vacuum to the graphite gasket material, as shown in Figure 3.15 above. Additionally, the L-shaped sheet aligned to the bottom left of the blank is needed to properly line up the work piece with the origin of the vacuum bed.

One sheet was taken and used in refining the laser cutter recipe. Because of the tool's wide range of capabilities, a specialized set of laser parameters needed to be specified for the unique graphite gasket material. Using the two small concentric circles from the reactor gasket pattern, the laser cutter parameters were iteratively refined until the laser satisfactorily cut through the 1.59 mm graphite gasket material. The final laser cutter parameters can be found in in Table 3.4 below.

Once the recipe had been refined, the gaskets were cut using the laser cutter. A finished gasket is depicted in Figure 3.16 below.

Table 3.4: LPKF laser cutter parameters for milling channels

Parameter	Units	Value
Current	A	56
Frequency	kHz	8
Power	W	5
Jump delay	μs	2000
Jump speed	mm/s	100
Laser off delay	μs	100
Laser on delay	μs	0
Mark delay	μs/s	100
Mark speed	mm/s	250
Polygon delay	μs	0
Air pressure	-	Yes
Repetitions	-	10
Tool delay	-	0
Tool z-offset	mm	1.59

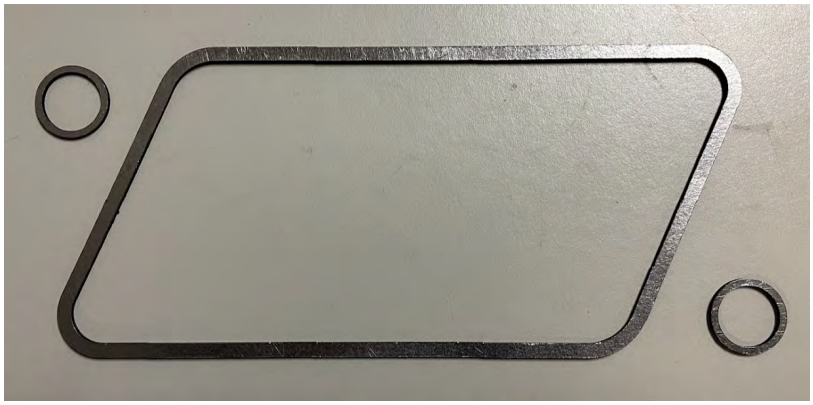

Figure 3.16: A finished graphite gasket for the reactant and coolant plates.

3.5.3 Instrumentation plate

To measure the temperature profile of the reactor, a fiber optic temperature sensor from Luna Innovations was incorporated into a special instrumentation plate in the reactor. This instrumentation is described further in detail in Section 5.7.4 of Chapter 5. The empty instrumentation plate, depicted in Figure 3.17 below, fits between a coolant and reactant plate. It features four gasket channels to prevent process fluids from leaking out through the plate.

Figure 3.17: A blank instrumentation plate.

In order to accommodate the fiber and fit the instrumentation plate flush with the other plates of the reactor, a channel needs to be grooved into the plate. To simplify manufacturing and to reduce the possibility of snapping a LUNA fiber, a straight groove was milled across the plate in the configuration depicted by Figure 3.18 below.

Figure 3.18: An image depicting the predicted milling path for the fiber channel.

The LPKF laser engraver was used to cut a guide of the channel placement into the plate. A rotary Dremel tool with a pointed carving bit was then used to clean, deepen, and widen the groove to fit the LUNA fiber into the plate. The process of developing the laser engraver recipe is described in Table 3.5 below. The final completed instrumentation plate is shown in Figure 3.19.

Table 3.5: LPKF laser cutter parameters for milling channels

Parameter	Units	Value
Current	A	56
Frequency	kHz	100
Power	W	8.06
Jump delay	μs	2000
Jump speed	mm/s	100
Laser off delay	μs	100
Laser on delay	μs	0
Mark delay	μs/s	600
Mark speed	mm/s	250
Polygon delay	μs	15
Air pressure	-	Yes
Repetitions	-	23
Tool delay	-	0
Tool z-offset	mm	0

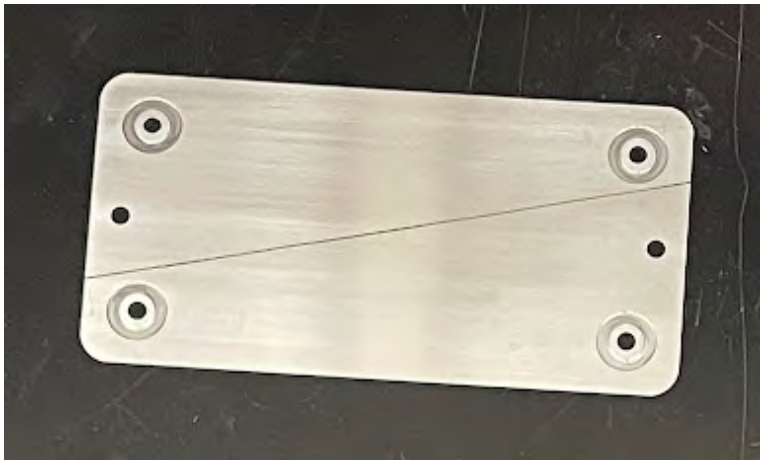

Figure 3.19: The straight fiber channel was milled into the plate from reaction channel inlet to the reaction channel outlet.

3.5.4 Reactor assembly

Once the fiber optic sensor channel had been manufactured on the instrumentation plate, the reactor was assembled. The gaskets were pressed into the plates by hand. Sealing surfaces were wiped clean using acetone and low-linting task wipes. A top view of the laid out reactor materials can be seen in Figures 3.20 and 3.21 below.

The plates were then assembled in the following order, from the bottom (first) to top (last), as visually numbered in Figure 3.22 below:

1. Bottom plate x1
2. Bottom gasket x1 (not pictured)
3. Bottom coolant plate x1
4. Unit cell x3
5. Instrumentation plate x1
6. Unit cell x3
7. Manifold x1
8. Top plate x1

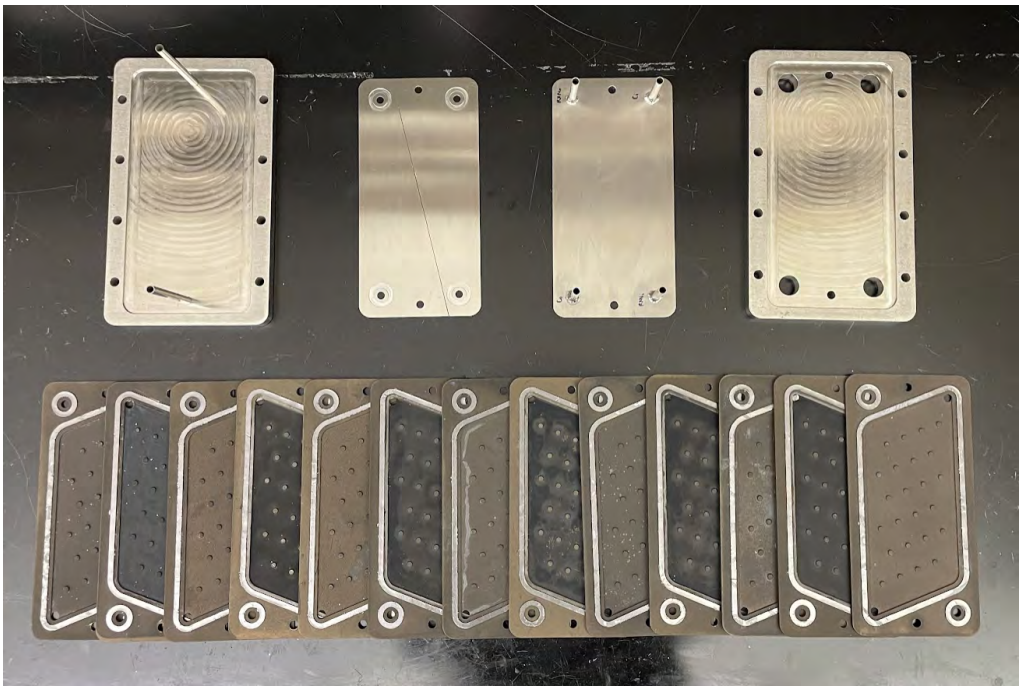

Figure 3.20: The reactor materials with unit cell plates facing upward.

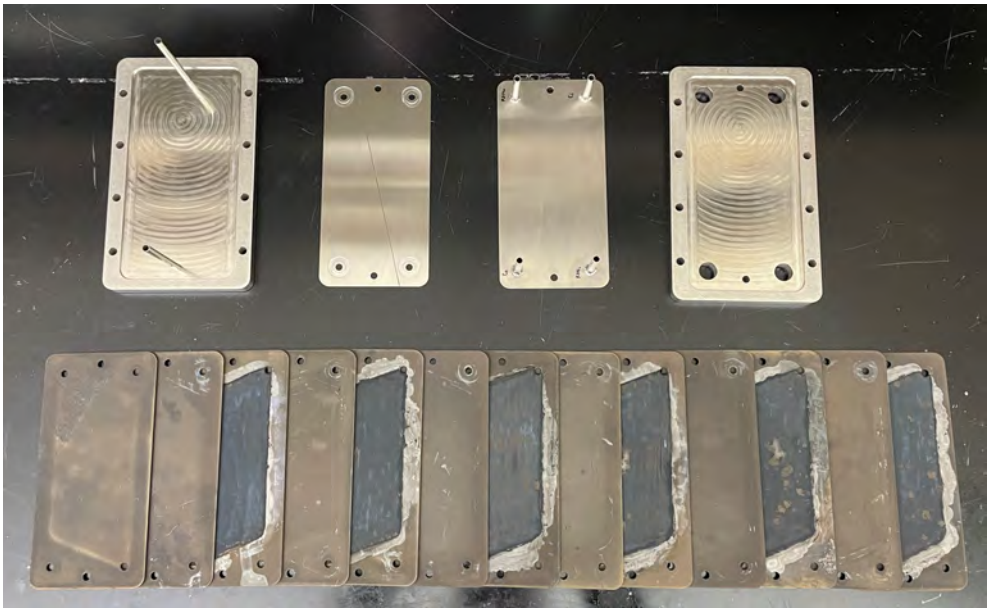

Figure 3.21: The reactor materials with unit cell plates facing downward.

Once assembled, the gaskets still needed to be compressed. A front view of the assembled reactor before compression can be seen in Figure 3.23 below. The reactor was compressed by tightening the eight nuts onto the reactor assembly bolts. Each nut was tightened 5 even rotations per cycle to guarantee even distribution of force between each bolt. Once tightened, the LUNA fiber was carefully threaded into the reactor. The fiber was pushed through such that approximately 50 mm of fiber was left sticking out of the reactor. A top view of the integrated fiber is shown in Figure 3.24 and an isometric view is presented in Figure 3.25. Finally, once assembled, the reactor was integrated onto the loop using Swagelok connectors, as depicted in Figure 3.26.

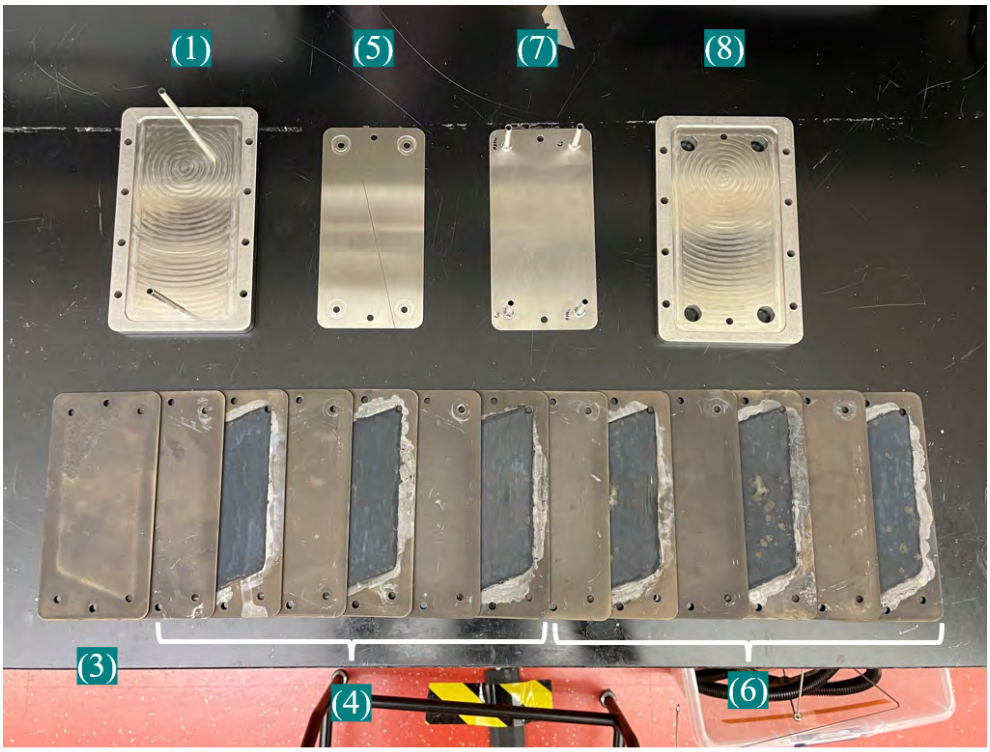

Figure 3.22: Order of assembly for the WGS reactor.

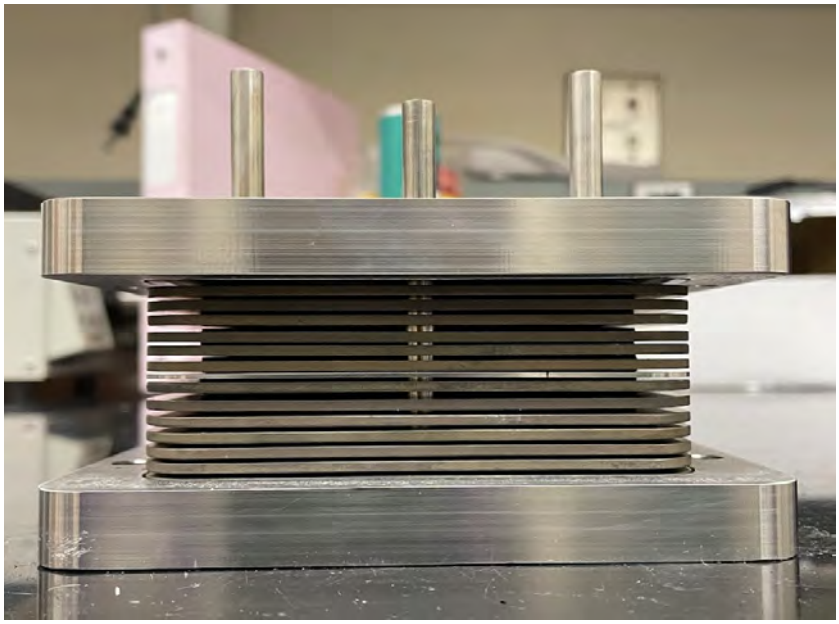

Figure 3.23: A front view of the reactor assembled before compression of gaskets.

Figure 3.24: A top view of the reactor assembled after compression of gaskets. The arrow points to the LUNA fiber integrated into the reactor via instrumentation plate.

Figure 3.25: An isometric view of the reactor assembled after compression of gaskets with integrated LUNA fiber.

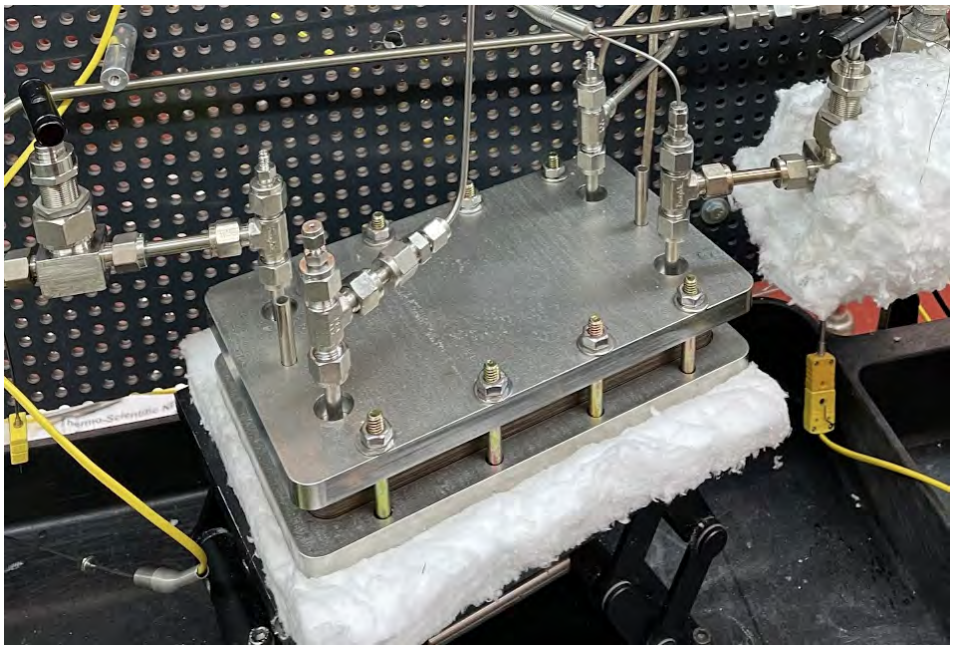

Figure 3.26: The reactor later integrated onto the test loop.

3.6 Reactor summary

The design and manufacture of the sub-scale diabatic water-gas shift microreactor was informed by the process conditions of the reaction, properties and limitations of the selected equipment and materials, ease of catalyst integration, feasibility of experimental realization, manufacturability, safety, and cost. A parallel plate architecture design was chosen because it is advantageous for the process intensified water-gas shift reactor. Parallel plate designs take advantage of enhanced heat and mass transfer phenomena at the microscale, enable the wash coating of catalyst onto the reaction channel walls, increase modularity, and enable the feasibility of a sub-scale design. The design underwent three iterations and features six unit cells, a fiber instrumentation plate, and graphite gaskets. The reactor plates were outsourced for manufacturing via sinker EDM while the graphite gaskets were manufactured in-house using the LPKF laser cutter. The instrumentation plate was post-processed in-house to enable integration of the fiber optic temperature sensor. A channel spanning the diagonal of the reaction channel was engraved into the instrumentation plate using the LPKF. Once all components were manufactured, the reactor was assembled and compressed before being integrated onto the test loop.

Chapter 4: Catalysis

4.1 Catalyst selection

The water-gas shift reaction is catalyzed heterogeneously in which a solid-phase catalyst is used to promote conversion of the gaseous reactants into gaseous products. As reviewed in Section 2.3, there are many feasible catalyst options for the WGSR.

4.1.1 Catalyst selection process

Given the wide range of available catalysts, a suitable catalyst and coating technique had to be chosen for this research, with many factors affecting the selection. The following factors were taken into consideration:

1. **Reactor geometries:** The architecture and geometries of the reactor have a substantial impact on the feasibility of certain catalysts. For example, with Tolley's original prototype WGS reactor, utilizing a metal foam insert would be have been impossible due to the monolithic structure of the prototype. Even a washcoated catalyst would have been infeasible to implement due to the enclosed architecture of the channels. With the plate architecture design, both a catalyst supported on a porous foam support and a washcoated catalyst would be feasible options.

2. **Process conditions:** The medium temperature, medium pressure conditions of the reaction also helped inform the catalyst selection. Conventional low- and high-temperature shift WGS catalysts such as $CuO - ZnO - Al_2O_3$ and $Fe_2O_3 - Cr_2O_3$, respectively, operate outside the range of the optimal operating conditions modeled by Tolley's simulations, so selecting a conventional catalyst would result in non-optimized catalytic performance and poor stability. Some precious metal catalysts, such as Rh and Ru based catalysts, promote the undesirable synthesis of methanol at the optimal process conditions [26].

3. **Catalyst properties:** The inherently poor performance and stability properties of these aforementioned catalysts at the desired process conditions make them, among other similar options, infeasible.

4. **Adhesion:** One major challenge in catalysis is adhesion of the catalyst support to the structural substrate [31]. Special attention had to be paid to the adhesion characterization of the catalysts reported in literature.

5. **Manufacturability:** Ease of manufacturability was another important consideration in the selection process. Limited prior knowledge and context of catalyst synthesis techniques intensified the need for a thoroughly documented preparation process for the selected catalyst. A large portion of the reviewed literature lacked the detail required to enable repeatability of the catalyst synthesis process described. Combined with the limited research-level catalyst manufacturing resources that were available for use, these factors narrowed down the scope of the selection significantly.

6. **Availability:** Availability was another factor that played into the selection of the catalyst. At the beginning of the selection process, there was initial interest in utilizing Nexceris's Reformance-WGS™for this research. This commercially available precious metal water-gas shift catalyst is based on nano-scale mixtures of ceria-based oxides and uniformly incorporated precious metal. It operates at 300-400°C and, according to the catalyst's white paper, claims to have the capability of shrinking the reactor size to 5-10 percent of current two-stage WGS system [47]. However, no response was received after attempts to reach out to the manufacturer, which eliminated this catalyst as a viable option. Additionally, supply chain disruptions caused by COVID-19 severely impacted the procurement of the catalyst materials, so this was additionally infeasible.

7. **Cost:** Budget limitations restricted the use of expensive pre-manufactured catalysts and high-cost catalyst components such as palladium or rhodium.

A washcoated platinum-ceria catalyst supported on alumina ($Pt/Ce/Al_2O_3$) was se-

lected from the reviewed catalysts because it satisfied all of the aforementioned selection characteristics. The selected catalyst is consistent with the catalyst composition and coating structure that was used in Tolley's model of the reactor, which simplifies model validation. $Pt/Ce/Al_2O_3$ exhibits excellent stability and catalytic activity for temperatures between 250-400°C, resists deactivation due to coking and thermal sintering, is non-pyrophoric, and does not require pretreatment. The preparation of this catalyst is well-documented by He et al. and shows excellent conversion in a microreactor configuration. The ingredients for preparing the catalyst were readily available and within budget through various chemical suppliers (Alfa Aesar, Sigma-Aldrich), which made this catalyst a viable and attractive option during the height of the pandemic.

4.2 Catalyst synthesis

The purpose of this section is to describe the materials and methods used in preparing a $Pt/Ce/Al_2O_3$ catalyst for the process intensified water-gas shift reactor.

The synthesis of the $Pt/Ce/Al_2O_3$ catalyst is based off of two recipes. The first recipe is derived from the method initially performed by Germani & Schuurman that characterized water-gas shift reaction kinetics over γ-structured $Pt/CeO_2/Al_2O_3$ catalysts. The secondary recipe was sourced from the preparation of a Pt/Al_2O_3 catalyst coating in microreactors by He et al. Together, these two recipes served as the basis for the $Pt/CeO_2/Al_2O_3$ catalyst that was synthesized for the process intensified water-gas shift microreactor.

This catalyst recipe is based primarily off of the recipe proposed by Germani & Schuurman because the kinetics of the WGS reaction used in Tolley's computational model are based off the performance of the catalyst synthesized by Germani & Schuurman. However, Germani & Schuurman lacked the full detail required to recreate the recipe, so the second recipe from He *et al.* was needed to fill the gaps in knowledge left from Germani & Schuurman. Specifically, the research performed by He *et al.* reports the use of a binder to improve adhesion of the slurry to the substrate. It also details the exact furnace programming required to heat treat the metal substrate and calcine the catalyst.

4.2.1 Catalyst materials

The raw materials and quantities described in Table 4.1 were procured for the synthesis of the $Pt/Ce/Al_2O_3$ catalyst.

Table 4.1: Bulk materials procured for $Pt/Ce/Al_2O_3$ catalyst

Quantity	Material	Details
100 g	γ-alumina powder	Alfa Aesar, 3 μm, 99.97% on metals basis
100 g	Polyvinyl alcohol	Alfa Aesar, 98-99% hydrolyzed
1 L	Deionized water	ATAMI, in-house bulk DI water
1 L	Acetic acid	Alfa Aesar, glacial, 99%+
10 g	Cerium (III) nitrate hexahydrate	Fisher Scientific, 99.5%
1 g	Tetraammineplatinum (II) hydroxide solution	Thermo Scientific, Pt 8-11% w/w)

4.2.2 Catalyst development on coupons

A 153 mm x 153 mm x 4.76 mm hot rolled plate of corrosion resistant 316/316L stainless steel was obtained from McMaster-Carr. The 316L stainless steel sheet was cut into twelve 38.1 mm x 38.1 mm (1.5" x 1.5") square coupons using a metal bandsaw. The edges of each coupon was deburred using a bench grinder and a metal file to make them safe to handle. Once complete, the coupons were cleaned with acetone. Half of the coupons were sandblasted with 60-120 mesh size glass beads to increase the surface roughness of the coupons and thus improve adhesion of the catalyst to the stainless steel substrate. The characterization of the surface roughness of the coupons before and after sandblasting is discussed later in Section 4.3.2.

The two sets of coupons were then calcined in a Thermolyne 47900 furnace, which is capable of reaching temperatures up to 1000°C. The importance of calcination at this step in the catalyst coating process is previously described in 2.3.5. The furnace chamber volume was 101.6 mm x 127 mm x 152.4 mm (4" x 5" x 6") in size, restricting each thermal cycle to four coupons. The temperature was ramped from room temperature at a rate of 20°C min-1 up to the final calcination temperature of 900°C, where it was held for 10

hours, then cooled to room temperature overnight before the coupons were removed from the furnace. The coupons were weighed using a high-precision laboratory scale and set aside for coating. This concluded the pretreatment process of the coupons for the three different types of stainless steel reactor materials.

The synthesis of the catalyst began by weighing out 0.5g of polyvinyl alcohol (PVA). This was done by scooping five 0.1g increments of the binder from the bulk container into a hexagonal anti-static polyvinyl weighing dish on a high-precision scale as depicted in Figure 4.1 below.

Figure 4.1: 0.5g of polyvinyl alcohol.

Once weighed, it was transferred to a 25 mL glass beaker then tared on the scale, as seen in Figure 4.2 below.

Next, 7.5g of deionized (DI) water was added to the glass beaker using a pipette. The mixture was then transferred into a 15 mL glass vial with a lid and placed on a Thermo Scientific Cimarec hot plate. A Teflon-coated egg-shaped 15.9mm x 6.35mm (5/8" x 1/4") spin bar was dropped into the PVA and DI water solution. The lid was screwed onto the vial and the vial was taped to the hot plate to ensure the vial does not move off the plate during the stirring process. The hot plate temperature was set to 120°C and stirred at max

Figure 4.2: 0.5g of polyvinyl alcohol in beaker, tared to zero.

rpm (1200 pm) for 2 h. Figure 4.3 depicts the solution after an hour of stirring.

Once stirring was complete and the PVA dissolved fully into the DI water, the now-viscous solution and stir bar was transferred into a larger 25 mL beaker and set back onto the hot plate. The temperature was turned down to 60°C to promote mixing by keeping the mixture at a lower viscosity.

2 g of alumina powder was measured into an anti-static weighing dish and poured into the PVA solution. The hot plate was set to stir for five minutes at a speed of 500 rpm to incorporate the alumina powder into the solution. Extraneous slurry deposited high up on the walls of the beaker was scraped back into the bulk mixture using a flat spatula.

After five minutes, the slurry visually looked homogeneous. Next, 5 µL increments of acetic acid was deposited into the beaker using a variable volume pipette and stirred in at 60°C and 500 rpm with a stir bar. The pH of the mixture was measured between each 5 µL deposition using paper pH strips (VWR Chemicals, 7-14 pH and 3.0-6.0 pH) until it was measured to be 3.5, which occurred after 25 µL of acetic acid were deposited into the mixture. The change in pH from 7 to 3.5 is showcased in Figure 4.4.

The slurry was removed from the hot plate and the hot plate was turned off. Agitation

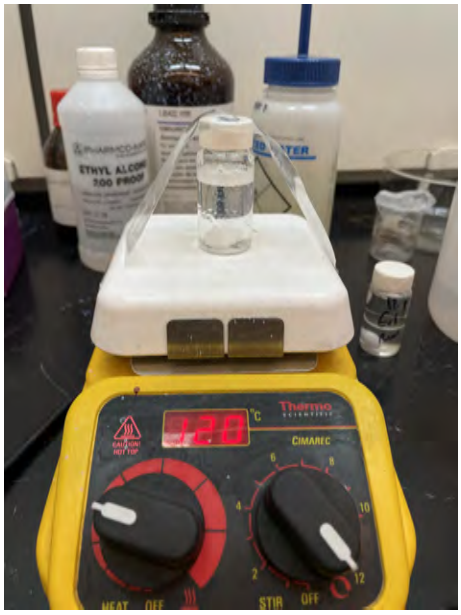

Figure 4.3: PVA and DI water solution stirring on hot plate.

of the mixture from the stirring process created excess bubbles in the catalyst slurry, which is disadvantageous for coating onto the coupons. When dried, bubbles in the slurry formed from the mixing process promote flaking of the washcoat layer and inhibit adhesion of the catalyst to the substrate. This can be seen in 4.5, where a dried washcoat layer is shown with many micro-pores of air introduced by the bubbles. Thus, the slurry was left to sit without disturbances for at least 5 hours, but preferably overnight, to allow the bubbles to disperse.

Once the alumina slurry was visually free of bubbles after at least 5 hours, each stainless steel coupon was placed onto the scale and coated with 0.5 g of the liquid slurry using a pipette. The washcoat was spread into a thin, even layer on the coupon using the tip of the pipette, using special care not to introduce bubbles into the coating. Each coupon was weighed after deposition of the alumina washcoat. Once weighed, the coupons were left to dry overnight for at least 8 hours. The coated coupons are depicted after being dried in Figure 4.6.

Once dried, the washcoated coupons were reduced in the furnace in 4 coupon cycles. The temperature was ramped from room temperature at a rate of 2°C min-1 to 120°C and

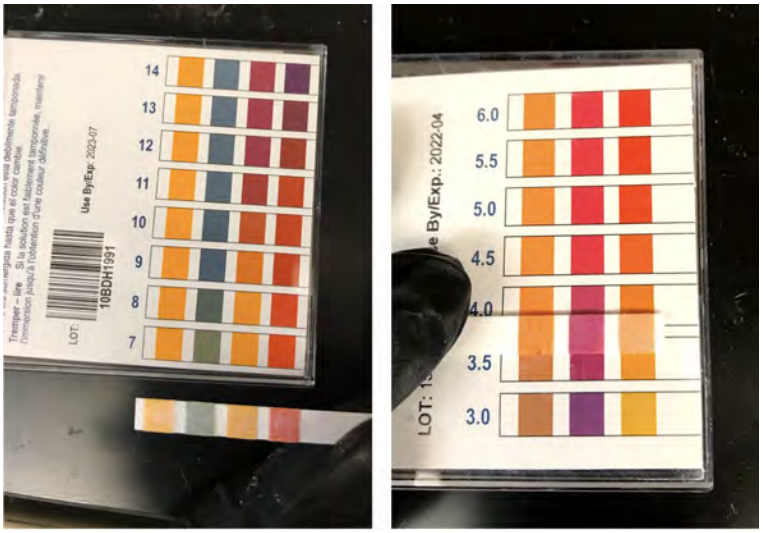

Figure 4.4: The pH of the alumina slurry mixture started at 7 (left) and reached 3.5 (right) after mixing in 25 µL of acetic acid.

held for 8 h. Then it was ramped at the same rate to the final calcination temperature of 600°C and held for 2 h. The coupons were then allowed to cool to room temperature before being removed from the furnace.

The coupons were weighed again on the scale to determine the dry alumina washcoat weight. 0.5 g of the procured cerium nitrate hexahydrate was mixed with 2.88 g of water in a beaker using a stir bar to create a ceria solution for incipient wetness impregnation onto the alumina support. 0.25 g of the ceria solution was pipetted onto each coupon and the final weight was recorded. The washcoat was left to dry overnight for at least 8 h before being calcined in the furnace. The temperature was ramped from room temperature to 400°C at a rate of 2°C min-1 and calcined for 2 h at the final temperature. The coupons were allowed to cool to room temperature before being removed from the furnace. The coupons were weighed on the scale to determine the dry weight of the ceria loading on the alumina support.

After determining the dry weight of the ceria support, the catalyst was incipient wetness impregnated with 0.05 g of the procured platinum solution with a pipette. The coupon was left to dry overnight for at least 8 h before being calcined in the furnace. The temperature

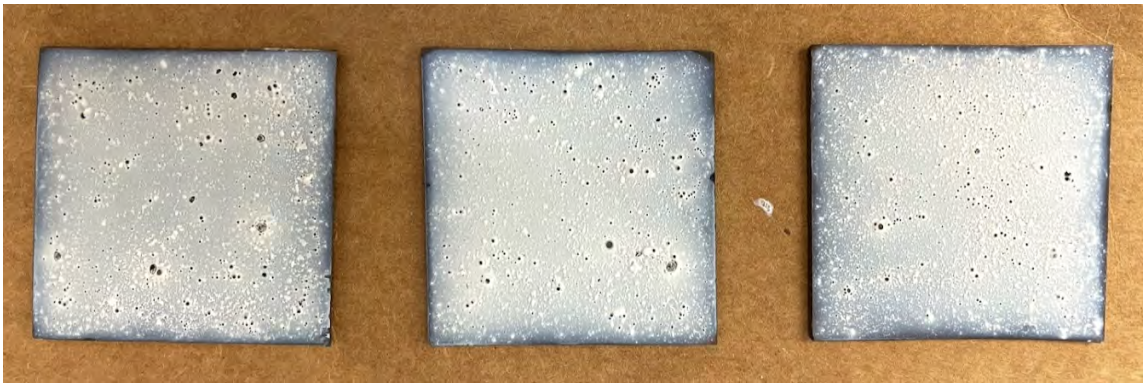

Figure 4.5: Depiction of a failed initial washcoat recipe that had too many bubbles. When dried, bubbles in the slurry formed from the mixing process broke up the homogeneity of the washcoat and inhibited proper adhesion of the thin film to the calcined stainless steel substrate.

Figure 4.6: Three coupons after drying of the initial alumina washcoat layer. The disruptions to the white washcoat are pieces of PVA that were unincorporated during the mixing of the binder in DI water because the mixing temperature was too low. The final recipe corrected this by increasing the mixing temperature to 120°C.

was ramped from room temperature to 550°C at a rate of 2°C min-1 and left for 10 h at the final temperature. The coupons were allowed to cool to room temperature before being remove from the furnace, then weighed on the scale to determine the dry platinum loading. This concluded the catalyst coating process for the coupons, but the process above was repeated several times to refine a recipe. The final catalyst coating on a coupon is depicted below in Figure 4.7.

The material quantities used in synthesizing the $Pt/Ce/Al_2O_3$ catalyst for coating the coupons are as described in Table 4.2.

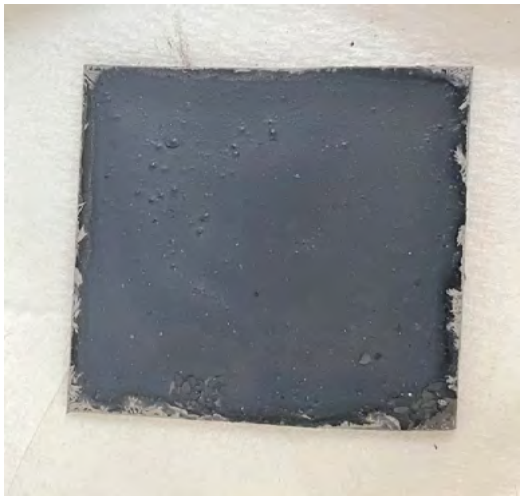

Figure 4.7: The final catalyst coating on a coupon.

Table 4.2: Materials and quantities used in synthesizing $Pt/Ce/Al_2O_3$ catalyst coating for coupons

Quantity	Material
2 g	γ-alumina powder
0.5 g	Polyvinyl alcohol
7.5 g	Deionized water
25 µL	Acetic acid
0.25 g (per coupon)	Cerium solution
0.05 g (per coupon)	Tetraammineplatinum hydroxide solution

4.2.3 Catalyst preparation on reactor

Once the catalyst recipe was finalized on coupons, it was ready to be applied to the walls of the reactant channel of the stainless steel reactor platelets. Before the final iteration of the catalyst recipe could be applied to the reactor plates, the plates first needed to be treated and masked to prevent catalyst from being coated on the mating surfaces between the reactors.

The coating process began with the six reactant platelets. Each of the six platelets were immersed in acetone in a Branson 2510 ultrasonic bath and sonicated for 5 minutes per plate at 40 kHz. The dimensions of the bath and plates were such that only one platelet at a could fit at a time into the ultrasonic bath, as depicted in Figure 4.8 below.

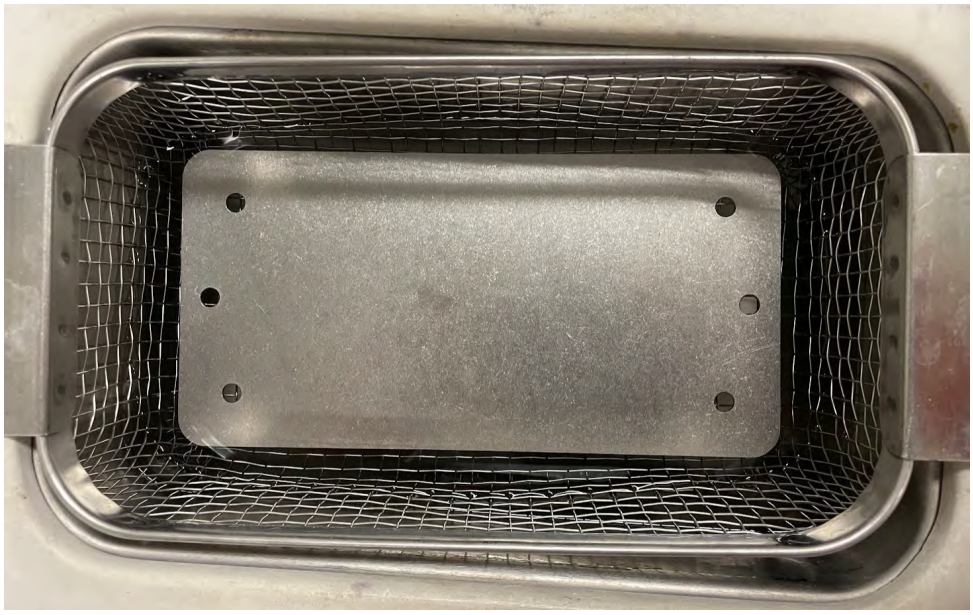

Figure 4.8: A reactor plate being cleaned in the sonicator.

Once cleaned, the plates were removed from the bath and weighed on a scale before being transferred to a furnace. Three of the six clean reactant plates are pictured below in Figure 4.9.

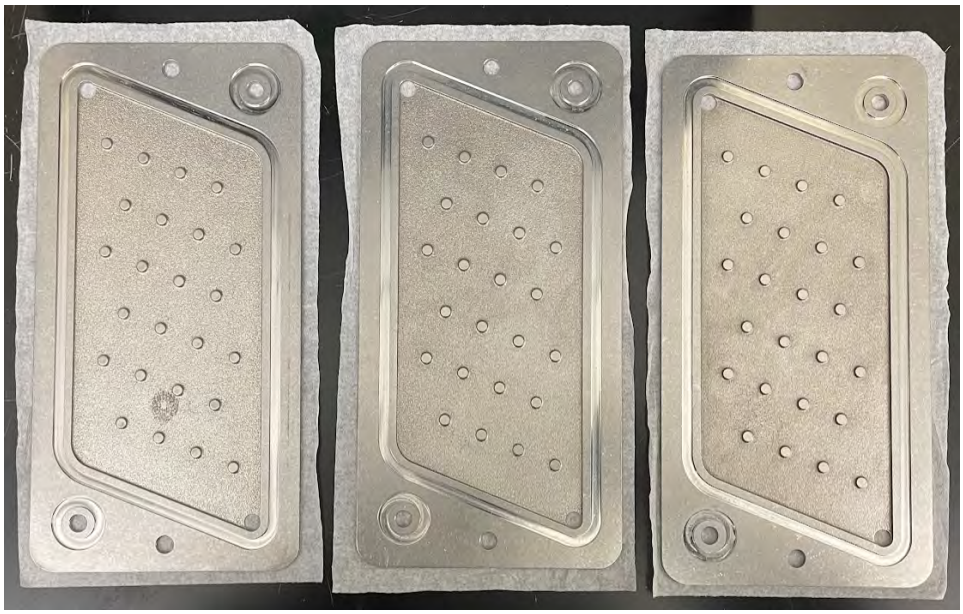

Figure 4.9: Three of the six reactant plates laid out after being cleaned with acetone.

The thermal pretreatment of the platelets reflects the same process applied to the coupons. Space constraints in the furnace, shown in Figure 4.10 below, limited the calcination to three plates per cycle.

Figure 4.10: Three of the six reactant plates arranged in the Thermolyne furnace before thermal pretreatment.

The six plates were then calcined in the furnace. The temperature was ramped from room temperature at a rate of 20°C min-1 up to the final calcination temperature of 900°C, where it was held for 10 hours, then cooled to room temperature overnight before the plates were removed from the furnace and weighed on a scale. The array of three plates is shown after the thermal pretreatment process in Figure 4.11 below.

The slurry recipe developed for the coupons was utilized for the reactor coating, but the material quantities were doubled to accommodate the greater surface area that needed to be coated. The exception was the amount of acetic acid added to the slurry, as this was added in 10 µL intervals until the desired pH of 3.5 was achieved.

A 50 mL beaker was tared on the scale and 1 g of polyvinyl alcohol (PVA) was scooped

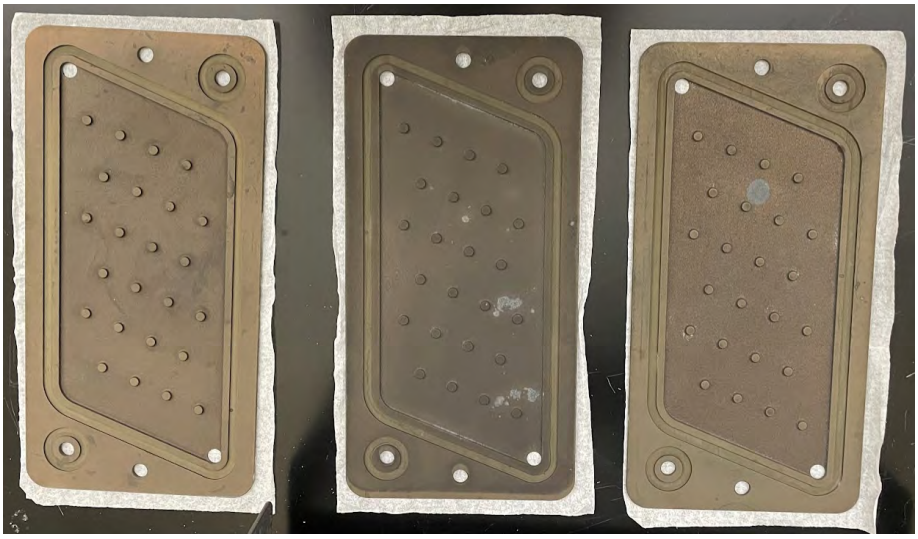

Figure 4.11: Three of the six reactant plates laid out after thermal pretreatment.

from the bulk container into the beaker. The beaker and PVA was tared on the scale and 15 g of water was added. A stir bar was deposited into the beaker and the beaker was transferred to a hot plate and covered using Parafilm to prevent moisture from escaping the beaker. The hot plate temperature was set to 120°C and the mixture was stirred at max rpm (1200 pm) for 2 h until the PVA was well-incorporated with the DI water.

The hot plate temperature was turned down to 60°C and 4 g of alumina powder was measured into an anti-static weighing dish and poured into the PVA solution. The hot plate was set to stir for five minutes at a speed of 500 rpm to incorporate the alumina powder into the solution. Extraneous slurry deposited high up on the walls of the beaker was scraped back into the bulk mixture using a flat spatula.

After ten minutes of stirring, the slurry looked visually homogeneous. Next, 10 µL increments of acetic acid was deposited into the beaker using a variable volume pipette and stirred in at 60°C and 500 rpm with a stir bar. The pH of the mixture was measured between each 10 µL deposition using paper pH strips (VWR Chemicals, 3.0-6.0 pH) until it was measured to be 3.5, which occurred after 40 µL of acetic acid was deposited into the mixture. The change in pH from 7 to 3.5 for each 10 µL deposition of acetic acid is showcased in Figure 4.12.

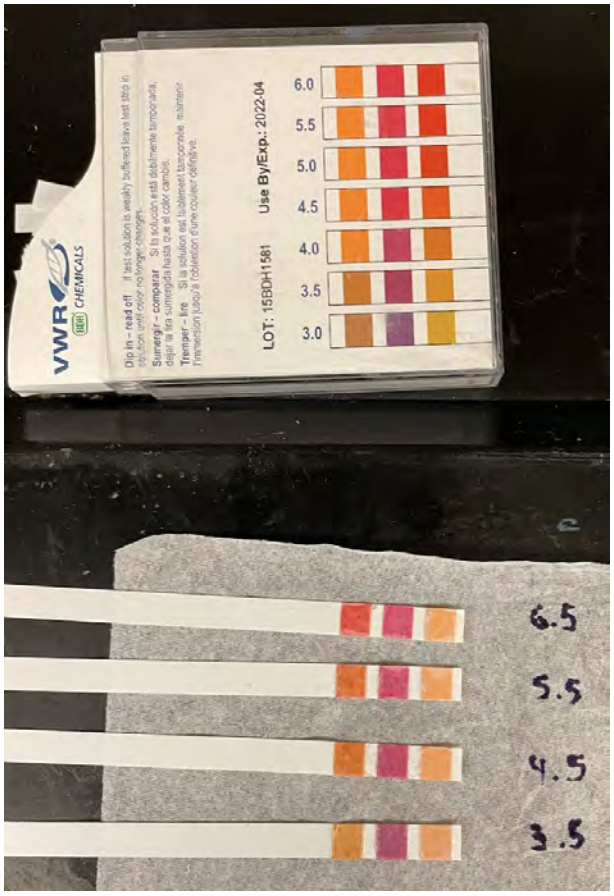

Figure 4.12: The pH of the slurry decreased from 7 to 3.5 after 40 µL of acetic acid was deposited into the solution.

Once reduced to the target pH, the slurry was removed from the hot plate and the slurry was left to sit without disturbances overnight to allow the air pockets formed during the mixing process to disperse.

While waiting for the bubbles to disperse, the calcined reactant plates were masked using a craft knife and aluminum foil tape. The tape was applied to the mating surfaces of the plate to ensure catalyst is not coated outside of the walls of the reactant channel. Strips of aluminum tape were adhered to the top surfaces of the posts inside the channel and the excess material was removed using the craft knife. The mating surfaces surrounding the exterior of the channel were then covered using strips of aluminum tape cut to length. These two steps are showcased below in Figure 4.13.

Figure 4.13: An aluminum tape mask was applied to the reactant plates to shield mating surfaces from being coated in catalyst.

Once all six plates were masked, a thin film of the alumina slurry was applied to the reaction channel walls using a flat paintbrush. For large surface areas, it was easier to apply a thin layer of the coating using a paintbrush than with a pipette, which fails to uniformly distribute the alumina slurry across the surface. Care was taken to ensure the sides of the posts were covered as well, though these geometries represent a small part of the reaction surface area.

Figure 4.14: Masked reactant channels coated with the alumina slurry. The mask was removed on the second plate.

After the alumina washcoat was applied, the reactant plates were set out to dry overnight for at least 8 h. Once dried, the mask was carefully removed from the plates using needle-nosed tweezers with care being taken to separate the coating from the mask. The washcoated plates were placed in the furnace to be reduced two at a time. The temperature was ramped from room temperature at a rate of 2°C min-1 to 120°C and held for 8 h. It was then ramped at the same rate to the final calcination temperature of 600°C and held for 2 h. The plates were then allowed to cool to room temperature before being removed from the furnace. The plates were weighed on the scale to determine the dry alumina washcoat weight.

One major difference between the coupon coating procedure and the reactor coating procedure is the amount of ceria and platinum solution deposited on the alumina support. For the coupon coatings, a specific weight of each solution was deposited onto each coupon, but results discussed later in Section 6.1.1 showed excessive platinum loading in the alumina support. As a result, for the reactor coating, the solutions were deposited only until incipient wetness to ensure a lower platinum loading.

To form the ceria solution, 1 g of the procured cerium nitrate hexahydrate was mixed with 5.76 g of water in a beaker using a stir bar. The solution was pipetted onto each plate to incipient wetness and the washcoat was left to dry overnight for at least 8 h before being calcined in the furnace. The temperature was ramped from room temperature to 400°C at a rate of 2°C min-1 and calcined for 2 h at the final temperature. The plates were allowed to cool to room temperature before being removed from the furnace. The reactant plates were then weighed on the scale to determine the dry weight of the ceria loading on the alumina support.

After determining the dry weight of the ceria support, the catalyst was incipient wetness impregnated with the procured platinum solution with a pipette. The plates were left to dry overnight for at least 8 h before being calcined in the furnace. The temperature was ramped from room temperature to 550°C at a rate of 2°C min-1 and left for 10 h at the final temperature. The plates were allowed to cool to room temperature before being remove from the furnace, then weighed on the scale to determine the dry platinum loading. This

concluded the catalyst coating process for the reactant plates.

The same catalyst coating process described for the reactant plates needed to be applied to the bottom side of the coolant plates, since this surface makes up almost half of the reaction channel surface area. The thermal pretreatment and coating process itself mirrors the process described for the reactant plates above, but the masking process differed since the bottom of the plate is completely flat.

To ensure the washcoat on the coolant plate lines up with the top of the reactant channel, a template of the reactant channel shape was laser cut using the LPKF laser cutter from 0.51 mm (0.02") thick 316 stainless steel shim stock. A standard recipe for stainless steel shim stock was already available on the laser cutter, which made the manufacturing of the template an easy process. The channel template is depicted in Figure 4.15 below.

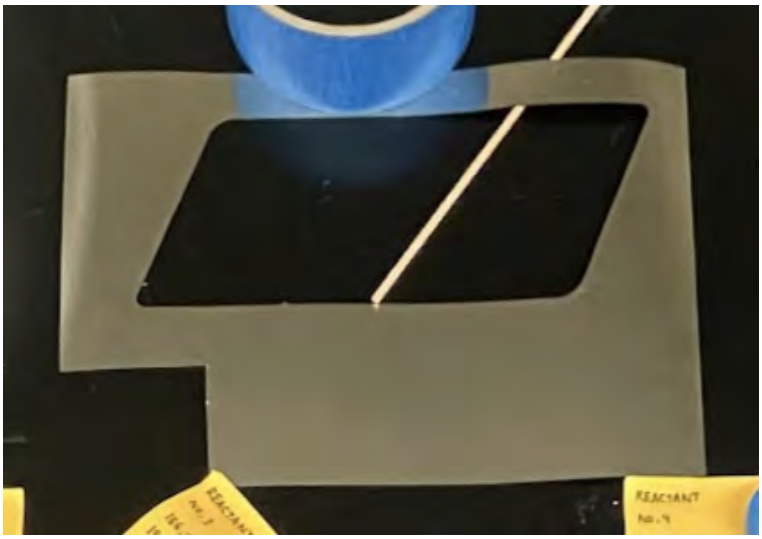

Figure 4.15: A reactant channel cutout laser cut from stainless steel shim stock and taped to the back of each coolant plate to act as a coating template.

After the coolant plates were thermally pretreated, the mask was aligned to the inlet and outlet holes of each coolant plate and taped down, with care being taken to ensure the shim was taut. Using the same catalyst coating recipe and technique previously described in this section, the bottom surface of the coolant plate was coated with the alumina slurry using a flat paintbrush. Once completed, the tape was peeled off and the template removed

from the coolant plate. Any excess slurry that bled under the template was removed using a wet paper towel. The slurry-coated undersides of the coolant plates are shown in Figure 4.16 below.

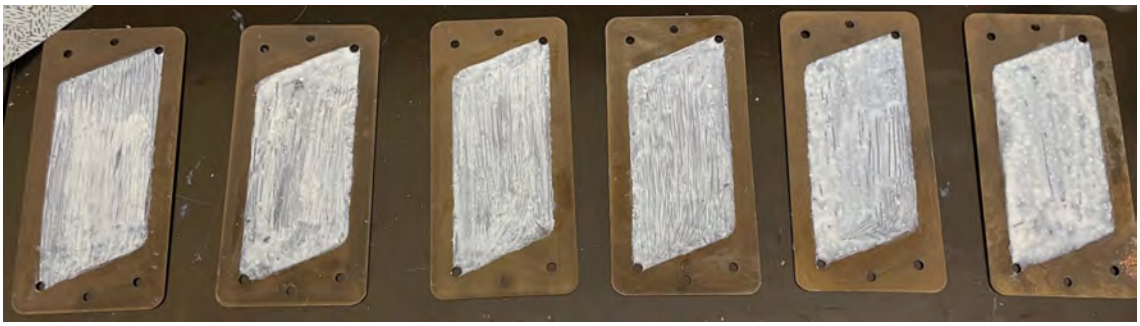

Figure 4.16: Alumina washcoated coolant plates.

The rest of the preparation steps are identical to the steps performed for the reactant plates. The alumina coated plates were calcined and weighed before being incipient wetness impregnated with the ceria solution. The catalyst was reduced in the furnace and weighed before being incipient wetness impregnated with the platinum solution. The final platinum catalyst was calcined in the furnace and the final results are showcased in Figure 4.17 below.

Figure 4.17: The final catalyst coating of the bottom surface of the coolant channel (which makes up the top half of the reaction channel).

4.3 Catalyst characterization

Once the catalyst had been coated to the walls of the reactor, it was necessary to characterize the coating to determine three important factors. First, the chemical composition and

loading of the catalyst needed to be characterized in order to verify with the composition reported in literature, which can then inform experimental trends and results. Second, the adhesion of the catalyst to the reactor was a very important factor in maximizing catalyst volume in the microchannel, which is needed to optimize CO conversion. Finally, the roughness of sandblasted coupons was characterized and the catalyst's adhesion to the coupons with surface area enhancement was compared to that of coupons without surface area enhancement to determine how sandblasting affects catalyst adhesion.

The characterization results for the catalyst composition and adhesion are described later in Section 6.1.1.

4.3.1 Composition

Surface analysis of the catalyst coatings on both the coupons and the reactor walls was performed using scanning electron microscopy (SEM) and energy-dispersive X-ray spectroscopy (EDS). The purpose of imaging the catalyst using SEM is to visualize the elements and microstructures present in an area of the catalyst coating. Once imaged, EDS analysis quantifies the percentage of each element present in the catalyst sample, which reveals the loading of the catalytically active components. The EDS results for the manufactured catalyst can then be compared to the results reported in literature to gain a sense of how the catalyst will perform.

The SEM and EDS analyses were performed at Oregon State's Electron Microscopy Facility located in the Linus Pauling Science Center on Oregon State University's main campus. The FEI QUANTA 3D dual beam scanning electron microscope at the facility was utilized to collect the SEM and EDS data. This piece of equipment is equipped with an X-ray energy dispersive spectrometer, which provides elemental composition spectra acquisition, elemental distribution mapping, and line transect element profiling capabilities. The SEM has a spatial resolution 1.2 nm in secondary electron imaging mode, 0.8 nm in scanning transmission electron detector imaging mode, and a magnification range of 30x to 100,000x. This SEM is depicted in Figure 4.18 below.

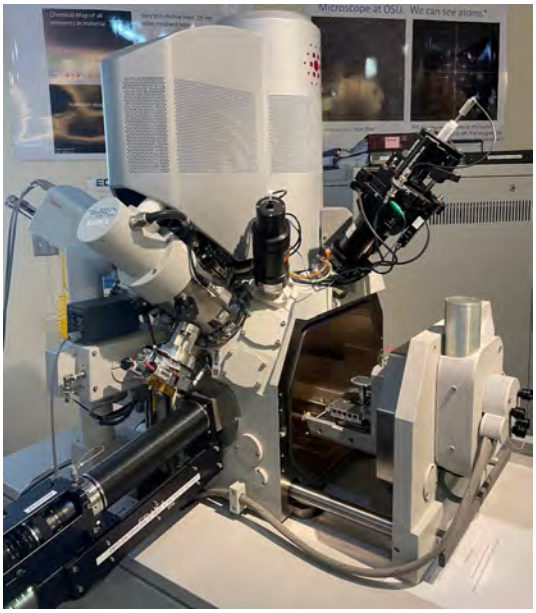

Figure 4.18: The FEI QUANTA dual beam SEM.

These analyses were performed for both the coupon coating and the coating on the reactor walls. Before collecting the SEM and EDS data, two training sessions were required to obtain certification to use the equipment. The training sessions were completed using an initial catalyst recipe developed on coupons, and the results of the EDS analysis were used to tune the recipe of the catalyst for another round of coupon coating. The elemental analysis results from these initial coatings were used to tune and dial in the final reactor coating procedure.

Because the coupons were 1.5" x 1.5" squares, they could be readily placed into the SEM chamber. Initially, the SEM images were taken without sputter coating, but the coating was charging in the high vacuum, high voltage electron beam SEM environment. A conductive coating was needed to prevent charging of the catalyst and coupon with the electron beam, so each subsequent sample was sputter coated for 30 seconds with a thin film of Au/Pd using a Cressington Au/Pd ion beam sputter coater. Some preliminary samples are shown in the sputter coater in Figure 4.19. Once coated, the sample was taken to the SEM and placed into the chamber. This is depicted in Figure 4.20.

The chamber was closed shut and vacuum was pulled in the chamber. The location of

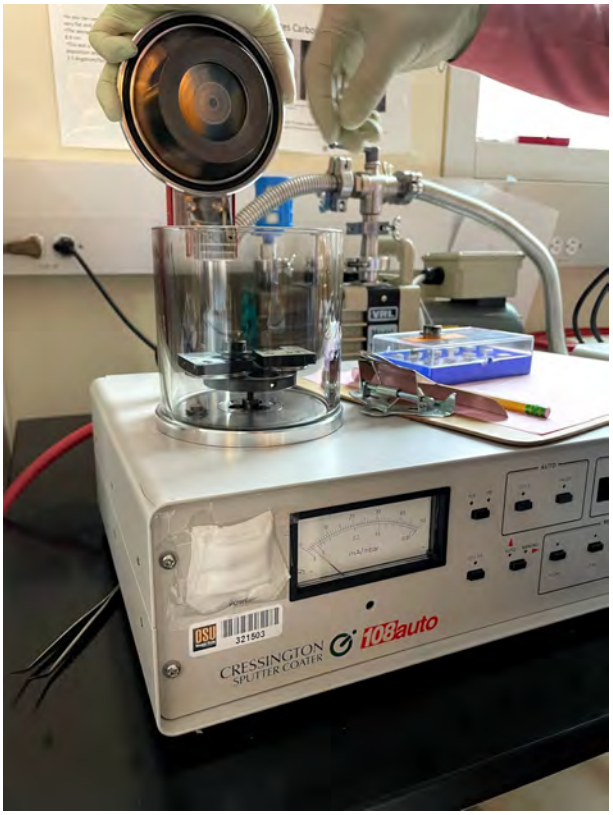

Figure 4.19: Samples in the sputter coater.

the sample was calibrated using the SEM software and the electron beam was turned on. The beam was brought to the area of focus and the magnification and focus of the camera was adjusted until the image looked satisfactory. The EDS software was opened and the EDS detector was turned on and the expected elements present in the sample (oxygen, aluminum, platinum, and ceria) were selected to limit the scope of the elemental analysis, which will only report the elements selected. Once set up was complete, an SEM image, EDS spectral map, and EDS elemental analysis were taken. The SEM image provides a visual depiction of the catalyst coating at the microscale. The spectral map provides insight on the dispersion of each element present in the EDS sample and is dictated by the number of x-ray counts that are taken. The higher the counts, the more detailed and accurate the spectral mapping is. The elemental analysis provides characterization of the weight percent of each selected element in the sample.

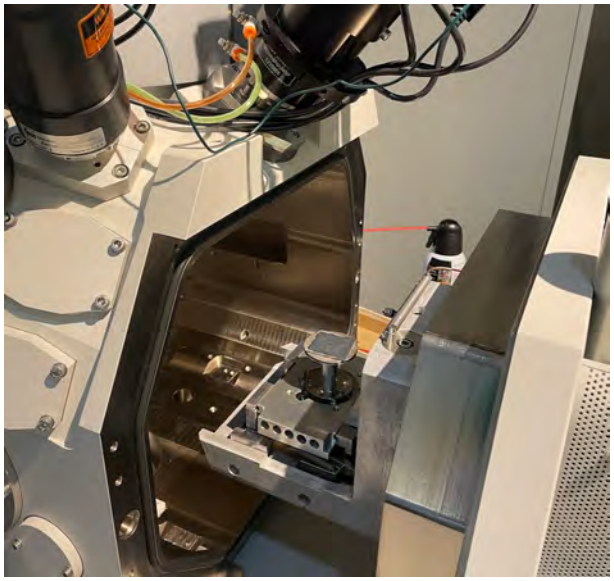

Figure 4.20: Coupon sample in the SEM chamber.

Once the final recipe had been developed and synthesized onto the reactor walls, a small amount of coated catalyst was scraped off the both reaction channel surfaces and transported to the SEM facility for characterization. The same process that was described for the coupons above was used again to gather images and composition data for the final coating. These images and elemental analyses are presented in Section 6.1.1 of the Results.

4.3.2 Adhesion

The adhesion of the $Pt/Ce/Al_2O_3$ catalyst to the 316 stainless steel reactor walls was characterized in two ways. First, an ultrasonic test was conducted to induce uniform vibrations in an attempt to characterize the catalyst's ability to withstand sustained mechanical disturbances, such as those caused by process gases flowing through the channel or other vibrations in an industrial environment. Second, a drop test was conducted to determine the catalyst's ability to withstand a sudden impact in an attempt to replicate an incident where the reactor is dropped suddenly.

Each test was performed on two coated coupons and two coated reactor plates. The

ultrasonic test came first and the drop test came second. For the reactor plates, to characterize the coating on both sides of the plate, each test was performed on two plates: one plate had only the reactant channel coated while another plate only had the coolant channel characterized.

For the ultrasonic test, the coupon was weighed before it was immersed in acetone in a beaker. The beaker was placed into the basket of a Branson 2510 ultrasonic cleaner (40 kHz output frequency). The rest of the Branson tank was filled with deionized water until the liquid level of the water was the same as the liquid level of the acetone in the beaker. This setup is depicted in Figure 4.21 below. For the reactor plate, each plate was placed into the basket and the tank was filled with acetone until the plate was fully immersed and the tank was covered with a lid.

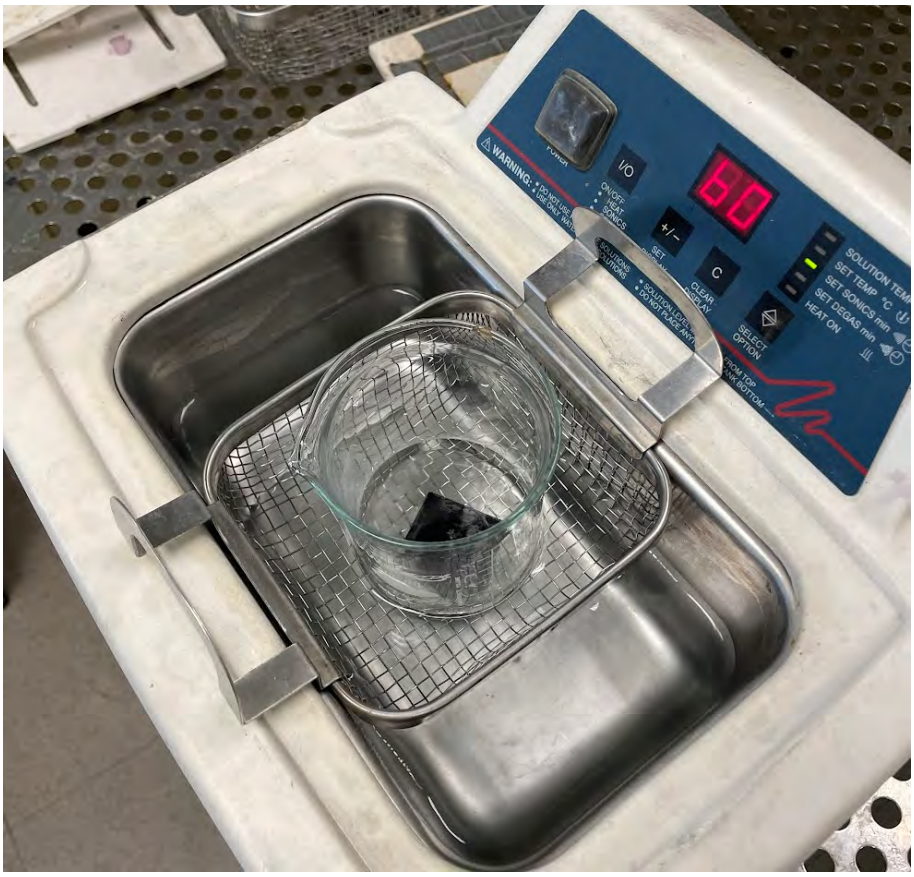

Figure 4.21: The ultrasonic adhesion test setup.

The beaker was covered with Paraffin wax to prevent the acetone from evaporating and the coupon was sonicated for 15 minutes at 20°C. Once complete, the coupon was removed from the beaker and weighed. The adhesion was characterized by calculating the catalyst's percentage weight loss before and after sonication, which is represented by the Equation 4.1:

$$\%\, weight\, loss = (\frac{weight_i - weight_f}{weight_i}) * 100 \tag{4.1}$$

where $weight_i$ is the initial catalyst weight and $weight_f$ is the final catalyst weight. The adhesion is then calculated using Equation 4.2 below:

$$\%\, adhesion\, loss = 100 - \%\, weight\, loss \tag{4.2}$$

For the drop test, the same test procedure applied for both the coupons and the plates. The weight of the test article was measured before it was held 1 m above the ground with the coated surface parallel to the floor and facing up. Each test article was then released and dropped once. The test article was then weighed and the same weight loss equation represented in Equation 4.1 was applied to determine the weight loss after drop testing.

4.3.3 Surface area enhancement

An investigation was performed on the effect of surface roughness on the adhesion of catalyst to the 316 stainless steel substrate material. As previously discussed, the recessed channel has surface area enhancements on the channel surface due to the sinker EDM process. However, with the available instruments and given time constraints, it was not feasible to characterize the surface area enhancement of the actual reactor channel itself. Instead, sandblasting was used to increase the surface roughness of coupons and compared to control coupons that were not sandblasted. The goal was to determine how the increased surface area corresponds to catalyst adhesion to get a sense of how the adhesion of the coating will differ on the enhanced vs. non-enhanced surfaces of the reactant channels of the prototype.

To perform this investigation, the surface roughness of ten (10) 1.5" x 1.5" 316 stainless steel coupons was characterized using a Mitutoyo SJ-210 Portable Surface Roughness Tester. Five (5) coupons were then sandblasted using the ATAMI in-house sandblaster with 60-120 mesh size glass beads. The surface roughness of these 9 coupons was characterized again using the SJ-210 and compared to the non-enhanced control coupons. The SJ-210 analyzer used to take readings is shown in Figure 4.22 below.

Figure 4.22: Top plate geometries and dimensions.

Once the surface roughness enhancement was characterized, the catalyst was coated onto each of the 10 coupons. Due to the length of time and resources required to perform the ultrasonic adhesion test described previously in Section 4.3.2, it was omitted for adhesion characterization of the coupon. Only the drop test was performed on the coupons and the

results were compared between the enhanced and non-enhanced coupons and coatings. The results of these tests are presented in Section 6.1.2 of Chapter 6.

4.4 Catalysis summary

Many variables played into the proper selection of a suitable catalyst recipe for the process intensified water-gas shift reaction. Considerations into the reactor geometries, process conditions, catalyst performance, ease of manufacturability, feasibility of procurement, and cost were all factored into selecting a platinum-ceria catalyst washcoated on a γ-alumina support. The recipe used is primarily based off of a recipe developed by Germani & Schuurman, with details supplemented from the recipe reported by He *et al.*

Once the recipe was identified, it was synthesized and coated on 316 stainless steel coupons. The coupons were cleaned and thermally pretreated. Alumina powder was added to a binder solution of polyvinyl alcohol and deionized water was coated onto the coupons before being calcined. A ceria solution was impregnated onto the alumina support and the coupons were calcined again. Finally, the platinum solution was impregnated onto the coupon and calcined. Once the coating process was complete, the loading of the catalyst was imaged and characterized using SEM and EDS analyses, respectively. Initial trials of the catalyst coating failed to adhere to the coupon, so the recipe was iteratively improved until the catalyst exhibited good adhesion onto the coupon surface.

The final recipe was synthesized and coated on the reactor platelets. An overview of the coating process for a reactant plate is shown in Figure 4.23 below.

First, the plate was clean and thermally pretreated. A mask was then applied to the plate to prevent catalyst from being coated on the mating surfaces between plates. The alumina washcoat solution was coated onto the channel before being calcined. Next, a ceria solution was incipient wetness impregnated onto the alumina support and calcined. Finally, the platinum solution was incipient wetness impregnated onto the support and calcined. This process was then repeated for the coolant plates. SEM and EDS analysis was used to image and characterize the loading of the catalyst on the plates of the reactor. Ultrasonic

Figure 4.23: From left to right: plate before thermal pretreatment, plate after thermal pretreatment, plate with mask, and plate after alumina slurry washcoat.

and drop tests were performed to characterize the adhesion of the catalyst to the reaction channel walls. The results of these characterizations are presented later in Chapter 6.

Chapter 5: Experimental approach

Previous chapters describe the design and manufacture of the sub-scale prototype of the differential temperature parallel-plate microreactor with integrated catalyst. To realize the modeled potential of the process intensified water-gas shift reactor, a physical test loop was designed and constructed to enable reacting flow experiments. The goal of performing experimental studies was to:

1. Achieve the optimal process conditions for the process-intensified WGS reactor as simulated in COMSOL,
2. Obtain the temperature profile of the WGS reactor under the optimal process conditions, and
3. Validate the modeled conversion of WGS products to reactants.

The purpose of this chapter is to provide a detailed description of the materials, design, and fabrication process of the experimental facility that was used for this research.

5.1 Introduction

In the interest of conserving resources and increasing collaboration between research groups, this test loop was designed and constructed in collaboration with Lucas Freiberg, a PhD candidate from Dr. Goran Jovanovic's research group, to attain the desired process conditions for both the WGS reactor and the methanol-dimethyl ether (MDME) reactor. The test loop was constructed in Dr. Jovanovic's laboratory space at Oregon State University's Advanced Technology and Manufacturing Institute (ATAMI) in Corvallis, OR.

The parameters from the simulations are required to inform the design of the test loop. The original 2D WGS model utilized air as the integrated coolant because the physics of air can be easily modeled for flow simulations. It was infeasible, however, to use air experimentally because it is highly compressible and exhibits poor heat transfer behavior

at high temperatures compared to liquid heat transfer fluids. As a result, there was a need to:

1. Select a new coolant fluid,
2. Reassess process conditions based on material limits of new fluid, and
3. Obtain simulation results based on these new considerations.

The results of the model informed the sizing and selection of physical test loop components, such as the mass flow controllers, the oil pump, and the pump driveline.

5.2 Process fluids

Both gaseous and liquid process fluids were needed to conduct the experimental flow studies through the WGS reactor. These fluids and their selection process are described below.

5.2.1 Gases

Ongoing research at the Pacific Northwest National Laboratory (PNNL) is investigating the intensification of hydrogen production via steam reforming of natural gas, and Table 5.1 below shows the measured effluent stream composition from the steam methane reformer (SMR) at PNNL. These were the exact conditions used in the modeling efforts performed by Tolley.

Table 5.1: PNNL SMR effluent flow composition

Gas	Mole fraction, y_1
CO	0.113
H_2O	0.244
CO_2	0.052
H_2	0.546
CH_4	0.055

The goal of the experimental studies at Oregon State is to replicate these conditions as closely as possible while since they are representative of the real conditions that the WGS

reactor would be subject to. In the interest of simplifying the kinetics and thermodynamics of the reaction, saving time and resources in building the test loop, and due to the small concentration in the effluent flow stream, CH_4 was excluded from the reaction. Argon was substituted in the place of methane as a baseline inert gas for the mass spectrometer. Thus, the final supplied gas stream composition and molar flow rates were as shown in Table 5.2.

Table 5.2: WGSR inlet flow composition

Gas	Mole fraction, y_1
CO	0.113
H_2O	0.244
CO_2	0.052
H_2	0.546
Ar	0.055

5.2.2 Integrated coolant fluid

Therminol 72 by Eastman was chosen as the heat transfer fluid because it exhibits excellent thermal stability for temperatures between -14°C to 380°C in liquid phase heat transfer systems at moderate pressures. These limits are visually depicted in Figure 5.1. Its upper temperature limit of 380°C is among the highest of commercially available high temperature liquid phase heat transfer fluids. Therminol 72 is resistant to fouling, which makes it attractive as a closed-loop testing solution.

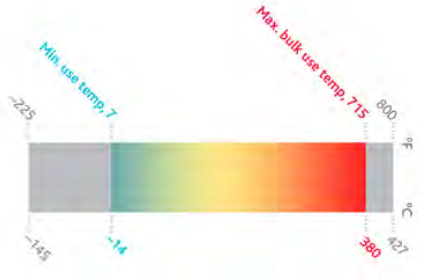

Figure 5.1: Temperature limit of Therminol 72 [48].

Therminol 72 is a clear amber liquid mixture of synthetic aromatic compounds. The

liquid properties of Therminol 72 can be seen in Table 5.3. Details of this heat transfer fluid are provided in Appendix A.2.

Table 5.3: Therminol 72 liquid properties

Temperature (°C)	Density, ρ (kg/m^3)	Specific heat, c_p (kJ/kg-K)	Viscosity, μ (cP)
0	1097	1.498	59.2
20	1079	1.552	13.5
50	1052	1.634	4.52
100	1007	1.769	1.61
150	961	1.905	0.83
200	916	2.050	0.50
250	871	2.176	0.33
300	825	2.311	0.23
350	780	2.447	0.17

5.3 Process conditions

The design criteria of the test loop was informed by in-depth simulations of the process-intensified WGS and the MDME reactions in conjunction with literature from existing experimental studies. This section describes the process conditions for the water-gas shift in more detail.

5.3.1 Coolant loop process conditions

As aforementioned in 5.1, there was a need to select a new coolant fluid and reassess the requirements needed to achieve the desired temperature profile.

The system design and operation must fall within the maximum bulk and film temperatures specified to ensure reliable operation, and one consequence of changing the integrated cooling fluid from air to Therminol 72 is a change in the maximum operable reactor temperature. The upper bulk temperature limit of 380°C/653 K, but the most optimal conversion requires an inlet temperature of 450°C/723 K. This is experimentally infeasible given the limits of the heat transfer fluid, so the computational model was tuned for an inlet

temperature of 300°C/573 K, which results in a peak reactor temperature of 367°C/640 K,which falls below the bulk temperature limit of the Therminol. This thus satisfies the material compatibility criteria for the chosen liquid.

Another consequence of using a different coolant fluid is a change in the coolant flow rate. While the actual magnitude of the rate of flow is inconsequential to the behavior of the system, the flow rate of coolant needs to be estimated because it is an important process condition for sizing pump equipment. The new flow rate needed to be quantified for Therminol 72 at an inlet temperature of 300°C/573 K. To do so, the density (ρ), specific heat capacity (c_p), and viscosity (cP) properties of Therminol 72 as a function of temperature were obtained from the technical data sheet provided by Eastman. These properties were input to the model to help determine the new coolant flow rate. A more detailed look at the material properties of Therminol 72 is provided in Appendix A.2.

Flow rate: Using Therminol 72 as the coolant fluid and an inlet temperature of 300°C, the model predicts a volumetric flow rate of 2.5 mL/min per plate. For the sub-scale reactor of 7 coolant channels, this equates to a flow rate of 17.5 mL/min.

Temperature: The coolant inlet temperature is 300°C.

Pressure: Eastman recommends operating and maintaining the liquid at a static pressure of at least 6 bar to maintain the liquid phase at high temperatures. To reduce bending stresses in the thin channels of the reactor that could be caused by a pressure differential between the coolant and reactant loop, the Therminol loop will be pressurized to the same pressure as the gases, which is 10 bar.

5.3.2 Gas loop process conditions

Flow rate: The full-scale reacting gas flow rate of 2.53 g/s is similarly informed by the same hydrogen process intensification research at PNNL. For the sub-scale prototype, a scaled-down reactant gas flow rate of 0.127 g/s will be used.

Temperature: The optimal reactant inlet temperature is 350°C/623K, as seen in the optimal temperature profile from the COMSOL studies shown in Figure 2.15.

Pressure: As aforementioned in Chapter 2, Atwood *et al.* experimentally concluded that the rate of the WGSR over an iron oxide-chromium oxide catalyst approximately doubled as the pressure increased from ambient pressures to 10 atmospheres (10.1325 bar), only increasing slightly as the pressure was further raised. These conclusions inform the starting operating pressure of 10 bar.

5.3.3 Summary of process conditions

Table 5.4 below summarizes the process conditions needed for the test loop.

Table 5.4: Summary of WGS/MDME process conditions

	WGS	MDME	Coolant
Composition	CO, H_2, H_2O	CO, H_2, CO_2	Therminol 72
Inlet temperature	350°C	285°C	250-300°C
Pressure	10 bar	40 bar	10-20 bar
Flow rate	0.127 g/s	0.103 g/s	10-100 mL/min

Table 5.5 below summarizes the process conditions needed for only for the process-intensified WGS reaction.

Table 5.5: Summary of WGS process conditions

	WGS	Coolant
Composition	CO, H_2, H_2O	Therminol 72
Inlet temperature	350°C	300°C
Pressure	10 bar	10 bar
Flow rate	0.127 g/s	10 mL/min

5.4 Process and instrumentation diagram

The experimental set-up consists of two loops: the reacting gas loop and the high temperature coolant loop. The reacting gas tract is an open system controlled by mass flow controllers and a back pressure regulator, shown in Figure 5.2, while the high temperature coolant fluid flows in counterflow in a closed loop, shown in Figure 5.3.

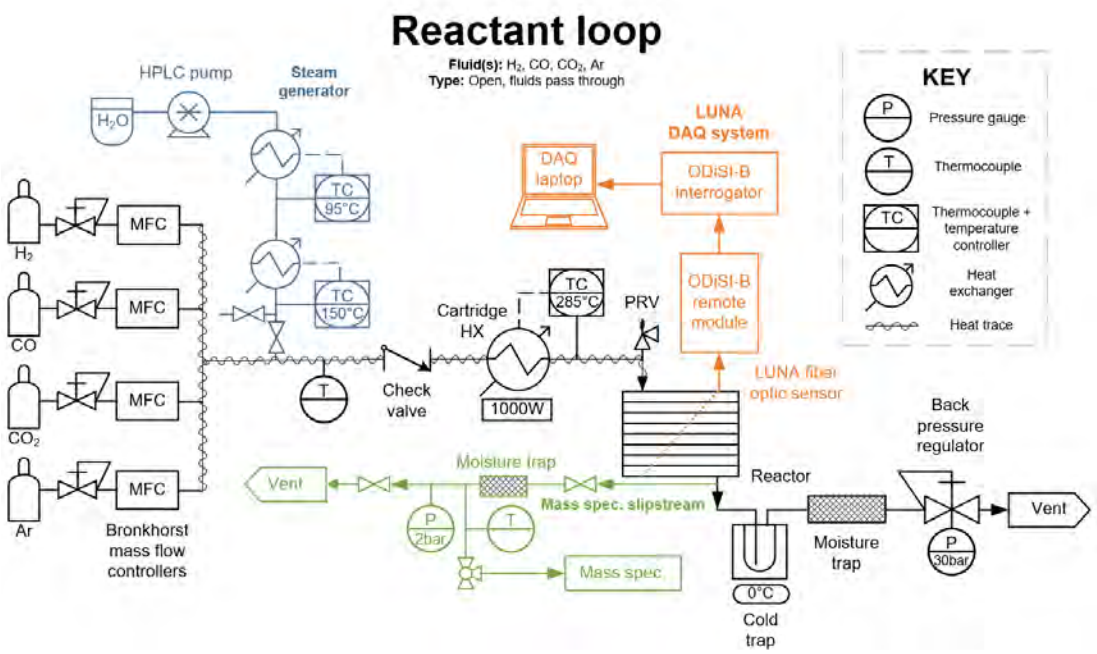

Figure 5.2: PID of the reactant loop.

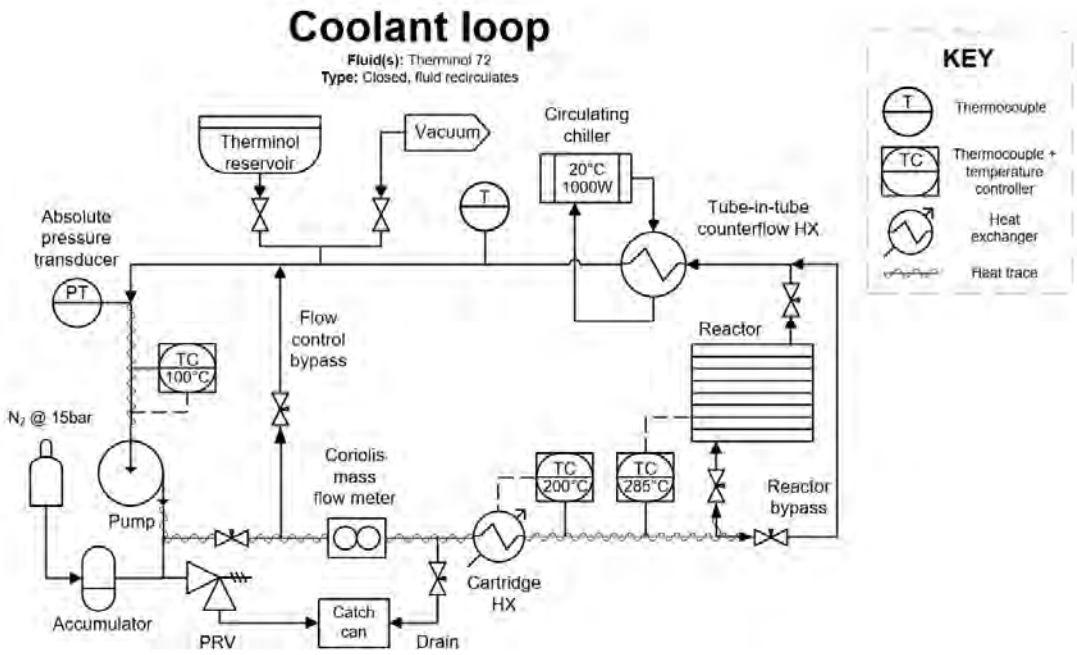

Figure 5.3: PID of the coolant loop.

5.5 Test loop operation

This section presents an overview of the process and operation of the WGS/MDME test loop shown in the P&IDs above.

5.5.1 Coolant loop operation

The test loop is housed on a durable plastic test cart consisting of two levels and a plastic peg board mounted on aluminum frame above the upper level. T-slot aluminum extrusion is mounted directly beneath the upper level of the test cart to support the weight of the heftier liquid flow components.

Figure 5.4: The liquid loop is vacuum filled from a reservoir of Therminol 72.

Therminol 72 was supplied to the closed liquid loop by means of vacuum fill, pictured in Figure 5.4. ATAMI house vacuum was applied to the loop through one of two charging ports so that HTF would fill all void spaces in the loop. The vacuum valve was closed and the Therminol valve was opened to complete the charging process.

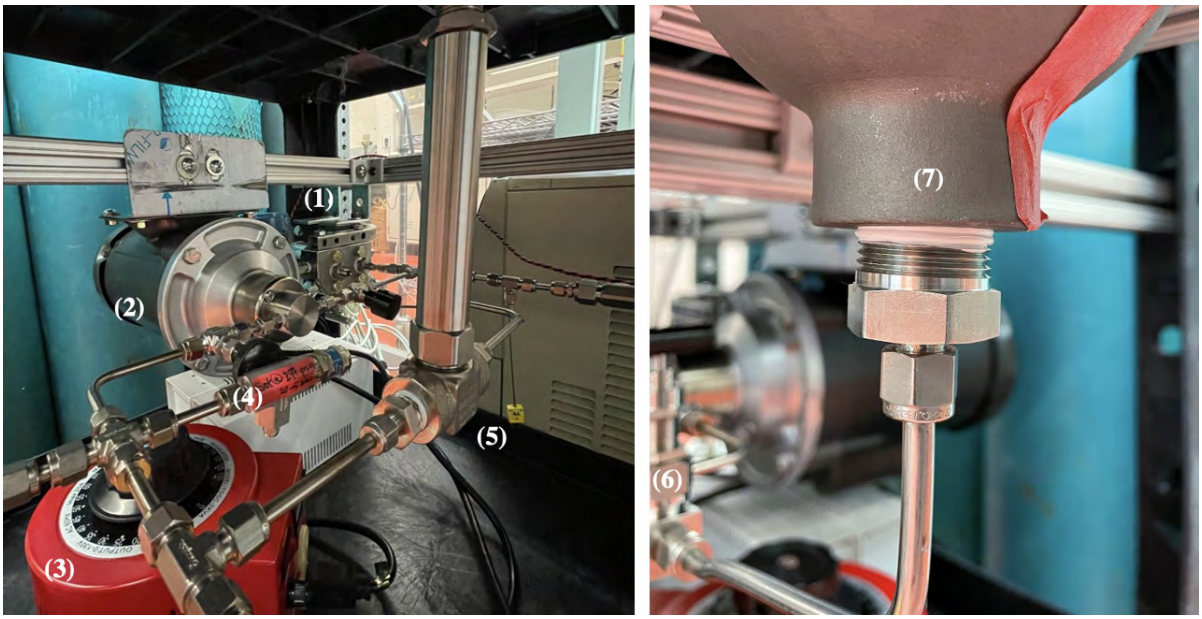

Figure 5.5: (1) Rosemount absolute pressure transducer, (2) Baldor motor and Micropump pump head assembly, (3) Variac variable voltage regulator, (4) pressure relief valve, (5) bypass valve, (6) acculumator isolation valve, and (7) accumulator.

The HTF flow components are mounted directly onto the extruded aluminum rail as seen in Figure 5.5 above. The loop begins at the Rosemount 3051SMV absolute pressure transducer and integral manifold assembly (1) which is used to measure the absolute pressure of the HTF before it enters the pump. The absolute pressure transducer was originally mounted vertically but was later mounted horizontally per recommendation of Emerson to prevent potential sediment deposits on the process isolators. After the pressure transducer, two valves isolate the Baldor single-phase 3450 RPM motor and Micropump pump head assembly (2) powered by a variable AC power supply (3). The desired flow rate can be achieved using a bypass line that redirects flow back to the inlet of the pump. The flow rate to the reactor can be verified using the Coriolis mass flow meter.

The HTF is pumped counterclockwise towards the accumulator (7) and pressure relief junction. A valve isolates the accumulator, which pressurizes the HTF up to 20 bar via one 3/4" female NPT connection. A 3/4" male NPT to 1/4” Swagelok fitting was procured from Swagelok, but sealing of male-to-female NPT fittings proved to be a persistent challenge in the construction of the test loop. A generous number of wraps (six to seven) of PTFE was used to eliminate leaking from the accumulator connection, labelled (7) in Figure 5.5 above.

The Blacoh accumulator is rated to a maximum pressure of 20.6 bar (300 psi), so a pressure relief valve (PRV) (4) was installed across from the accumulator to prevent overpressurization of the coolant loop. The original PRV spring was replaced with one with an operational range within the maximum accumulator pressure. The spring was set to a cracking pressure of 20 bar and this was verified using bottled nitrogen and a pressure regulator. The accumulator was charged via its Schrader port with nitrogen until the desired process pressure of around 18 bar was achieved.

After flowing past the accumulator and pressure relief valve junction, the HTF branches off towards the aforementioned bypass that will be used to tune the flow rate of Therminol. As the bellows valve (4) shown in Figure 5.6 is opened, the pressure differential will cause HTF to flow through the bypass and discharge upstream of the absolute pressure transducer.

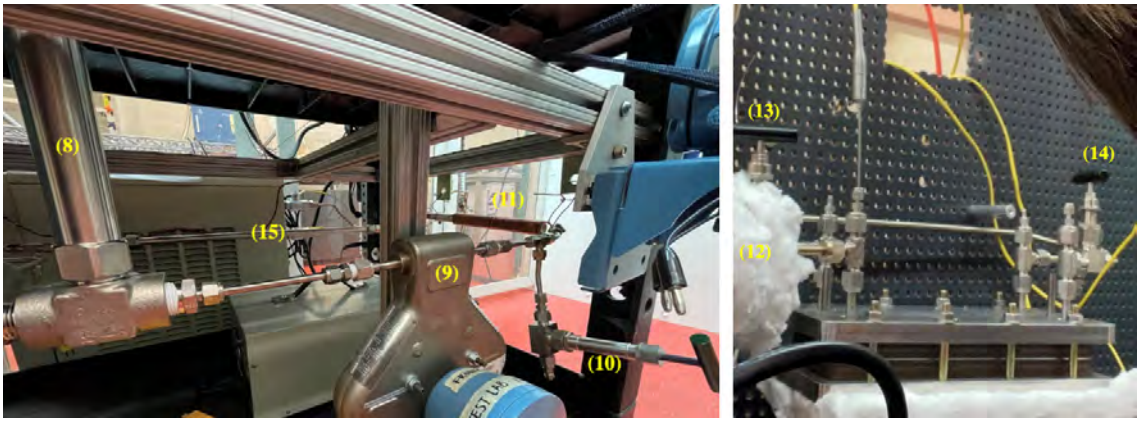

Figure 5.6: (8) Bellows valve, (9) Coriolis mass flow meter, (10) purge valve, (11) pre-heater HX, (12) heat trace HX, (13, 14) high-temperature isolation valves, and (15) post-cooler HX.

Figure 5.6 depicts the rest of the HTF loop. Another bellows valve (8) was installed upstream from the Coriolis mass flow meter (9) to provide finer tuning of the flow rate using the bypass line. Past the mass flow meter, a purge valve (10) was installed to drain HTF from the loop. The flow is reduced into a pre-heater HX (11) comprised of 1/8" copper tubing wrapped around a 1 kW cartridge heater controlled by a PID temperature controller. A thermocouple inserted between the copper tubing and the heater measures the temperature of the Therminol through the HX and controls the output of the heating rod. The Therminol, now closer to its desired process temperature, travels to the top reactor level through tubing wrapped in 1 kW heat trace controlled by a PID temperature controller, bringing it to the exact desired process temperature.

The HTF then flows in and out of the reactor. The reactor can be isolated from the HTF by use of two high-temperature valves placed before the inlet (13) and after the outlet (14) of the reactor. These valves can be used to stop flow to the reactor in the case of emergencies or to prevent HTF draining when reactors are swapped in the apparatus. Another high-temperature valve (15) can be opened to allow the HTF to bypass the reactor.

The blast shield, shown in Figure 5.6 above, slides into place around the reactor piping and over the reactor stand to allow for easy access to the reactor. It was manufactured from 26 gauge galvanized steel sheet metal as a shield to prevent pressurized spray of HTF in the case of gasket failure.

The HTF is cooled after it exits the reactor as it flows through the center of 0.5 m tube-in-tube post-cooler HX (15). A 50/50 ethylene glycol and water mixture is supplied by a Merlin M33 chiller and sits statically in the annulus of the heat exchanger at an ambient room temperature of 20°C. Thermal testing confirmed that flow was not needed to cool the Therminol within pump and instrumentation equipment limits. A thermocouple measures the temperature of the Therminol as it exits the post-cooler to ensure a temperature less than 150°C for safe pump and flow meter operation.

5.5.2 Gas loop operation

The original configuration of the reacting gas loop is pictured below in Figure 5.7.

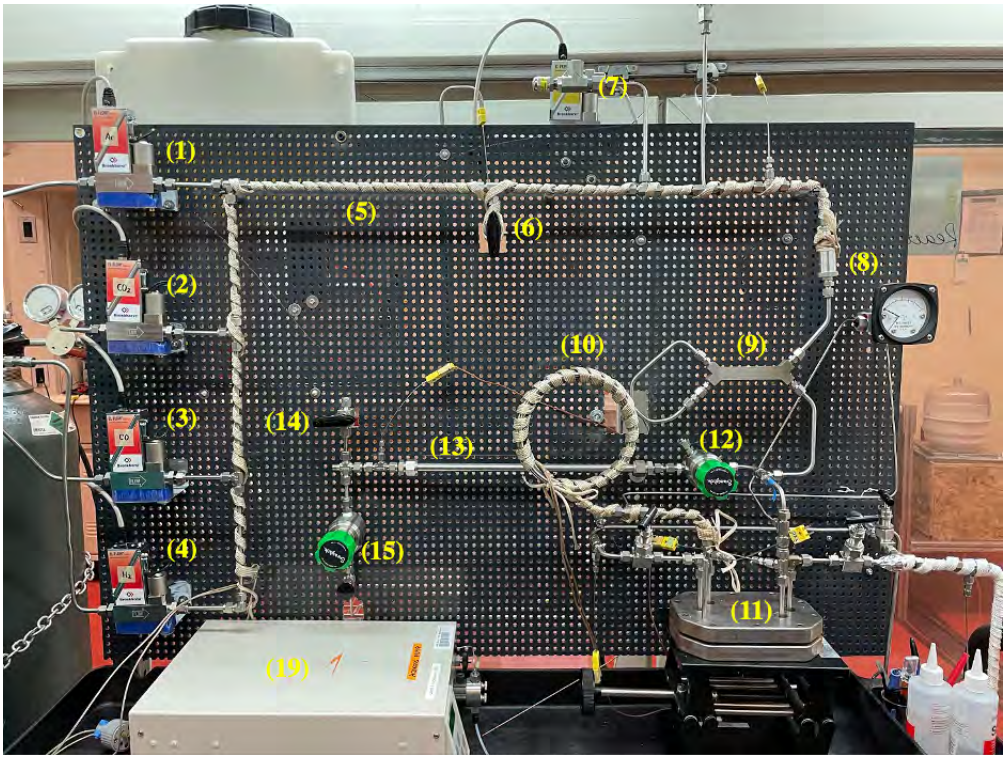

Figure 5.7: Gas loop components mounted on front side of the peg board.

Bronkhorst mass flow controllers flow a predetermined mixture composition of argon (1), carbon dioxide (2), carbon monoxide (3), and hydrogen (4) to the reactor at a specified flow rate and pressure. These gases are mixed and preheated by 10 m of 1 kW heat trace (5). A three-way valve (6) initially vents water vapor from the steam generator (see Figure Y below) to the atmosphere. When a consistent stream of steam has been generated, the valve will be manually turned to route the steam to mix with the dry gases. A pressure relief valve (7) was set to a cracking pressure of 50 bar as a safety measure to prevent overpressurization of the gas loop. The gases then flow through a check valve (8) before entering an additively manufactured recuperative HX (9) printed using laser powder bed fusion, which was manufactured previously for a RAPID project as a sub-scale HTR for

the SMR system. This recuperator routes the hot effluent from the outlet of the reactor in counterflow with the colder unreacted gases, decreasing the overall heating duty the ring heat exchanger (10) needs to provide to heat the stream to process temperatures. In the final iteration of the test loop, the recuperative HX was removed and the ring-shaped heat exchanger was converted to a rod-style heat exchanger. A thermocouple is placed before the inlet of the reactor and meters the heating duty supplied by the heat trace (10) via PID control. The reacting gases, now at the desired temperatures, enter and exit the reactor (11). In the final version of the test loop, the reacting gases exit to the cold and moisture trap, vent, and mass spectrometer.

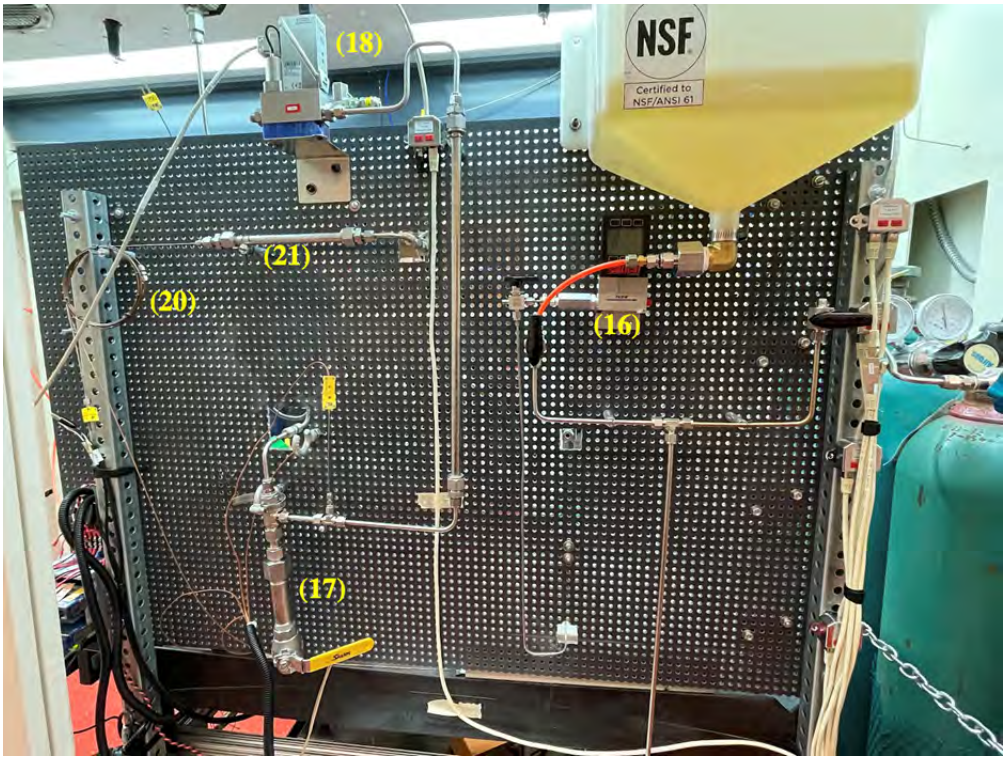

Figure 5.8: Gas loop components mounted on back side of the peg board.

Figure 5.8 above depicts the backside of the pegboard, which primarily consists of gas loop components. The previously discussed Therminol reservoir and vacuum fill line is also mounted to the backside. Steam generation begins at the high performance liquid chromatography (HPLC) pump (19), which resides on the top level of the test cart shown

in Figure 5.7. The HPLC pump directs deionized water from a reservoir through 1/16" copper tubing (20) to the backside of pegboard, shown in Figure 5.8, where it is preheated to 95°C by means of heat trace PID temperature control. The water flows through a heated packed bed of stainless steel ball bearings (21) where it vaporizes. The steam is then routed to the front of the pegboard where it mixes with the dry gases.

After the effluent stream exits the recuperator, it is routed to the backside of the test loop. It enters and travels to the bottom of the cold trap (17) by means of a bored-through connector. The cold trap will be immersed in an ice bath and the mixture will be cooled to temperatures below 70°C before it travels back up through the annulus of the cold trap and through the Bronkhorst back pressure pressure regulator (18), which maintains the desired system pressure (15 to 40 bar). The now-cold stream is vented out of the back pressure regulator to the top of the fume hood.

A slipstream is diverted from the main stream at the exit of the reactor, and a pressure reducer (12) reduces the stream from system pressure to lower pressures for sampling with the QGA mass spectrometer. The stream flows through the pressure reducer to a packed bed of of silica desiccant beads (13) to remove moisture from the system. A three-way valve (14) allows the QGA to sample atmosphere before the slipstream conditions are appropriate for the capillary mass spec. inlet. The Swagelok back pressure regulator (15) and pressure reducer (12) will be adjusted in tandem to tune the mass flow rate of this stream. The slip stream is diverted to the back of the board where an Alicat mass flow meter (16) will verify that flowrate is sufficient for sampling. Conversion within the MDME and WGS reactors will be quantified using the measured product mixture composition from the spectrometer.

5.6 Coolant loop materials

Proper material and component selection is critical in building a robust test loop that can withstand the high temperature, moderate pressure, reacting flow requirements for both the water-gas shift reaction and the methanol-dimethyl ether reaction. The purpose of this section is to provide a detailed description of the components and materials that were

selected for the liquid coolant loop.

5.6.1 Accumulator

A Viton bladder accumulator was specified and ordered from Blacoh Fluid Control. Viton was chosen as the bladder material because it is compatible with Therminol 72. The accumulator is used to maintain fluid pressure of the Therminol liquid coolant and to protect the loop against surges in pressure. It is pressurized via Schrader valve using house nitrogen. The dimensions of the accumulator are shown in Figure 5.9 and the specifications of the accumulator are listed in Table 5.6 below.

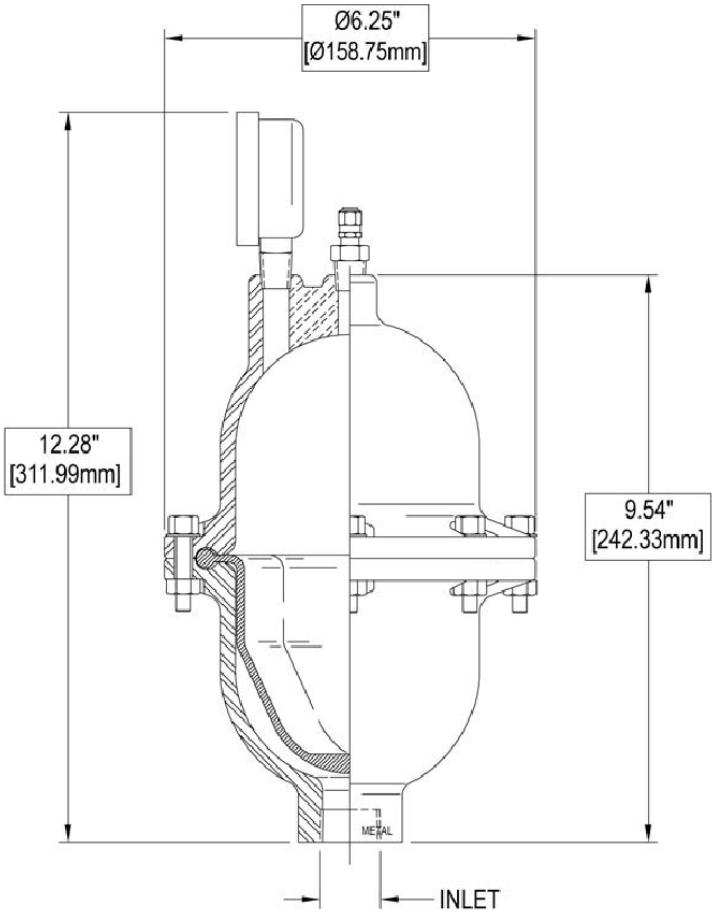

Figure 5.9: Accumulator dimensions.

Table 5.6: Accumulator specs

Parameter	Specification
Manufactuter	Blacoh
Model	CT3020V
Air control	Charge
Bladder material	Viton
Capacity	1.4 L (85 in^3)
Inlet	0.75" FNPT
Max pressure	20.6 bar
Mininum temperature	-23°C (-10°F)
Maximum temperature	177°C (350°F)
Non-wetted housing	Stainless steel
Wetted housing	Stainless steel
Weight	6.8 kg (15 lbs)

5.6.2 Initial driveline specification

Initially, a pump head, motor with accompanying gearbox, and variable frequency drive (VFD) were specified for the coolant loop. The purpose of the driveline is to provide the electromechanical power required to pump the Therminol coolant fluid at the desired flow rate through the reactor and to enable control of the fluid flow rate based on test loop configuration (MDME or WGS).

Pump: A magnetic gear drive GA-X21 Micropump pump was specified and selected from Ryan Herco Flow Solutions. An image of the pump head and its corresponding dimensions are shown below in Figure 5.10. The specifications and details of the pump are listed in Table 5.7 on the next page.

Motor: The pump head was paired with a Nord 3-phase electric gear motor. This motor was used initially because it was a pre-existing resource that was specified for a similar use case. The purpose of the motor is to supply the rotational power required to drive the pump. The nameplate and specifications of the motor are shown in Figure 5.11 and Table 5.8 below, respectively. At its full speed of 1720 rpm, the motor is capable of driving the pump head to its maximum flow rate of 31.5 mL/min. However, because the required flow rate for the WGS application is 10 mL/min and because of the viscous nature

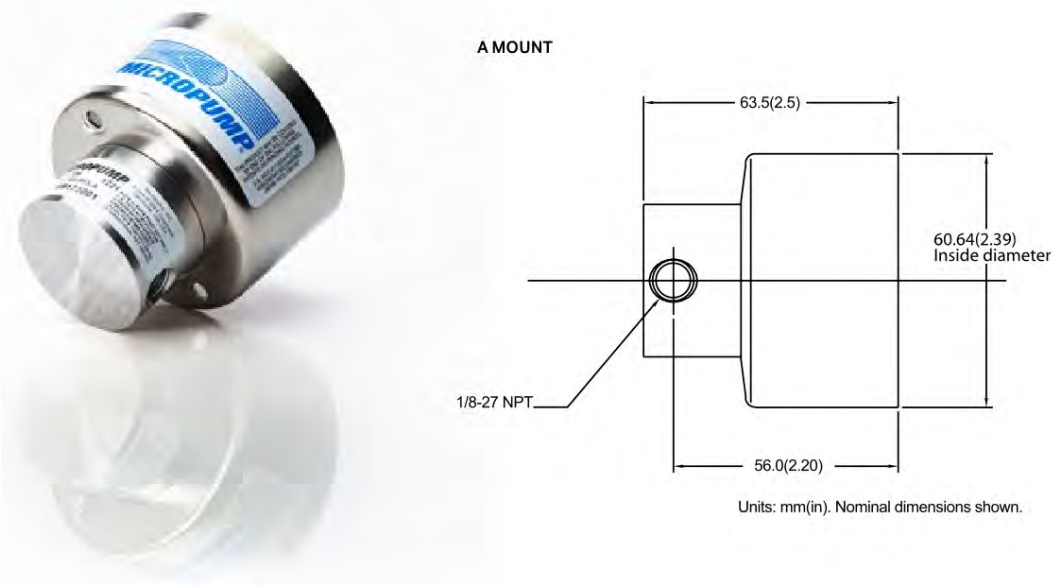

Figure 5.10: The GA-X21 pump head (left) with corresponding dimensions (right) [49].

Table 5.7: GA-X21 pump head specifications

Specification	Description
Manufacturer	Micropump
Series	GA
Gear set	X21
Displacement	0.017 mL/rev
Min flow rate	7 mL/min @ 500 rpm
Max flow rate	56.8 mL/min @ 3450 rpm
Min temperature	-46°C
Max temperature	177°C
Max differential pressure	2.8 bar
Max allowable working pressure (MAWP)	21 bar
Viscosity range	0.2 to 1500 cP
Ports	1/8-27 FNPT side ports
Drive adapter	NEMA 56C
Gear material	PEEK
Static seal material	Viton
Base material	316 stainless steel
Magnet material	Samarium cobalt (SmCo)

of the Therminol being pumped, a solution was needed both to increase the torque supplied to the pump head and to decrease the motor output speed.

Figure 5.11: Nord gear motor nameplate.

Table 5.8: Nord motor specifications

Specification	Description
Manufacturer	Nord
Model number	SK71L/4CUS
Mount type	NEMA 56C
Line frequency	60 Hz
Input voltage	208-230/460 V
Input current	1.9/0.95 A
Output speed	1720 rpm
Output power	0.37 kW (0.5 hp)
Full load torque	-
Service factor	1.15
Power factor	0.69
Efficiency	71%
Weight	9 kg

Variable frequency drive: A variable frequency drive (VFD) was paired with the 3-phase motor to enable variable flow control. VFDs are used to control motor output speed and torque by varying the input frequency supplied to the motor. An Eaton PowerXL DC1 VFD was specified and procured from Platt to enable variable control of the Nord motor. The VFD nameplate is shown in Figure 5.12 below.

Figure 5.12: Eaton VFD nameplate.

Gearbox: A pre-existing in-line Nord gearbox was paired with the motor. This gearbox is specifically designed to be paired with the motor and was sold with the motor as a packaged assembly. The purpose of the gearbox is to increase the torque and decrease the shaft speed supplied to the pump head to achieve the desired pumping rate. The nameplate and specifications of the gearbox are shown in Figure 5.13 and Table 5.9 below, respectively.

Table 5.9: Nord gearbox specifications

Specification	Description
Manufacturer	Nord
Model number	SK 171.1F-71L/4CUS
Input power	0.37 kW (0.5 hp)
Max output torque	114 lb-in
Max output speed	277 rpm
Gear ratio	6.2:1
Weight	23 lbs
Service factor (SF)	2.0
Oil type	Mobil 600 XP220
Oil quantity	0.233 qts

Figure 5.13: Nord gearbox nameplate.

The gearbox steps down the output speed from 1720 rpm to 277 rpm. However, when looking at the GA-X21 pump curve for a water at 1 cP shown in Figure 5.14, it can be seen that 277 rpm is too low of a speed to attain a 10 mL/min flow rate.

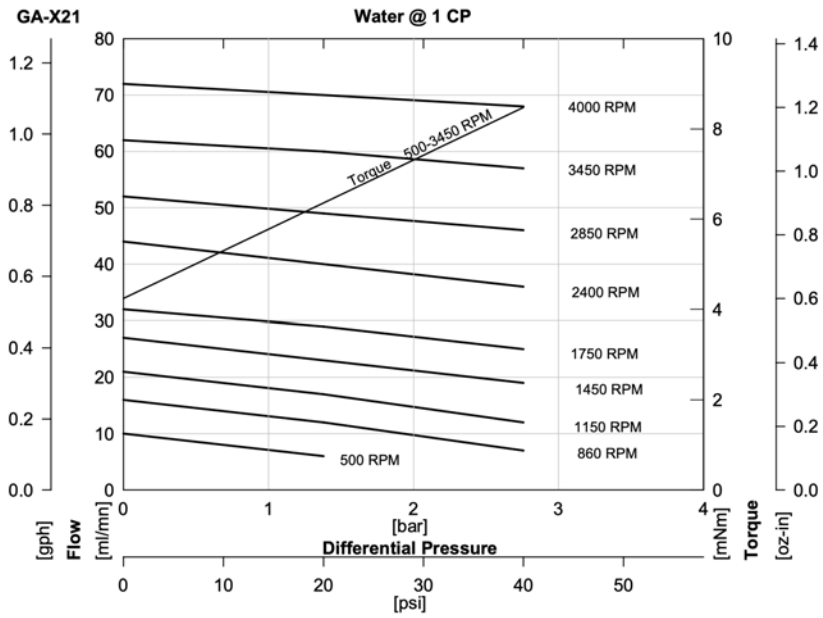

Figure 5.14: GA-X21 pump curve for water at 1 cP.

While it was possible to use this drive without the gearbox, the decision was made to pursue a different solution to satisfy the flow rate requirements because, after experimental tuning, a simpler approach was implemented. The motor and accompanying gearbox that was borrowed could then be used for its original intended research application.

5.6.3 Final driveline components

During construction and tuning of the test loop, it was determined that it would be easier and more feasible to utilize a different pump and motor combination without the use of a VFD. The flow rate could then be controlled downstream via a bypass loop.

Pump: An existing Micropump GA-V23 pump was used in the final construction of the test loop. This was sourced from IDEX in 2018, along with a motor to drive the pump. Similar to the GA-X21, this pump is a magnetic gear pump with a NEMA 56C mount. The specifications and details of the pump are listed in Table 5.10 below. An image of the pump head and its corresponding dimensions are shown below in Figure 5.15.

Table 5.10: GA-X21 pump head specifications

Specification	Description
Manufacturer	Micropump
Series	GA
Gear set	V23
Displacement	0.084 mL/rev
Min flow rate	42 mL/min @ 500 rpm
Max flow rate	438 mL/min @ 5500 rpm
Min temperature	-46°C
Max temperature	177°C
Max differential pressure	5.2 bar
Max allowable working pressure (MAWP)	21 bar
Viscosity range	-
Ports	1/8-27 FNPT side ports
Drive adapter	NEMA 56C
Gear material	PEEK
Static seal material	PTFE
Base material	316 stainless steel
Magnet material	Ferrite

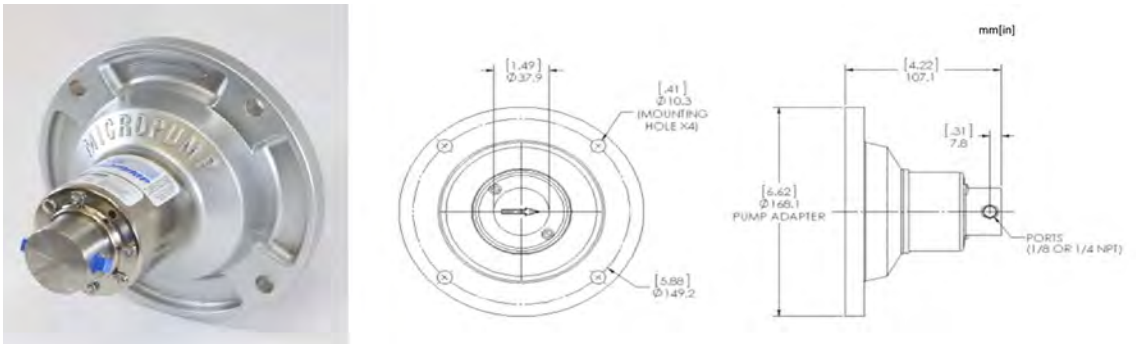

Figure 5.15: The GA-V23 pump head (left) with corresponding dimensions (right) [49].

Motor: Instead of using a 3-phase motor to enable variable frequency control, a pre-existing Baldor single phase motor was used to simplify the operation of the test loop. A photo of the motor and pump head assembly can be seen in Figure 5.16 and the specifications of the motors are listed in Table 5.11 below.

Figure 5.16: The Baldor motor and Micropump GA-V23 pump head assembly.

Table 5.11: Baldor CL3405 motor specifications

Specification	Description
Manufacturer	Baldor
Model number	CL3405
Mount type	NEMA 56C
Line frequency	60 Hz
Input voltage	115/208-230 V
Input current	6/3.2-3 A
Output speed	3600 rpm
Output power	0.25 kW (0.33 hp)
Full load torque	0.68 N-m (0.5 lb-ft)
Service factor	1.35
Power factor	0.66
Efficiency	58.8%
Weight	9 kg

Power supply: A Variac TDGC-2KM transformer was used to supply power the motor. Variacs are variable AC power supplies that provide adjustable AC voltage. The details of the Variac TDGC-2KM are provided in Table 5.12 below. For this application, the Variac was set to the required 3.7A at 208V. An image of the Variac can be seen in Figure 5.12 below.

Table 5.12: Variac TDGC-2KM transformer specifications

Specification	Description
Manufacturer	Variac
Model number	TDGC-2KM
Input voltage	110VAC @ 60Hz
Output voltage	0-130 VAC
Output current	0-20 A
Maximum output power	2000 VA
Weight	24 lbs

Figure 5.17: A Variac TDGC-2KM transformer.

5.6.4 Heat exchangers

A series of heat exchangers was needed to heat the Therminol coolant fluid to the desired inlet temperature of 350°C. Two sets of heating elements were used to heat the fluid: an insertion heater rod was used to preheat the fluid to 280°C and then ultra-high temperature heat tape was wrapped around the piping leading up to reactor coolant fluid inlet to bring the fluid temperature up to 350°C.

Pre-heater: The pre-heater consists of 1/8" OD copper tubing wrapped tightly around a 3/4" diameter x 10" long 1000W rod heater procured from McMaster-Carr. The Therminol heats up to 280°C as it travels through 1/8" copper tubing wound tightly around a 3/4" rod heater. An image of the pre-heater can be seen in Figure 5.18 and the details of this heater are provided in Table 5.13 below.

Figure 5.18: The coolant fluid pre-heater.

Table 5.13: Coolant fluid pre-heater specifications

Specification	Description
Procurement source	McMaster-Carr
Model number	3618K997
Heating element diameter	0.745"
Heating element length	10"
Heated length	8.625"
Wattage	1000 W
Watt density	50 W/sq. in.
Maximum exposure temp.	538°C
Voltage	120 VAC
Current	4.2 A
Sheath material	Incoloy

Post-heater: The post-heater is comprised of ultra-high temperature heat trace in the form of a flat heated cable, commonly referred to as heat tape, wrapped around the 1/4" tubing. This style of heater can be wrapped around tubing to heat the process fluid to temperatures up to 760°C. Heat tape can be advantageous because it supplies the same wattage regardless of the surrounding temperature, so they're less prone to power surges than self-regulating heaters. To prevent burnout, care was taken not to overlap the tape when wrapping the heat trace around the length of piping between the pre-heater and the coolant inlet of the reactor. The details of the heat trace used are described in Table 5.14 below.

Table 5.14: Coolant fluid post-heater specifications

Specification	Description
Procurement source	McMaster-Carr
Manufacturer	HTS/Amptek
Model number	-
Wattage	624 W
Watt density	78 W/ft.
Voltage	120 VAC
Current	1.7 A
Length	8 ft.
Width	1"
Maximum heat output	760°C
Cable cover material	Fiberglass

5.6.5 Instrumentation

Various forms of instrumentation were integrated into the coolant loop to measure temperature, pressure, and mass flow rate of the coolant fluid. These pieces of instrumentation are crucial in ensuring safe operation of the loop, protecting sensitive equipment from overpressurization or overheating, and validating the correct mass flow required to impose the optimal temperature profile onto the process gases flowing through the sub-scale WGS reactor. This subsection describes the instrumentation used to achieve these goals.

Thermocouples: Two K-type thermocouples from Omega were inserted into the coolant stream via bored-through T-junction thermocouple wells, one directly after each of the heaters. Before use, the thermocouples were calibrated using a Fluke 7109A portable calibration bath using a five-point calibration from 100°C to 140°C. The properties of these thermocouples are described in Table 5.15 below.

Each thermocouple was then plugged into a PID temperature controller that were used to control the power output of the heater to the desired fluid temperatures of 280°C and 350°C for the pre-heater and post-heater, respectively. The pre- and post-heater were also plugged into their respective temperature controller. A photo of a temperature controller can be seen in Figure 5.19 below. The input from the thermocouple controls the output power provided to the heater plugged into the temperature controller.

Table 5.15: K-type thermocouple specifications

Specification	Description
Manufacturer	Omega Engineering
Model number	SCASS-062G-6
Temperature range	-200°C to 1250°C
Probe diameter	1.58 mm
Probe length	152 mm
Sheath material	304 stainless steel
Connector style	Miniature
Measurement uncertainty	±2.2°C

Figure 5.19: A PID temperature controller.

Since the maximum operating temperature of many of the flow components on the coolant loop is 177°C (350°F), temperature controllers were similarly used to control the coolant liquid temperature to 150°C to protect the temperature-sensitive components. Thermocouples were placed between the tubing and the insulation directly before the components to measure the surface temperature of the tubes, which is approximately the same as the temperature of the fluid. The temperature was held at 150°C through these components to maintain a high liquid viscosity and decrease the pressure drop through the loop, since the pump has both a differential pressure limit as described previously in Table 5.10.

Pressure transducer: A Rosemount 3051SMV absolute + differential pressure transmitter paired with a Rosemount 305 manifold was used to measure the absolute pressure of the coolant loop. The transmitter is the electromechanical portion of the device that outputs the measurement signal to data acquisition hardware and software. The manifold is the purely mechanical portion of the instrumentation that measures the absolute or differential pressure of the process fluid. These two pieces of equipment cannot be used without being paired with one another. In tandem, these devices form the pressure transducer.

The Rosemount pressure transducer was installed at a T-junction prior to the inlet of the pump. The pressure after the outlet of the pump is set and reported by the accumulator, so the absolute pressure transducer was installed prior to the inlet of the pump to measure the pressure drop over the length of the test loop. The specifications of the pressure transducer are described in Table 5.16. An image of the transducer and manifold combination can be seen in Figure 5.20 below.

Table 5.16: Rosemount 3051SMV pressure transducer specifications

Specification	Description
Manufacturer	Emerson
Product line	Rosemount
Transmitter model	3051SMV-5M23A4N2A11A1AM5
Manifold model	0305RC32B11
Static pressure range	0.5 to 250 bar(a)
Differential pressure range	-2.5 to 2.5 bar(a)
Temperature range	-50°C to 204°C
Wetted material	316L stainless steel
Measurement uncertainty	±0.04%

The pressure drop through the Therminol loop was initially estimated to be about 1.5-2-5 bar with a liquid viscosity estimated at 150°C and 10 bar or greater. The pressure reading from the accumulator in tandem with the absolute pressure reading from the Rosemount pressure transducer confirms that the true pressure drop across the loop was about 1 bar.

Mass flow meter: A Micro Motion Coriolis mass flow meter was used to measure the mass flow of the Therminol coolant liquid flowing through the coolant loop tubing. Like the Rosemount pressure transducer, the Coriolis mass flow meter consists of a Micro Motion

Figure 5.20: The Rosemount 3051SMV pressure transducer mounted on the test loop.

ELITE CMF010M mass flow sensor and a Micro Motion 2700 transmitter. The transmitter was configured using ProLink III using the procedure described in Appendix B.1. When paired together, these components form the Coriolis mass flow meter.

The Coriolis mass flow meter was installed after the accumulator and prior to the pre-heater. It was installed in this location because of the temperature limitations of the instrumentation. These limits and other specifications are described in Table 5.17 below. The installed mass flow meter on the coolant loop is depicted in Figure 5.21 below.

Table 5.17: Micro Motion Coriolis mass flow meter specifications

Specification	Description
Manufacturer	Emerson
Product line	Micro Motion
Transmitter model	CMF010M323NQBUEZZZ
Sensor model	2700R11BBUEZZZ
Sensor MAWP	125 bar(g)
Temperature range	-50°C to 204°C
Wetted material	316L stainless steel
Measurement uncertainty	±0.0032 % reading

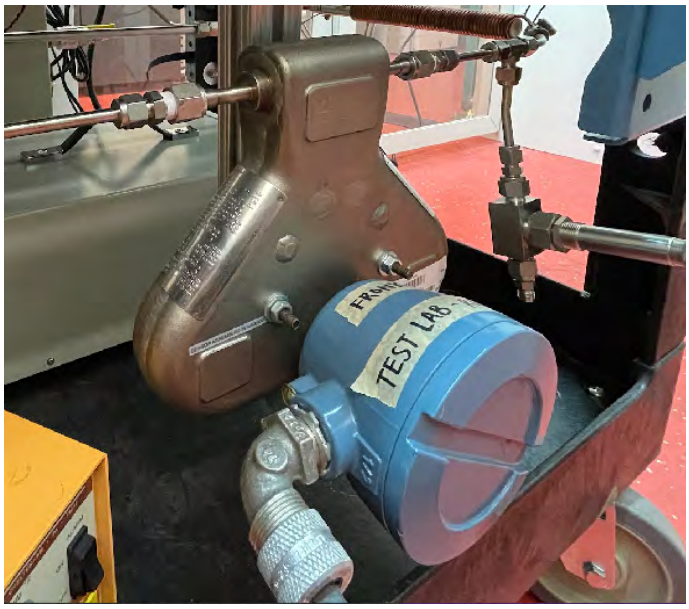

Figure 5.21: The Micro Motion Coriolis mass flow meter mounted on the test loop.

5.7 Reactant loop equipment

The purpose of this section is to provide a detailed description of the components and materials that were selected for the reacting gas loop. In similar fashion to the coolant loop, the selected components and materials for the reactant loop must be able to provide and withstand the temperature, pressure, and mass flow requirements for the water-gas shift reaction.

5.7.1 Mass flow controllers

Mass flow controllers are precision pieces of equipment that measure and control the flow of gases. The controller must be built, tested, and calibrated for the specific operating conditions required for the WGS research as aforementioned in Subsection 5.3.2 and the MDME research performed by Freiberg using the same test loop. These instruments control the gas flow rate by comparing the measured mass flow value to the setpoint value, which varies between 0 to 100% of its full-scale range. The software in the controller modulates a control valve that quickly adjusts the flow by opening and closing the valve until the setpoint value is reached.

Four gas mass flow controllers were specified and ordered from Bronkhorst by Freiberg to meter argon, carbon dioxide, carbon monoxide, and hydrogen to the reactor prototypes. Argon is needed as an inert gas for testing and as a baseline for mass spectrometry while the other gases are process gases. The four mass flow controllers are depicted in Figure 5.22 below. The Bronkhorst data acquisition system is later discussed in Subsection 5.9.3.

5.7.2 Steam generator

In order to supply steam for the reaction, a steam generator was created by pumping liquid water using a high performance liquid chromatography (HPLC) pump through a series of two heaters. The first heater is a copper coil wrapped with a 2 ft/156 W heat tape from HTS/Amptek. The pre-heater is temperature controlled to 95°C. Next, the pre-heated water is pushed through a packed bed of ball bearings wrapped by heat tape. The heat tape is temperature controlled to 150°C to ensure the water is in vapor phase as steam as it mixes with the preheating gases. The steam generator subsystem can be seen shaded in blue in the reactant loop P&ID in Figure 5.2 above.

Figure 5.22: The four Bronkhorst mass flow meter mounted on the test loop.

5.7.3 Heat exchangers

As aforementioned in Subsection 5.3.2, the gases need to be heated to a reactor inlet temperature of 350°C. Just like the coolant loop, a series of heaters were used to bring the gas up to 350°C. Unlike the coolant loop, four heaters were needed to bring the gas up to the desired temperature. This subsection describes the specification of each heater used.

Heater 1: The first pre-heated section is comprised of a 10 ft. 520 W heat tape wound around the 1/4" stainless steel tubing leading from the mass flow controllers to the check valve. This heater is used in conjunction with a temperature controller to preheat the stream to 100°C. The details of the first heat trace used are described in Table 5.18 and an image of the first pre-heated section of tubing is depicted in Figure 5.23 below.

Table 5.18: Reactant gas heater 1 specifications

Specification	Description
Procurement source	McMaster-Carr
Manufacturer	HTS/Amptek
Model number	-
Wattage	520 W
Watt density	52 W/ft.
Voltage	120 VAC
Current	4.3 A
Length	10 ft.
Width	1/2"
Maximum heat output	760°C
Cable cover material	Fiberglass

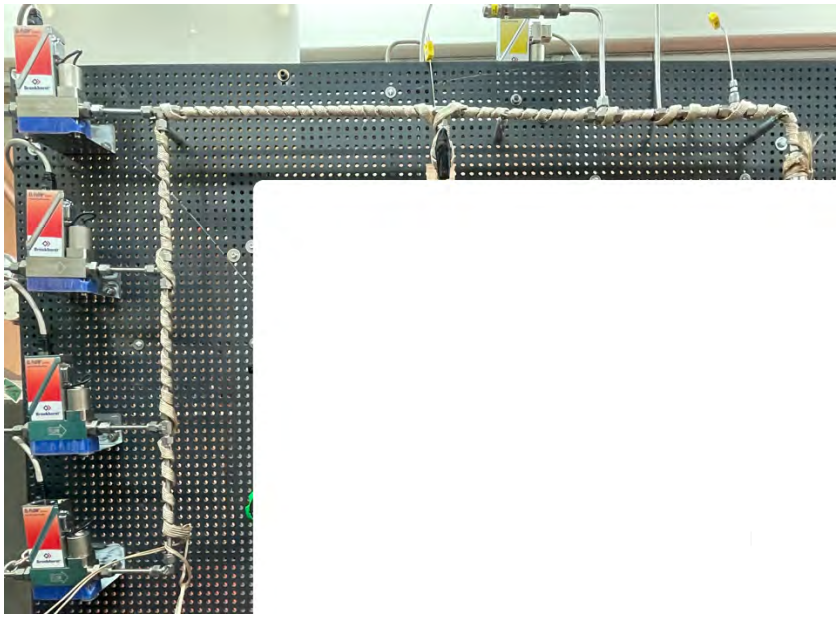

Figure 5.23: The first heater for the reactant gases.

Heater 2: The second preheated section is comprised of a 6 ft. 468 W heat tape wound around the 1/4" stainless steel tubing between the check valve and the start of the 3rd heater. This heat trace has a higher watt density to account for the shorter length of available piping to wind the tape around. This section of heat trace is used with a temperature controller to bring the gas stream to 200°C. The details of the second heat trace used are described in Table 5.19.

Table 5.19: Reactant gas heater 2 specifications

Specification	Description
Procurement source	McMaster-Carr
Manufacturer	HTS/Amptek
Model number	-
Wattage	468 W
Watt density	78 W/ft.
Voltage	120 VAC
Current	3.9 A
Length	6 ft.
Width	1/2"
Maximum heat output	760°C
Cable cover material	Fiberglass

Heater 3: The third heater consists of 1/8" 316 stainless steel tubing wrapped tightly around a 3/4" diameter x 8" long 1000W rod heater procured from McMaster-Carr. This third and main heater is paired with a temperature controller to bring the gas as close as possible to the desired inlet temperature of 350°C. The thermocouple used for the input to temperature controller is inserted into the inlet gas manifold of the reactor. This heat exchanger was coated in Tracit 600A, a hardening high-temperature heat transfer compound. The purpose of the heat transfer compound is to evenly distribute the heat around the tubing to increase the heat transfer area provided to the fluid from the tubing. The compound arrived in a putty-like form and was applied evenly around the rod heater using a metal spatula. Once the compound had dried, a separate thermocouple was placed on the hardened surface of the heat transfer compound at the beginning of the heater to monitor the temperature of the heater to ensure it did not experience overheating.

The heat transfer putty and thermocouple for monitoring were found to be a necessary

addition because, during a previous thermal test, the entirety of the heater had burned up due to heat loss issues between the heater and the area of the reactor where the temperature input to the temperature controller was being measured. Because all the heat being transferred into fluid through Heater 3 was being lost to the ambient atmosphere due to poor insulation and test loop design, this caused the temperature controller to dramatically overshoot the power supplied to the heater.

The details of this heater are provided in Table 5.20 below. An image of the third heater before being coated in the heat transfer putty can be seen in Figure 5.24. Later on, the heater was rotated to minimize the section of unheated tubing between the heater and the reactor inlet to minimize the heat losses.

Table 5.20: Specifications of reactant gas main heater (heater 3).

Specification	Description
Procurement source	McMaster-Carr
Model number	35025K534
Heating element diameter	0.745"
Heating element length	8"
Heated length	6.6875"
Wattage	2000 W
Watt density	130 W/sq. in.
Maximum exposure temp.	538°C
Voltage	120 VAC
Current	16.7 A
Sheath material	Incoloy

Figure 5.24: The third heater for the reactant gases.

Heater 4: The final heater was a short, 2 ft. long section of heat tape that was wrapped

around the short length of piping between the main heater and the inlet of the reactor. This was to prevent heat loss from this section of piping to the reactor. This heater was pre-existing in the ATAMI lab and the specifications for it were unknown. Since it was only 2 ft. in length, it was not used in conjunction with a temperature controller due to the low possibility of overheating. The temperature of the heater was measured and noted from time to time using a spare thermocouple.

Counterflow HX: The initial design also included the use of an additively manufactured counterflow heat exchanger. This heat exchanger was designed and created by Kijoon Lee as part of separate research funded by the RAPID Institute. However, after initial thermal trials using the heat exchanger, it was deemed infeasible for use due to leakage issues through the NPT fittings and excessive heat loss. The heat loss issues were not due to the heat exchanger itself, as it was previously discussed that heat was being lost through the unheated sections of piping due to poor insulation.

5.7.4 Instrumentation

Just as instrumentation was needed on the coolant loop, the reactant loop also incorporated various forms of instrumentation to measure temperature, pressure, and mass flow rate of the process gases. These pieces of measurement equipment are crucial in ensuring safe operation of the loop, protecting sensitive equipment from overpressurization or overheating, and validating the temperature profile of the sub-scale WGS reactor. This subsection describes the instrumentation used to achieve these goals.

Temperature: Seven (7) K-type thermocouples were used to measure the reactant loop temperatures. Three of these thermocouples were inserted into the gas stream via bored-through T-junction thermocouple wells, one for each of the temperature controllers. Two more were used as surface measurements as a safety precaution. The last two thermocouples were used on the back of the loop for the steam generator. The properties of these thermocouples are described previously in Table 5.15 above.

Fiber optic temperature sensor: As previously mentioned in Chapter 3, a fiber

optic temperature sensor from LUNA Innovations was integrated into the reactor to obtain discrete measurements of the differential temperature across the length of the reactor. The fiber was paired with a LUNA's commercial laser and fiber optic sensing system to obtain the temperature profile of the reactor. This data acquisition system is described later in Subsection 5.9.2.

The fiber is made of silica glass and is 125 microns in diameter with a spatial resolution along the length of the fiber of 0.625 mm. Figure 5.25 below from LUNA shows the spatial resolution and resulting distributed temperature profile.

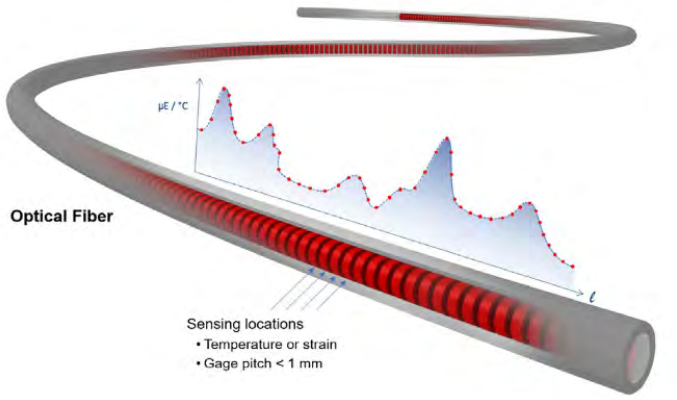

Figure 5.25: At 0.125 mm in diameter, the LUNA fiber is able to provide a spatial resolution of 0.625 mm at up to a 250 Hz measurement rate [50].

The measurement principle of the fiber optic sensor is based on measuring Rayleigh backscatter. As the temperature of the fiber and its environment change, the reflection patterns through the fiber also change. This method relies on correlating the change in reflection patterns to a temperature based on the thermal expansion and thermal stress properties of the physical silica glass material. This technique is known as coherent optical fiber domain reflectometry [51].

Experimental challenges arose because the fiber channel in the instrumentation plate was too thin to account for expansion of the steel, which introduced mechanical stresses onto the fiber and severely impacted the accuracy of the temperature measurement from the fiber. To correct this, the channel was widened to allow both the steel and the fiber room

to expand at high temperatures. Once the channel was widened, the mechanical stresses were alleviated from the fiber and the temperature reading was more accurate. However, even at room temperature, mechanical stresses are still present in the fiber and had to be tared out using the LUNA software.

Mass spectrometer: A Hiden Quantitative Gas Analysis (QGA) mass spectrometer was used to measure the composition of the reactant effluent stream and obtain a chemical spectrum. It is necessary to pair the mass spectrometer with a vacuum pump to maintain a low-pressure, high vacuum analysis chamber. This reduces the chance of ions colliding with other molecules as it is being analyzed by the mass analyzer.

5.8 Supporting materials

The purpose of this section is to provided a detailed description of the materials that were used in supporting the process loop.

5.8.1 Infrastructure

This subsection describes the materials and components used in the supporting structures of the test loop.

Rolling test cart: A pre-existing durable plastic test cart originally obtained from McMaster-Carr was used to house the test loop. The cart features two levels with lipped shelves, rounded corners to protect walls from damage, and storage compartments near the handle to contain smaller items. The cart has two rigid and two swivel casters for ease of steering.

Aluminum extrusion: Square aluminum extrusion was attached below the top level of the test cart to enable flexibility in mounting of the bulkier and heavier components.

Perforated back board: A pre-existing 45" x 25" perforated plastic backboard came attached to the plastic test cart. This back board was used to mount the lighter test loop components onto. The perforations enable flexibility in locating materials and components.

Adjustable riser: An adjustable riser was placed onto the test cart as a surface for the reactor to rest on. The riser enables modularity in the test loop design.

An image of the supporting infrastructure prior to construction of the loop is depicted below in Figure 5.26.

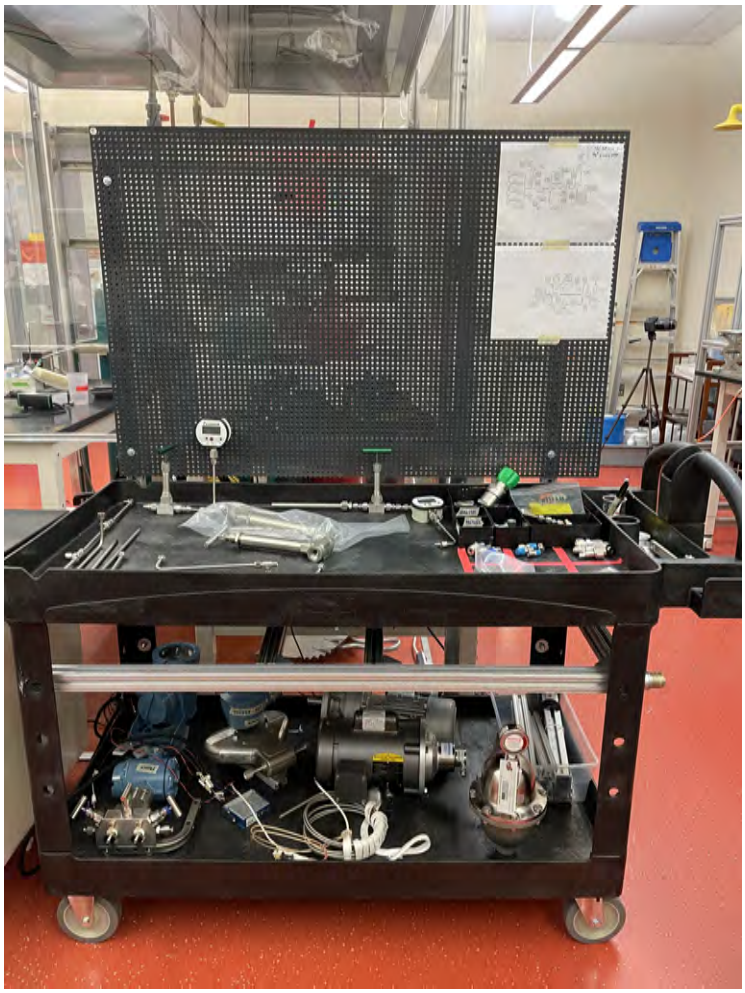

Figure 5.26: The supporting infrastructure of the test loop before construction began.

5.8.2 Basic components

This subsection describes the materials and components used to pipe and connect the test loop together.

Tubing: The coolant loop tubing mainly utilized 1/4" x 0.035" wall thickness 316 stainless steel. The majority of the tubing used for the reactant loop was 1/8" OD x 0.028" wall thickness 316 stainless steel tubing. 316 stainless steel was used because it is compatible with all of the other materials and fluids used in the test loop and exhibits good heat transfer properties. For the portions of the loop such as the tubing around the process gas heaters, thinner 1/8" OD x 0.028" ID copper tubing was used.

Fittings: Swagelok compression fittings were used to join together the piping, valves, and components. Compression fittings work under the principle . Swagelok fittings are advantageous at the research scale because they enable a leak-free seal without the use of Teflon and other sealant materials, but they are disadvantageous at an industrial scale because they are costly and limited to smaller tube geometries. Some components, such as the accumulator, utilized National Pipe Thread (NPT) fittings that needed adapters to integrate with the other compression fittings.

Valves: Swagelok bellows valves were utilized for flow control of the coolant fluid because these valves enable fine control of the flow path. Swagelok high-temperature ball valves were utilized to isolate the reactor from the rest of the loop because these were the only types of valves with packing material designed to withstand the temperatures. Check valves were utilized for flow direction control on the gas side. Pressure relief valves were utilized and vented to the walk-in fume hood atmosphere to prevent over-pressurization of the loop.

Fasteners: An assortment of alloy steel button head hex drive metric screws were used to fasten components to the test cart and backboard. Hex head screws are advantageous for applications of this scale because hex keys are easier to fit into confined spaces than other types of drivers. Assorted alloy steel nuts and washers already available in the laboratory space were used in conjunction with the screws.

5.8.3 Insulation

Two types of material were used to insulate the high-temperature portions of the test loop from the ambient conditions. A base layer of 1" width x 1/16" thick calcium aluminum

silicate ceramic fiber strip insulation procured from McMaster-Carr (rated up to 815°C) was first wrapped around the piping and components. The gas cartridge heater is shown in Figure 5.27 below wrapped in only the silica strip insulation.

Figure 5.27: The gas cartridge HX wrapped in a base layer of the silica strip insulation.

A 1" thickness x 24" width x 300" length roll of Cerablanket, a ceramic thermal insulation product made by Morgan Thermal Ceramics (rated up to 1315°C), was procured from High Temperature Inc. Strips of insulation were cut to size from the rolled-up sheet using shears and wrapped around the primary layer of insulation to prevent further heat loss. The reactor is shown coated in the Cerablanket sheet insulation in Figure 5.28 below.

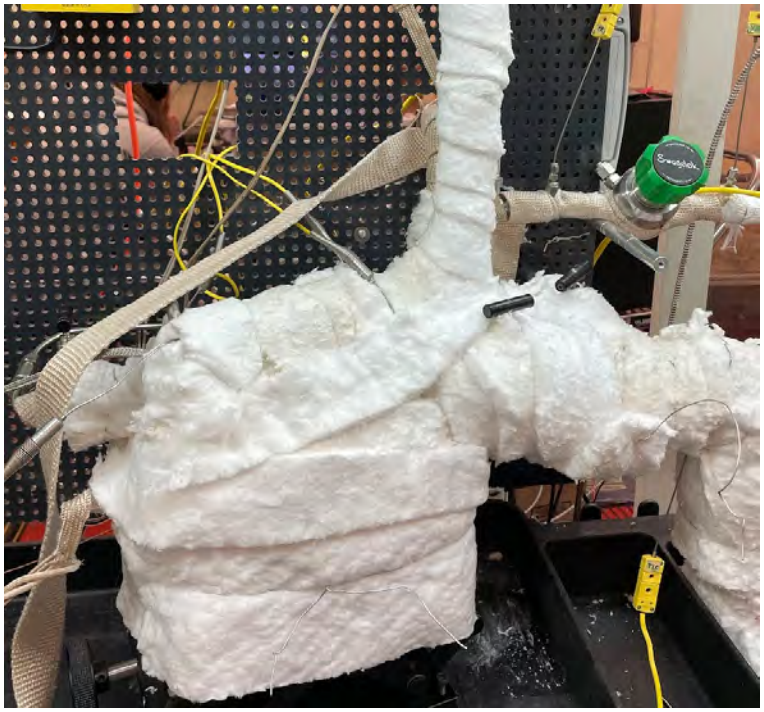

Figure 5.28: The reactor wrapped in the white Cerablanket sheet insulation.

5.9 Data acquisition

The data acquisition (DAQ) system for the MDME/WGS test loop ranged from simple pen-and-paper measurements to sophisticated DAQ programs. This loop integrated many different types of measurement devices such as thermocouples, a mass flow meter, a pressure transducer, flow controllers, a mass spectrometer, and fiber optic temperature sensors.

5.9.1 NI LabVIEW

The LabVIEW data acquisition system by National Instruments (NI) was utilized to monitor and acquire temperature and flow rate data for the MDME/WGS test loop. The LabVIEW 2016 software was paired with an NI CompactDAQ chassis and two C Series I/O modules to acquire data.

The NI-9208 16-channel C series current input module was used to process signals

from the Micro Motion 2700 mass flow transmitter and the Rosemount 3051SMV absolute pressure transducer transmitter. The wiring to the NI-9208 DAQ can be seen in Figure 5.29 below.

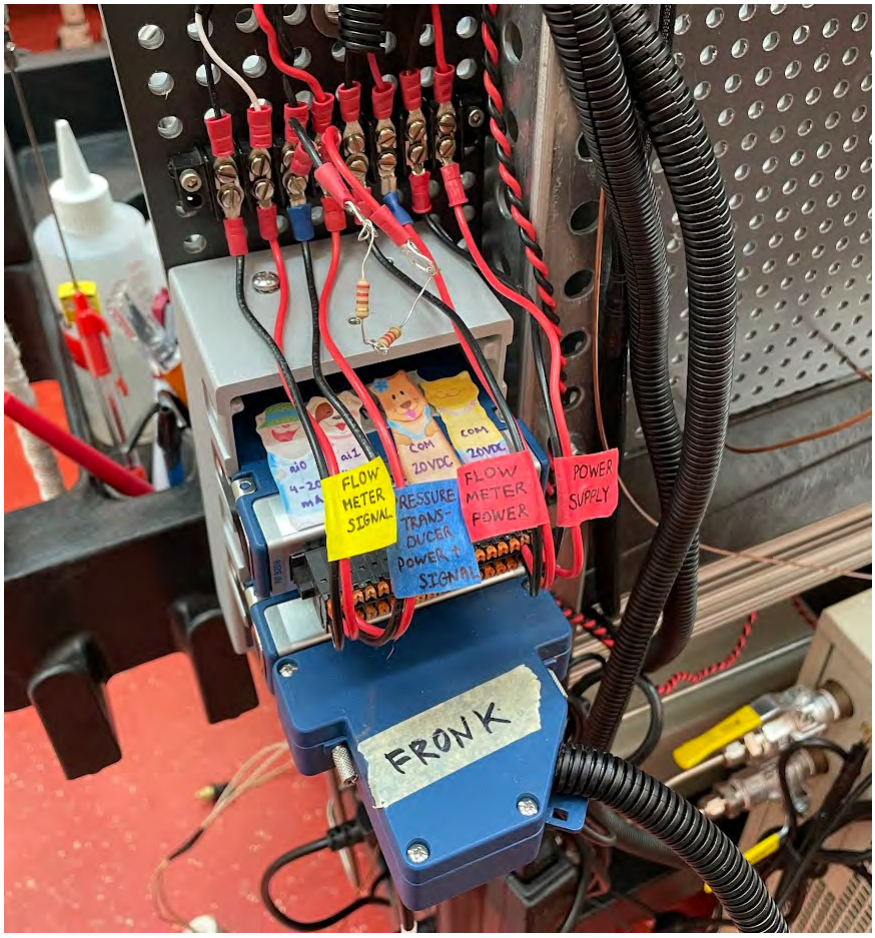

Figure 5.29: Wiring of NI-9208 current input module.

A 20 VDC power supply with a maximum current of 0.3 A provides power to one of two COM ports of a NI-9208 DAQ module. The Micro Motion 2700 is powered through the second COM port and provides a 4-20 mA signal to analog input port 0. The Rosemount 3051SMV receives 20 VDC power and transmits 4-20 mA signals through a single set of wires wired to analog input port 1.

The NI-9214 16-channel isothermal C series temperature input module was used to process signals from the thermocouples on the gas and liquid loop. The eleven thermocouples

procured and used on the test loop were wired into the module. The NI-9214 module is shown below the NI-9208 module in Figure 5.29 above.

A LabVIEW Virtual Instrument (VI) file and graphical user interface (GUI) was created to monitor the two aforementioned process variables. An image of the GUI can be seen in Figure 5.30 below. The GUI was used to confirm signals to be working and accurately reporting during the test loop commissioning process, as well as to monitor the test loop temperatures and Therminol flow rate during testing.

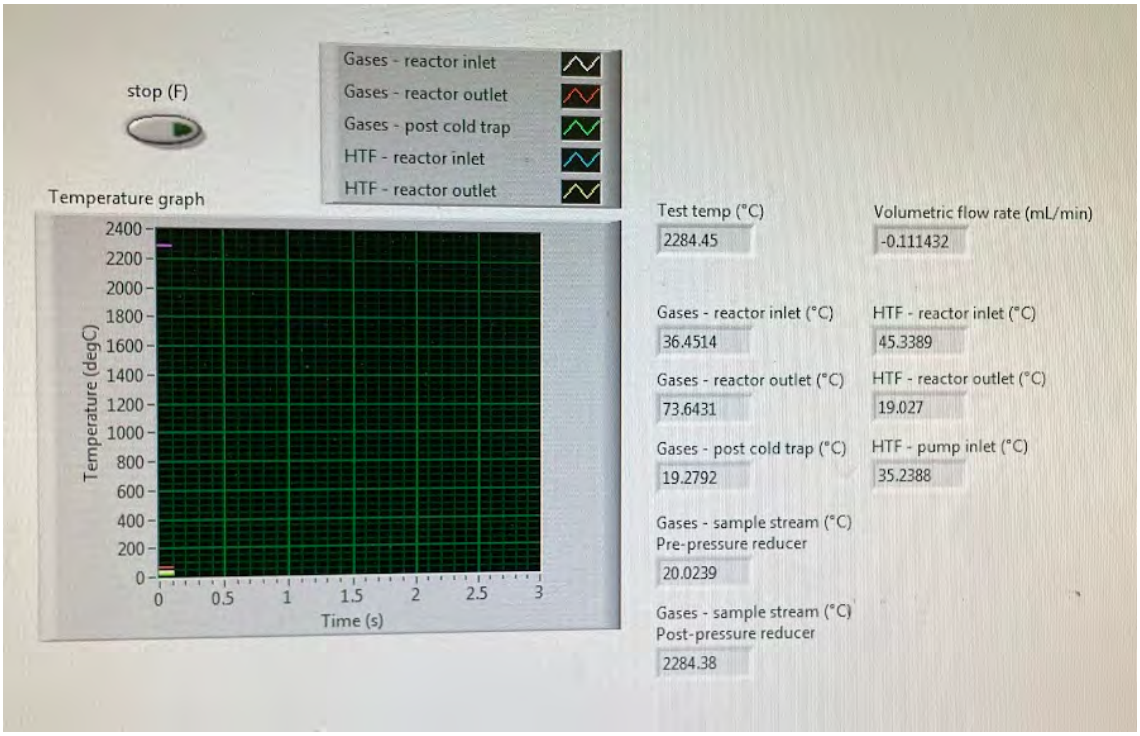

Figure 5.30: The LabVIEW GUI.

The LabVIEW 2016 application was installed on a desktop computer and the computer was placed onto a rolling cart placed outside of the walk-in test hood. This enabled remote remote monitoring of the test loop temperatures and coolant loop flow rate.

5.9.2 LUNA ODiSI-B

The LUNA temperature data acquisition system is known as the Optical Distributed Sensor Interrogator, nicknamed ODiSI. The ODiSI-B system was used for this research. The system consists of the following hardware and software components:

1. Dedicated instrument controller (Dell Precision laptop)
2. ODiSI-B data acquisition software
3. ODiSI-B interrogator
4. Remote modules for sensor interfacing
5. Standoff cables
6. Fiber optic temperature sensors

An overview of the ODiSI system and how it interfaces from the DAQ to the measurement article is shown in Figure 5.31.

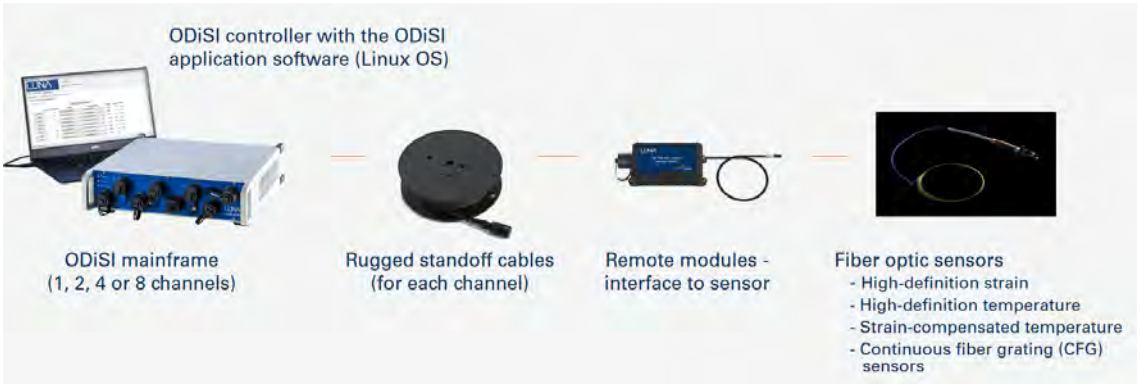

Figure 5.31: The ODiSI system [50].

The laptop and interrogator were placed onto the same rolling cart as the LabVIEW data acquisition computer. This enabled remote monitoring and logging of the reactor temperature data at a safe distance from the hot test loop. The LUNA DAQ subsystem is highlighted in orange in the process and instrumentation diagram shown in Figure 5.2.

5.9.3 Bronkhorst FlowSuite

The Bronkhorst mass flow hardware was paired with the Bronkhorst FlowSuite software to enable remote mass flow control, monitoring, and data logging. The software is capable of dynamic plotting of the the system back pressure and individual gas flow rates, which was a critical feature that was used during the leak checking process of the test loop. The test loop could only be called leak-free after passing a 30 minute hold test at 10 bar of pressure, which was easy to visually check using the FlowSuite software. Figures 5.32 and 5.33 below show the GUI for the FlowSuite software.

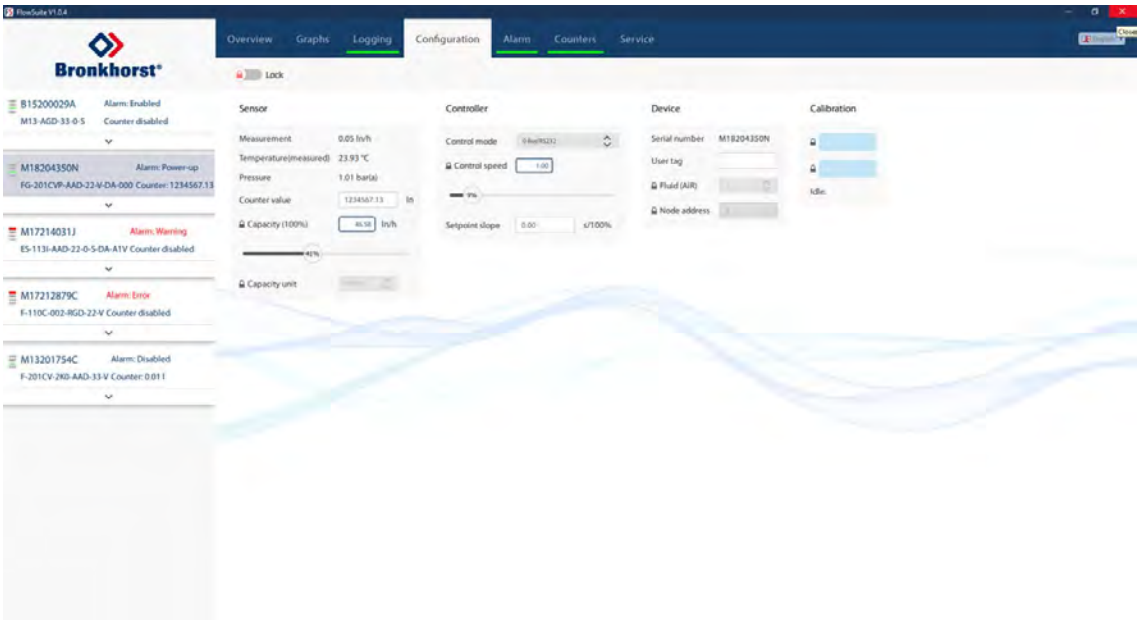

Figure 5.32: On the "Configuration" page of the FlowSuite application, one can control the mass flow controllers and back pressure regulator.

5.9.4 Hiden MASsoft Professional

The Hiden QGA mass spectrometer plugs into an intermediary interface unit, which translates the mass spectrum data to the Hiden MASsoft Professional software. MASsoft enables control, calibration, data logging, and real-time monitoring of the mass spectrum collected

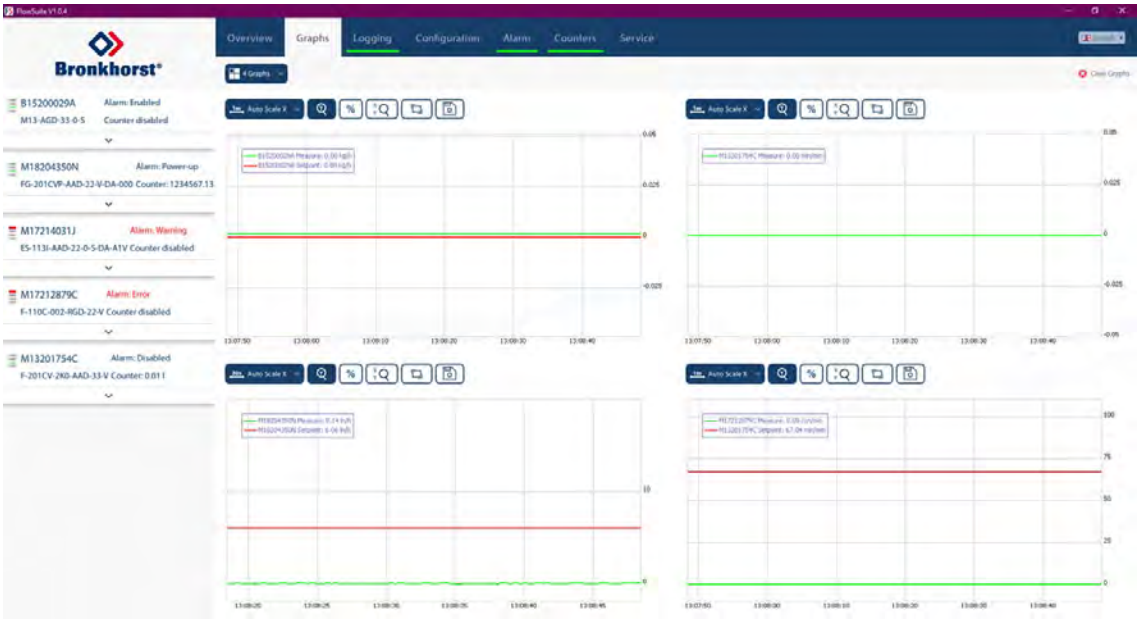

Figure 5.33: On the "Graphs" page of the FlowSuite application, one can plot the dynamic behavior of the back pressure regulator, flow controllers, and mass flow conditions.

by the mass spectrometer. The MASsoft software was not used extensively for this research because reactive testing was not conducted for safety reasons.

5.10 Safety considerations

There were numerous safety concerns regarding the operational requirements of the WGS-MDME test loop that were addressed prior to construction. The safety concerns in the operation of the moderate-pressure high-temperature test loop were related to:

1. Hydrogen embrittlement

    - **Problem:** Hydrogen deteriorates the structural properties of solid metals in a process known as hydrogen embrittlement. Hydrogen diffuses into the micro-structures of the metal, causing cracking and reducing the ductility of the metal.
    - **Solution:** Type 316 stainless steel has been shown to show sufficient resistance to hydrogen embrittlement. All surfaces in contact with hydrogen gases comprised

of 316L stainless steel.

2. Toxic and flammable gases

   - **Problem:** Carbon monoxide, hydrogen, and methane are colorless, odorless, and tasteless gases. CO is toxic to humans when inhaled in high concentrations while H_2 and CH_4 are extremely flammable. Additionally, hydrogen burns with a nearly colorless flame, so it is difficult to detect the presence of a hydrogen leak.
   - **Solution:** To prevent leaks, Swagelok tube fittings were used to provide a reliable leak-free seal. Thorough leak checks were performed prior to data collection. To detect leaks, a hazardous gas alarm (Industrial Test Equipment, Model HIC-822) was installed to detect CO, H_2, and CH_4 leaks.

3. Chemical reactors

   - **Problem:** The parallel-plate reactors are sealed with gaskets, which can fail.
   - **Solution:** A blast shield was manufactured as secondary containment to shield the vicinity in the case of a gasket failure.

4. High temperature, moderately pressurized fluids

The test cart was placed inside a walk-in fume hood. Gases are vented into the fume hood from the outlet of the reactor and the sampling slip stream to prevent the accumulation of harmful gases within the confined space of the laboratory. Entry into the test loop was prohibited and warning signs were placed on the doors of the fume during active testing. All data acquisition instrumentation and power to electrical components was turned on prior to operation of the loop or remotely toggled from the data acquisition station outside of the fume hood. Gloves were used at all times when handling the insulation.

5.11 Test procedures

Various test procedures were defined and executed to ensure safe and efficient operation of the test loop. The purpose of this chapter is to chronologically document the procedures taken while preparing and operating the test loop.

5.11.1 Test loop leak checks

Once the test loop had been built and properly set up, it needed to be leak checked. Leak checking, especially on the gas loop, is essential to ensure the process fluids stay within the loop and do not diffuse out into the environment for the reasons previously discussed in Section 5.10 above.

To leak check the gas loop, first, all bypass and isolation valves internal to the system were opened. A length of bypass tubing was installed in lieu of a reactor. The argon flow rate was set to 0.5 L/min and the system was charged to 30 bar, the maximum pressure it would see. Snoop, a liquid leak detector by Swagelok, was applied to the fittings, joints, and other potential leakage surfaces along the gas loop. If the Snoop creates bubbles, that means gas is escaping from the interior to the exterior of the loop. The bigger the bubbles formed, the bigger the leak. The majority of the connections on the loop are compression fittings, so to fix this, simply tightening down the connector stops the leak. Once the liquid leak check was complete, an argon gas detector was passed over each part of the system to detect any missed connections. If a leak is detected, then Snoop was reapplied to all the connectors in the near vicinity and the the connections are retightened.

For fixing leaks through non-compression fittings such as threaded NPT connections, the system needed to be depressurized and the items connected together were separated from each other. Teflon was applied to the male connector (recommended 5-6 wraps) in order to create a better mechanical seal between the threads. The Bronkhorst mass flow controllers and Blacoh accumulator featured NPT fittings, so the male NPT-to-Swagelok adapter had to be wrapped in Teflon to prevent leaks.

After leak checking, the gas flow was stopped and the system underwent a hold test. The loop held at 30 bar for 30 minutes. If the system did not lose more than 1 bar of pressure over the 30 minutes, it passed the hold test. If it did not pass the hold test, the leak checking process above was repeated until the system passed the hold test.

For the liquid loop, instead of using argon and a back pressure regulator, an Omega pressure gauge was attached to the oil drain to measure the system pressure. The oil loop was charged to 15 bar of pressure using house nitrogen. The same leak checking process was applied to the liquid loop. Instead of using an argon detector, a nitrogen leak detector was used. The liquid loop needed to pass the same hold test to be deemed leak-free.

5.11.2 First reactor leak check

Once both systems of the test loop had been leak checked, the reactor was carefully installed into the system with the LUNA fiber integrated into the reactor. Both systems were pressure to 10 bar using argon and nitrogen in the reactant and coolant loop, respectively. Once pressurized, Snoop was applied to the exterior of the reactor at the plates. Large leaks were detected through the plates of the reactor during the first leak check of the reactor, which can be seen in Figure 5.34.

To remedy this, the system were purged to atmospheric pressure and the Therminol was drained from the system. The reactor was removed from the loop and the bolts were tightened.

5.11.3 Therminol charge

After leaking checking the test loop and the reactor, the Therminol loop could be charged. This subsection describes the process of charging and pressuring the liquid loop with Therminol 72.

The system starts with the vacuum valve open and the Therminol reservoir valve closed. First, the liquid loop was pulled to house vacuum pressure (needs confirmation) through

Figure 5.34: Leak checking reactor with Snoop.

the vacuum port. Once the system was at vacuum, the vacuum port valve was shut and the Therminol reservoir was opened. The Therminol liquid flows from the reservoir into the void spaces of the oil loop due to the pressure differential caused by the vacuum. After 5 minutes and once the reservoir had stopped visibly decreasing in level, the reservoir valve was shut to isolate the coolant loop before charging.

Once charged with Therminol at atmospheric pressure, the liquid loop was pressurized using the Blacoh accumulator. House nitrogen was applied to the air side of the bladder via Schrader port to 10 bar of pressure. Because liquid is incompressible, the Therminol pressurizes to 10 bar. The pressure of the stationary liquid was confirmed to be 10 bar using the Rosemount absolute pressure transducer.

5.11.4 First thermal test

Before reactive testing could be conducted, thermal validation of the system's capability in providing the process temperatures at realistic testing flow rates was required. Previous iterations of thermal testing were performed using the MDME reactor and modifications were made to improve the thermal capabilities of the loop. These challenges that arose are described later in Section 6.3 of the last chapter. This subsection describes the process of the steam generation subsystem and thermal testing of the main system and reactor.

First, to validate the test loop's ability to generate steam, the steam generation system was isolated from the rest of the system by utilizing the installed isolation and vent valves. The heat trace pre-heater and the packed bed heater were turned on and temperature controlled to 95°C and 150°C, respectively. Once at temperature, the HPLC pump was turned on and fed deionized water from a beaker. The pump was set to an initial rate of (needs confirmation) through the steam generator. After a few minutes, steam was visually confirmed to be exiting through the vent valve and into the fume hood. The pump flow rate was adjusted to provide a constant flow of steam generation. Once complete, the steam generation subsystem was turned off and left isolated from the rest of the system during thermal pretesting of the other sections of the test loop.

To begin thermal testing of the main system and reactor, the Therminol loop was confirmed to be at 10 bar of pressure before turning the pump on. The oil bypass valves were adjusted to provide 12.5 mL/min of coolant flow through the reactor. Next, the gas system was pressurized to 10 bar using argon at a rate of 0.5 L/min. Excluding the steam generation subsystem, the temperature controllers and heating elements for both loops were turned on. The gas pre-heater and gas cartridge heater was controlled to 150°C and 300°C, respectively. The heat trace between the cartridge heater and the inlet of the reactor was not temperature controlled because the full power of the short 2 ft. heat trace was required to maintain the gas temperature at 300°C into the inlet manifold of the reactor.

The LUNA subsystem was turned on and the fiber optic sensor inserted in the reactor reported the temperature profile of the reactor to the ODiSI-B software. The four

thermocouples inserted into the manifold of the reactor reported temperatures of (needs confirmation) as shown in the image of the LabView VI below.

The fiber optic measurements and thermocouple measurements saw good agreement, which confirmed the test loop's ability to bring the reacting gases, coolant fluid, and reactor to the desired process temperatures. The back pressure was still being regulated to 10 bar without evidence of leaking, so it was confirmed that preliminary reactive studies could proceed. The thermal testing concluded by shutting off the heating elements and pump. The liquid and gas loops were depressurized to atmospheric pressure and the system was left overnight to come to room temperature.

5.11.5 Second reactor leak check

Before the reactive testing could begin, the reactor was leak checked at room temperature once more using the same methodology described in Subsection 5.11.2. The Therminol was pressurized to 10 bar and the argon gas was flowed through the loop at 0.5 L/min. Using Snoop, leaks were detected through the plates of the reactor. The system was shut down and depressurized before the Therminol was drained from the liquid loop. The reactor was removed from the loop and the bolts were tightened until they could no longer be tightened. The reactor was reinstalled onto the loop and the Therminol loop was charged using the methodology described in Subsection 5.11.3. Once charged, the gas and liquid loops were brought up to pressure and leak checked with Snoop. At room temperature, the reactor exhibited leaking from the gas side.

5.11.6 Second thermal test

To investigate the sealing behavior of the reactor at higher temperatures, the test loop was brought up to process temperatures for a second thermal test. Using the LUNA fiber, the temperature profile was captured once the coolant fluid temperature had reached 300°C. The temperature profile of the reactor is presented later in Section 6.1.4 of the next chapter.

At 300°C, the gas side of the reactor was losing pressure with a 0.5 L/min flow rate for argon, which is indicative of even worse leaking than what was observed at room temperature. Smoke was also visible inside the fume hood and the source of the vaporization could not be pinpointed. At this point in the testing process, the reactor could not pass a hold test either at room temperature or at process conditions. It was deemed unsafe to perform reactive testing with the leaking issue, and time constraints prevented completion of the chemical portion of the experimental investigation. The discussion of this is presented later in Section 6.2.3.

5.12 Conclusion

To realize the modeled potential of the sub-scale water-gas shift microreactor prototype, an experimental setup was designed and constructed in collaboration with Dr. Goran Jovanavic's group to enable reacting flow experiments of both the WGS and MDME reactors.

The WGS experimental setup was housed on a rolling test cart placed inside of a fume hood. It consists of two loops: a liquid coolant loop and a gaseous reactant loop. The coolant fluid loop is a closed loop that utilizes Therminol 72 as its coolant fluid. The reactor simulation was tuned to determine the new required liquid flow rate. For the sub-scale prototype, it was determined that a flow rate of 17.5 mL/min was needed to achieve the same temperature profile and conversion as previously modeled using air. The reactant loop is an open loop whose process conditions are informed by the reactant effluent of the STARS steam methane reformer. Once the process conditions for both sets of experiments were determined and the design solidified, the components for the loop were specified and procured, and the test loop was constructed.

On the liquid side, the newly determined heat transfer liquid flow rate was used to specify and procure a pump head and accompanying driveline (motor, gearbox, and VFD) to enable variable Therminol flow control through the reactor. After experimental tuning, a bypass line was implemented to enable flow control while simplifying the driveline and test loop operation. An accumulator was procured to provide pressure control of the

liquid loop. Heating elements such as cartridge heaters and heat trace were procured to heat the Therminol to moderate temperatures. An existing Coriolis mass flow meter and Rosemount absolute pressure transducer were integrated into the loop to measure mass flow and pressure, respectively.

For the reactant loop, four mass flow controllers were specified and procured to provide the required process flow rates and pressures. A steam generation system consisting of heat exchangers was integrated into the loop to provide the steam needed for the WGSR. The gases flow through the reactor and into a vented fume hood to atmosphere. An effluent slipstream was diverted into a mass spectrometer to measure the concentration of gases and characterize CO conversion. To measure the temperature profile of the reactor, a fiber optic temperature system was integrated into the reactor. The NI-DAQ system was used to collect temperature data from thermocouples integrated into both the coolant and reactant streams.

Once the test loop was constructed, it went through a number of iterations and improvements until the final design of the loop was achieved. Leaks were removed from the loop through a set of leak checks. Once leak-free, a thermal pre-test confirmed the test loop's capability of heating the fluids to the required conditions. However, the chemical feasibility of a process intensified microscale water-gas shift reactor with integrated platinum-ceria catalyst was not experimentally characterized because it could not be done in a safe manner.

Chapter 6: Results, challenges, and discussion

This chapter presents the results, challenges, and discussion of the studies performed during the investigation of the feasibility of using a plate architecture microreactor design with integrated catalyst to enable the process-intensified water-gas shift reaction.

6.1 Results

The first section of this chapter showcases the results obtained during catalyst coating characterizations, characterization of surface roughness enhancement on coupons, and thermal testing.

6.1.1 Catalyst composition results

The composition of four $Pt/Ce/Al_2O_3$ catalyst samples (Sample 1 through Sample 4) were quantified using SEM/EDS analysis. The first preliminary recipe was coated onto a coupon with no surface area enhancement. The second improved recipe was coated onto a coupon with enhanced surface roughness. The final catalyst recipe was coated onto the enhanced reactant channel surface on the reactant channel and then the non-enhanced reaction channel surface on the underside of a coolant plate.

Sample 1 was coated with an initial iteration of the catalyst recipe. It was the first recipe that adhered to the coupon without flaking off. This sample is depicted in Figure 6.1 below. The catalyst coating starts off white but eventually turns black in color after calcination of the impregnated platinum solution. This particular sample showed excellent adhesion to the coupon, as evidenced by the lack of cracks and flakes. This sample's adhesion properties were also tested and the results are described in Subsection 6.1.3.

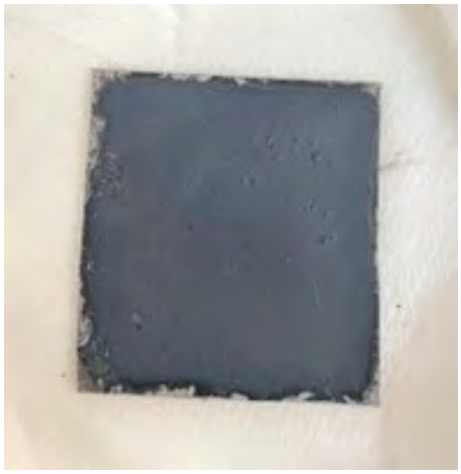

Figure 6.1: Sample 1, a coupon coated with an initial $Pt/Ce/Al_2O_3$ catalyst recipe.

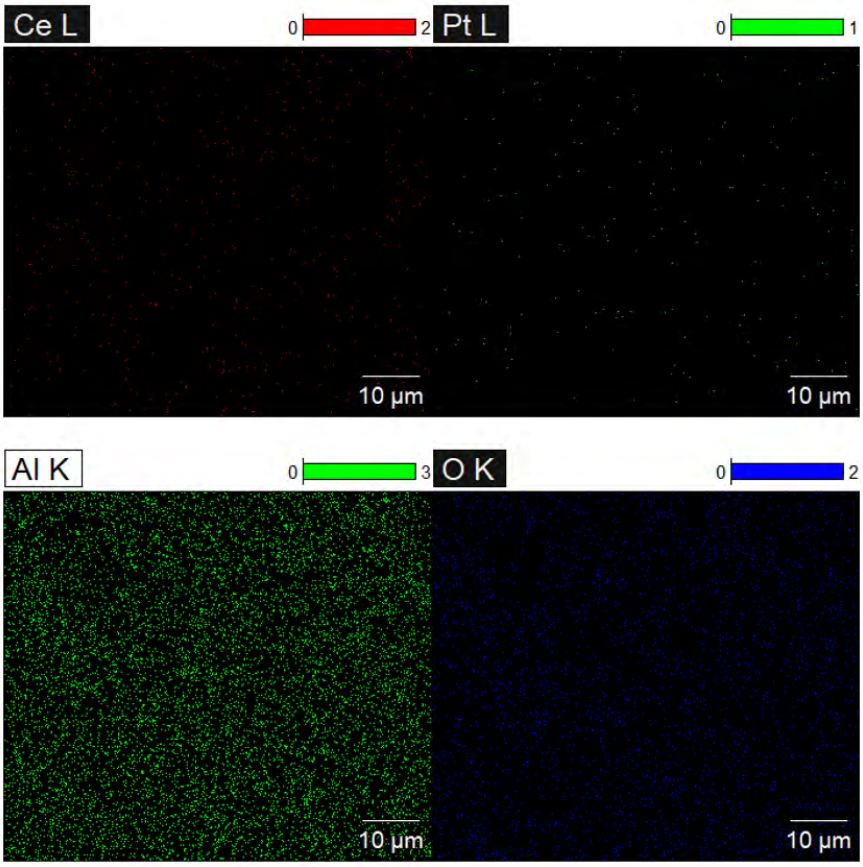

Figure 6.2: EDS spectral map of Sample 1.1 at 2000x magnification.

Two SEM/EDS analyses were performed on Sample 1. The first EDS spectrum was taken at 2000x magnification to investigate the catalyst composition at the microscale. The dispersion of the elements in the imaged region for this first sample are depicted in spectral map in Figure 6.2 above. The spectral map displayed 2644 full scale counts, which is low for this type of analysis. The number of x-ray counts needed to be increased for subsequent images to increase the resolution and accuracy of the elemental analysis. Even with a low count, it can still be seen that the platinum and ceria are well-dispersed in the sample region. The corresponding EDS spectrum is shown in Figure 6.3.

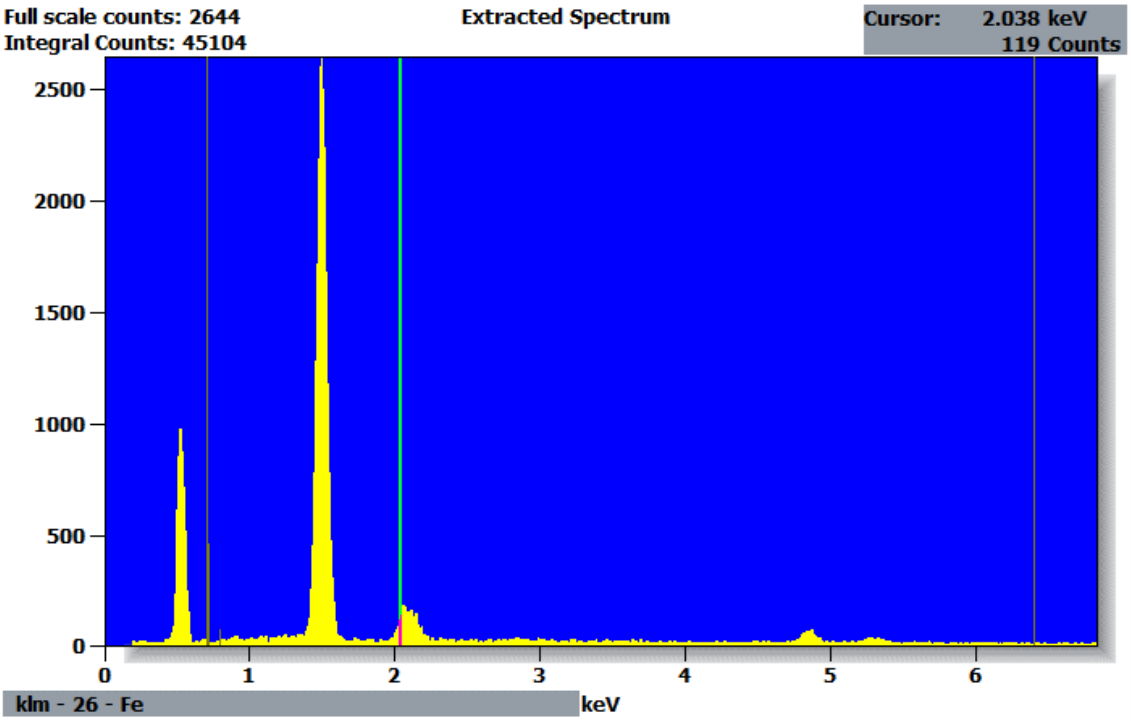

Figure 6.3: EDS elemental spectrum of Sample 1.1. From left to right, energy peaks shown in this spectrum correspond to the oxygen, aluminum, platinum, and ceria excitation keV values, respectively.

The higher the peak, the greater the number of counts for that element, but this does not necessarily translate to the same catalyst composition in terms of a weight percentage. The net counts, atom percentage, and weight percentage of each element present in the EDS analysis is presented in Table 6.1 below. The $Pt/Ce/Al_2O_3$ catalyst composition of 8

wt% Pt, 6.68 wt% Ce, 45.55 wt% Al, 39.73% O for this microscale image of Sample 1 was a bit high when compared to the values reported by He *et al.*

Table 6.1: EDS elemental composition of Sample 1.1.

Element	Net counts	Weight %	Atom %
O	5527	39.73	58.28
Al	22000	45.55	39.63
Ce	1157	6.68	1.12
Pt	268	8.04	0.97

A second EDS spectrum (Sample 1.2) was taken at a different location in the same sample. The elemental spectrum graph for Sample 1.2 is displayed in Figure 6.4. This spectrum corresponds to the net counts, atom percentage, and weight percentage of each element as presented in Table 6.2 below. The increased counts compared to the first EDS analysis provided finer resolution of the location of each element, but the counts still needed to be increased for a more detailed spectral map and more accurate elemental analysis.

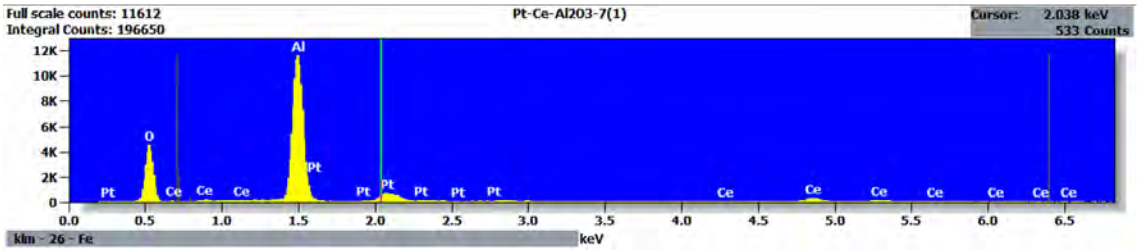

Figure 6.4: EDS elemental spectrum of Sample 1.2.

Table 6.2: EDS elemental composition of Sample 1.2.

Element	Net counts	Weight %	Atom %
O	24686	39.54	58.96
Al	94690	43.73	38.66
Ce	5473	6.96	1.19
Pt	1483	9.77	1.19

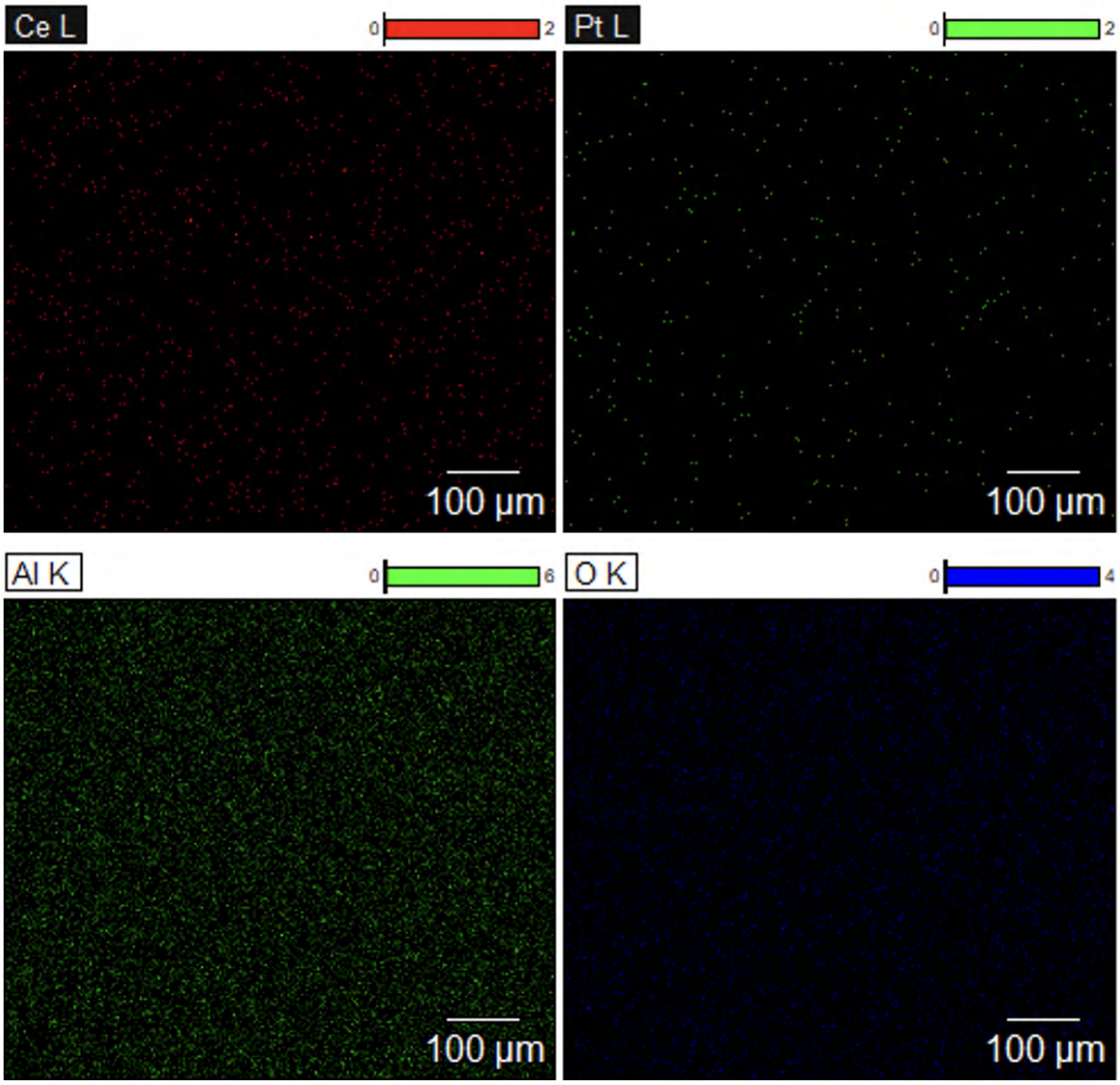

Figure 6.5: EDS spectral map of Sample 1.2 at 200x magnification.

For this second spectrum, the number of counts was increased from 2644 to 11,612 and the magnification was decreased to 200x. The spectral map of the EDS data in Figure 6.5 above shows that, at the macro scale, the platinum particles were still found to be well-dispersed throughout the aluminum oxide support.

The EDS spectrum of Sample 2 was taken at 193x magnification. For this sample, the number of counts was significantly increased such that the spectral map displays fine resolution of the ridges and edges of the catalyst piece being analyzed. For this spectral map, a total of 56,588 full scale counts were collected to provide the fine resolution of the image shown in Figure 6.6. The spectral map of this sample is shown below in Figure 6.7. The elemental composition of Sample 2 is presented in Table 6.3 and the corresponding EDS spectrum is presented in Figure 6.8.

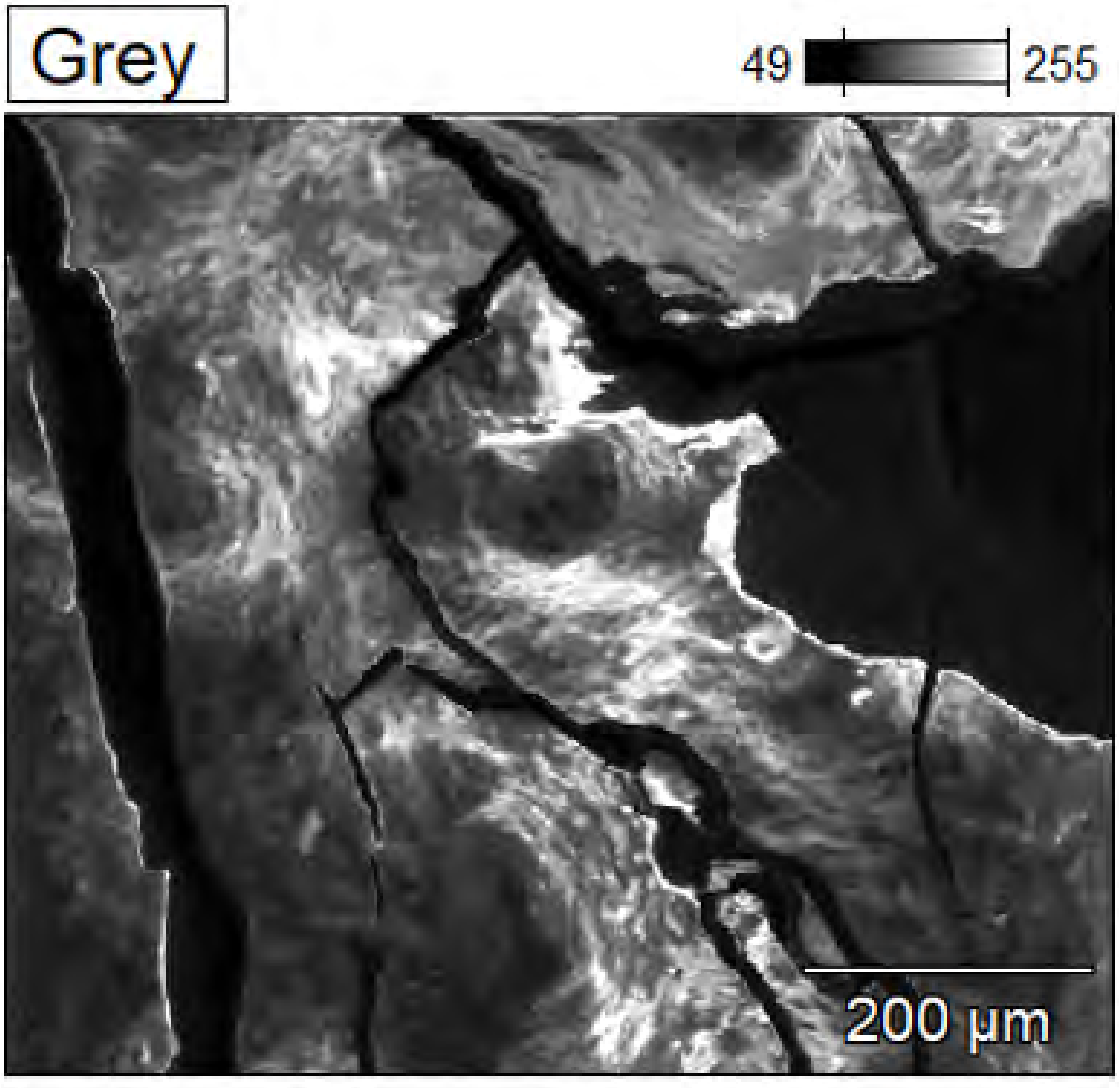

Figure 6.6: SEM image of Sample 2 at 193x magnification.

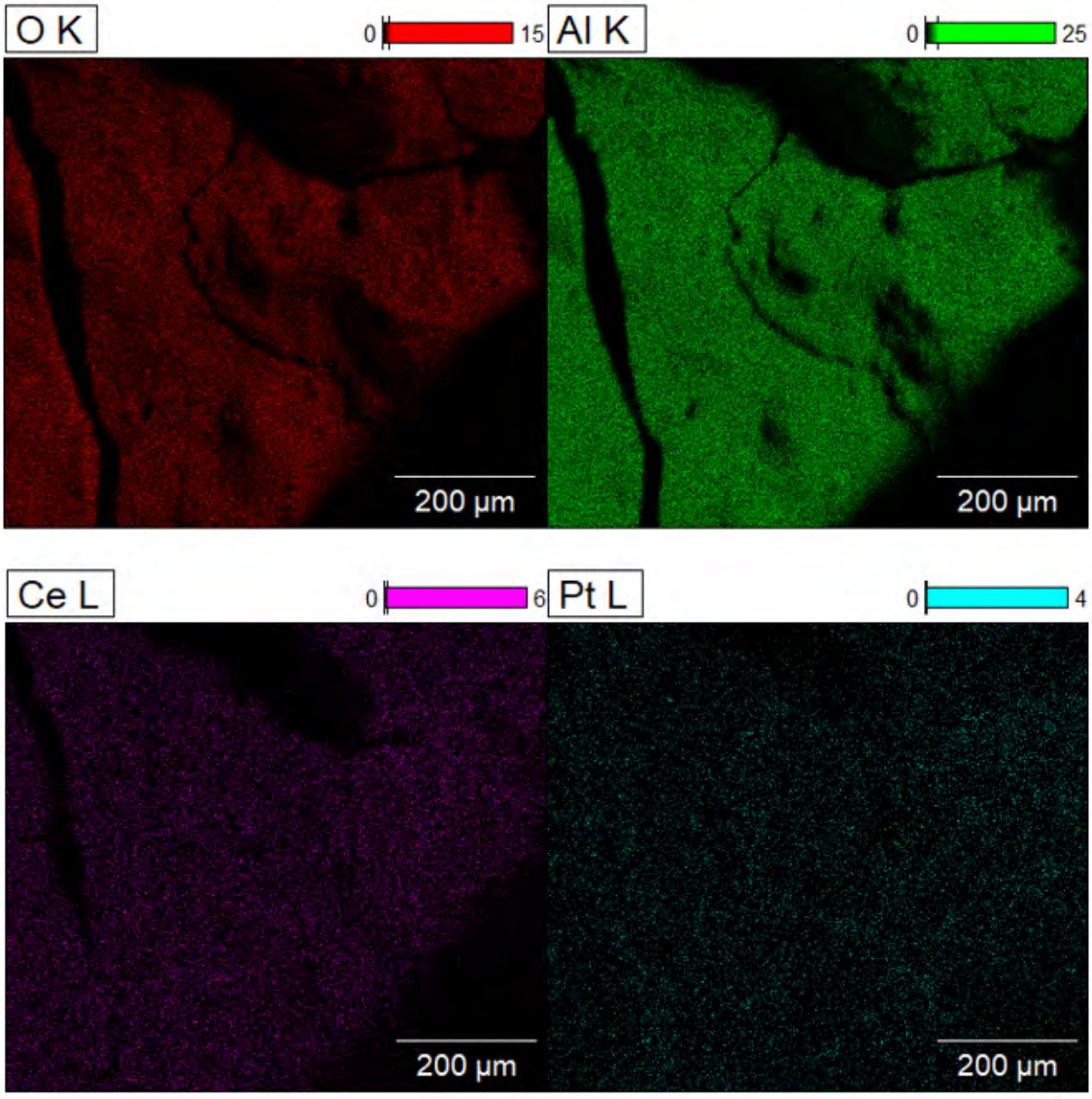

Figure 6.7: EDS spectral map of Sample 2 at 193x magnification.

Table 6.3: EDS elemental composition of Sample 2.

Element	Net counts	Weight %	Atom %
O	268559	29.58	49.42
Al	1512451	47.14	46.70
Ce	160154	12.96	2.47
Pt	24854	10.32	1.41

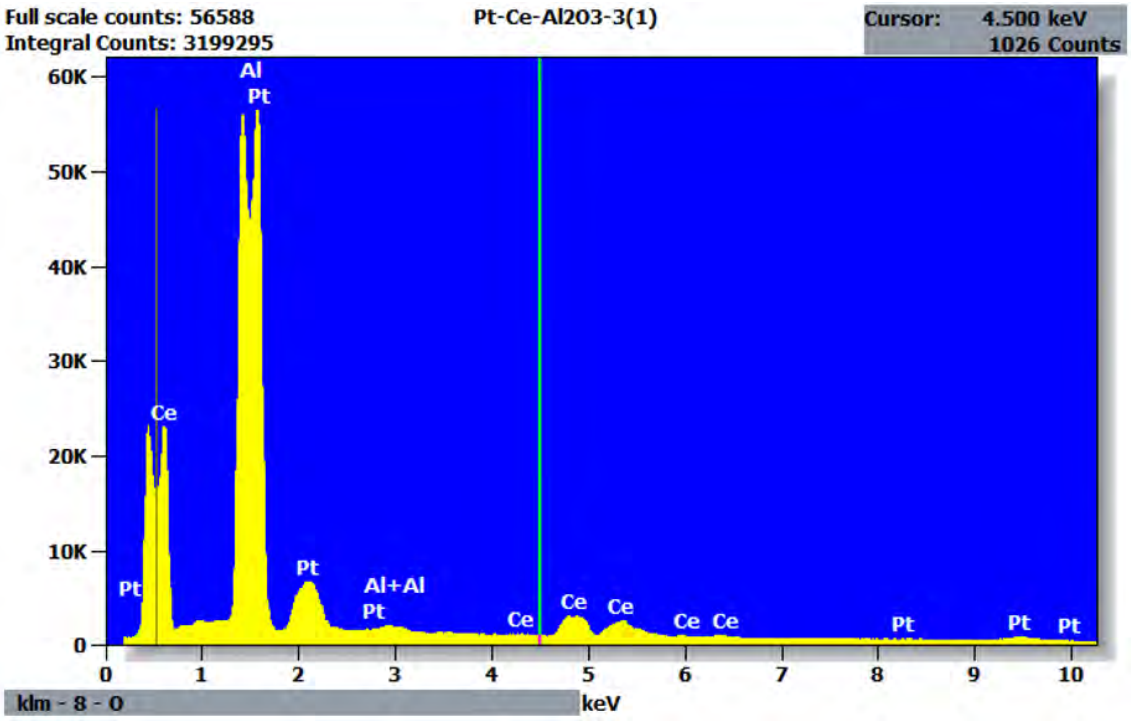

Figure 6.8: EDS elemental spectrum of Sample 2.

It can be seen in Figure 6.7 that the areas with a high density of counts is where the catalyst coating is, and the area with less counts is where the stainless steel substrate material is visible. The platinum spectral map does not follow the same trend, as it can be seen uniformly covering the whole space. This is because, before platinum impregnation, this sample had cracked and a piece of the catalyst had fallen off of the sample, exposing the substrate material underneath. The platinum, however, was uniformly impregnated in the form of a solution, so it uniformly coated the exposed surfaces. The elemental composition analysis shows a platinum loading of 10.32wt%, but this may not be the true loading of the platinum on the catalyst, since the platinum was also coated onto the substrate.

Sample 3 and Sample 4 were reactor plates that were coated with the final coating of the catalyst. Two image samples were collected per plate. Sample 3 plate was a reactant plate with the enhanced reaction channel surface coated with catalyst. The second plate was a coolant plate with the non-enhanced surface coated with catalyst. When sealed together, these two plates form a single reaction channel of the reactor.

The SEM image of Sample 3.1 was captured at 295x magnification and is presented in Figure 6.9. The coating was scraped off the channel of the reactant plate due to size constraints of the microscope's vacuum chamber, which is why the SEM image depicts a fractured catalyst surface. However, given the uniform coating procedure and even distribution of platinum and ceria as shown by previous EDS spectral maps, the composition can still be accurately determined using this sample. The corresponding EDS elemental spectrum is shown in Figure 6.10 while the weight and atomic percentage of each element present is shown in Table 6.4. It can be seen how the atomic percentage of the platinum and ceria are very low compared to the alumina oxide, but due to the disproportionately high mass of these metal molecules, the weight percentage of the platinum and ceria is high.

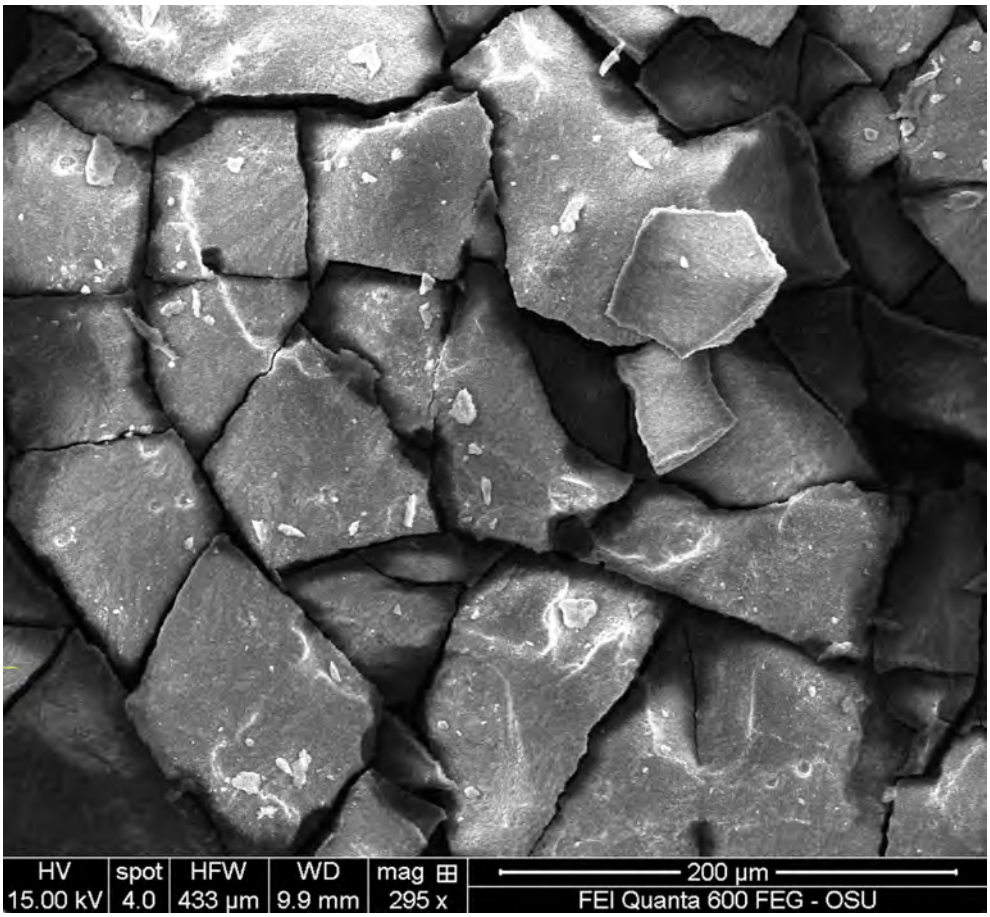

Figure 6.9: SEM image of Sample 3.1 at 295x magnification.

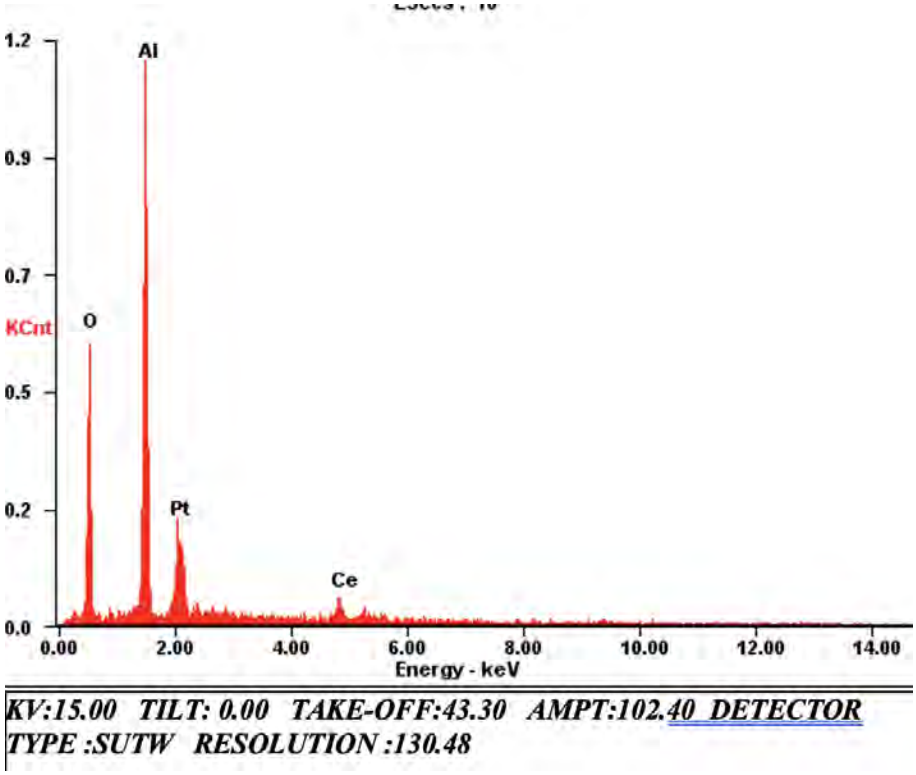

Figure 6.10: EDS elemental spectrum of Sample 3.1.

Table 6.4: EDS elemental composition of Sample 3.1.

Element	Weight %	Atom %
O	33.65	60.71
Al	31.17	33.35
Ce	12.69	2.61
Pt	22.49	3.33

The second SEM image of Sample 3 was captured at 497x magnification in a different area of the sample (Sample 3.2). The SEM image is presented in Figure 6.11. Similar to the first image, the second SEM image depicts a fractured catalyst surface, which has the possibility of interfering with the platinum loading characterization. The corresponding EDS elemental spectrum is shown in Figure 6.12 and the weight and atomic percentage of each element present is shown in Table 6.5. The elemental analysis of Sample 3.2 shows a platinum loading of 23.56%, which is about the same platinum loading characterized in the analysis of Sample 3.1.

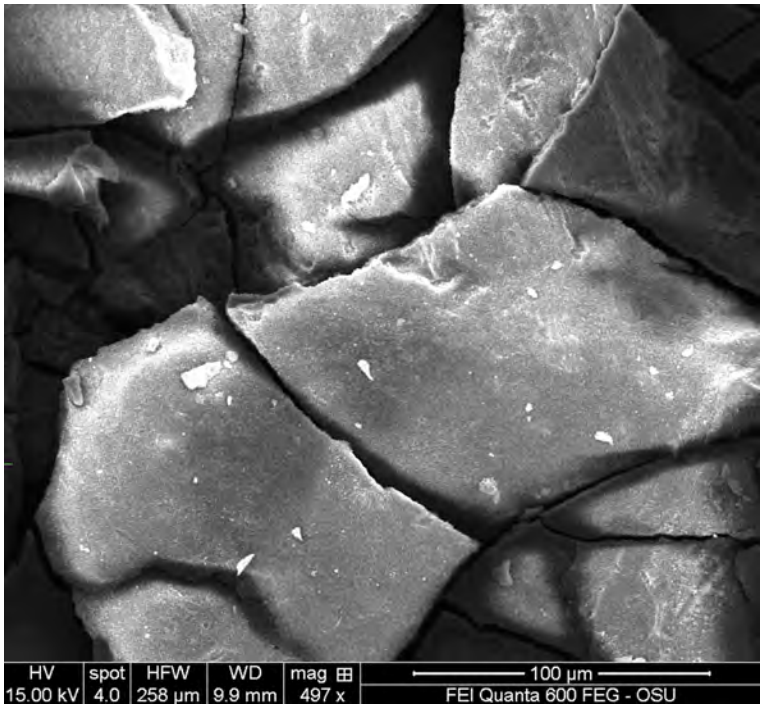

Figure 6.11: SEM image of Sample 3.2 at 497x magnification.

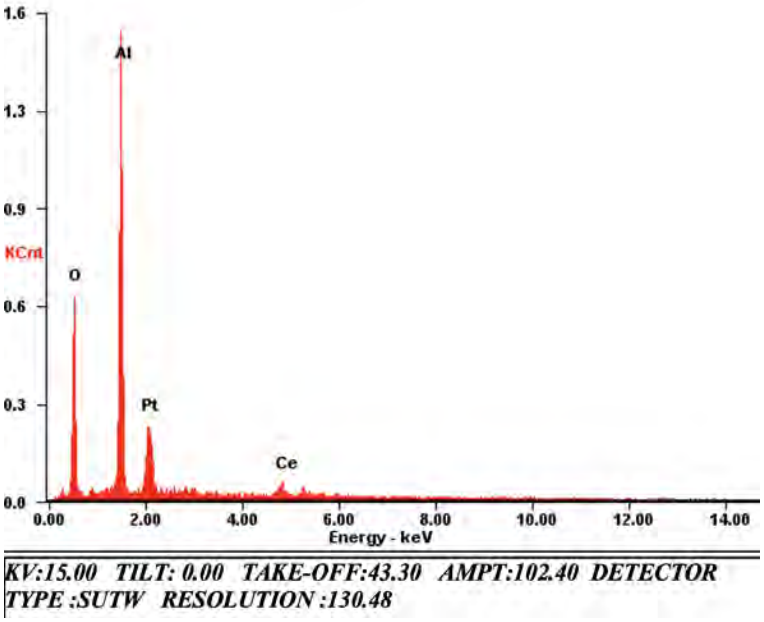

Figure 6.12: EDS elemental spectrum of Sample 3.2.

Table 6.5: EDS elemental composition of Sample 3.2.

Element	Weight %	Atom %
O	32.44	59.24
Al	32.09	34.75
Ce	11.91	2.48
Pt	23.56	3.53

The analysis of the first area of Sample 4 (Sample 4.1) was taken at 213x magnification. The SEM image of the coolant plate coating is shown in Figure 6.13. The image depicts a large area of unbroken catalyst surface, which was chosen to provide a more accurate look into the true composition of the catalyst. The first EDS elemental composition is shown in Table 6.6 and the corresponding elemental spectrum for Sample 4.1 is depicted in Figure 6.14 below.

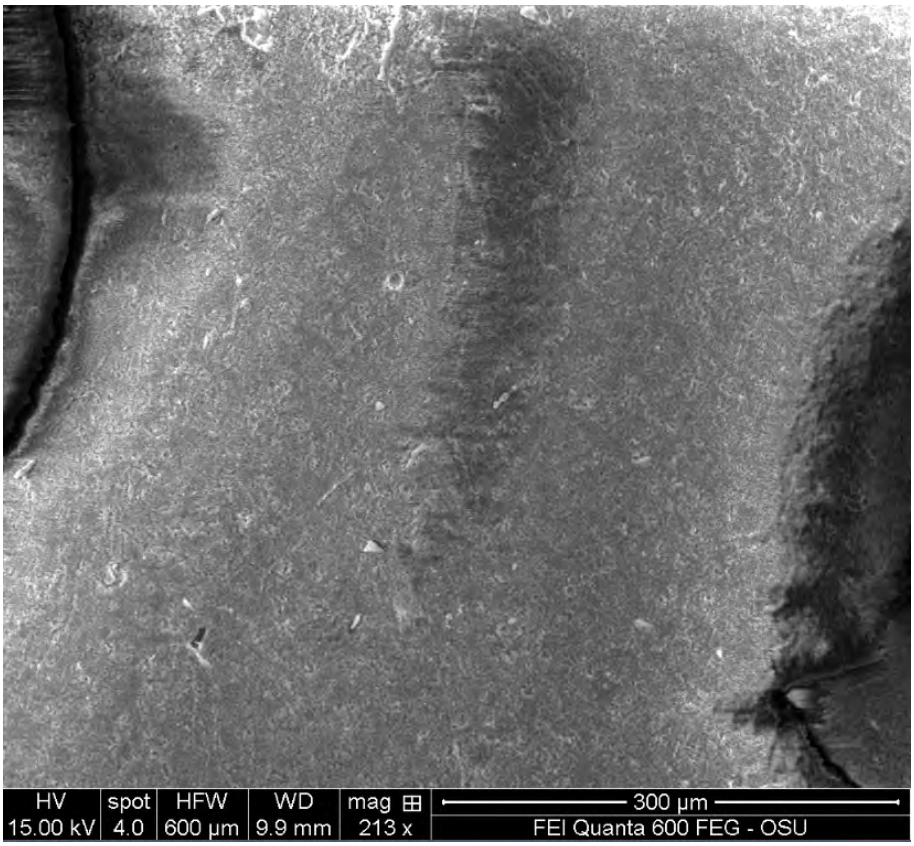

Figure 6.13: SEM image of Sample 4.1.

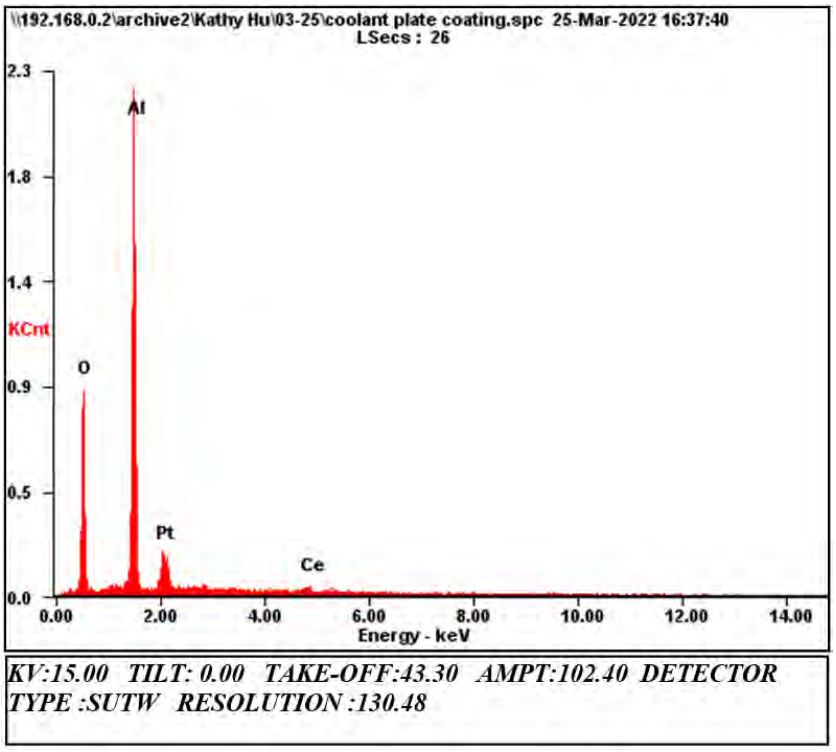

Figure 6.14: EDS elemental spectrum of Sample 4.1.

Table 6.6: EDS elemental composition of Sample 4.1.

Element	Weight %	Atom %
O	38.32	60.69
Al	38.22	35.90
Ce	7.11	1.29
Pt	16.35	2.12

A second set of data was taken for a different area of the coolant plate sample (Sample 4.2). The EDS elemental spectrum for Sample 4.2 is depicted in Figure 6.15 and the corresponding elemental composition is shown in Table 6.7.

Table 6.7: EDS elemental composition of Sample 4.2.

Element	Weight %	Atom %
O	38.41	60.63
Al	38.42	35.95
Ce	8.40	1.51
Pt	14.77	1.91

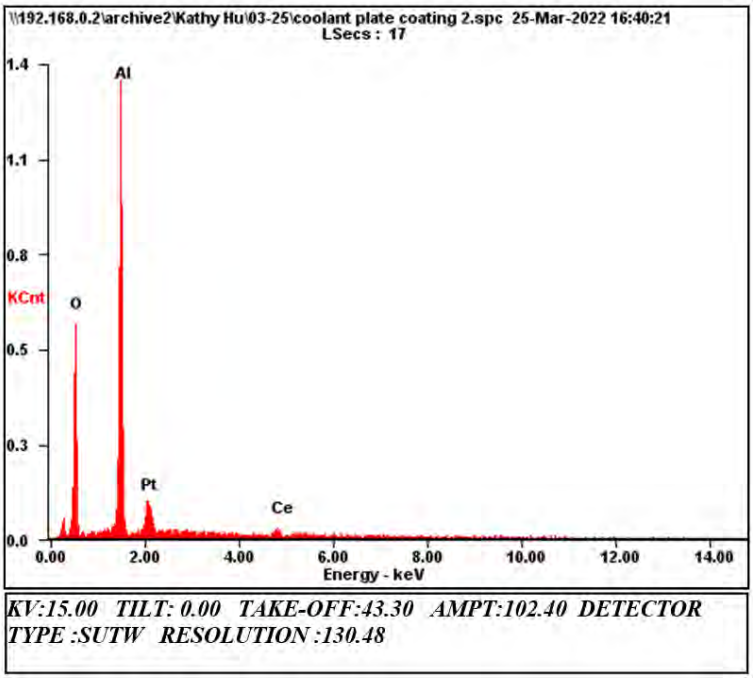

Figure 6.15: EDS elemental spectrum of Sample 4.2.

Overall, the coolant plate coating shows a lower platinum and ceria loading than the reactant plate coating. On average, the composition of the catalyst coated on the coolant plate was found to be 15.56 wt% Pt, 7.75 wt% Ce, 38.32 wt% Al, 38.37 wt% O while the reactant plate coating was found to be 23.03 wt% Pt, 12.3 wt% Ce, 31.63 wt% Al, 33.05 wt% O.

6.1.2 Catalyst adhesion on coupons

Section 4.3.3 previously discussed the process and importance of investigating the surface roughness of the substrate material, as this has been reported in literature to have a big impact on washcoat adhesion of the platinum-ceria catalyst.

Surface roughness characterization using the Mitutoyo SJ-210 before and after sand-blasting of the coupons revealed revealed that, on average, sandblasting using 60-120 mesh size glass beads increases the surface roughness of 316 stainless steel from 0.221 μm to 0.483

μm, which corresponds to a 2.19x enhancement factor in wt% of adhesion.

After the surface roughness of the coupons was characterized, all coupons were coated with the final catalyst recipe. When dried, the catalyst adhered to four of the five enhanced coupons but only two of the five non-enhanced coupons. The coupons that exhibited adhesion were then dropped using the drop test procedure described in Section 4.3.2 and weighed. The results of the drop tests are shown in Table 6.8 below.

Table 6.8: Weight loss comparison between coupons with and without surface area enhancement.

Batch description	No. coupons	Average adhesion wt%
Enhanced, all	5	67.1
Non-enhanced, all	5	19.7
Enhanced, adhered	4	83.9
Non-enhanced, adhered	3	32.8

Of the coupons that showed adhered catalyst, the enhanced coupons showed an average of 83.9wt% adhesion while the non-enhanced coupons showed an average of 32.8wt% adhesion. This means that, for this application, sandblasting 316 stainless steel coupons with 60-120 mesh size glass beads improved wt% adhesion by 2.56 times.

6.1.3 Catalyst adhesion on plates

Ultrasonic and drop tests were performed both for a plate with catalyst coated on the enhanced surface area of the reaction channel and a plate with catalyst coated on the non-enhanced surface area of the reaction channel. The results of the tests for both surfaces are shown in Table 6.9 below, where:

1. w_1 is the starting catalyst weight,
2. w_2 is the weight after an ultrasonic test, and
3. w_3 is the weight after a drop test.

The enhanced channel surface exhibited no weight loss after ultrasonic testing and 2% weight loss to drop testing, showing 98wt% adhesion. For the non-enhanced surface, the

Table 6.9: Weight percent adhesion of the platinum-ceria catalyst on the enhanced (E) and non-enhanced (NE) reactant channel surfaces.

Plate	w_1 (g)	w_2 (g)	w_3 (g)	Adhesion (wt%)
Enhanced	0.42	0.42	0.41	98
Non-enhanced	0.27	0.26	0.15	56

overall adhesion was observed to be worse at 56wt%, with 4wt% lost during ultrasonic testing and 52wt% lost during the drop test. The surface area enhancement from the sinker EDM manufacturing process nearly doubled the catalyst's ability to adhere to the reaction channels.

6.1.4 Reactor thermal test results

The temperature profile of the reactor as measured by the LUNA fiber during the second round of thermal testing is presented in Figure 6.16 below. A soldering iron was used to determine the distance along the length of the wire where the fiber exits the reactor, which is depicted in orange on the graph. This was also done for the inlet, but when the soldering iron was touched to the end of the fiber, the measurement did not appear on the graph. The spatial data is taken at a 0.6 mm spatial resolution but presented with a 20 mm resolution for ease of viewing.

The temperature profile as reported by the fiber instrumentation plateaus around 300°C for most of the reactor length before dipping to 252°C as it exits the reactor. At the same time, another set of temperature measurements was collected using the thermocouples that were inserted into the fluid streams of the test loop. The fluid temperatures at the inlet and outlet manifolds as measured by the thermocouples are reported in Table 6.10 below.

Table 6.10: Thermocouple point measurements of the coolant and inert argon gas at the reactor inlet and outlet.

Fluid	Inlet temp. (°C)	Outlet temp. (°C)
Argon	295	277
Therminol	276	288

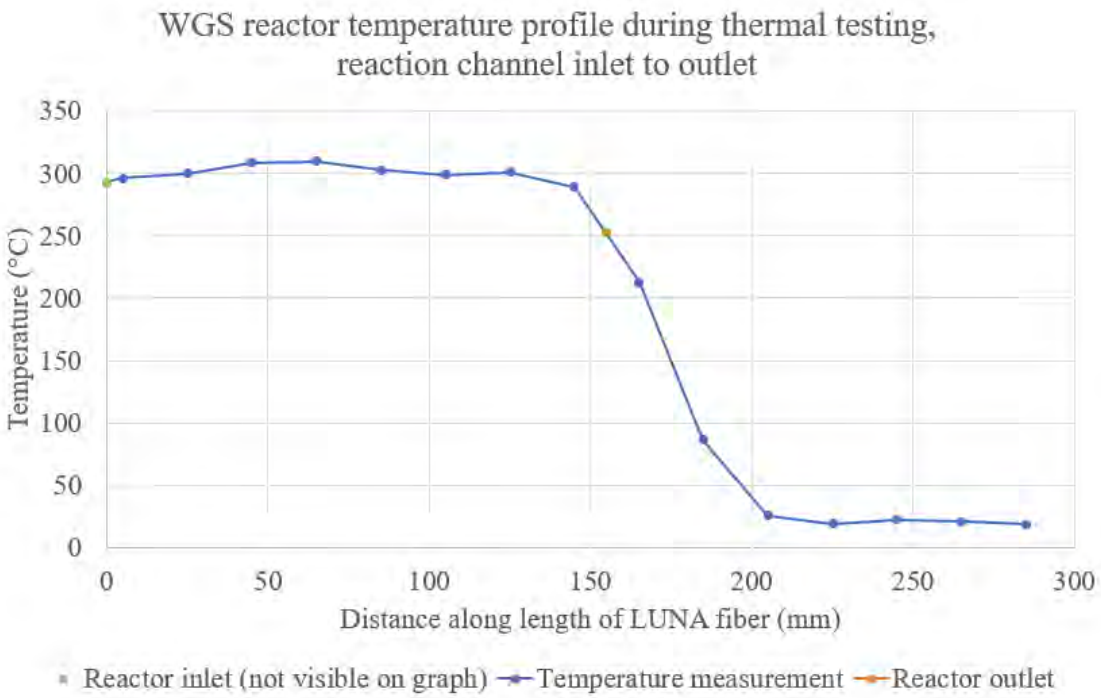

Figure 6.16: The thermal profile of the reactor achieved during the second thermal test.

The argon gas enters at 295°C, the hottest temperature reported by the thermocouples. It then cools down to a 277°C as it travels through the reactor, which is close to the Therminol inlet's measured temperature of 276°C. As the Therminol travels through the reactor, it picks up heat from the gas stream flowing in counterflow and warms to 288°C before it exits the reactor. The LUNA fiber measurement, which displays a plateau from the inlet to outlet, shows a fairly flat temperature profile. Discussion regarding this observation is found later in Section 6.2.3.

6.2 Discussion

This section delves into the various discussions regarding the catalyst characterization results, the impact of different factors on the adhesion and composition properties, and the implication of thermal testing results.

6.2.1 Catalyst adhesion discussion

Subsequent trials of the coating included a step in the catalyst preparation process to allow the slurry to settle and bubbles to dissipate from the bulk solution before it was coated onto the coupon, which helped improved adhesion. The surface area of the coupon was also enhanced using the sandblasting method described in Chapter 4.

When coating the coupons using the initial renditions of the alumina washcoat recipe and prior to the surface enhancement investigation, it was observed that any bubbles, cracks, or other imperfections induced in the catalyst before drying would cause the slurry washcoat to flake off of the coupon once dried in an all-or-nothing type effect. When drop tested, 100wt% loss of the catalyst was observed, meaning the suspension showed 0wt% adhesion to the substrate. Figure 6.17 below depicts a dried coating of the initial recipe before calcination.

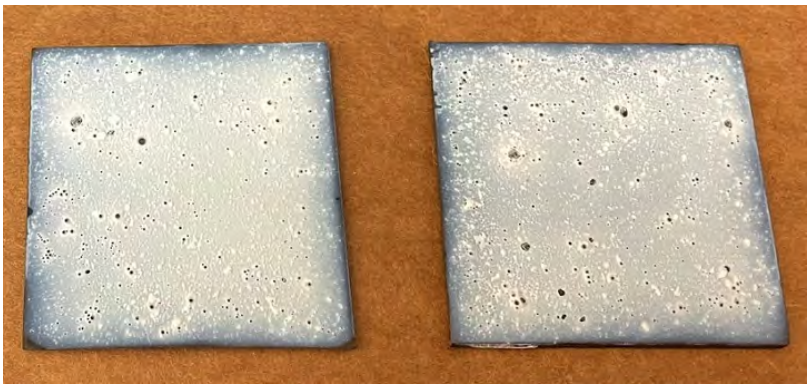

Figure 6.17: Dried alumina washcoat layer with bubbles on steel coupons before calcination.

The presence of air bubbles in the slurry caused by the agitation of the stir bar during the washcoat mixing process induced the bubbles shown in these two coupons. The washcoat adhered to the coupon after drying, but once the coupons were calcined in the furnace, the washcoat developed cracks and flaked off the surface of the coupon as depicted in Figure 6.18 below.

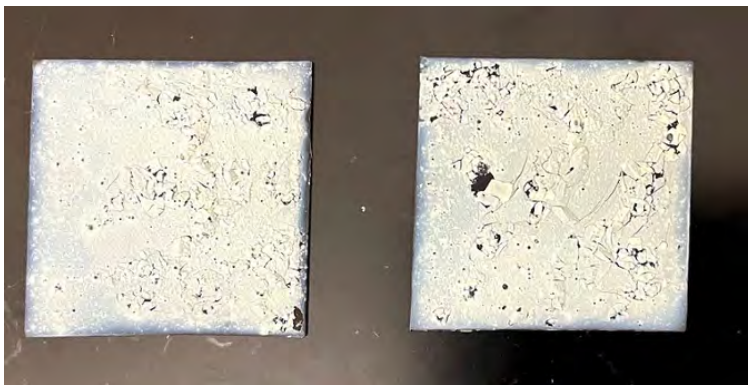

Figure 6.18: Bubbly alumina washcoat layer on steel coupons after calcination. The washcoat flaked completely off after being picked up.

After these initial trials, it was discovered that the PVA binder used to thicken and bind the alumina slurry together was not being heated to sufficient temperatures to melt the binder particles, which is why the characteristic cracking behavior was observed. The PVA particles were not completely incorporated into the slurry, which decreased the effectiveness of the polymer as an adhesive for the slurry itself. After increasing the mixture temperature and fully incorporating the PVA into the slurry, the cracking behavior was no longer observed and the all-or-nothing flaking behavior also disappeared. The temperature of the PVA, acetic acid, and alumina mixture is important in homogenizing the solution and ensuring proper adhesion.

Arguably the most important factor for adhesion, however, is increasing the surface roughness of the substrate material. Once the reactor was coated with catalyst, better catalyst adhesion was observed on the rough walls of the reactant plate channels than on the smooth underside of the coolant, which was expected due to the surface are enhancement of the reactant channel walls. The reactant channel walls were rougher and had enhanced

surface area compared to the underside of the coolant channel because of the sinker EDM die used to imprint the channel shape into the plate. The process of sinker EDM leaves small surface irregularities on the substrate, which is advantageous for enhancing adhesion. No manufacturing processes were applied to the underside of any of the plates, which meant that the adhesion behavior of the coating onto the underside of the coolant plates behaved more similarly to the non-enhanced coupon coating.

When applying catalyst to the second coupon, the coupon's surface area was enhanced via sandblasting, which was not applied to the plates. It was determined that creating and applying a mask for the bare underside of the coolant plates would be too technically challenging and risky given the resources on hand. Sandblasting is primarily used to remove impurities from a work piece and provide a matte finish, so it is only secondarily used as an imprecise method of surface area enhancement. It is easy to sandblast improperly, the substrate material could be unevenly removed and contribute to leaks in the reactor. Additionally, enhancing the surface area on the sealing surfaces would also increase the chance of leaks. Thus, in order to maintain smooth sealing surfaces, the plates were not sandblasted, even though increasing surface roughness was the best

Interestingly enough, in general, the catalyst coating on the plates showed much better adhesion than the coatings on the coupons. Much of this can be attributed to the fact that the plates were subject to the adhesion tests that the coupons were subject to. Though the plates did not undergo the same level of vibration as induced during the adhesion tests, the handling of the plates during reactor assembly/disassembly and installation/removal from the test loop still induced vibration that simulates real-world use and operation. After withstanding three full re-assemblies, the swapping of all gaskets, multiple installations/removals from the loop, and numerous flow tests through the coated channels, no catalyst was visually observed to have flaked off the enhanced reaction channel wall. With the non-enhanced surface, it was more difficult to discern since there was weight loss observed directly after the final coating had been calcined. It is hypothesized that differences in coating strategy, true surface area enhancement, and deviations in the recipe could also have affected the difference in adhesion.

The reactor plate that was dropped and characterized for catalyst adhesion was the plate that, visually, exhibited the smallest amount of coated surface area, and thus, the wt% adhesion reported in the results is as expected. From visual inspection, had any other plate been selected for characterization, it is likely the measured wt% adhesion would be higher than 45%.

6.2.2 Catalyst composition discussion

The composition of the catalyst coated onto the reactor plates shows a much higher catalyst loading observed on the coupons. The weight percent of platinum reported for Sample #3 in Table 6.4 is 22.49% while the ceria loading is 12.69%, which is very high when compared to the loadings characterized on Sample #1 and #2. This implies the platinum solution was impregnated into the alumina support significantly past incipient wetness during the synthesis process, so more robust methods of incipient wetness impregnation need to be implemented to guarantee the same platinum loading across all reactant channel surfaces.

The results obtained from the catalyst composition and adhesion characterizations highlighted the variety in catalyst loading and thickness using this method of coating. Tolley's modeling suggests that a thicker catalyst layer promotes better conversion. However, thicker slurry layers were shown to flake off when dried more readily than thinner layers, so care was taken to coat a thinner layer of the alumina washcoat onto the reactor plate walls. However, with a thinner washcoat layer, the same wt% loading of the ceria and platinum would equate to a lower physical amount of precious metal activation sites. Increasing the loading could potentially compensate for the reduction in catalyst thickness, and it is possible that loading the substrate with platinum past what is reported in other literature is advantageous for maximizing conversion. However, the effects of the density of the loading on the performance of the platinum-ceria catalyst were not reported in literature and such an investigation is not within scope of this research.

In Table 6.6 and Table 6.7, we can compared the platinum and ceria weight percentages between the two analyzed areas of the coolant plate coating. They are both very close,

which shows that the composition of the coating is homogeneous across the coolant plate.

6.2.3 Thermal testing discussion

Thermal testing with inert argon gas confirmed the expected heat transfer behavior of a plate architecture design, but since the process conditions were not completely reached for this test, the measured temperature profile and fluid temperature results are inconclusive. The test was stopped due to excessive leaking of the argon gas. If argon is capable of diffusing out through the plates of the reactor, then hydrogen, which has a smaller molecule than argon, would also diffuse out into the hot environment. Though hydrogen has an auto-ignition temperature of 500°C, the hot environment and high surface temperatures of the heating elements could cause combustion of the hydrogen, which is a massive safety concern. Additionally, the process gases lost to the atmosphere through the reactor would affect the mass spectrum reading and not give an accurate representation of the conversion rate.

The reactor initially passed a leak check, but the rate of leaking increased after the first thermal cycle. It is theorized that thermal expansion of the steel reactor material during the first thermal cycle caused irreversible gasket compression. The gaskets had deformed plastically past the sealing surface of the plates, rendering the gasket ineffective at sealing now that there was metal-to-metal contact of the plates. The design of the plates and gaskets should have factored in the thermal expansion of the steel plate material to prevent over-compression of the graphite gasket material.

6.3 Challenges

Many challenges were faced and addressed over the course of the studies reported in this document. This section seeks to highlight general challenges and encapsulate the technical obstacles related to the reactor, catalyst adhesion, and the test loop, as well as their impact on the results of this research.

6.3.1 General challenges

One major overarching obstacle that delayed the timeline of this research was the onset of the COVID-19 pandemic in March of 2020. The start of the pandemic limited access to physical resources at ATAMI and on campus as the world moved towards remote work to limit the spread of the virus, which was detrimental towards advancing progress of experimental work. However, with the installation of proper restrictions, limitations, and precautions, experimental work was allowed to continue at ATAMI and experimental research was allowed to progress, albeit at a slower pace due to stricter resource management.

The impact of the COVID-19 pandemic spanned far beyond local restrictions. The pandemic caused massive worldwide supply chain disruptions, which caused serious delays to the procurement of the reactor, which was outsourced to a local machine shop. The PO for the reactor was submitted to the vendor, Ram-Z Fab, in May 2021. Initially, the reactor was quoted to be complete in July 2021, but due to material shortages and supply chain delays, Ram-Z Fab was unable to deliver the reactor until December 2021, which is when the project was set to end. While an extension was received from the RAPID Manufacturing Institute for the research deliverables, research funding expired, so other means of funding had to be secured to continue the research.

As with most research, the budget for this investigation was limited. The expensive nature of the test loop equipment motivated collaboration with Freiberg from Dr. Jovanovic's group to create a shared test loop and make better use of the existing resources and expertise of both labs. The sharing of the created additional physical requirements and testing constraints.

6.3.2 Technical challenges

Many physical challenges related to the reactor and test loop were experienced due to the complicated technical nature of the experimental research. Ultimately, the technical challenges described below were the most difficult to overcome.

The adhesion of the catalyst was a great challenge to dial in. As previously discussed, initial trials of the catalyst did not adhere to coupons. At first, the slurry washcoat didn't adhere because the PVA wasn't fully incorporated into the alumina solution. After the mixture temperature was increased, this solved the slurry adhesion process, but then the impregnation process for the ceria and platinum caused catalyst weight loss because the catalyst coating was too thick. Only after multiple recipe iterations and surface area enhancements did the adhesion of the catalyst improve.

Recipe development for the LPKF laser cutter also proved to be an iterative task. The laser cutter has 10+ parameters that can be adjusted to provide the desired cutting/manufacturing action, but the variety and number of the parameters makes it challenging to dial in a precise recipe for both cutting gaskets and milling a channel into stainless steel. A few parameters were parametrically swept in an attempt to investigate the effects of the parameters on the cut. However, this proved to be an unfruitful effort. A final recipe that was capable of completely cutting through the graphite gasket was never established, which introduced manual post-processing of the gaskets. The cut was completed from the sheet by inserting thin stainless steel shim stock into the outline of the cut and pushing completely through the sheet. Sometimes, the removal of the gasket was imperfect, and the layers of graphite material was inconsistent throughout a single gasket. The imperfectly manufactured gaskets had to be used because there was little excess material. During milling of the fiber channel onto the instrumentation plate, the LPKF laser recipe that was used was not capable of removing enough material from the plate to enable the fiber to sit flush inside the channel. Thus, the Dremel was required to widen and deepen the channel, which effectively meant the laser engraved portion was simply used as a guide for the Dremel, which did the majority of the material removal. The LPKF also faults constantly at seemingly random times, which requires a full restart of the system that takes a half hour at minimum. These difficulties in utilizing the LPKF laser manufacturing equipment led to post-processing techniques in both applications, which increased labor and manufacturing time.

During construction of the test loop, an additively manufactured counterflow recuperator

designed by Kijoon Lee, a PhD candidate in Dr. Brian Paul's research group, was initially incorporated into the test loop to pre-heat the gas stream using the effluent coming out of the reactor. However, during an initial round of thermal testing, it was discovered that rapid heat loss to the surrounds caused the reactant effluent stream to cool dramatically before entering the recuperative HX, effectively acting as a cooler for the product stream instead of a heater. It was also challenging to seal the NPT connector to the recuperator, as multiple layers of Teflon needed to be wrapped around the fitting to stop the leaking from the HX.

Similarly, sealing the NPT connector to the accumulator was also a challenge. It was initially hypothesized that a scar on the 3/4" FNPT threads on the accumulator was causing leaks from the accumulator, so a 3/4" tap was used to clean the threads. This did not help because the the scar was not the issue. Simply applying more wraps of Teflon to the MNPT threads solved the leaking issues.

A Swagelok pressure regulator was modified to create a 1/4" FNPT hole in the regulator. A tap was used to create the threads, but the tap was turned using an adjustable crescent wrench instead of the correct tooling, causing the tap to break inside of the pressure regulator. The tap needed to be drilled out of the pressure regulator before the it could be used to support the gas chromatograph used for MDME testing.

While thermally testing the loop, the main heat exchanger was burned out as a result of excessive heat loss due to poor insulation. The temperature controller supplying power to the HX was measuring the temperature downstream of the heater, and this distance was enough for the gas to lose all its heat and cool back down to room temperature. The temperature controller, thinking the heater needs more power to reach the setpoint, supplies even more power to the heater and the cycle repeats itself until the heater overheats and burns out due to being powered to full in a short amount of time. An image of the burnt-out heater is depicted in Figure 6.19 below.

To prevent this from happening in the future, the thermocouple for the main HX's temperature controller was moved closer to the heater. The heater was rotated to minimize the unheated length of tubing between the heater and the thermocouple, as depicted in

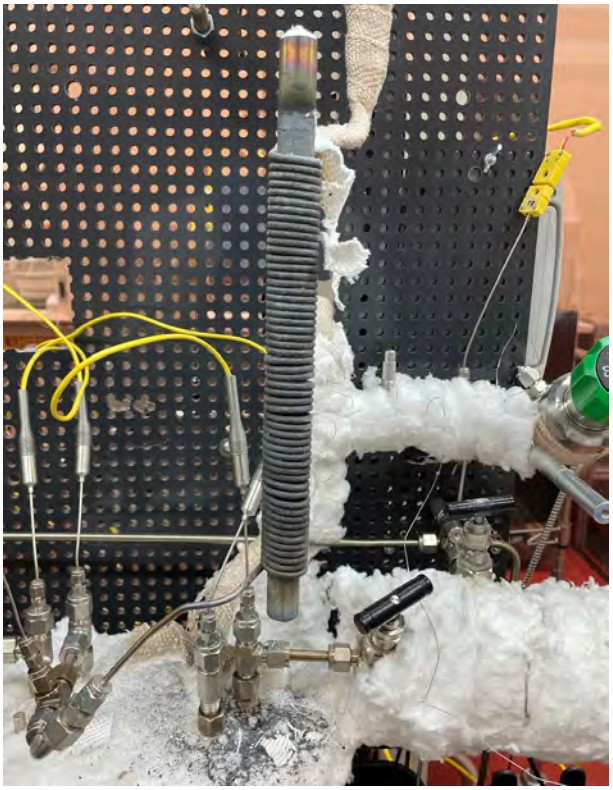

Figure 6.19: Main gas heater burnt out after initial thermal testing revealed excessive heat loss through the thin insulation layer.

Figure 6.20 below. Additionally, less turns of the tubing were wrapped around the heater to reduce contact resistance between the tubing and the heater surfaces. A high-temperature heat transfer compound was coated and hardened onto the heater to enable even heating of the tube from all directions. Finally, the Cerablanket insulation layer was thickened to reduce the heat loss. These fixes enabled much more consistent heating of the gases.

During the calibration investigation of the instrumentation, the 20 VDC power supply of was incorrectly wired to the COM port of the NI-9208 DAQ module instead of the power port. This fried the NI-9208, which had to be replaced. These modules are expensive and the lead time was long due to the effects of the COVID-19 pandemic, which shifted the schedule and impacted the budget.

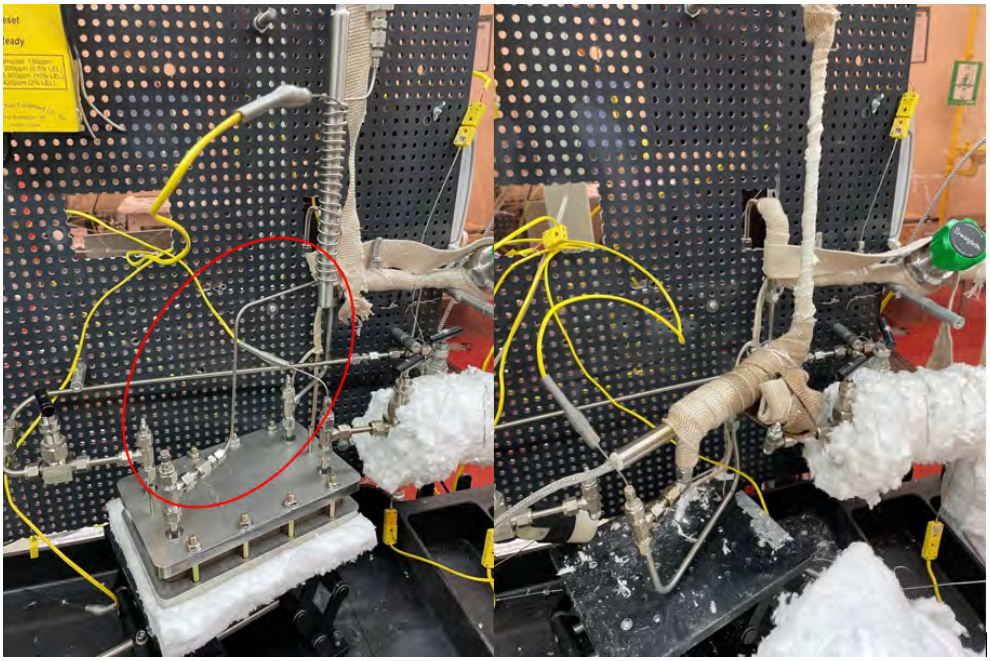

Figure 6.20: The original configuration (left) included a long section of unheated tubing before the inlet of the reactor. This section of piping was replumbed to the updated configuration (right) to decrease the unheated length of piping between the rod heater and the reactor.

6.4 Summary

The elemental composition of the initial coatings of the platinum-ceria catalyst on coupons was quantified using energy-dispersive X-ray spectroscopy. A composition of 8 wt% Pt, 6.68 wt% Ce, 45.55 wt% Al, and 39.73% O was reported for a coating on a 1.5"x1.5" 316 stainless steel coupon. The same EDS analysis process was used to quantify the Pt/Al_2O_3 catalyst coated on the plates. A small sample was taken from the two coatings of the reaction channel and analyzed. It was found that, on average, the composition of the catalyst coated on the coolant plate was found to be 15.56 wt% Pt, 7.75 wt% Ce, 38.32 wt% Al, 38.37 wt% O while the reactant plate was 23.03 wt% Pt, 12.3 wt% Ce, 31.63 wt% Al, 33.05 wt% O.

Sandblasting 316 stainless steel coupons with 60-120 mesh size glass beads increased the surface roughness of from 0.221 μm to 0.483 μm, and this surface area enhancement improved wt% adhesion by 2.56 times from 32.8wt% adhesion to 83.9wt%. On the reactor

plates, the enhanced channel surface exhibited no weight loss after ultrasonic testing and 2% weight loss to drop testing, showing 98wt% adhesion. For the non-enhanced surface, the overall adhesion was observed to be worse at 56wt%, with 4wt% lost during ultrasonic testing and 52wt% lost during the drop test. The surface area enhancement from the sinker EDM manufacturing process nearly doubled the catalyst's ability to adhere to the reaction channels.

Thermal testing with inert argon gas confirmed the expected heat transfer behavior of the WGS reactor's plate architecture design. However, since the process conditions were not completely reached for this test, the measured temperature profile and fluid temperature results are inconclusive. Testing at the high process temperatures introduced thermal expansion of the steel reactor plates, which compressed the gaskets irreversibly. After thermal cycling, the gaskets were unable to seal the reactor as intended and reacting flow experiments could not be conducted due to safety concerns.

Chapter 7: Conclusions and future work

This chapter wraps up this research by discussing the major conclusions drawn from the efforts presented across this thesis. It then outlines the major research contributions offered by this study and discusses opportunities for future work.

7.1 Conclusions

Through an extensive and iterative catalyst synthesis process, the final recipe developed for coating the reaction channels of the plate architecture water-gas shift reactor was shown to exhibit good adhesion to the plates of the microscale WGS reactor. Ultrasonic and drop tests of the catalyst coating showed 98wt% adhesion of the catalyst on the enhanced side of the reaction channel. On the non-enhanced surface of the reaction channel, the adhesion was shown to be worse at 55%. It can be concluded that increasing the surface roughness of the substrate greatly enhances the adhesion of the catalyst to the reactor channels.

SEM analysis and EDS spectral mapping of the catalyst surface showed that the platinum and ceria were well dispersed across the alumina support. EDS elemental analysis showed an average catalyst composition of 15.56 wt% Pt, 7.75 wt% Ce, 38.32 wt% Al, 38.37 wt% O on the coolant plate and 23.03 wt% Pt, 12.3 wt% Ce, 31.63 wt% Al, 33.05 wt% O on the reactant plate. The adapted catalyst coating technique adequately impregnates the platinum and ceria into the alumina support.

A plate architecture, sub-scale WGS microreactor prototype was realized using advanced manufacturing techniques. The reactor was manufactured using sinker electrical discharge machining and the graphite gaskets were cut to shape using a laser cutter. The gasket material's expansion and compression properties should be carefully considered and factored into the design of plate architecture style reactors. While plate architecture microreactor designs take advantage of enhanced mass and heat transfer phenomena at the microscale, this type of reactor design has a high number of mechanically sealed surfaces, which leads

to a greater number of diffusion paths for process gases to leak out of. High conversion is possible, desirable, and important for the scope of this research, but it should be emphasized that from the experiences and results of the work performed, the design of a process intensified water-gas shift reactor should attempt to minimize the amount of mechanically sealed surfaces. Preventing hydrogen leaks is important in enabling the feasibility of a process-intensified WGS reactor.

A test loop capable of supporting reacting water-gas shift studies was designed, manufactured, and operated with the prototype reactor integrated on the loop. To realize thermal success of a test loop with CO_2, CO, H_2, and steam operating up to 350°C, a robust insulation strategy utilizing both insulation strips and ceramic fiber blanket must be employed to provide a sufficient amount of insulation to minimize heat loss to the atmosphere. Thermal testing with inert argon gas near process flow, temperatures, and pressures confirmed the expected heat transfer behavior of the WGS reactor's plate architecture design.

It can be concluded that a plate architecture water-gas shift microreactor design can be mechanically realized using advanced manufacturing methods, with an integrated Pt/Al_2O_3 catalyst deposited using a novel coating procedure. While *feasible*, a plate architecture design is *impractical* for realizing the potential of the process-intensified water gas shift reaction because of sealing challenges. Reactor design for processes involving hydrogen should seek to minimize the number of required mechanical seals in the reactor, which would help to reduce the risk of leaks, decrease assembly and commissioning time, save cost, increase reusability, and improve the feasibility of a process intensified differential temperature water-gas shift microreactor.

7.2 Future work

Future work on this research can be approached from a variety of different angles. The main path in concluding this research would be to investigate the chemical feasibility of the sub-scale water-gas shift microreactor prototype. To do so, the reactor gaskets would need to be re-manufactured using thicker gasket material to improve the sealing capabilities of

the reactor. There is also opportunity in scaling down the number of unit cells in the reactor to decrease the number of mechanical seals required in the reactor. Taking these steps would help mitigate the leakage issue and enable reacting flow studies to characterize the WGSR's CO conversion through the process intensified reactor. Once the initial reacting flow studies are conducted, parametric studies that vary the reaction and coolant process conditions (temperature, flow rate, and pressures) and reactant gas concentrations could be conducted to further optimize conversion. The data from these studies can be used to further refine the model and bring it closer to the reality observed during testing.

This can also be done on a smaller scale, as another feasible path would be to validate the performance of the catalyst recipe developed for this research by conducting reacting flow studies through a single unit cell of the reactor. This would alleviate challenges with sealing a large number of sealing surfaces and provide a baseline performance for a single unit cell, which can then be scaled up to predicted reactor performance for multiple unit cells. However, investigations would also need to be made at scale to test the realistic performance and tune the model to better match reality. When looping back to the holistic goal of improving hydrogen production from natural gas and reducing the cost associated with this, there is currently limited analysis on how the cost effective this type of reactor design is.

Further research can work towards developing a cost model for the cost per kg of hydrogen produced through scaled-up manufacturing of this reactor design. Alongside the cost studies, investigations can be conducted into the projected carbon emissions from this process step in the steam-methane reformation process. The data from the cost and emissions model can then be used to inform the financial and environmental benefits and/or downsides of using a process intensified plate architecture water-gas shift microreactor design when compared to the conventional high-temperature to low-temperature shift reactor designs that exist today.

APPENDICES

Appendix A: Supplementary materials

A.1 Reactor drawings

The drawings on the following pages were submitted to Ram-Z Fab for fabrication. The only change that was applied was regarding the tubing connections to the test loop. These connections were updated to 1/4" diameter piping instead of 1/8".

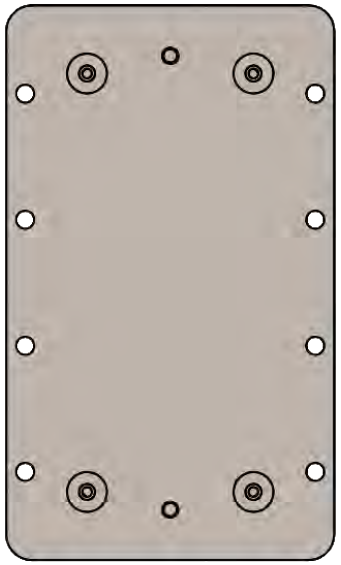

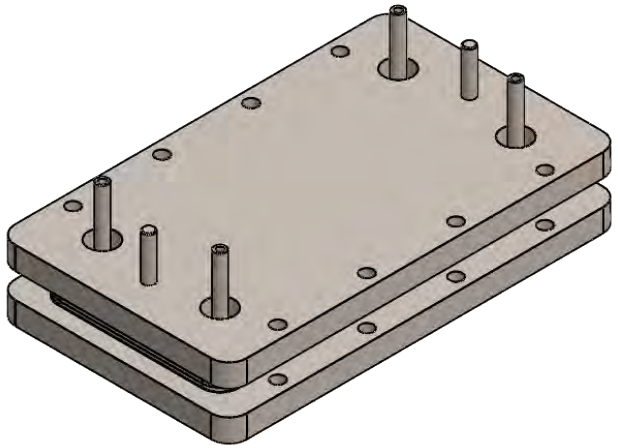

		UNLESS OTHERWISE SPECIFIED:		NAME	DATE
		DIMENSIONS ARE IN MM TOLERANCES: FRACTIONAL ± ANGULAR: MACH ± BEND ± TWO PLACE DECIMAL ± THREE PLACE DECIMAL ±	DRAWN		
			CHECKED		
			ENG APPR.		
			MFG APPR.		
		INTERPRET GEOMETRIC TOLERANCING PER:	Q.A.		
		MATERIAL	COMMENTS:		
NEXT ASSY	USED ON	FINISH			
APPLICATION		DO NOT SCALE DRAWING			

DRAFTED BY: KATHY HU

TITLE:

WATER GAS SHIFT REACTOR

187

SIZE	DWG. NO.	REV
A	00	A

SCALE: 1:3 | WEIGHT: | SHEET 1 OF 1

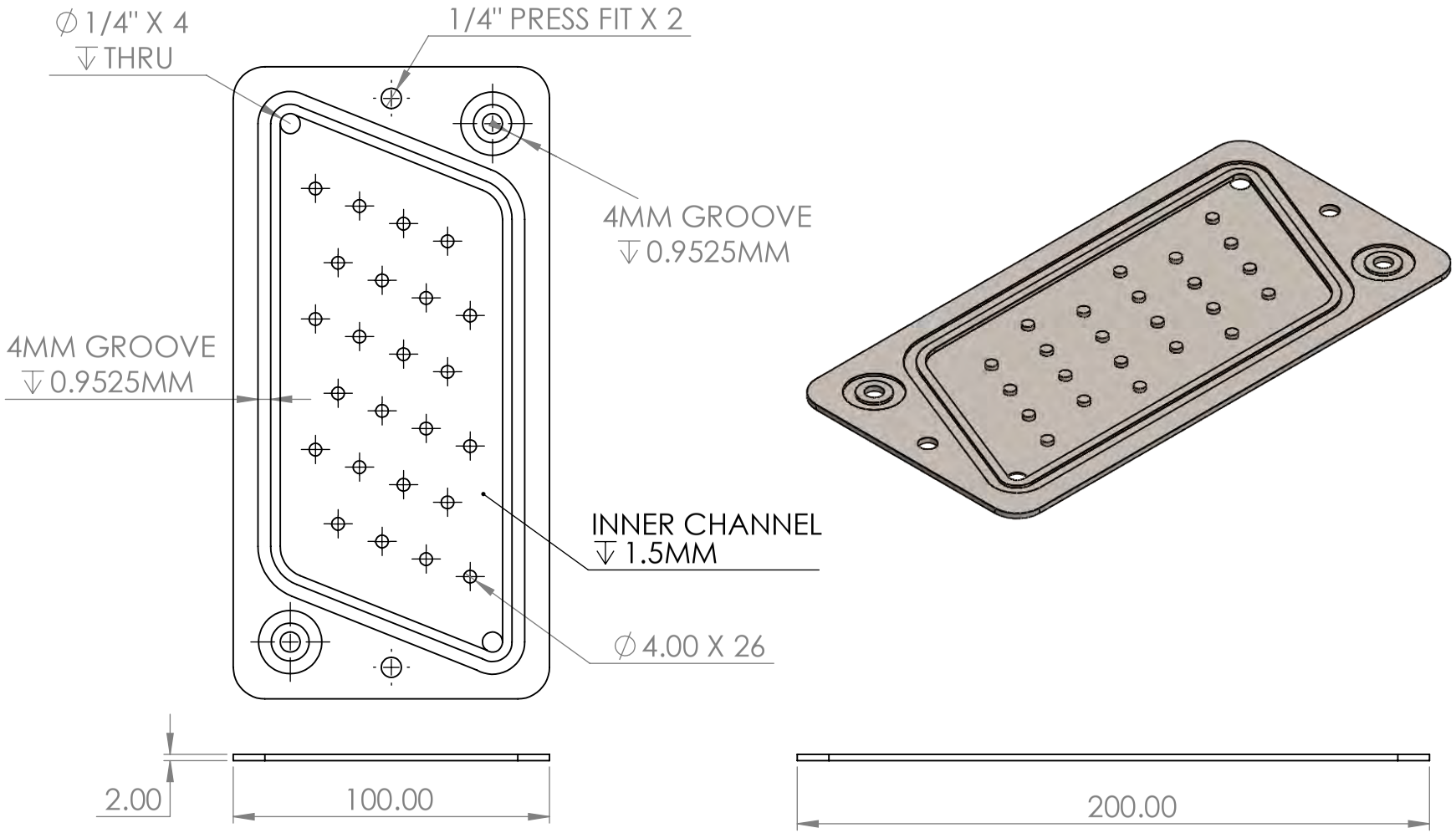

		UNLESS OTHERWISE SPECIFIED:		NAME	DATE
		DIMENSIONS ARE IN MM TOLERANCES: FRACTIONAL ± ANGULAR: MACH ± BEND ± TWO PLACE DECIMAL ± THREE PLACE DECIMAL ±	DRAWN		
			CHECKED		
			ENG APPR.		
			MFG APPR.		
		INTERPRET GEOMETRIC TOLERANCING PER:	Q.A.		
		MATERIAL 2MM 316 SS	COMMENTS:		
NEXT ASSY	USED ON	FINISH			
APPLICATION		DO NOT SCALE DRAWING			

DRAFTED BY: KATHY HU

TITLE:

REACTANT PLATE

188

SIZE	DWG. NO.	REV
A	01	A

SCALE: 1:2 | WEIGHT: | SHEET 1 OF 1

PLEASE REFERENCE DRAWING NO. 1
FOR MORE DETAILED INFORMATION.

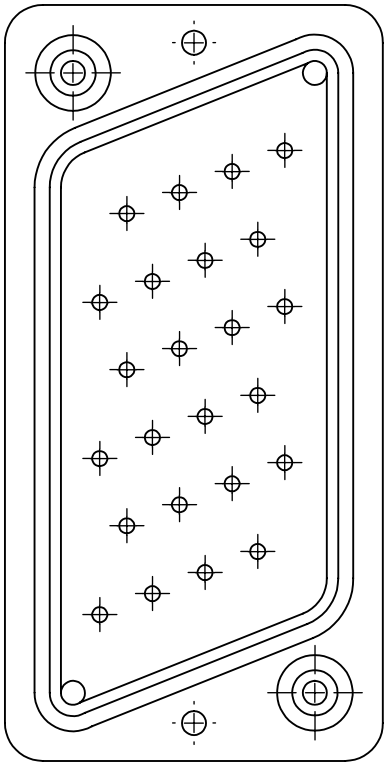

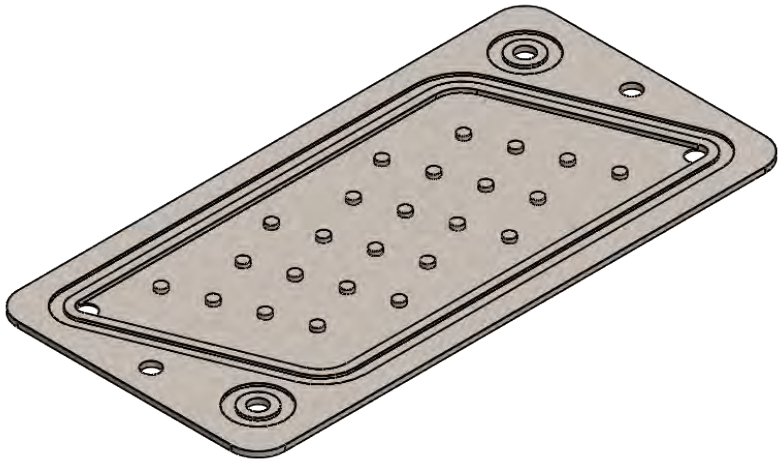

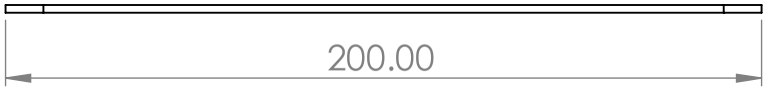

		UNLESS OTHERWISE SPECIFIED:		NAME	DATE
		DIMENSIONS ARE IN MM TOLERANCES: FRACTIONAL ± ANGULAR: MACH ± BEND ± TWO PLACE DECIMAL ± THREE PLACE DECIMAL ±	DRAWN		
			CHECKED		
			ENG APPR.		
			MFG APPR.		
		INTERPRET GEOMETRIC TOLERANCING PER:	Q.A.		
		MATERIAL 2MM 316 SS	COMMENTS:		
NEXT ASSY	USED ON	FINISH			
APPLICATION		DO NOT SCALE DRAWING			

DRAFTED BY: KATHY HU

TITLE:

COOLANT PLATE

189

SIZE	DWG. NO.	REV
A	02	A

SCALE: 1:2	WEIGHT:	SHEET 1 OF 1

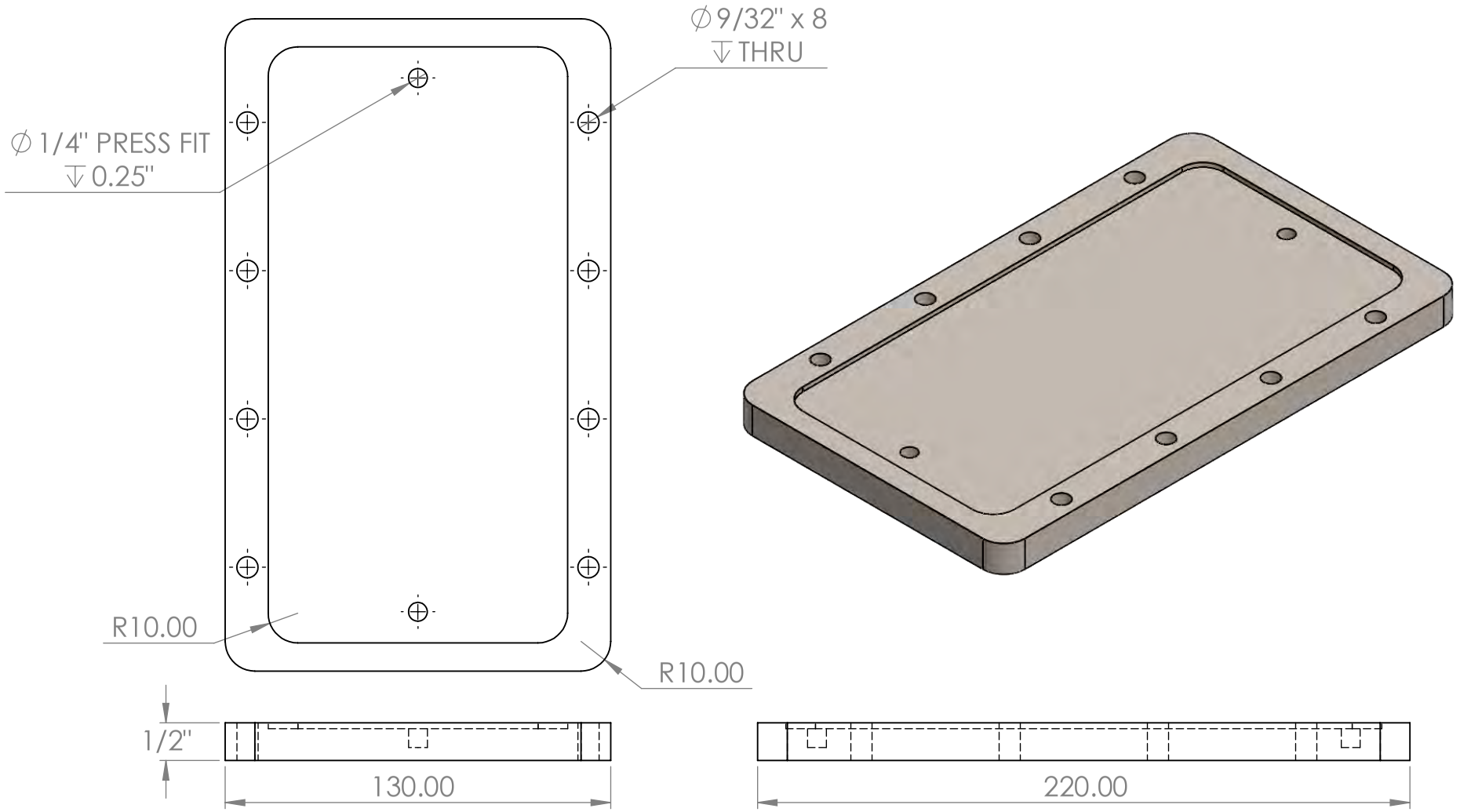

		UNLESS OTHERWISE SPECIFIED:		NAME	DATE
		DIMENSIONS ARE IN MM TOLERANCES: FRACTIONAL ± ANGULAR: MACH ± BEND ± TWO PLACE DECIMAL ± THREE PLACE DECIMAL ±	DRAWN		
			CHECKED		
			ENG APPR.		
			MFG APPR.		
		INTERPRET GEOMETRIC TOLERANCING PER:	Q.A.		
		MATERIAL 1/2" 316 SS	COMMENTS:		
NEXT ASSY	USED ON	FINISH			
APPLICATION		DO NOT SCALE DRAWING			

DRAFTED BY: KATHY HU

TITLE:

BOTTOM PLATE

190

SIZE	DWG. NO.	REV
A	03	A

SCALE: 1:5 | WEIGHT: | SHEET 1 OF 1

ALL HOLES ARE THROUGH HOLES.

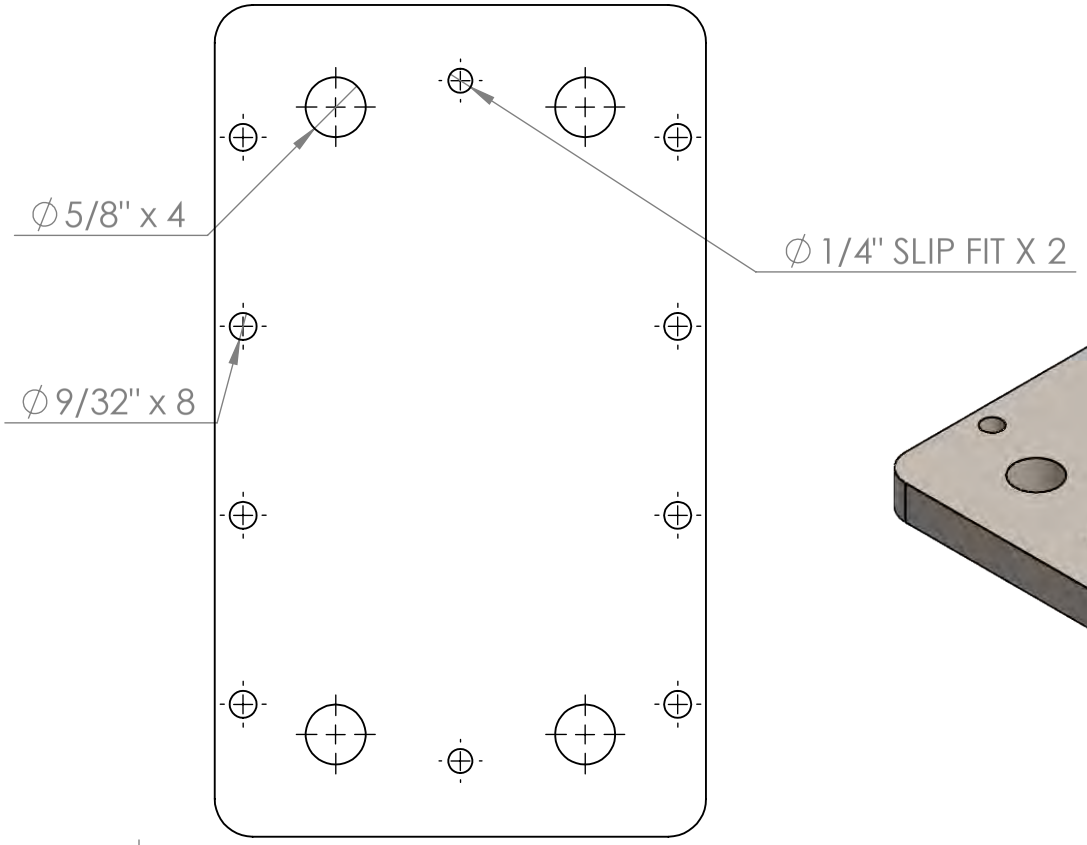

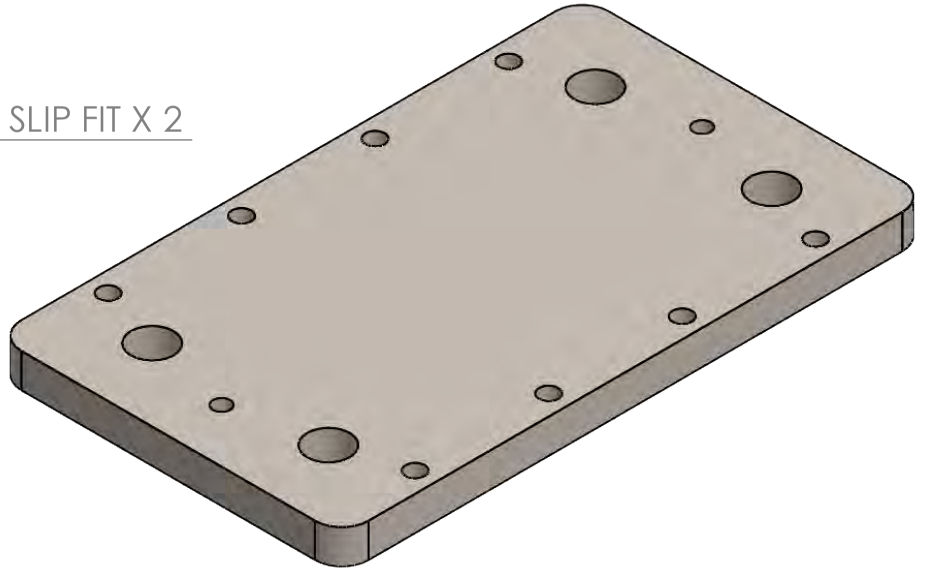

		UNLESS OTHERWISE SPECIFIED:		NAME	DATE
		DIMENSIONS ARE IN MM TOLERANCES: FRACTIONAL ± ANGULAR: MACH ± BEND ± TWO PLACE DECIMAL ± THREE PLACE DECIMAL ±	DRAWN		
			CHECKED		
			ENG APPR.		
			MFG APPR.		
		INTERPRET GEOMETRIC TOLERANCING PER:	Q.A.		
		MATERIAL 1/2" 316 SS	COMMENTS:		
NEXT ASSY	USED ON	FINISH			
APPLICATION		DO NOT SCALE DRAWING			

DRAFTED BY: KATHY HU

TITLE:

TOP PLATE

191

SIZE	DWG. NO.	REV
A	04	A

SCALE: 1:2	WEIGHT:	SHEET 1 OF 1

VERY SMOOTH BOTTOM SURFACE
FOR SEALING.

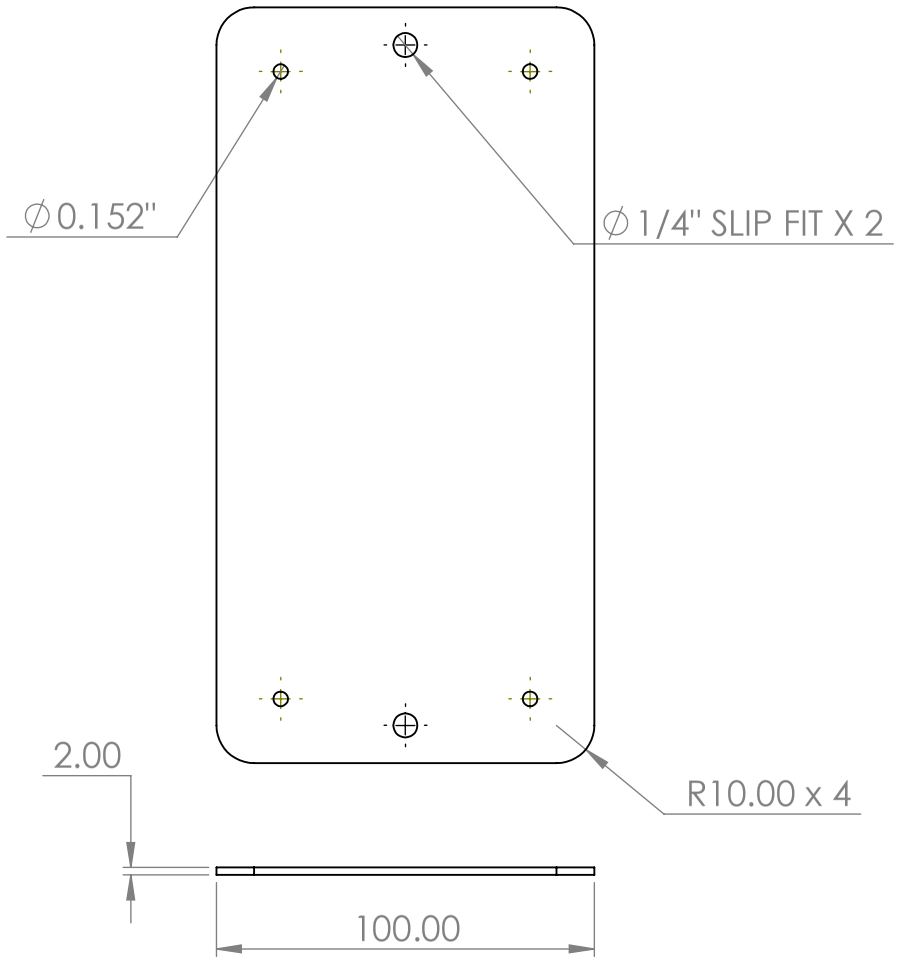

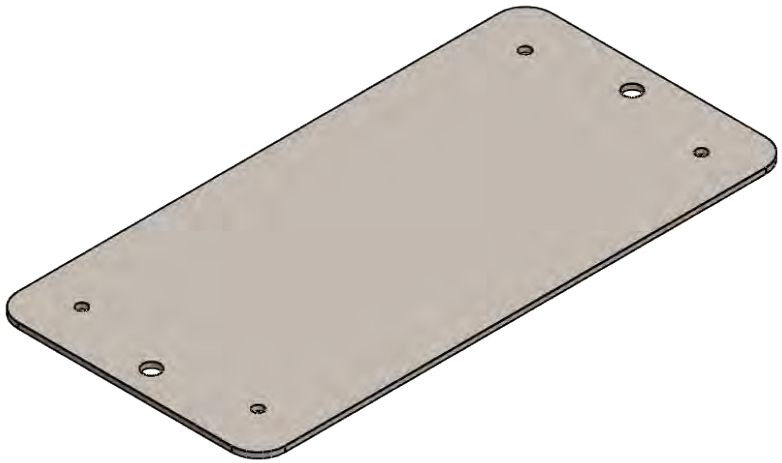

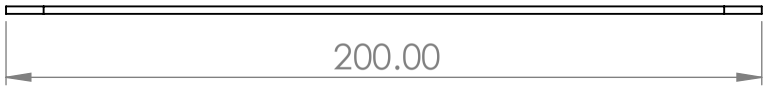

		UNLESS OTHERWISE SPECIFIED:		NAME	DATE
		DIMENSIONS ARE IN MM TOLERANCES: FRACTIONAL ± ANGULAR: MACH ± BEND ± TWO PLACE DECIMAL ± THREE PLACE DECIMAL ±	DRAWN		
			CHECKED		
			ENG APPR.		
			MFG APPR.		
		INTERPRET GEOMETRIC TOLERANCING PER:	Q.A.		
		MATERIAL 2 mm 316 SS	COMMENTS:		
NEXT ASSY	USED ON	FINISH			
APPLICATION		DO NOT SCALE DRAWING			

DRAFTED BY: KATHY HU

TITLE:

SEALING PLATE

192

SIZE	DWG. NO.	REV
A	05	A

SCALE: 1:2	WEIGHT:	SHEET 1 OF 1

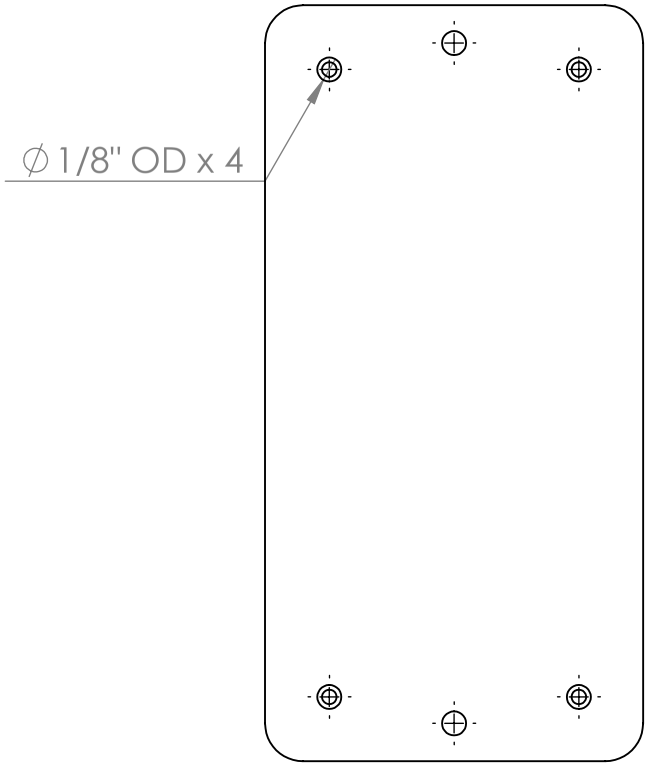

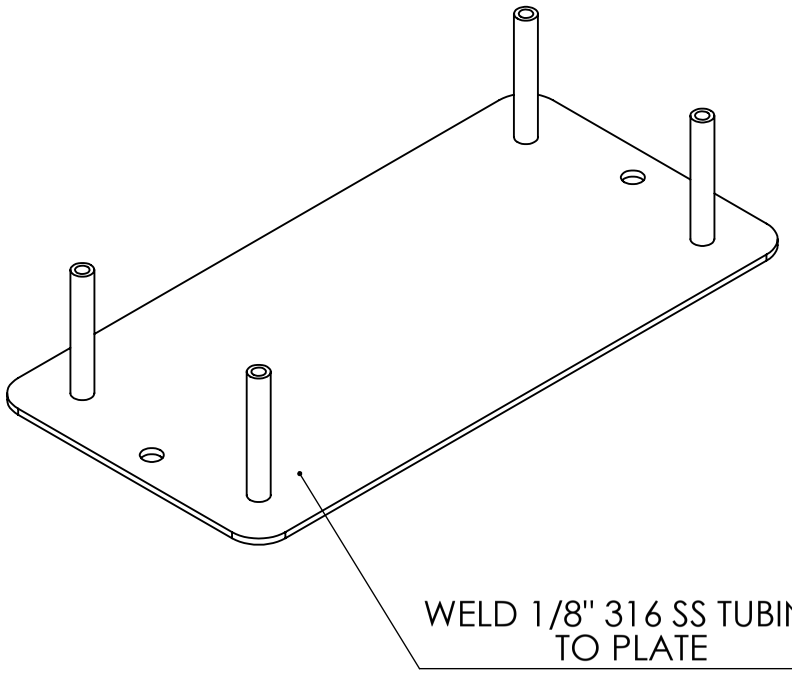

		UNLESS OTHERWISE SPECIFIED:		NAME	DATE
		DIMENSIONS ARE IN MM TOLERANCES: FRACTIONAL ± ANGULAR: MACH ± BEND ± TWO PLACE DECIMAL ± THREE PLACE DECIMAL ±	DRAWN		
			CHECKED		
			ENG APPR.		
			MFG APPR.		
		INTERPRET GEOMETRIC TOLERANCING PER:	Q.A.		
		MATERIAL 1/8" OD 316 SS TUBING	COMMENTS:		
NEXT ASSY	USED ON	FINISH			
APPLICATION		DO NOT SCALE DRAWING			

DRAFTED BY: KATHY HU

TITLE:

WELD

193

SIZE	DWG. NO.	REV
A	06	A

SCALE: 1:2	WEIGHT:	SHEET 1 OF 1

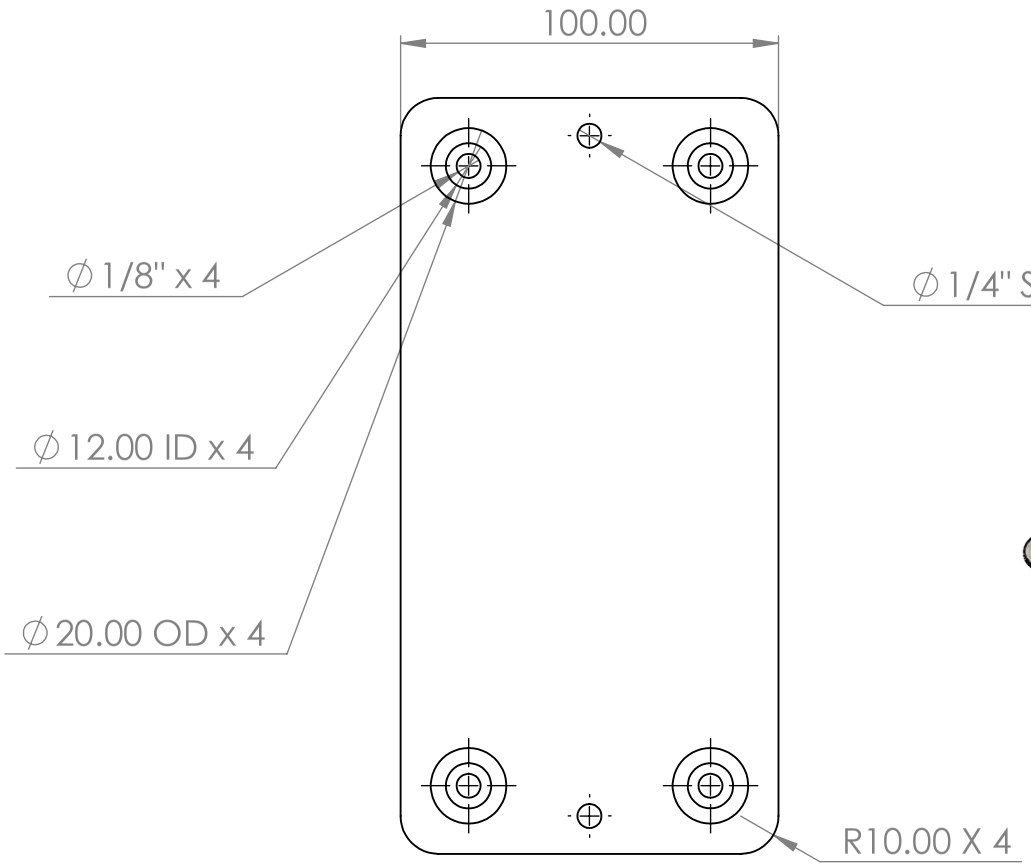

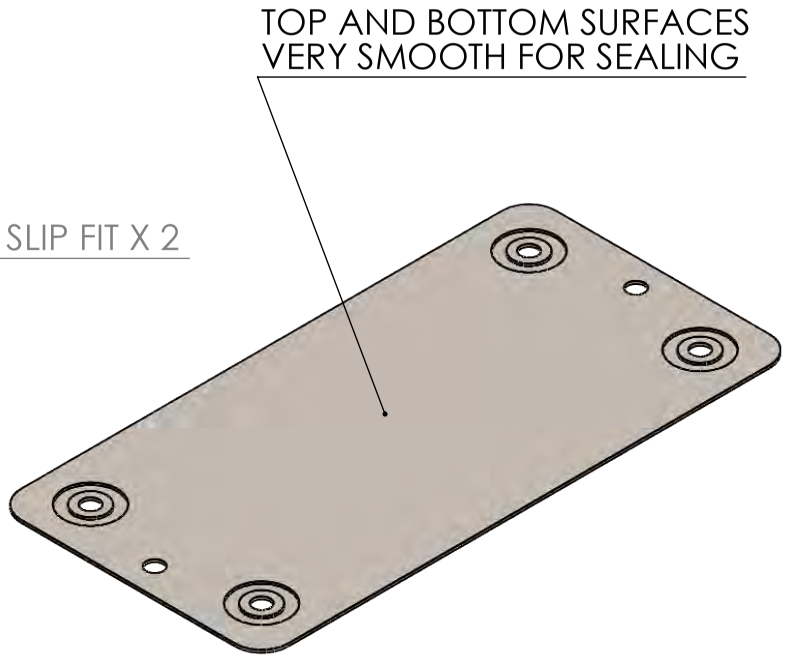

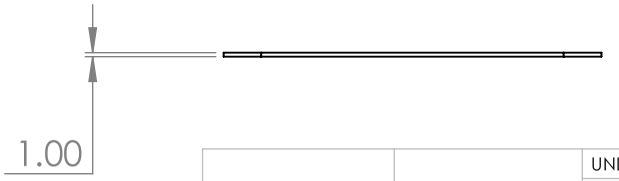

		UNLESS OTHERWISE SPECIFIED:		NAME	DATE
		DIMENSIONS ARE IN MM TOLERANCES: FRACTIONAL ± ANGULAR: MACH ± BEND ± TWO PLACE DECIMAL ± THREE PLACE DECIMAL ±	DRAWN		
			CHECKED		
			ENG APPR.		
			MFG APPR.		
		INTERPRET GEOMETRIC TOLERANCING PER:	Q.A.		
		MATERIAL 1 mm 316 SS	COMMENTS:		
NEXT ASSY	USED ON	FINISH			
APPLICATION		DO NOT SCALE DRAWING			

DRAFTED BY: KATHY HU

TITLE:

INSTRUMENTATION PLATE

194

SIZE	DWG. NO.	REV
A	07	A

SCALE: 1:2 | WEIGHT: | SHEET 1 OF 1

A.2 Therminol liquid properties

Liquid properties of Therminol® 72 heat transfer fluid by temperature[a] (SI units)

Temperature		Liquid density	Liquid heat capacity	Liquid thermal conductivity	Liquid viscosity[b]		Vapor pressure[c]
°C	°F	kg/m³	kJ/(kg·K)	W/(m·K)	cP (mPa·s)	cSt (mm²/s)	kPa
–14	7	1110	1.460	0.144	3971	3580	—
–10	14	1106	1.471	0.143	383	346	—
0	32	1097	1.498	0.142	59.2	54.0	—
10	50	1088	1.525	0.141	24.4	22.4	—
20	68	1079	1.552	0.140	13.5	12.5	0.001
30	86	1070	1.579	0.138	8.68	8.11	0.002
40	104	1061	1.606	0.137	6.09	5.74	0.006
50	122	1052	1.634	0.136	4.52	4.30	0.013
60	140	1043	1.661	0.135	3.50	3.35	0.028
70	158	1034	1.688	0.134	2.79	2.70	0.056
80	176	1025	1.715	0.132	2.28	2.23	0.105
90	194	1016	1.742	0.131	1.90	1.87	0.189
100	212	1007	1.769	0.130	1.61	1.60	0.326
110	230	997	1.796	0.129	1.38	1.39	0.545
120	248	988	1.823	0.127	1.20	1.21	0.879
130	266	979	1.850	0.126	1.05	1.07	1.38
140	284	970	1.877	0.125	0.93	0.96	2.10
150	302	961	1.905	0.124	0.83	0.86	3.12
160	320	952	1.932	0.123	0.74	0.78	4.54
170	338	943	1.959	0.121	0.66	0.70	6.47
180	356	934	1.986	0.120	0.60	0.64	9.04
190	374	925	2.013	0.119	0.55	0.59	12.4
200	392	916	2.040	0.118	0.50	0.54	16.8
210	410	906	2.067	0.117	0.46	0.50	22.3
220	428	898	2.094	0.115	0.42	0.47	29.3
230	446	889	2.121	0.114	0.39	0.43	38.0
240	464	880	2.148	0.113	0.36	0.40	48.6
250	482	871	2.176	0.112	0.33	0.38	61.6
260	500	862	2.203	0.111	0.31	0.36	77.1
270	518	853	2.230	0.109	0.28	0.33	95.7
280	536	844	2.257	0.108	0.27	0.31	118
290	554	834	2.284	0.107	0.25	0.30	143
300	572	825	2.311	0.106	0.23	0.28	173
310	590	816	2.338	0.104	0.22	0.27	208
320	608	807	2.365	0.103	0.20	0.25	248
330	626	798	2.392	0.102	0.19	0.24	293
340	644	789	2.419	0.101	0.18	0.23	345
350	662	780	2.447	0.100	0.17	0.22	403
360	680	771	2.474	0.098	0.16	0.21	469
370	698	762	2.501	0.097	0.15	0.20	542
380	716	753	2.528	0.096	0.14	0.19	623

[a]Maximum recommended bulk temperature 380°C (715°F). These data are based on samples tested in the laboratory and are not guaranteed for all samples. Contact us for complete sales specifications for Therminol 72 fluid. [b]1 cSt = 1 mm²/s and 1 mPa•s = 1 cP. [c]100 kPa = 1 bar

Liquid properties of Therminol® 72 heat transfer fluid by temperature[a] (English units)

Temperature		Liquid density		Liquid heat capacity	Liquid thermal conductivity	Liquid viscosity[b]		Vapor pressure[c]
°F	°C	lb/gal	lb/ft³	Btu/(lb·°F)	Btu/(ft·h·°F)	lb/(ft·h)	cSt (mm²/s)	psia
7		9.26	69.3	0.349	0.0831	8480	3160	—
20	–7	9.21	68.9	0.354	0.0826	393	147	—
40	4	9.13	68.3	0.361	0.0818	91.3	34.5	—
60	16	9.04	67.6	0.368	0.0810	41.5	15.8	—
80	27	8.96	67.0	0.375	0.0802	24.1	9.26	0.0003
100	38	8.88	66.4	0.382	0.0795	15.8	6.16	0.0007
120	49	8.78	65.7	0.390	0.0787	11.3	4.43	0.0018
140	60	8.70	65.1	0.397	0.0779	8.46	3.35	0.0041
160	71	8.62	64.5	0.404	0.0771	6.60	2.64	0.0087
180	82	8.54	63.9	0.411	0.0763	5.30	2.14	0.0174
200	93	8.45	63.2	0.418	0.0756	4.35	1.78	0.0330
220	104	8.37	62.6	0.426	0.0748	3.64	1.50	0.0597
240	116	8.29	62.0	0.433	0.0740	3.09	1.29	0.103
260	127	8.19	61.3	0.440	0.0732	2.65	1.12	0.173
280	138	8.11	60.7	0.447	0.0724	2.31	0.98	0.278
300	149	8.03	60.1	0.454	0.0717	2.02	0.87	0.434
320	160	7.94	59.4	0.462	0.0709	1.78	0.78	0.659
340	171	7.86	58.8	0.469	0.0701	1.59	0.70	0.975
360	182	7.78	58.2	0.476	0.0693	1.42	0.63	1.41
380	193	7.70	57.6	0.483	0.0685	1.28	0.57	1.99
400	204	7.61	56.9	0.490	0.0678	1.16	0.52	2.77
420	216	7.53	56.3	0.498	0.0670	1.05	0.48	3.77
440	227	7.45	55.7	0.505	0.0662	0.96	0.44	5.06
460	238	7.35	55.0	0.512	0.0654	0.88	0.41	6.68
480	249	7.27	54.4	0.519	0.0646	0.80	0.38	8.70
500	260	7.19	53.8	0.526	0.0639	0.74	0.36	11.2
520	271	7.11	53.2	0.534	0.0631	0.68	0.33	14.2
540	282	7.02	52.5	0.541	0.0623	0.63	0.31	17.8
560	293	6.94	51.9	0.548	0.0615	0.59	0.29	22.2
580	304	6.86	51.3	0.555	0.0607	0.54	0.27	27.3
600	316	6.76	50.6	0.562	0.0600	0.51	0.26	33.3
620	327	6.68	50.0	0.570	0.0592	0.47	0.24	40.3
640	338	6.60	49.4	0.577	0.0584	0.44	0.23	48.3
660	349	6.52	48.8	0.584	0.0576	0.41	0.22	57.5
680	360	6.43	48.1	0.591	0.0568	0.39	0.21	68.0
700	371	6.35	47.5	0.598	0.0561	0.36	0.20	79.9
715	379	6.28	47.0	0.604	0.0555	0.35	0.19	89.7

[a]Maximum recommended bulk temperature 380°C (715°F). These data are based on samples tested in the laboratory and are not guaranteed for all samples. Contact us for complete sales specifications for Therminol 72 fluid. [b]1 cSt = 1 mm²/s and 1 mPa•s = 1 cP. [c]100 kPa = 1 bar

A.3 Catalyst weights

Figure A.1: Reactant plate 1 and corresponding weights measured after drying and calcination for each step of the catalyst coating process.

Figure A.2: Reactant plate 2 and corresponding weights measured after drying and calcination for each step of the catalyst coating process.

Figure A.3: Reactant plate 3 and corresponding weights measured after drying and calcination for each step of the catalyst coating process.

Figure A.4: Reactant plate 4 and corresponding weights measured after drying and calcination for each step of the catalyst coating process.

Figure A.5: Reactant plate 5 and corresponding weights measured after drying and calcination for each step of the catalyst coating process.

Figure A.6: Reactant plate 6 and corresponding weights measured after drying and calcination for each step of the catalyst coating process.

Figure A.7: Coolant plate 1 and corresponding weights measured after drying and calcination for each step of the catalyst coating process.

Figure A.8: Coolant plate 2 and corresponding weights measured after drying and calcination for each step of the catalyst coating process.

Figure A.9: Coolant plate 3 and corresponding weights measured after drying and calcination for each step of the catalyst coating process.

Figure A.10: Coolant plate 5 and corresponding weights measured after drying and calcination for each step of the catalyst coating process.

Figure A.11: Coolant plate 6 and corresponding weights measured after drying and calcination for each step of the catalyst coating process.

Appendix B: Instrument configuration

B.1 Micro Motion 2700 transmitter configuration

The Micro Motion 2700 transmitter for the Coriolis mass flow meter was configured using Emerson ProLink III to measure 0-350 mL/min of volumetric flow rate. The transmitter was configured using the HART/Bell 202 communication protocol. The following procedure, adapted from Emerson, was used to perform the configuration:

1. Ensure the Micro Motion 2700 transmitter is powered.
2. Locate and identify the Viator USB HART Interface signal converter (commonly referred to as the HART modem). This is required to enable communication between the workstation and the transmitter.
3. Plug the HART modem into the USB port of the PC.
4. HART/Bell 202 connections require a voltage drop of 1-5 VDC across the signal wires. To achieve this, add a resistor of 250–600Ω between the two signal wires running from the transmitter to the NI-DAQ chassis.
5. Connect the leads of the HART modem to the opposite ends of the resistor.
6. Launch the ProLink III software on the mobile workstation.
7. Choose **Connect to Physical Device.**
8. Set **Protocol** to HART Bell 202 and enable **Toggle RTS**.
9. Click **Poll** to identify the transmitter.
10. Set the **PC Port** value to the PC COM port that is being used for the connection.
11. Select **Connect.**

12. To configure the measurement range for the mass and volume flow measurements, select **Device Tools → Configuration → Process Measurement → Flow**.
13. Set the minimum reported flow rate to 0.1 mL/min.
14. Set the maximum reported flow rate to 350 mL/min.
15. Apply the changes.

More detailed directions can be found in the Micro Motion 2700 configuration and use manual.

Bibliography

[1] *Monthly Energy Review (April 2022)*, tech. rep. (U.S. Energy Information Administration, 2022).

[2] *The Future of Hydrogen*, tech. rep. (International Energy Association, 2019).

[3] *Hydrogen Production: Natural Gas Reforming | U.S. Department of Energy*, 2021.

[4] S Nalley and A LaRose, *Annual Energy Outlook 2021*, tech. rep. (U.S. Energy Information Administration, 2021).

[5] *Hydrogen Production Processes | U.S. Department of Energy.*

[6] J Vickers, D Peterson, and K Randolph, *Cost of electrolytic hydrogen production with existing technology*, 2020.

[7] F Ullmann, *Ullmann's Encyclopedia of Industrial Chemistry* (Wiley, 2006), p. 12142.

[8] *The United States Energy Policy Act*, 2005.

[9] *Hydrogen Shot | U.S. Department of Energy*, 2021.

[10] EV Moeller, SM Harvey, MP Joshi, E Teplinsky, ME Dajani, and MC Hammond, *Hydrogen Highlights in the Bipartisan Infrastructure Bill*, 2021.

[11] *Biden-Harris Administration Announces $750 Million To Accelerate Clean Hydrogen Technologies | U.S. Department of Energy*, 2022.

[12] P van Beurden, "On the catalytic aspects of steam-methane reforming", in (2004).

[13] R Wegeng, R Diver, and P Humble, "Second law analysis of a solar methane reforming system", Energy Procedia **49**, 1248–1258 (2014) 10.1016/j.egypro.2014.03.134.

[14] ES Kikkinides, VI Sikavitsas, and RT Yang, "Natural gas desulfurization by adsorption: feasibility and multiplicity of cyclic steady states", Industrial & Engineering Chemistry Research **34**, 255–262 (1995) 10.1021/ie00040a027.

[15] TE Tolley and BM Fronk, "Investigation of the benefits of diabatic microreactors for process intensification of the water-gas shift reaction within the steam reforming process", International Journal of Hydrogen Energy **45**, 31507–31522 (2020) https://doi.org/10.1016/j.ijhydene.2020.08.282.

[16] C Callaghan, *Kinetics and catalysis of the water-gas-shift reaction: a microkinetic and graph theoretic approach* (2006).

[17] R Smith, M Loganathan, and MS Shantha, "A review of the water gas shift reaction kinetics", International Journal of Chemical Reactor Engineering **8**, doi:10.2202/1542-6580.2238 (2010) doi:10.2202/1542-6580.2238.

[18] K Atwood, MR Arnold, and EG Appel, "Water-gas shift reaction. effect of pressure on rate over an iron- oxide-chromium oxide catalyst.", Industrial & Engineering Chemistry **42**, 1600–1602 (1950) 10.1021/ie50488a038.

[19] C Song, "Fuel processing for low-temperature and high-temperature fuel cells: challenges, and opportunities for sustainable development in the 21st century", Catalysis Today **77**, 17–49 (2002) https://doi.org/10.1016/S0920-5861(02)00231-6.

[20] I Kocemba, I Śmiechowicz, M Jędrzejczyk, J Rogowski, and JM Rynkowski, "High catalytic activity of pt/al2o3 catalyst in co oxidation at room temperature: a new insight into strong metal-support interactions", Catalysts **11** (2021).

[21] C Ratnasamy and JP Wagner, "Catalysis Reviews Water Gas Shift Catalysis Water Gas Shift Catalysis", Catalysis Reviews **51**, 325–440 (2009) 10.1080/01614940903048661.

[22] J Wang, M Musameh, R Laocharoensuk, O González-García, J Oni, and D Gervasio, "Pt/ru-functionalized magnetic spheres for a magnetic-field stimulated methanol and oxygen redox processes: towards on-demand activation of fuel cells", Electrochemistry Communications **8**, 1106–1110 (2006) https://doi.org/10.1016/j.elecom.2006.04.019.

[23] C Wheeler, A Jhalani, E Klein, S Tummala, and L Schmidt, "The water–gas-shift reaction at short contact times", Journal of Catalysis **223**, 191–199 (2004) https://doi.org/10.1016/j.jcat.2004.01.002.

[24] RA Dagle, A Karim, G Li, Y Su, and DL King, "Chapter 12 - syngas conditioning", in *Fuel cells: technologies for fuel processing*, edited by D Shekhawat, JJ Spivey, and DA Berry (Elsevier, Amsterdam, 2011), pp. 361–408, https://doi.org/10.1016/B978-0-444-53563-4.10012-4.

[25] P Panagiotopoulou and D Kondarides, "Effect of the nature of the support on the catalytic performance of noble metal catalysts for the water–gas shift reaction", Catalysis Today **112**, 10.1016/j.cattod.2005.11.026 (2006) 10.1016/j.cattod.2005.11.026.

[26] O Thinon, F Diehl, P Avenier, and Y Schuurman, "Screening of bifunctional water-gas shift catalysts", Catlysis Today **137**, 29–35 (2008) 10.1016/j.cattod.2008.01.001.

[27] G Germani and Y Schuurman, "Water-gas shift reaction kinetics over μ-structured Pt/CeO2/Al2O3 catalysts", AIChE Journal **52**, 1806–1813 (2006) 10.1002/AIC.10764.

[28] A Gavriilidis, R Hayes, and S Kolaczkowski, "Introduction to catalytic combustion", Chemical Engineering Research and Design **78**, 678 (2000) 10.1205/026387600527644.

[29] V Perrichon, L Retailleau, P Bazin, M Daturi, and J Lavalley, "Metal dispersion of $ceo_2\breve{}zro_2$ supported platinum catalysts measured by h2 or co chemisorption", Applied Catalysis A: General **260**, 1–8 (2004) 10.1016/j.apcata.2003.09.031.

[30] M Valentini, G Groppi, C Cristiani, M Levi, E Tronconi, and P Forzatti, "The deposition of γ-al2o3 layers on ceramic and metallic supports for the preparation of structured catalysts", Catalysis Today - CATAL TODAY **69**, 307–314 (2001) 10.1016/S0920-5861(01)00383-2.

[31] L He, Y Fan, L Luo, J Bellettre, and J Yue, "Preparation of pt/γ-al2o3 catalyst coating in microreactors for catalytic methane combustion", Chemical Engineering Journal **380**, 122424 (2020) https://doi.org/10.1016/j.cej.2019.122424.

[32] J Regalbuto, *Catalyst preparation: science and engineering* (CRC Press, 2016).

[33] J Lu, B Fu, MC Kung, G Xiao, JW Elam, HH Kung, and PC Stair, "Coking- and sintering-resistant palladium catalysts achieved through atomic layer deposition", Science **335**, 1205–1208 (2012) 10.1126/science.1212906.

[34] X Wang, R Gorte, and J Wagner, "Deactivation mechanisms for pd/ceria during the water–gas-shift reaction", Journal of Catalysis **212**, 225–230 (2002) https://doi.org/10.1006/jcat.2002.3789.

[35] A Goguet, M FC, J Breen, R Burch, M Petch, and A Ghenciu, "Study of the origin of the deactivation of a pt/ceo2 catalyst during reverse water gas shift (rwgs) reaction", Journal of Catalysis **226**, 382–392 (2004) 10.1016/j.jcat.2004.06.011.

[36] A Sirijaruphan, JG Goodwin, RW Rice, D Wei, KR Butcher, GW Roberts, and JJ Spivey, "Metal foam supported pt catalysts for the selective oxidation of co in hydrogen", Applied Catalysis A: General **281**, 1–9 (2005) https://doi.org/10.1016/j.apcata.2004.10.019.

[37] A Pestryakov, E Yurchenko, and A Feofilov, "Foam-metal catalysts for purification of waste gases and neutralization of automotive emissions", Catalysis Today **29**, Second Japan-EC Joint Workshop on the Frontiers of Catalytic Science and Technology for Energy, Environment and Risk Prevention, 67–70 (1996) https://doi.org/10.1016/0920-5861(95)00266-9.

[38] PS Roy, NK Park, and K Kim, "Metal foam-supported pd–rh catalyst for steam methane reforming and its application to sofc fuel processing", International Journal of Hydrogen Energy **39**, 4299–4310 (2014) https://doi.org/10.1016/j.ijhydene.2014.01.004.

[39] P Chin, X Sun, GW Roberts, and JJ Spivey, "Preferential oxidation of carbon monoxide with iron-promoted platinum catalysts supported on metal foams", Applied Catalysis A: General **302**, 22–31 (2006) https://doi.org/10.1016/j.apcata.2005.11.030.

[40] MaterialsHub, *Fecralloy®*, 2021.

[41] O Levenspiel, *Chemical Reaction Engineering*, 3rd ed. (Wiley, 1999).

[42] A Tonkovich, J Zilka, M LaMont, Y Wang, and R Wegeng, "Microchannel reactors for fuel processing applications. i. water gas shift reactor", Chemical Engineering Science **54**, 2947–2951 (1999) https://doi.org/10.1016/S0009-2509(98)00346-7.

[43] TE Tolley, "The feasibility of process intensification of the water-gas shift reaction using differential temperature microreactors", PhD thesis (Oregon State University, 2020).

[44] Graphel, *What is sinker edm?*, 2022.

[45] CW San Marchi, BP Somerday, X Tang, and GH Schiroky, *Hydrogen effects in type 316 stainless steel and SAF 2507 Super Duplex Stainless Steel*, 2006.

[46] J Crane, *Crane-Foil® Packing*, 2020.

[47] RQ Long, *Reformance WGS: non-pyrophoric water gas shift catalyst*, 2020.

[48] Eastman, *Therminol 72 Heat Transfer Fluid*, 2021.

[49] Micropump, *GA series pump heads*, 2021.

[50] Luna, *ODiSI 6000 series*, 2022.

[51] G Gaudin, "Distributed temperature measurement in an additively manufactured heat exchanger using embedded fiber optic sensors", MA thesis (Oregon State University, 2021).